SELF-REGULATED CENTRIFUGAL DEPLOYMENT OF PASSIVE SPACE STRUCTURES

A thesis submitted to the University of Manchester
for the degree of Doctor of Philosophy
in the Faculty of Science and Engineering

2018

Rui Wu
School of Mechanical, Aerospace and Civil Engineering

Contents

List of Tables

List of Figures

Self-Regulated Centrifugal Deployment of Passive Space Structures

Rui Wu, 2018
PhD Aerospace Engineering
The University of Manchester

Abstract

Large lightweight compliant structures can be spin deployed, utilising centrifugal forces to achieve a compression-free stress distribution. The present research starts from the idea that self-regulating passive centrifugal deployment can be achieved when the spinning motion is driven by an environmental torque that is coupled to the deployment condition. In this thesis, the idea is applied to a deployable atmospheric entry heat shield and a heliogyro-type solar sail. The heat shield is based on a flexible fabric shell that induces aerodynamic roll-torque during descent and thus deploys by autorotating. Deployment leads to shape morphing that varies the aerodynamic roll-torque. Passive self-regulated deployment is thereby achieved as the rate of autorotation is determined by the shape, or in other words the deployment condition of the aeroshell. Active deployment modulation using conventional attitude control devices is also proposed, which can provide structural oscillation suppression as well as downrange manoeuvring of over 300 km during simulated re-entry from LEO for vehicles with 3 kg - 5 ton entry mass. Flight characteristics and structural dynamic behaviours are investigated using analytical analyses and numerical simulations. Low-fidelity experiments including low-speed drop test and wind tunnel test are carried out to verify the simulator and validate the design. Owing to its unique operating principle, the design has shown various advantages over existing solutions including inflatable and mechanically deployable systems. Based on the similar principle, the study also proposes a heliogyro that spins up under a torque generated from a meta-structure reflector and thereby deploys centrifugally. The magnitude of the spin-up torque depends on centrifugal-stress and thus realises self-regulated spin and deployment. Meanwhile, the reflector is based on a self-folding origami that can automatically fold up when exposed to sunlight and thus allows fully passive operation. Critical functions of the meta-structure and the heliogyro are proven by numerical simulations, while the self-folding material is validated through laboratory tests. This concept enables a concise system that prevents the structural dynamic issues faced by existing heliogyro designs, and also provides a practical method to realise multi-functional gossamer structures. In conclusion, the study has shown that self-regulated centrifugal deployment could enable new types of deployable space systems that benefit from being lightweight, compact, scalable, concise and robust.

Declaration

No portion of the work referred to in the thesis has been submitted in support of an application for another degree or qualification of this or any other university or other institute of learning.

Copyright Statement

i. The author of this thesis (including any appendices and/or schedules to this thesis) owns certain copyright or related rights in it (the "Copyright") and s/he has given The University of Manchester certain rights to use such Copyright, including for administrative purposes.

ii. Copies of this thesis, either in full or in extracts and whether in hard or electronic copy, may be made **only** in accordance with the Copyright, Designs and Patents Act 1988 (as amended) and regulations issued under it or, where appropriate, in accordance with licensing agreements which the University has from time to time. This page must form part of any such copies made.

iii. The ownership of certain Copyright, patents, designs, trade marks and other intellectual property (the "Intellectual Property") and any reproductions of copyright works in the thesis, for example graphs and tables ("Reproductions"), which may be described in this thesis, may not be owned by the author and may be owned by third parties. Such Intellectual Property and Reproductions cannot and must not be made available for use without the prior written permission of the owner(s) of the relevant Intellectual Property and/or Reproductions.

iv. Further information on the conditions under which disclosure, publication and commercialisation of this thesis, the Copyright and any Intellectual Property and/or Reproductions described in it may take place is available in the University IP Policy (see http://documents.manchester.ac.uk/DocuInfo.aspx?DocID=487), in any relevant Thesis restriction declarations deposited in the University Library, The University Library's regulations (see http://www.manchester.ac.uk/library/aboutus/regulations) and in The University's Policy on Presentation of Theses.

Acknowledgements

I would like to first thank Dr Peter Roberts for the extraordinary advice and inspirations, as well as the freedom he has given to me during my PhD study. The achievement made in this research cannot be decoupled from his insights and knowledge. Working with him has been such a great pleasure that makes me feel three years is so short. My PhD would not be possible without the generous support from Prof. Costas Soutis. To him I would like to offer my deepest gratitude, for his encouragement, motivation, guidance, and the numerous fantastic opportunities he offered during the last five years, which have left such a profound impact on my career that I feel so lucky to have.

I would also like to express my appreciation to Dr Carl Diver and Dr Kate Smith, for their advice and help throughout my study, as well as the opportunities they have offered to me to engage with undergraduate projects. Those experience have become a vital part of my life in Manchester. I am also grateful to Dr Sergey Utyuzhnikov and Dr Shan Zhong for their expert advice, which enlightened the path at the very early stage of this research.

My special thanks goes to my colleague Dr Bradley Robertson Welsh, for all the unforgettable memories, as well as the critical help he has kindly offered when I was trying to find a PhD position. I would also like to thank Yuanhong Ma, Shida Lyu, Fei Zheng, and Lulu Xu for their valuable insights, and the pleasure to work

together with them.

I would also wish to acknowledge Daniel Vidal Rodriguez. His Masters project has become a part of the trajectory simulator, which serves an important role in this research. My acknowledgement also goes to Dr Hugo Ricketts, Dr Peter Hollingsworth, Prof Paulo Bartolo, and Mr Thomas Lawton for their technical support. I would also like to thank the companies 3M and CASIC for providing material samples that are really helpful to the development.

The present PhD project is funded by the School of Mechanical Aerospace and Civil Engineering, University of Manchester Aerospace Research Institute and the Cookson Memorial Fund supported by Professor Henry Wright Baker. I would like to express my appreciation to those funding sources that have given me this great opportunity to learn, to study, to innovate, and to enjoy my life here in Manchester.

I believe the best way to say thanks is to pass the same kindness, the motivation, and the knowledge to other people, and use what I have learned to undertake challenging tasks for the progress of humanity.

Author list of publications

Journal Papers:

Rui Wu, Peter C.E. Roberts, Constantinos Soutis, Carl Diver, *"Flexible Heat Shields Deployed by Centrifugal Force"*. Accepted by Acta Astronautica, In Press, July 2018

Rui Wu, Peter C.E. Roberts, Constantinos Soutis, Carl Diver, *"Downrange Manoeuvre and Oscillation Suppression of a Self-Moderating Centrifugally Deployed Flexible Heat Shield Using Controlled Reaction Wheel"*. Submitted to Acta Astronautica, July 2018

Rui Wu, Peter C.E. Roberts, Lulu Xu, Constantinos Soutis, Carl Diver, *"Flexible Heat Shield with Self-Moderating Centrifugal Deployment: Design Scalability and Low Altitude Drop Test "*. Manuscript to be submitted to Acta Astronautica

Rui Wu, Peter C.E. Roberts, Constantinos Soutis, Carl Diver, *"Heliogyro Solar Sail with Self-Regulated Centrifugal Deployment Enabled by an Origami-Inspired Morphing Reflector"*. Accepted by Acta Astronautica, In Press, August 2018

Rui Wu, Peter C.E. Roberts, Shida Lyu, Constantinos Soutis, Fei Zheng, Carl Diver, Matthieu Gresil, Jonny J Blaker, *"Rigidisation of Deployable Space Polymer Membranes by Heat-Activated Self-Folding "*. Published on Smart Materials and Structures, September 2018

Chapter 1

Introduction

1.1 Background, motivation and scope

Most artificial systems use material stiffness to stabilise a structure and resist loads. The present study starts from the idea of utilising inertial forces induced from motion (acceleration) rather than static (elastic) force to deploy and maintain a structural shape:

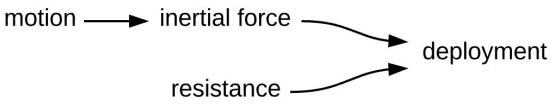

Figure 1.1: Utilisation of inertial forces induced from motion to overcome resistance and achieve structural deployment, centrifugal deployment is a practical example

Spinning motion is used to realise this idea as it can provide a centrifugal force with a constant magnitude while having a constant kinetic energy. To deploy a structure and inhibit deflection using centrifugal force is not a new proposition in the aerospace industry. The well-studied effect of spin on a helicopter rotor is an example of centrifugal stiffening, where the centrifugal force on the rotor increases the

blades' bending stiffness [1]. In the field of space systems, centrifugal deployment has been studied since the 1960s to deploy large space gossamer structures such as solar sails [2, 3, 4], antennae [5, 6], and space webs [7, 8]. It combines centrifugal force and material's tensile stiffness to provide a flexible compression-free structure. This eliminates the risk of buckling and offers advantages including being lightweight, compact, and having low requirements on deployment power [9, 10]. However, these structures are large, lightly loaded, and operate in a low-damping orbital environment, thus the spin-induced dynamic effects including Coriolis forces and gyroscopic moments are significantly stronger than in the well-studied systems such as helicopter rotors [5]. For this reason, in-orbit centrifugal deployment remains a challenge, while controlled spin and optimised deployment sequences are usually employed to stabilise the structure [9, 11, 12].

Meanwhile, centrifugal deployment is controllable by adjusting the spinning motion, and a rarely-explored aspect is that, the dependence on active control can be eliminated if the spinning motion was driven by an environmental torque through a feedback from the deployment condition:

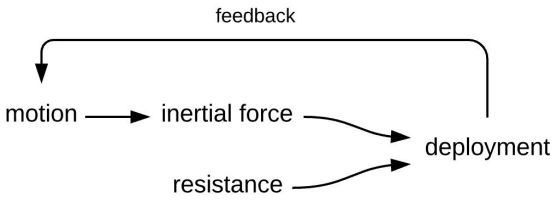

Figure 1.2: Self-regulation of centrifugal deployment is enabled when the motion is depending on the deployment condition, which is the fundamental principle used in the present design studies

Demonstration of such a structural dynamic system can be found in centrifugal governors invented by James Watt in 1788 (Figure 1.3), which is a device widely used to control the speed of steam engines, and is still used in some of today's

combustion engines [13]. Considering the governor mechanism itself, it spins together with the engine and deploys against gravity under the centrifugal force of "flyballs" (ballast weight). The deployment condition of the governor then determines the position of the throttle valve through a linkage and regulates the flow rate of steam, which is the external power source that drives the spinning motion. The closed loop in Figure 1.2 is thereby completed, with the spin rate and the degree of deployment converging to an equilibrium point [14].

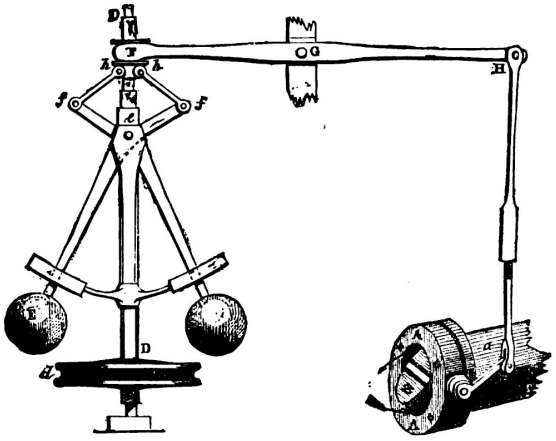

Figure 1.3: James Watt's centrifugal governor used to control the speed of steam engines, which demonstrates the self-regulated centrifugal deployment, with the governor on the left, and a throttle valve on the right [13]

The present study shows that this operating principle can be applied to modern space deployable systems and provide a self-regulated centrifugal deployment that is fully passive. As the result, a flexible deployable heat shield design and a heliogyro-type solar sail concept are proposed, which overcome challenges faced by the existing solutions, while benefiting from simplicity, being lightweight and compact.

1.2 Deployable aerodynamic decelerators

Many space missions require a spacecraft to descend from orbit and soft land onto a planetary surface, or reduce velocity when passing by a planet (i.e. aerocapture). In the case of a planet with atmosphere, this can be done conveniently by dissipating the kinetic and potential energy into heat through atmospheric entry. The most common entry system utilises a blunt heat shield with a high drag profile to decelerate the payload through a ballistic entry. The blunt shape allows most of the heat to be dissipated into the surrounding air, and effectively reduces the velocity [15]. Meanwhile, parachutes are usually deployed at lower speed and altitude to further decelerate the vehicle for a soft landing.

Current Mars landers are based on the Viking heritage system with a rigid blunt aeroshell and a supersonic parachute. However, the thin Martian atmosphere requires a low ballistic coefficient (m/AC_D, where m is entry mass, A is decelerator frontal area, C_D is drag coefficient) for a soft landing. In addition, with the lander size constrained by the fairing diameter of launch vehicles, the payload mass is approaching the limit, and high-elevation Martian surfaces are difficult to access [16, 17]. Since a larger supersonic parachute is not yet a viable solution [18], it is necessary to explore other approaches, such as using a larger heat shield to reduce the ballistic coefficient and effectively decelerate the vehicle at high altitude. This requires the large heat shield to be folded up for storage in a launch vehicle, then deployed before or during entry. Mars exploration, as the frontier of space technology, has attracted numerous researchers into this area since the 1960s [19, 20].

Meanwhile, the demand for a low-cost sample recovery from orbital scientific platforms, which could be based on a CubeSat-class vehicle operating at Low Earth Orbit (LEO), calls for a small Earth re-entry system. Such a system should include

a deployable heat shield to realise a low ballistic coefficient while being accommodated within a small payload volume. The low ballistic coefficient allows a soft landing without a parachute, thus only one step of deployment is needed during re-entry, and the vehicle can burn up in case of deployment failure, which makes the system safe and robust. Furthermore, since a smaller vehicle has a higher surface-to-area ratio and a higher surface curvature, a reduced ballistic coefficient is beneficial for effective thermal control [21]. A few efforts towards recovering payloads from LEO have been reported, which adapts either deployable or rigid aeroshells [22, 23, 24, 25, 26]. In addition, such entry systems can also find applications in launch vehicle assets recovery [27], or enable new types of planetary exploration missions using small vehicles as secondary payloads or probe swarms [28, 29, 30].

To address these demands, three types of deployable aerodynamic decelerators have been investigated: inflatable decelerators, mechanically deployed decelerators, and rotary wing decelerators, which are discussed in §1.2.1 - §1.2.3.

1.2.1 Inflatable aerodynamic decelerators (IAD)

IAD is an inflatable structure connected to the rigid entry vehicle to induce extra drag. It utilises inflatable chambers fabricated from flexible air-tight materials and maintains a stable shape under internal pressure raised by gas generators, ram-air, or both [18, 31]. The concept of IAD has been around for over five decades, with various configurations analysed and tested [32, 33]. However, since the Disk-Gap-Band supersonic parachute has satisfied the mission requirements so far, little development has been seen after the mid-1970s until recent years. As Mars robotic systems are becoming increasingly sophisticated, and with manned Mars missions on the agenda, the interest in IAD is renewed. Figure 1.4 shows the two typical

IAD configurations: trailing IAD and attached IAD [18].

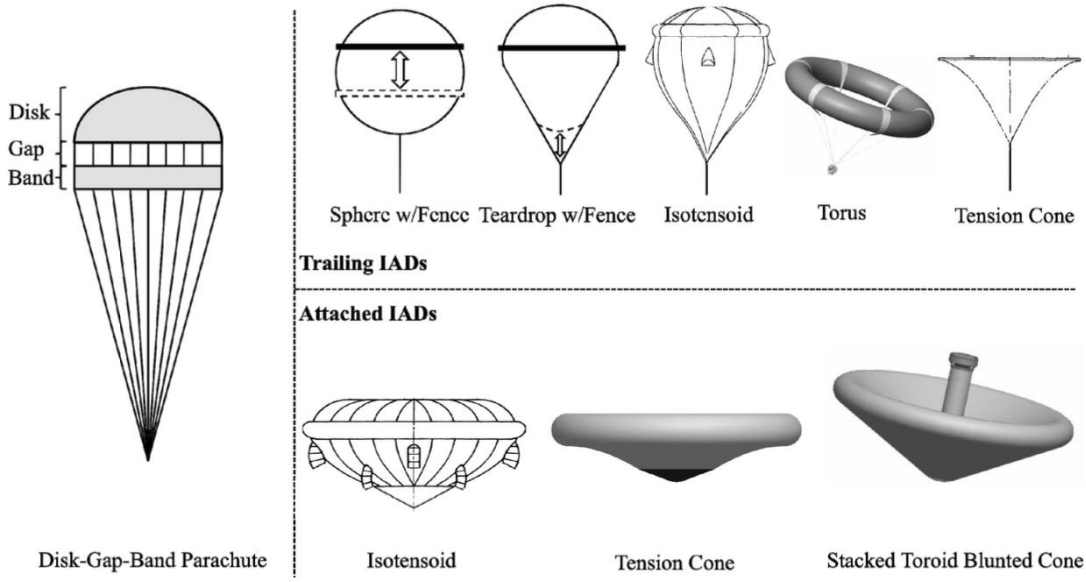

Figure 1.4: Examples of typical Disk-Gap-Band supersonic parachute, trailing IADs and attached IADs [18]

Trailing IAD

Similar to a parachute, trailing IAD is tethered to the entry vehicle. The fact that it combines the features of a "balloon" and a "parachute" gives it another name "ballute" [34, 35]. In comparison with the attached IADs, a ballute usually generates lower drag and therefore is less efficient in terms of structural mass since it operates in the wake of the rigid entry vehicle, where the dynamic pressure is lower than freestream. The flow unsteadiness also complicates the dynamic behaviour of the system, making the exact behaviour difficult to analyse [18]. Meanwhile, the reversed flow induced by the ballute increases heating to the backside of the vehicle, thus requires a massive backshell [35]. Despite the disadvantages, trailing IAD is viewed as a candidate for planetary aerocapture missions since the drag can be "turned off" mid-flight by simply detaching the ballute from the vehicle

(which can be difficult for attached IADs). This reduces the effect of atmosphere uncertainty and improves trajectory precision [35, 36].

Attached IAD

Attached IAD is directly connected to a blunt entry vehicle with no aerodynamic component operating in the wake, allowing higher drag generation than the trailing IADs especially at high Mach numbers [18]. The structural dynamic behaviour is also more predictable [37, 38]. Meanwhile, utilisation of attached IAD can reduce the aft side heating on the entry vehicle, thus eliminating the vehicle backshell. This saves structural mass, enables easy access to the payload and reduces system complexity [39].

The present study focuses on developing an attached deployable aerodynamic decelerator rather than a trailing one for its potential advantages mentioned above. The three existing types of attached IADs are shown in Figure 1.4, including attached isotensoid, attached tension cone, and stacked torus, as discussed below.

Attached isotensoid

Attached isotensoid was first proposed in the late 1960s. It has a shape that induces uniform stress in the bladder material under a specified internal and external pressure distribution. This prevents wrinkles and allows a simple and lightweight construction with constant material thickness throughout the inflatable chamber [33]. Typical attached isotensoid is shown in Figure 1.5, which is inflated by ram-air through the inlets. It uses a burble fence to regulate the flow separation in order to remain stable at subsonic speed [40].

However, the ram-air inlet and the burble fence induce stress discontinuities as

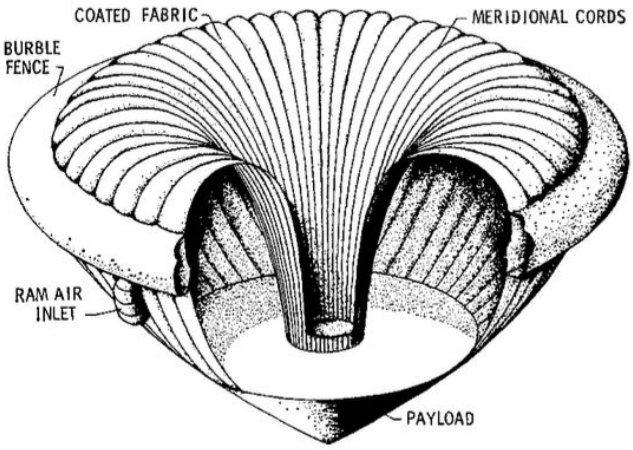

Figure 1.5: Cutaway view of a typical attached isotensoid [33]

well as severe heating during hypersonic flight. The limited drag coefficient from the isotensoid shape also prevents it from achieving high structural efficiency [41].

NASA's Low Density Supersonic Decelerator (LDSD) Project has recently developed two attached IADs for future Mars missions, one of which is an inflatable isotensoid with a 8 m diameter attached to a 4.7 m rigid aeroshell [42]. It is designed to deploy at Mach 4 and a dynamic pressure of 2000 Pa. Gas generators are used for initial inflation, while full inflation is achieved by ram-air [43].

Attached tension cone

Tension cone, also known as tension shell, was proposed in the mid 1960s and revisited in recent years [44, 45, 46, 47]. It consisted of a thin conical shell with the frontal edge attached to a rigid blunt aeroshell and the trailing edge attached to an inflatable torus. The name "tension cone" comes from the fact that the conical shell is tensioned and stabilised by the torus. Figure 1.6 shows a typical design [48].

Tension cones have the potential to be lightweight in comparison with isotensoid

Figure 1.6: Front view of a tension cone IAD wind tunnel model under aerodynamic pressure [48]

when designed to deploy at a low dynamic pressure [49]. Studies have also suggested that simple structural reinforcement can be used to stiffen the structure and reduce inflation pressure requirement at little expense of structural mass [48]. However, the conical shell inevitably forms a concave shape under aerodynamic load (Figure 1.6), which can induce attached shock waves that lead to excessive heating and may hinder its application for hypersonic flight [18].

The Japanese "flare-type membrane aeroshell" which has successfully performed a sub-orbital test in 2012, uses a tension cone design. It has a diameter of $1.2\,m$ and survived re-entry at Mach 4.6 and a dynamic pressure of $500\,Pa$, and stable flight was achieved despite of the flexibility of the tension cone structure [50, 51, 52].

Stacked torus

Stacked torus is a promising design developed in the Inflatable Re-entry Vehicle Experiment (IRVE) by NASA's Hypersonic Inflatable Aerodynamic Decelerator

(HIAD) project [53, 54]. It can be viewed as a derivative from the tension cone configuration, where the tension shell is supported by a stack of tori and thus achieves significantly higher structural stiffness and more stable aerodynamic profile [55]. This allows the IAD to be used during a hypersonic entry and reliably form a wide variety of shapes with high drag coefficient including lift-generating bodies with unsymmetrical characteristics [56, 57].

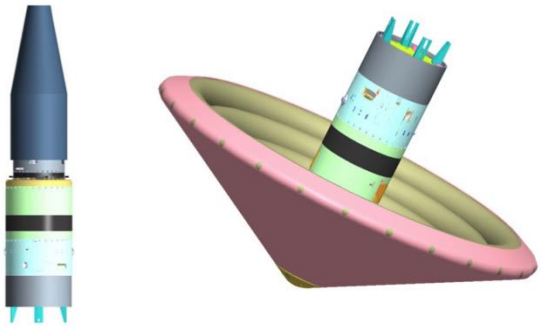

Figure 1.7: Stacked torus IAD on the IRVE-4 vehicle under stowed (left) and deployed (right) conditions [54]

Three IRVE vehicles similar to Figure 1.7 have been successfully tested through sub-orbital flights, reaching a speed of Mach 10, a peak deceleration of 20 g, and a peak heating of 14 W/cm^2 [38, 39, 58]. The decelerator consisted of seven toris with the maximum diameter of 3 m inflated by internal gas generators. A scaled-up version with 8.3 m diameter and 5 ton entry mass is also proposed [59]. Other designs that use extra inflatable chambers to reinforce a tension shell have also been reported, such as the inflatable Re-entry and Descend Technology (IRDT) vehicle developed and tested by ESA [60, 61, 62, 63, 64].

The high structural stiffness of stacked torus IADs allows none-zero angle of attack (AoA) and thus enables lifting manoeuvres. The manoeuvre can be realised by steering (rolling) the vehicle with a Centre of Gravity (CG) offset or an unsymmetrical aeroshell, or actively moving the CG [54, 57, 65, 66]. Unconventional

methods have also been proposed, including mechanically distorting/morphing the shape of the IAD [67, 68], or using a controlled flap [69].

Flexible Thermal Protection Systems (FTPS)

Thermal protection is an important restraining factor of IADs, which can occupy a significant portion the decelerator's mass as well as stowage volume. Unlike conventional rigid heat shield, a deployable decelerator requires Flexible Thermal Protection System (FTPS) to protect the structure while allowing stowage. Since delicate elastomers such as silicone coatings are used on the inflatable chambers to achieve air-tightness, the chamber surface temperature is limited to $250°C$ [70]. This thereby requires thick FTPS materials to warp around the inflatable structure. Various commercial off-the-shelf products have been validated by high temperature wind tunnel tests, with 3M^{TM}Nextel^{TM}BF-20 woven ceramic fabric identified as a suitable heat-resisting frontal layer [71, 72, 73, 74, 75]. Figure 1.8 is the FTPS layup used on the flight-proven IRVE-3 vehicle which survived $14 W/cm^2$ heating. It consisted of Nextel^{TM}frontal layers, Pyrogel® insulating layers, Kapton^{TM}gas barriers as well as a Kevlar^{TM}structural layer [70]. The HEART vehicle concept has provided a mass estimation, where FTPS with a similar layup weighs 1.4 times of the inflatable bladders [59].

1.2.2 Mechanically deployed decelerators

Deployable mechanisms based on hinges, sliding joints and rigid linkages, such as umbrella, have been evolving for a long time. They have achieved impressive packing ratio, lightweightness, and strength.

In 1959, AVCO-Everett Research Laboratories developed a variable area air brake

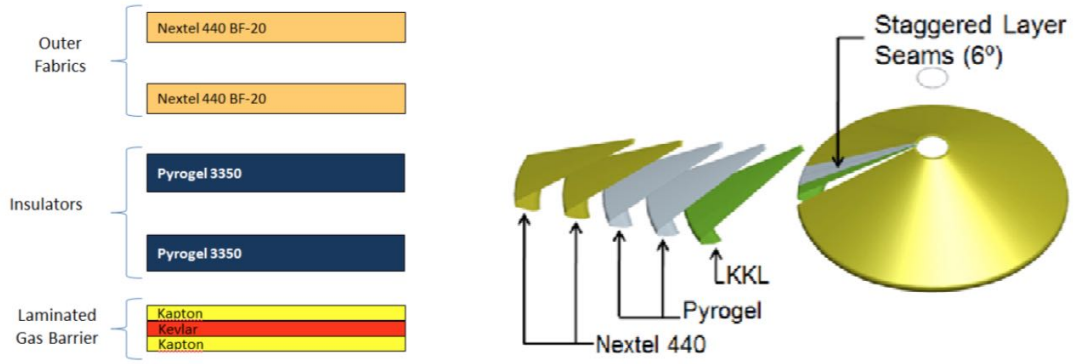

Figure 1.8: FTPS layup used on the flight-proven IRVE-3 vehicle, including temperature-resisting frontal layers, insulating layers and gas barriers [70]

system based on hinged flaps for a manned capsule to enable various manoeuvres [76]. The development was affected by the lack in high strength materials at that time, and the adaptation of the design has not been reported. In 1989, an umbrella-like deployable heat shield called ParaShield was developed in the University of Maryland [77]. In 1996, a ParaShield consisted of flexible silicon-oxide skirt and titanium arms was proposed for the return of BREM-SAT-2 satellite with 86 kg entry mass [78].

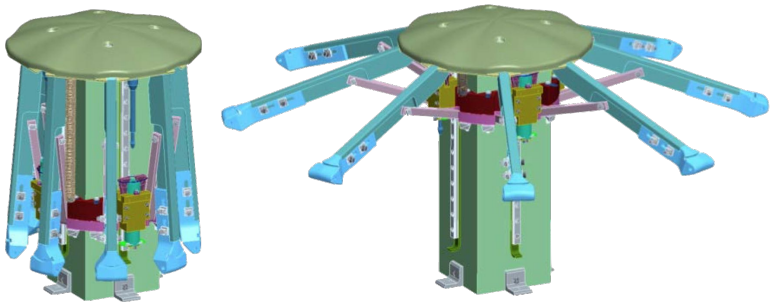

Figure 1.9: ADEPT mechanically deployed vehicle consisted of deployable struts and flexible carbon fabric skirt (skirt not shown) [79]

An increasing number of design concepts have been reported since the beginning of the new century. The most studied concept is NASA's Adaptive Deployable Entry Project (ADEPT), which uses ribs and struts to deploy and support a 3D woven

carbon fabric skirt, forming a near-rigid aeroshell with either axisymmetrical or unsymmetrical shape [80]. Various design variations are proposed for a range of missions, including manned mission to Mars [81], CubeSat-sized probe to Mars [82], low ballistic entry system to Venus [83], as well as small payload recovery to Earth [84]. Other umbrella-like design concepts include the Italian Re-Entry Nacelle (IRENE) [85, 86], the CubeSat De-orbit and Recovery System (DCRS) [22], and another study has proposed an adjustable heat shield that can control the degree of deployment for de-orbiting control, then fully deploy during entry [87].

Another design called Tube Deployed Re-entry System (TDRV) uses an uncommon but concise configuration with a slender cylindrical front body and a flat-disk-shaped skirt loosely supported by four struts. During a sub-orbital test at near Mach 5, it recovered from a tumbling motion despite the extreme structural flexibility [25].

1.2.3 Rotary wing decelerators (RWD)

In 1959, deployable rotors have been proposed to assist the Entry Descent and Landing (EDL) of conventional entry vehicles [88, 89]. The proposed design has a unpowered helicopter-like rotor that spins up in upward stream and utilises the local horizontal velocity induced by the autorotation to generate lift. The lift therefore decelerates the vehicle and enables landing manoeuvres. It follows the operating principles similar to an autogyro [90]. Figure 1.10 shows a typical rotary wing decelerator proposed for a NASA crewed vehicle [91].

However, wind tunnel tests have suggested that high lift-drag ratio ($L/D > 2$) can be achieved only at $<$ Mach 0.3 descent rate when the rotor is not stalled

Figure 1.10: NASA Mars crewed vehicle concept equipped with a free-spinning foldable rotary wing decelerator that deploys at subsonic speed and stratosphere altitude, to enable precise landing manoeuvres [91]

and the local dynamic pressure experienced by the rotor blades can be notably higher than the freestream [92]. Furthermore, the rotor cannot be deployed during the hypersonic flight regime without over-speeding unless precise pitch control is implemented [93, 94]. Deployment during the flight regime with severe heating has to be strictly avoided since the blade experiences high heat flux as a result of its inevitably high surface curvature and shock impingement from the capsule body [95]. Therefore, later designs usually have the RWDs deployed at supersonic or subsonic speed including a NASA four-rotor foldable Venus descending system [96], a single rotor NASA crewed vehicle with foldable blades (Figure 1.10) [91], an ESA Martian lander with a inflatable rotor [97], and a NASA probe to Titan [98]. In these concepts, the proposed mass ratio of the rotor system in the vehicle gross weight is usually close to 15%, which is similar to IADs [59]. However, the rotor decelerator is an improved alternative for parachute to enhance landing performance rather than optimising the whole entry trajectory, thus will not provide a solution for Mars heavy entry system or small sample return vehicle/probe as mentioned at the beginning of §1.2.

Although RWD is not a solution to the entry problem in the scope of the present study, it is discussed here because it not only demonstrates autorotation and centrifugal stiffening, but also has the potential to achieve self-regulated passive operation. In fact, the rotor decelerator design was first reported in the 1940s, known as Rotochute (combination of words "rotor" and "parachute"), and was intensively studied as an aerial delivery system by the Kaman Aircraft Corporation during the 1950s [92]. It uses a slender vehicle with a variable-pitch rotor at the rear end. The rotor blades are folded back when the Rotochute leaves the aircraft, then deploys under centrifugal force due to auto-rotation. The blade pitch is regulated by an empirically designed spring-loaded centrifugal governor to limit the spin rate to a prescribed value. The deployment angle of the blades also reacts to the spin rate and descent velocity [99, 100].

It is therefore a self-regulating passive centrifugal deployment, where the spinning motion is generated by harvesting the descending kinetic energy, and the blade deployment determines the blade pitch and thereby regulates the autorotation. However, no passive governor has been proposed in the RWD entry systems, which usually use active blade pitch control to serve the purpose of landing manoeuvre.

1.2.4 Summary of deployable aerodynamic decelerators

To realise an entry system that can be stowed in a limited volume and deploy to achieve low ballistic coefficient, various deployable aerodynamic decelerators have been developed.

Inflatable Aerodynamic Decelerator (IAD) is intuitively a reasonable solution to a lightweight deployable structure since it combines the superior tensile strength of

flexible fibrous materials (inflatable bladder material) with the compressive resistance of gas, and gas is the ultimate flexible and lightweight material. However, inflation requires an actively controlled gas storage system or gas generator that adds weight and complexity to the system, or ram-air inlets that limit the flight regime to super/subsonic due to excessive local stress and heating. Meanwhile, the flexible air-tight materials used on the pressurised chamber require a low operating temperature, which means a massive Thermal Protection System (TPS) is usually needed.

The umbrella-like deployable mechanism is a conventional and straightforward approach. According to a low-fidelity analysis, mechanically deployed decelerators tend to provide higher payload mass fraction and thus are advantageous to the stacked tori IADs when the decelerator is large ($> 6\,m$ diameter) and ballistic ratio is high ($> 20\,kg/m^2$) (note that a precise and detailed comparison between the two types of deployable decelerators is not yet viable due to the immaturity of both and the lack in high fidelity design studies) [83]. However, it is difficult for the mechanically deployed decelerators to achieve the stowage compactness of an IAD due to the constraint from rigid structural components.

Rotary Wing Decelerator (RWD) can slow down a spacecraft or an aerial vehicle and enable manoeuvres during the final descent and landing. However, the excessive aerodynamic heating on rotor blades as well as the risk of over-spin has limited its application to super/subsonic speed and lower altitude. Nevertheless, it demonstrates a self-regulated passive centrifugal deployment, thus has similarity to the decelerator design proposed in the present study.

Meanwhile, centrifugal deployment, which is particularly useful in deploying a large axisymmetric structure, has not been explored in the field of EDL systems. Although in-orbit centrifugal deployment of large space structures is still a challenge,

a spin-deployed aerodynamic decelerator operates in a damping environment (atmosphere), and has significantly higher structural stiffness than a gossamer space structure, thus can be more easily stabilised. The potential of realising a robust and concise system with self-regulating passive operation also remains to be explored.

1.3 Solar sailing

In comparison with aerodynamic decelerators, gossamer spacecraft such as solar sails have significantly stricter requirement on structural weight and packing ratio, which makes it an early adopter of centrifugal deployment.

The vision of utilising Solar Radiation Pressure (SRP) to propel a spacecraft was first recorded in 1610 by Johannes Kepler, who observed the inclination of comet tails due to solar radiation: "...provide ships or sails adapted to the heavenly breezes, and there will be some who will brave that void" [101]. Efforts towards the technical realisation of this vision started in the 1960s [102, 103], and the existing solar sail design concepts can be classified into three types [101]: rigid solar sails, spinning disk sails, and heliogyros, which are discussed in §1.3.1 - §1.3.3.

The acceleration gained from SRP, a_{SRP} follows the relationship below, where m is the vehicle mass, S_{sail} is the sail area, and σ_{sail} is defined as the sail loading [101]:

$$a_{SRP} = \frac{P_{SRP} \cdot m}{S_{sail}} = \frac{P_{SRP}}{\sigma_{sail}} \tag{1.1}$$

It can be seen that minimising the sail loading is crucial for maximising a_{SRP}. Therefore, solar sails strongly demand a lightweight compact reflector that can

deploy to realise a very large sail area. As a result, centrifugal deployment has been considered since the early stage of its technological development in the 1960s, as seen in the spinning disk sail and heliogyro designs.

In addition, solar sail technology could also benefit other gossamer space structures such as solar wind electric sails [104] and drag sails [105].

1.3.1 Rigid solar sails

Rigid solar sail uses rigidisable deployable structures [106, 107], inflatable booms [108] or deployable mechanisms [109] to form a skeleton, which provides overall stiffness against structural loads from SRP and flight manoeuvres. The reflective sail membrane can be stowed compactly as a folded origami and then unfolded when stretched out from the package by the skeleton. Figure 1.11 provides an example, where a Kapton film is unfolded and supported by deployable Carbon Fibre Reinforced Polymer (CFRP) booms [110].

However, due to the nature of elastic rigidity, the supporting skeleton does not scale up well. Studies suggest that rigid sails become increasingly disadvantageous in comparison with centrifugally deployed sails when the sail area exceeds approx. $50,000\,m^2$, due to the high structural mass required to overcome Euler buckling limit [111]. However, the rigid sail is a typical configuration among early demonstrators [112, 113].

1.3.2 Spinning disk sails

The spinning disk sail achieves a compression-free condition under the spin-induced centrifugal force, thus eliminating the elastically rigidised supporting structures

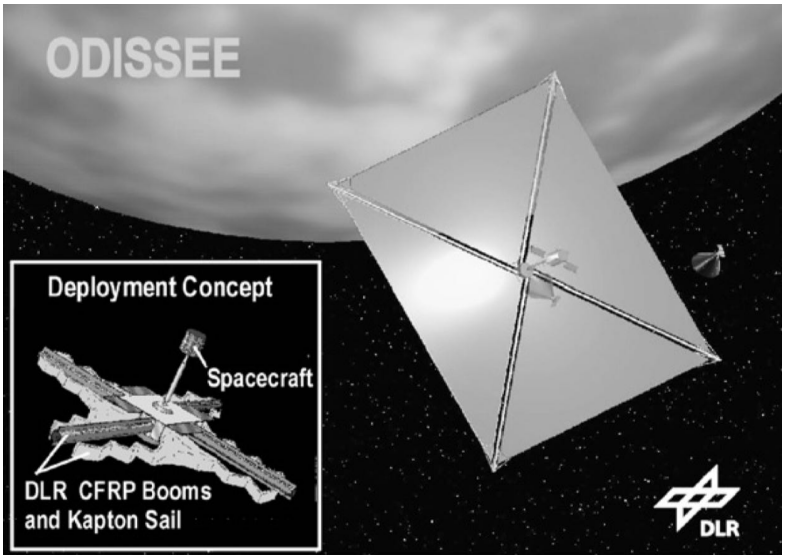

Figure 1.11: Solar sail demonstrator designed by DLR, which utilises a rigid sail architecture with 10 m rigidisable booms that form a deployable load-carrying skeleton [110]

and thereby the risk of buckling [111]. Deployment of this type of structure was first successfully demonstrated in 1993 [9], and the first interplanetary solar sail IKAROS launched and deployed by JAXA in 2010 was a spinning disk sail (Figure 1.12) [114]. IKAROS uses a $14\,m \times 14\,m$ square sail centrifugally deployed from a $1.6\,m$ diameter central vehicle following quasi-static deployment steps [12, 115]. It has also demonstrated propellant-less attitude manoeuvres using Reflectance Control Devices (RCD) [4, 116]. The RCD, which is similar to a Liquid Crystal Display (LCD), has controllable reflectivity and thus varies the magnitude of SRP [117, 118].

However, although a spinning disk configuration is naturally suitable for large sails from a sail loading point of view [111], folding of an origami sail becomes increasingly challenging for a larger reflector. This is not only due to the practical difficulties of folding the sail, but also because the increasing film-thickness-effect restricts the packing ratio [119, 120].

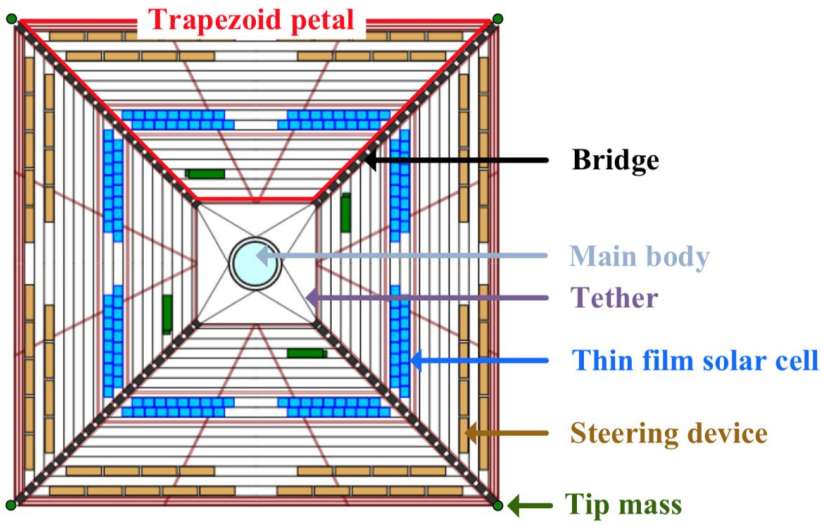

Figure 1.12: Interplanetary spinning disk sail, IKAROS, developed by JAXA, which demonstrates quasi-static centrifugal deployment as well as propellant-less attitude control using Reflectance Control Devices (RCD) [114]

1.3.3 Heliogyros

First proposed in the 1960s [2], the heliogyro is also centrifugally deployed and stiffened, but unlike a disk sail, it uses slender rectangular reflectors that resembles helicopter rotor blades (Figure 1.13) [3]. This enables a concise and elegant system, where the sail can be stowed by simply winding onto a mandrel on the central vehicle rather than folding along complicated patterns like a disk sail, thereby providing the optimum packing ratio. Six Degree of Freedom (DoF) attitude manoeuvres can be achieved by actively adjusting the pitch of the blades similar to a helicopter rotor. In the late 1970s, NASA has proposed an ambitious Halley Rendezvous sailer with twelve $8\,m \times 7.5\,km$ blades [121]. However, the sheer blade slenderness ratio and the spinning motion lead to complex dynamic behaviours, which is further complicated by the blade pitch control as it induces blade twisting-distortion and out-of-plane deflections [122, 123, 124].

Very few design concepts have been reported until recently, as the successful

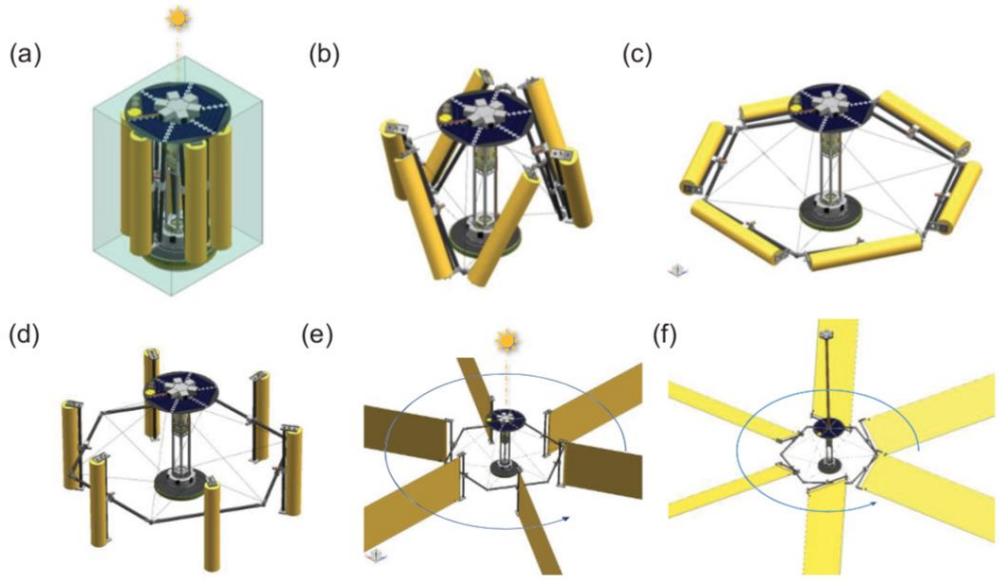

Figure 1.13: Heliogyro demonstrator designed by NASA, which is a 18.3 kg vehicle with six 0.75 $m \times 200\,m$ blades rotating at $\sim 1\,rpm$, note that the blades are centrifugally deployed by rolling-off from mandrels, and the mandrels actively adjusts the blade pitch to realise attitude manoeuvres [3]

IKAROS mission in 2010 has renewed the interest in solar sailer technologies within NASA [125], and low-cost demonstrator concepts have started emerging. The concept named HELIOS uses a conventional design with six 0.75 $m \times 200\,m$ blades (Figure 1.13). Enabled by modern computational tools, studies based on HELIOS have been carried out to understand its dynamic and solar-elastic behaviours, which have suggested that an actively controlled spin rate is required to prevent flutter especially during deployment [125, 126]. Tip-mounted RCD is also proposed for active blade pitch control, which could significantly improve the blade twist (pitch) dynamics [127, 128, 129]. Another conceptual design of a 2-blade CubeSat-based demonstrator has proposed an innovative attitude control method where the blades are actively extended/retracted to offset the centre of SRP from the centre of mass and thereby steer the spacecraft [130]. This design overcomes the complexity of blade twisting behaviours as it keeps the blades flat

during manoeuvres, though the effect of rapid change in angular inertia caused by such control remains to be explored.

It worth noticing that the utilisation of RCD has created an innovative solution to the heliogyro control problem, which varies the material's response to sunlight rather than directly inducing structural distortions. However, RCD only controls the magnitude of SRP, while more advanced active materials with adjustable SRP direction, if possible, could potentially be used to achieve flight control while inducing less structural deformation and realise a more intelligent system.

1.3.4 Advanced space gossamer materials

Expanding the functionality of materials can relieve the requirement on supporting structures, actuators and controllers, thus enabling a lightweight, concise, and potentially intelligent system [131, 132, 133]. Advances in space gossamer materials could benefit or even radically change the design of solar sails as well as other gossamer spacecrafts.

Shape memory alloys or polymers can return to a pre-defined shape from a highly distorted configuration, or achieve active shape control without using complicated actuators and controllers [134, 135]. Similarly, a lightweight porous material made of interlinked short fibres called "microtruss fabric" can elastically return to a designed shape owing to its high elastic limit [136]. Self-rigidising composites can rigidise an inflated bladder using resins that cure when exposed to ultraviolet radiation in space, and acquire structure stiffness without maintaining gas pressure [137]. Electroactive morphing materials such as piezoelectric ceramics can actively damp vibrations or induce precise structural distortions while allowing a flexible and lightweight construction [138, 139, 140]. Membranes with residual

stress can automatically roll-up into a cylinder when unconstrained, and realise a self-assembled structural reinforcement [123]. Flexible thin film solar cells can be embedded into gossamer membranes to harvest solar energy and supply power to actuators and controllers, thereby eliminating the need for other power sources [4].

On the other hand, recent advances in origami meta-structures and self-folding smart membranes could provide a new type of advanced space gossamer material, which can transform from a 2D sheet into a 3D structure by environmentally-triggered folding along an origami crease pattern. The folded origami can realise design-able mechanical properties and load-carrying capability. It could also serve as a building block for future tuneable meta-structures with built-in functionalities [141, 142, 143, 144, 145]. Meanwhile, various self-folding smart materials have been reported, with morphing activated by environmental changes such as heat and light [146, 147, 148], and self-folding along origami patterns have been proven possible [149, 150].

However, smart space gossamer materials of this type have not been reported so far, and no self-folding membrane has been developed with space applications in mind, while low-cost mass-production is usually not feasible.

1.3.5 Summary of solar sailing

In order to maximise the Δv gained from solar propulsion, the major objectives of a practical solar sail design are: minimising structural mass, and maximising sail area. Therefore, among the three existing sail configurations, the option of rigid sails can be eliminated since the reliance on elastic structural rigidity makes it disadvantageous. The spinning disk configuration is also questionable for very large sails due to the issue of packaging. Heliogyro, for which the behaviour is not

thoroughly understood, and no orbital test has been attempted, tends to be the most scalable configuration among the three.

One of the issues faced by the heliogyro is the complex and uncooperative structural dynamic behaviours of the extremely flexible structure in a low-damping space environment. With the interest in heliogyro renewed in recent decades, researchers are proposing solutions including actively controlling the spin rate during deployment to avoid unstable regimes, and utilising Reflectance Control Devices (RCD) to damp blade oscillation.

On the other hand, developments in smart materials such as RCDs and thin film solar cells have extended the functionality of gossamer space structures. Similarly, self-folding origami membranes, if feasible, could create a new paradigm that provides a universal design methodology. It could allow mechanical, and potentially other physical properties such as optical properties, to be "programmed" into the gossamer structure by converting the membrane into an origami meta-structure. Combined with a space-grade and mass-producible self-folding material, such gossamer structure could enable an intelligent system that self-assembles and operates passively.

1.4 Research contributions and thesis structure

The present study starts from the understanding that a self-regulated passive centrifugal deployment can be achieved if the spinning motion was driven by an environmental torque with passive feedback from the deployment condition. The study demonstrates that this principle can be applied to deployable space systems whilst realising an elegant design that is concise, lightweight, and can be compactly stowed. Specifically, in this thesis, two deployable systems are developed, which

respond to the demand from two particular space applications: deployable atmospheric entry system and solar sail. The thesis is therefore divided into two parts: centrifugally deployed flexible aerodynamic decelerator; and passive centrifugal deployment of heliogyro.

The major research contributions to the field of deployable entry systems include:

1. Proposed a heat shield design with self-regulated passive centrifugal deployment, based on an autorotating flexible stitched fabric shell with a spin rate determined by its deployment condition;

2. Revealed its potential to realise a concise deployable entry system with less critical components, higher tolerance to heating thus lightweight thermal protection system, better stress distribution thus lower structural mass.

3. Demonstrated a method to actively control the deployment using conventional attitude control devices, which enables downrange manoeuvre and structural oscillation suppression with a concise control algorithm;

4. Provided a scaling law, and demonstrated its excellent scalability, which makes the design suitable for a wide variety of missions from landing heavy payloads on Mars to sending swarms of miniaturised probes, with the vehicle entry mass ranging from 5 ton to 30 g.

The major research contributions to the field of solar sails include:

1. Proposed a heliogyro-type solar sail with meta-structure reflectors to enable passive self-regulated spin and deployment;

2. Demonstrated its ability to follow a “programmable” deployment history, as well as its quasi-static operation that prevents structural dynamic issues;

3. Designed an origami meta-structure with high level of control over solar

radiation pressure and design-able mechanical properties;

4. Proposed a smart space membrane with self-folding behaviour triggered by sunlight, which is based on commercial space-grade materials and is mass-producible.

The specific thesis structure is described below:

- Chapter 1 presents the main research idea of utilising self-regulated passive centrifugal deployment in space systems, as well as the two specific objectives demonstrated by a survey of the demand for deployable aerodynamic decelerators and solar sails.

Part I describes the development of the deployable heat shield, which contains three chapters based on three standalone but related studies:

- Chapter 2 includes a published paper where the baseline design of a CubeSat-sized vehicle with a centrifugally deployed flexible heat shield is proposed. Analytical analyses and numerical simulations are used to predict the dynamic behaviours of the heat shield during atmospheric entry and demonstrate its self-regulating passive centrifugal deployment. The study also shows the potential benefits including being lightweight, compact, and having a reduced surface temperature.

- Chapter 3 is based on another submitted paper that demonstrates the active deployment control of the heat shield proposed in Chapter 2. With a clearer understanding of the heat shield system, an active control loop is added into the self-regulating system using a reaction wheel. It achieves considerable downrange manoeuvrability and suppresses the limit-cycle structural oscillation of the heat shield during simulated re-entry.

- Chapter 4 contains another paper, which shows that the vehicle can be scaled

to have entry mass between $30\,g - 30\,ton$ to allow a variety of missions while having advantages over existing solutions. Ground experiments and drop tests are carried out to verify the trajectory simulator while revealing the low-speed flight dynamics.

Part II describes the development of a heliogyro-type solar sail, and consists of two chapters, capturing the two aspects of the proposed design concept:

- Chapter 5 includes a submitted paper on a heliogyro concept with self-regulated passive centrifugal deployment. The design uses an origami meta-structure reflector to propel the rotation of the heliogyro while achieving a closed-loop passive control over spin rate and sail deployment. Simulations are used to demonstrate its ability to follow a pre-defined spin rate history during deployment, while preventing over-spin after full deployment. Meanwhile, the sail remains flat and thereby has simplified dynamic behaviours.
- Chapter 6 contains a submitted paper, which proposes a self-folding membrane that transforms a 2D reflective film into the 3D meta-structure reflector of Chapter 5 upon exposure to sunlight. The smart membrane is based on space-qualified materials and is potentially mass-producible. The heat activated formation of the origami reflector is demonstrated in the laboratory.

Finally, Chapter 7 summarises the achievements presented in this thesis, with conclusions drawn, and future works suggested.

Part I

Application to Deployable Aerodynamic Decelerators

Chapter 2

Passive centrifugal deployment of a CubeSat re-entry heat shield

This chapter includes a published paper where the baseline design of a CubeSat-sized vehicle with a centrifugally deployed flexible heat shield is proposed. Analytical structural dynamic and aerodynamic models are constructed, compared to numerical simulations, and incorporated into a trajectory simulator. The simulator is then used to predict the dynamic behaviours of the heat shield during atmospheric entry and demonstrate its self-regulating passive centrifugal deployment. The paper also illustrates the benefits of utilising centrifugal deployment on an aerodynamic decelerator, including being lightweight, compact, and having a reduced structural temperature.

2.1 Paper I: Design concept and preliminary analyses

Flexible Heat Shields Deployed by Centrifugal Force

Authors: Rui Wu, Peter Roberts, Constantinos Soutis, Carl Diver

Journal: Acta Astronautica, (**Impact factor:** 1.536)

Publication date: July 2018

Statement of own contributions in joint authorship:

Main research idea and technological development;

Preparation of tables, figures, and the manuscript;

Modelling and analytical analysis;

SIMULINK structural dynamic model construction and incorporation into pre-existing trajectory simulator, MATLAB program development for result interpretation;

ANSYS Finite element transient structural analyses.

Statement of other contributions:

The 3 DoF trajectory simulator, which is a part of the SIMULINK model, is constructed by Daniel Vidal Rodriguez during his Masters project.

Note: Supplementary material is available in Appendix A.1 and A.2.

Flexible Heat Shields Deployed by Centrifugal Force

Rui Wu[a,*], Peter C.E. Roberts[a], Constantinos Soutis[b], Carl Diver[a]

[a] *School of Mechanical, Aerospace and Civil Engineering, UK*
[b] *The University of Manchester Aerospace Research Institute, UK*

Abstract

Atmospheric entry aerodynamic decelerators which also provide thermal protection do not scale well for smaller payloads (e.g. CubeSat) or where the planets atmosphere is significantly less dense than the Earth's (e.g. Mars entry). Both cases require heat shields larger than can be accommodated either within the launch vehicle fairing, or within acceptable payload volumes, so deployable shields are required. Unlike previous designs proposed to fulfil this requirement like inflatable structures or deployable solid mechanisms, the presented research addresses this by utilising inertial force, or specifically, centrifugal force generated from autorotation to deploy and stiffen a flexible heat shield. Structural dynamic analyses including the trajectory simulation on a CubeSat sized system has shown that the autorotation and deployment form a closed loop which reliably leads to an equilibrium of deployment, while the heat shield is near fully deployed at altitudes higher than 30 km with tolerable spin rate (< 6 rps) and oscillation. Thermal analysis suggests that a front surface temperature reduction of 100K is achievable on a CubeSat sized vehicle as unlike inflatable structures, no thermal insulation is needed around the flexible material. This design concept can realise a lightweight, compact and concise entry system.

*Corresponding author
Email address: rui.wu@manchester.ac.uk (Rui Wu)

Keywords:
heat shield, entry vehicle, deployable aerodynamic decelerator, centrifugal deployment, origami, aeroelastic oscillation, thermal protection, morphing

---

Nomenclature

a	=	ratio of the first stage diameter in the second stage generatrix length
a_{dec}	=	deceleration (m/s^2)
C_D	=	drag coefficient
d	=	heat shield thickness (m)
e	=	surface emissivity
$f_{struc.}$	=	structural natural frequency (Hz)
f_{pitch}	=	aerodynamic pitching frequency (Hz)
f_ω	=	spin rate of autorotation in Hz (Hz)
I_{deploy}	=	shell's angular inertia associated with its deploying motion ($kg \cdot m^2$)
I_{spin}	=	spin angular inertia of the vehicle ($kg \cdot m^2$)
k	=	maximum angle of autorotation per unit descent (rad/m)
l	=	length along generatrix (m)
L	=	length, or the generatrix length of the flexible second stage (m)
m	=	mass (kg)
M	=	total deploying moment ($N \cdot m$)
M_{FC}	=	Deploying moment caused by centrifugal force ($N \cdot m$)
M_g	=	Deploying moment caused by deceleration ($N \cdot m$)
M_{load}	=	Anti-deploying moment caused by load ($N \cdot m$)
NC	=	normalised conductivity ($W/K \cdot m^2$)
N_d	=	cross-sectional diameter scaling factor

N_L	=	length scaling factor
N_m	=	mass scaling factor
N_{m_ε}	=	mass scaling factor for constant stiffness
N_{m_σ}	=	mass scaling factor for constant strength
Δp	=	pressure difference
q	=	dynamic pressure (Pa)
Q_C	=	conductive heat flux through the heat shield thickness ($\mathrm{W/m^2}$)
Q_R	=	radiative cooling heat flux ($\mathrm{W/m^2}$)
Q_S	=	stagnation point heat flux ($\mathrm{W/m^2}$)
r	=	radius of a ring element (m)
R	=	radius of stagnation point surface curvature (m)
S	=	area ($\mathrm{m^2}$)
t	=	time (s)
T	=	temperature (K)
v	=	descending velocity (m/s)
α	=	angle of attack
θ	=	deployment angle (rad)
θ_{dstb}	=	deployment angle at a disturbed condition (rad)
κ	=	effective torsional stiffness of the second stage associated with the deploying motion ($\mathrm{N \cdot m/rad}$)
λ	=	thermal conductivity ($\mathrm{W/m \cdot K}$)
ρ	=	atmospheric density ($\mathrm{kg/m^3}$)
ρ_S	=	surface density of the heat shield ($\mathrm{kg/m^2}$)
σ	=	Stefan-Boltzmann Constant = 5.67×10^{-8} $\mathrm{W/(m^2K^4)}$
τ	=	axial aerodynamic torque ($\mathrm{N \cdot m}$)

ω	=	spin rate (rad/s)
ω_{dstb}	=	spin rate at a off-equilibrium condition (rad/s)
ADEPT	=	Adaptable Deployable Entry and Placement Technology
DoF	=	Degree of Freedom
FTPS	=	Flexible Thermal Protection System
HEART	=	High-Energy Atmospheric Reentry Test
IAD	=	Inflatable Aerodynamic Decelerator
IRVE	=	Inflatable Reentry Vehicle Experiment
LEO	=	Low Earth Orbit

Subscripts

front	=	front surface
back	=	back surface

1. Introduction

Atmospheric entry reduces the kinetic and potential energy of a spacecraft, allowing soft landing on a planetary surface. However, the entry process depends on the atmospheric properties, and the entry system design has to be adapted for various planetary environments as well as payloads. Current Mars entry systems usually consist of a rigid blunt aeroshell that decelerates the payload from hypersonic to supersonic speed, and a parachute that deploys at supersonic velocities and lower altitudes. However, Mars entry requires a low ballistic ratio, m/SC_D, to effectively slow down the vehicle through the thin Martian atmosphere, meaning the size of rigid aeroshells is approaching the fairing capacity of existing launching vehicles and future missions with heavier robotic systems or manned vehicles are not achievable

using the current rigid aeroshell technology. The quest for a new system that could enable heavier payloads to be landed on Mars calls for a deployable aeroshell that can be stowed compactly in a launch vehicle while creating large drag area when deployed [1, 2, 3, 4, 5]. Meanwhile, a deployable aeroshell could also address the demand for a CubeSat-sized recoverable platform for in-orbit scientific experiments since a low ballistic ratio is favourable for thermal control. This is challenging due to the high surface curvature and surface area to volume ratio of small vehicles. Furthermore, the low ballistic ratio could waive the necessity for a parachute due to the low terminal velocity. This also enables a single decelerator system that is inherently safe since it burns up in the atmosphere in case of deployment failure. A few efforts have been reported in this area [6, 7, 8].

To realise a deployable aeroshell, various designs were investigated during the 1960s and the 1970s. Although very little research has been reported from the mid 1970s to the mid 2000s, the recent demand for more advanced missions outside the existing systems' performance envelope has promoted renewed interest. The Inflatable Aerodynamic Decelerator (IAD) is the most studied concept, which has seen various adaptations in recent years [9, 10, 11, 12, 13, 14], such as the Inflatable Reentry Vehicle Experiment-4 (IRVE-4) vehicle shown in Fig. 1a [13]. An IAD forms a blunt shape using flexible pressure chambers inflated by either internal or external gas sources. It utilises the superior tensile strength and stiffness of the pressure chambers made from a flexible fabric, as well as the compressive properties of gas, which is the ultimate lightweight and flexible material. In addition to IAD, there have been a few published concepts on conventional umbrella-like mechanisms consisting of rigid structural elements connected by revolving or sliding joints [15, 16, 17], such as the Adaptable Deployable Entry and Placement Technology (ADEPT) concept shown in Fig. 1b [18]. Such a structure could allow shape morphing during the entry,

and therefore, enable trajectory control [6, 19].

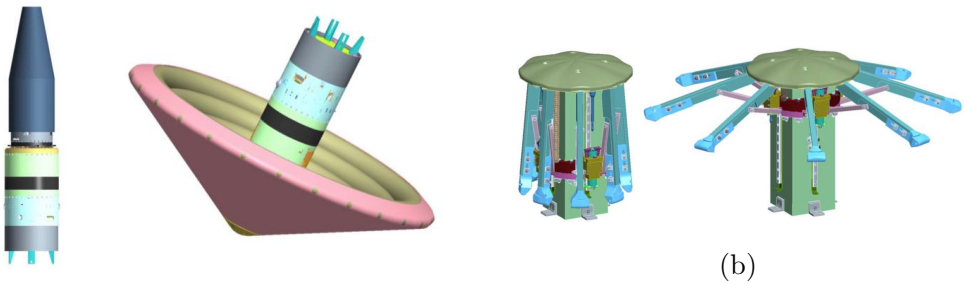

(a) (b)

Figure 1: Two types of deployable entry system concepts, (a) the IRVE-4 vehicle with an IAD [13], (b) the ADEPT concept with a mechanically deployable heat shield [18].

On the other hand, while both the mechanically deployable structures and the inflatable structures are deployed and stabilised by elastic forces from solid or gaseous materials, a structure can also be deployed and achieve stiffness using inertia forces. For example, the increased bending stiffness of a spinning helicopter rotor is a well-studied phenomenon of centrifugal stiffening [20]. Meanwhile, studies have also shown that centrifugal force can be utilised to deploy large flexible space structures. Although the lack in internal and external damping is a challenge for flexible structures in an orbital environment, the Anamya-2 experiment has successfully demonstrated the centrifugal deployment of a 20-metre wide space mirror [21, 22, 23]. The application of inertia forces could open up new types of entry systems that may potentially benefit from the advantages of centrifugal deployment, including being lightweight, compact and needing low power for deployment [24, 25].

The presented study shows that it is feasible to use centrifugal force to deploy and stabilise an aerodynamic decelerator by utilising a flexible morphing heat shield that passively regulates its deployment and centrifugal force. Specifically, §2 provides a

very basic comparison between the mass of elastically and centrifugally supported beams, §3 discusses the design concept in detail and proposes a baseline CubeSat sized vehicle. Structural dynamic analyses using analytical and numerical methods, as well as a trajectory simulation on the baseline vehicle are included in §4. The thermal analyses in §5 shows that the proposed concept also has advantages in terms of thermal control.

2. Structural Advantages of Centrifugal Deployment and Stiffening

Structural mass is a major concern for space systems. Here a simplified comparison is made between two types of structures deployed by elastic and centrifugal forces respectively according to the behaviour of a basic structural element. For an elastically deployed structure, consider a cantilever beam under a transverse aerodynamic load with a unit load density (thus a constant dynamic pressure), as shown in Fig. 2a. Consider the nature of aerodynamic load, the overall load on the beam can be assumed to be $\propto {N_L}^2$, where N_L is the scaling factor of the beam's length. The scaling factor of a parameter means the ratio between the values of the parameter before and after scaling. Assuming constant material modulus, when scaling the size of the beam up, a constant deflected shape, thus a constant stiffness can be achieved by keeping a constant aeroelastic-bending parameter according to the linear beam theory: ${N_d}^4/{N_L}^4 = 1$ (according to the aeroelastic bending similitude parameter from [26]), where N_d is the scaling factor of the beam's cross sectional diameter. Similarly, keeping the maximum normal stress constant requires ${N_L}^3 N_d/{N_d}^4 = 1$ (according to Eq. 5-13 from [27]). Therefore, the mass scaling factor $N_m \propto {N_d}^2 N_L$ for achieving constant stiffness (N_{m_ε}) and strength (N_{m_σ}) become:

$$N_{m_\varepsilon} \propto {N_d}^2 N_L \propto {N_L}^3, \qquad N_{m_\sigma} \propto {N_d}^2 N_L \propto {N_L}^3 \tag{1}$$

Meanwhile, instead of a cantilever beam, the most efficient way for a rod to carry load by elasticity is to align the load along the rod axis such as in a truss structure, as shown in Fig. 2b, so the material is evenly stressed. To analyse a rod under such a condition, the previous model is used with the distributed load changed to a force along the rod with its magnitude $\propto {N_L}^2$. Ignoring the effect of buckling for a compression scenario, the similitude of stiffness and strength can be achieved if the strain/stress in the rod remains constant during scaling, which requires: ${N_L}^2/{N_d}^2 = 1$. Then the mass scaling factors become $N_{m_\varepsilon} = N_{m_\sigma} \propto {N_d}^3$.

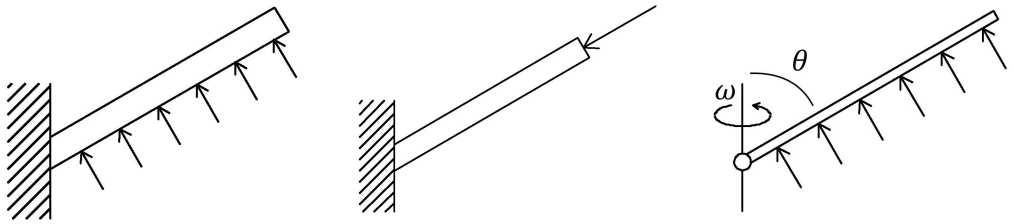

(a) (b) (c)

Figure 2: Schematic view of three types of basic structural elements, (a) cantilever beam supported by elastic force, (b) axially loaded rod, (c) spinning rod supported by centrifugal force.

For a structure deployed by centrifugal force, consider a rod with a mass of m and a length of L hinged on one end and spins around an axis that passes through the hinged point at a spin rate of ω, as shown in Fig. 2c. Now apply a uniformly distributed lateral aerodynamic load with a unit magnitude, and ignore its elastic deformation which has minor effect on the deployment. Statically the equilibrium can be reached when the deploying moment from centrifugal force, M_{FC}, equals the anti-deploying moment from the load, M_{load}, under a certain deployment angle of θ, which is the angle between the rod and the spin axis. Since the total aerodynamic load is proportional to L^2 as mentioned above, the moment from the aerodynamic

load becomes $M_{load} \propto L^3$. Meanwhile, the centrifugal force can be expressed as:

$$m\,\omega^2\ \sin(\theta)\ L \tag{2}$$

Where the term $\sin(\theta)L$ is proportional to the radius of the circular motion. Then from equilibrium, we have:

$$\frac{M_{load}}{M_{FC}} = 1 \propto \frac{L^3}{(m\,\omega^2\ \sin(\theta)\ L \cdot \cos(\theta)\ L)} \tag{3}$$

Where the term $\cos(\theta)L$ is proportional to the moment arm of centrifugal force. Then the mass scaling factor for stiffness (or in other words, the condition to achieve a constant deflection θ) can be calculated by solving Eq. 3 for m while assuming constant ω and θ. The result gives $m \propto L$. The scaling factor for strength can be determined based on the tensile stress in the rod induced by centrifugal force. According to Eq. 2, this requires:

$$N_{m_\sigma}\,\omega^2\ \sin(\theta)\ N_L/{N_d}^2 \propto 1 \tag{4}$$

Assuming a uniform scaling with $N_L/N_d = 1$, we have $N_{m_\sigma} \propto N_L$. The results are summarised in Table 1.

Table 1: Comparison between a cantilever beam, an axially loaded rod and centrifugally deployed rod.

Condition	Stabilisation force	Mass scaling factor for constant stiffness	Mass scaling factor for constant strength
Cantilever beam	Elastic	$N_{m_\varepsilon} \propto {N_L}^3$	$N_{m_\sigma} \propto {N_L}^3$
Axially loaded rod		$N_{m_\varepsilon} \propto {N_L}^3$	$N_{m_\sigma} \propto {N_L}^3$
Centrifugally deployed rod	Centrifugal	$N_{m_\varepsilon} \propto N_L$	$N_{m_\sigma} \propto N_L$

From Table 1, it can be seen that in order to carry a load, the mass of a cantilever beam or an axially loaded bar has to increase more rapidly with size than a centrifugally deployed rod. Therefore, to deploy a large heat shield, centrifugal deployment could be advantageous to elastic deployment in terms of structural mass. Meanwhile, Table 1 only provides the dependence of mass on linear dimension, while the effects of other parameters on a centrifugally deployed rod are provided by Eq. 3. For instance, a higher attainable spin rate ω or a lower required deployment angle θ leads to lower mass.

Besides the mass saving potential for a large vehicle, centrifugal deployment could also benefit a small vehicle, such as a CubeSat-sized re-entry vehicle, since it eliminates the actuators or pressure vessels in inflatable or mechanically deployed heat shields and allows a concise system that is self-regulated (as further discussed in §3).

In addition, since a centrifugally deployed structure could minimise the dependence on elastic support and be designed to carry solely tension, it can be constructed from materials with low flexural rigidity. Therefore, it provides more freedom for packaging and is likely to achieve higher compactness than a solid deployable mechanism.

3. Design Concept

The core of the design concept for the entry heat shield is a flexible thin shell with a spiral characteristic and a uniform surface density (Fig. 3a). The shape generates an axial aerodynamic roll-torque that causes autorotation during descent, thus the spiral characteristic of the shape determines the spin rate at certain descent velocity. Meanwhile, the autorotation produces a centrifugal force that stiffens the shell but also flattens it (Fig. 3b), thus the spin rate determines the shell's deployment under certain external conditions and hence the roll-torque that is produced. Therefore,

the deployment, the characteristic of the spiral shape and the spin rate form a closed loop that regulate each other. Since the deployment of the shell can flatten the spiral shape and reduce the induced roll-torque, the roll-torque is self regulating, leading to an equilibrium spin rate.

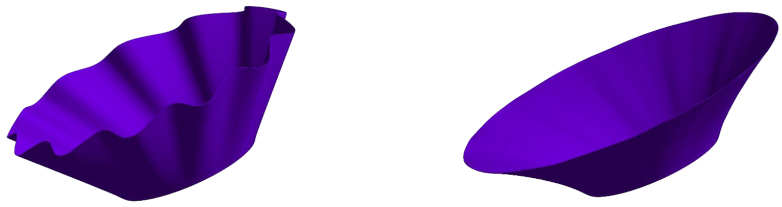

(a) (b)

Figure 3: Shapes of the shell at different deployed states according to FE (Finite Element) simulations, (a) a partially deployed state that tends to produce high roll-torques, (b) a near fully deployed state that leads to low roll-torques and stabilises spin rate.

The spiral shape shown in Fig. 3 is based on an origami pattern, which allows the heat shield to be packed into a cylindrical shell with a diameter close to the rigid nose cone of the payload vessel, as shown in Fig. 4. The packing method is similar to "Wrap-Rib" described in [28]. The ridges and valleys of the spiral shape are aligned along the folding lines, and the pattern could be tailored to adapt to different spiral shapes. The spiral characteristics formed by those ridges and valleys leads to an aerodynamic roll-torque as discussed in Fig. 3. Since the origami guarantees that no folding lines pass across the ridges and valleys of the shell during folding, the creep of material (when the shell is packed) will not significantly change the spiral characteristics of the shape. This could enable longer mission duration and allow packaging prior to the spacecraft assembly.

The heat shield is divided into two stages, as shown in Fig. 4. The whole shell can be unpacked when the first stage deploys, which may be achieved by an

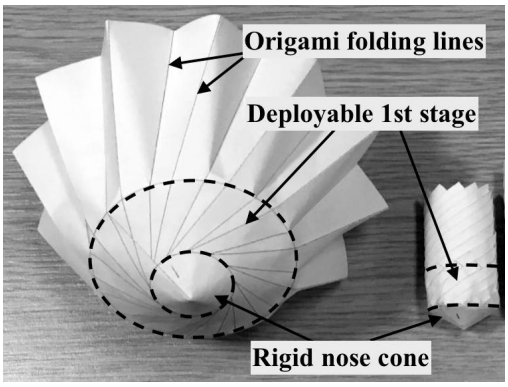

Figure 4: Deployed (left) and packed (right) configurations of paper prototypes, showing that the origami pattern upon which the spiral shape is based allows the heat shield to be packed into a cylindrical shell. The first stage that can rigidify after deployment, as well as the rigid nose cone of the payload vessel are labelled.

inflatable or a mechanically deployable structure. The first stage becomes rigid after deployment, then the flexible second stage can deploy by centrifugal force as discussed above and increase the drag area significantly. The first stage not only enables the initial unpacking, but also assists the second stage deployment since it increases the diameter and therefore, the centrifugal force on the second stage. In the absence of such a first stage, the flexible second stage could be entangled near the spin axis where the centrifugal force is low as shown later in the discussion associated with Fig. 7. The payload vessel is located behind the rigid nose cone, which can be a conventional thermal protection system (Fig. 5). Although the concept contains an elastically deployed first stage, the design could still benefit from the advantages of centrifugal deployment of the second stage as discussed in §2 and potentially achieve higher packing ratio and lower mass.

In terms of thermal control, such a heat shield requires a FTPS (Flexible Thermal Protection System) to protect the structure from aerothermodynamic heating while

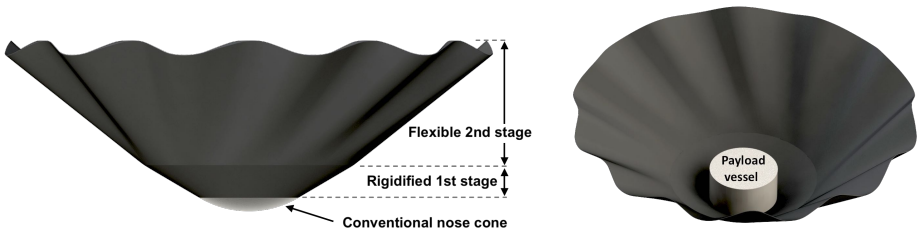

(a) (b)

Figure 5: Conceptual design of a vehicle with centrifugally deployed heat shield, (a) front view showing the basic components, (b) tilted view showing the payload vessel behind the nose cone.

allowing packing and shape morphing. The development of IADs has raised similar demand, and various material systems including ceramic and organic fibres as well as flexible insulating materials have been tested in lab environment and in flight tests [29, 30]. Meanwhile, unlike the airtight pressure chambers of IADs, the proposed heat shield is a single wall structure that potentially allows high surface temperatures, which not only eliminates the requirement for heat insulation, but also allows effective radiative cooling from the aft surface, which is analysed in §5.

For instance, the heat shield can be constructed using stitched woven ceramic fabrics where the spiral shape is formed using the stitched seams or local reinforcements along the origami pattern, or thermally protected elastomers for lower energy missions (e.g. suborbital), where the spiral shape is formed by material elasticity. Meanwhile, the edge (shoulder) of the flexible shell can be rounded by a fold hem created by folding and stitching similar to the ADEPT concept to prevent excessive local heating [31].

4. Structural Analysis

Operation of the heat shield begins after the initial deployment, which rigidises the first stage and unpacks the second stage. Therefore, the structural analyses presented here are focused on the behaviour of the flexible second stage during the ballistic entry. To assess the static and dynamic structural response associated with the deploying-folding motion of the flexible stage, analytical analysis based on a simplified model as well as FE simulations with higher fidelity were conducted. A trajectory simulator was also developed, which accounts for the simplified structural dynamic model and the 3 DoF (Degree of Freedom) trajectory (assuming the shield points stably into the flow at zero angle of attack).

A sample re-entry mission from Low Earth Orbit (LEO) is used to characterise the trajectory as well as structural dynamic behaviours of a CubeSat-sized baseline vehicle. The baseline vehicle has a total mass of 1.3 kg, a cone semi-vertex angle of 60°, a base diameter of 0.7 m when fully deployed and 0.125 m when fully packed.

4.1. Deployment

In this section, analytical equations are derived to predict the spin rate and deployment angle at certain static conditions, which show satisfactory agreement with FE simulations. The equations also demonstrate the ability of the shell to recover after an instantaneous disturbance, and the effects of different design parameters are illustrated.

To conduct analytical analysis, a simplified geometrical model similar to the origami shown in Fig. 4 is made, which consists of panels that are hinged together along the origami's folding lines, and allows an axisymmetrical deploying-folding motion with one degree of freedom. Since this motion is unique, the shapes and orientations of the panels can be determined by geometry using solely deployment

angle θ, then the aerodynamic pressures on the panels can be calculated using the Newtonian method.

Similar to Eq. 3, deployment requires:

$$M = M_{F_C} - M_{load} + M_g \geq 0 \tag{5}$$

M_{F_C} can be evaluated by dividing the shell into ring elements with the mass of dm (Fig. 6), then integrating the moment generated by the centrifugal force from each ring element. Each ring element is assumed to be circular and is perpendicular to the vehicle axis with a certain radius $r = aL + l \cdot \sin(\theta)$. The term $\cos(\theta) \cdot l$ in the following equation is the moment arm of the centrifugal force.

$$M_{F_C} = \int_0^L dm \cdot \omega^2 r \cos(\theta) l \tag{6}$$

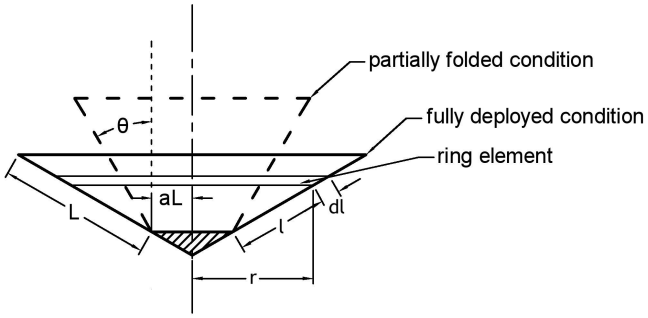

Figure 6: Vehicle schematic view, showing the major dimensions of the rigid first stage and the flexible second stage, as well as the ring element used in calculation.

Note that the heat shield with a certain spiral shape behaves like an unloaded wind turbine in autorotation, which has a maximum spin rate proportional to descending velocity:

$$\omega = k \cdot v \tag{7}$$

Where k is determined by the characteristics of the spiral shape and depends on L, a, and θ (those variables are illustrated in the vehicle schematic view shown in Fig. 6). It is numerically evaluated using the simplified geometrical model and Newtonian aerodynamics.

Meanwhile, the mass of the ring element, dm can be expressed as below, where the term $2\pi \cdot [\sin(60^\circ) \cdot l + aL]$ is the length of the heat shield material around the ring element:

$$dm = dS \cdot \rho_S = 2\pi[\sin(60^\circ)l + aL]\rho_S \cdot dl \tag{8}$$

According to Newtonian Aerodynamics, the aerodynamic pressure normal to a surface is [32]:

$$\Delta p = \rho v^2 \sin^2(\alpha) \tag{9}$$

Then similar to Eq. 6, M_{load} can be evaluated by integrating the anti-deploying moment caused by the aerodynamic load, which has a moment arm of l, while assuming the second stage is a conical surface with a semi-vertex angle of θ.

$$M_{load} = \int \rho v^2 \sin^2(\theta) l \cdot dS \tag{10}$$

Where $dS = 2\pi r \cdot dl$ is the surface area of the ring element, and α (in Eq. 9) is approximated by θ for simplicity. Higher fidelity analysis has also been carried out to evaluate Eq. 10 using α determined from the geometrical model, which yields similar results for θ within $\pi/6 \sim \pi/3$ ($30^\circ \sim 60^\circ$). Similarly, M_g can be evaluated

by integrating the deploying moment from the inertial force induced by deceleration, which has a moment arm of $\sin(\theta) \cdot l$:

$$M_g = \int_0^L dm \cdot a_{dec} \sin(\theta) l \tag{11}$$

The deceleration a_{dec} can be expressed as below, where C_D can be evaluated using Eq. 9 as a function of θ.

$$a_{dec} = \frac{qSC_D}{m} \tag{12}$$

By substituting Eqs. 6-12 into Eq. 5, the deployment criteria can be derived. In order to save computational resource, the expression is simplified by setting parameters based on a baseline vehicle design: $a = 0.577$, and the mass scaling law $m \propto L^3$, then some near-linear terms containing θ are linearised. The result is shown as Eq. 13. According to the discussions associated with Table 2, the linear regression has no significant effect on calculation results, but can considerably reduce the computation time.

$$M \approx v^2[k^2 \rho_S L(0.573\theta + 0.788)\cos(\theta) - \rho(1.01\theta - 0.431)\sin(\theta)] \geq 0 \tag{13}$$

From Eq. 13, it can be seen that a thinner atmosphere, a higher heat shield surface density, a larger heat shield size, and a higher k are beneficial to the deployment, as all leads to a higher value of M.

Meanwhile, ω can be determined by substituting Eq. 7 into Eq. 13. The result is shown below as Eq. 14. For a certain vehicle design, it can be used to calculate the required spin rate ω to achieve a deployment angle θ under a certain condition of q by evaluating the term on the right hand side of the equation. However, this equation does not provide information on whether the overall equilibrium is achieved,

since the overall equilibrium also depends on the roll-torque generated at such a spin rate, or in other words, the dependence of k on other factors, which is numerically analysed in §4.2.

$$\omega \approx \sqrt{\frac{\tan(\theta) q (2.01\theta - 0.861)}{\rho_S L (0.573\theta + 0.788)}} \tag{14}$$

To validate Eqs. 13 and 14, a series of FE simulations have been conducted to determine whether the predicted deployment angles can be achieved under certain conditions. A flexible second stage is modelled as shown in Fig. 3, which is based on the baseline design of a CubeSat sized vehicle that has a base diameter of $0.7\,m$, a cone semi-vertex angle of 60° when fully deployed, a total mass of $1.3\,kg$, an a value of 0.577, and a surface density ρ_S of 1.1kg/m^2. The effect of rotation, deceleration and Newtonian aerodynamic load are taken into account, and static non-linear simulations are carried out. The results are shown in Table 2, which also corresponds the simulated conditions to the flight regimes predicted by the trajectory simulation discussed in §4.2. The results from the equations with linear regressions are also reported.

It can be seen that the predictions from analytical equations are not significantly changed by linear regression. Meanwhile, in comparison with FE simulations, the equations over-predict the deployment angles by no more than 6° throughout descent, which is acceptable for providing a preliminary understanding about the flight performance.

Equations 13 and 14 assume a static condition where the total deploying moment on the shell is zero. However, disturbances during the flight such as abrupt change in the atmospheric density or structural oscillation could rapidly change the deployment angle and lead to off-equilibrium conditions. The stability of deployment, or in other

Table 2: Comparison between the deployment angles predicted by the analytical equations before and after linear regression as well as FE simulations.

Dynamic pressure	Spin rate	Deploy. angle (analytical)	Deploy. angle (regression)	Deploy. angle (FE)	Condition
180 Pa	5.2 rps	58°	60°(full deploy)	56°	Peak dynamic pressure
26 Pa	1.7 rps	55°	55°	52°	35 km altitude
31 Pa	1.6 rps	50°	49°	46°	24 km altitude
43 Pa	1.4 rps	44°	42°	38°	12 km altitude
60 Pa	1.2 rps	36°	35°	30°	Sea level

words, the ability of the shell to recover from disturbance and regain equilibrium is critical to the survivability of the vehicle. For example, instability could occur after an abrupt disturbance in case more than one deployment angle could satisfy the deployment criteria under the disturbed condition, e.g. under certain scenario the shell may rest near the spin axis where the centrifugal force is low. To analyse the possibility of instability, Eq. 13 can be rearranged to evaluate the deploying moment at a certain off-equilibrium condition:

$$M \propto {\omega_{dstb}}^2 \rho_S L \cdot \cos(\theta)(0.573\theta_{dstb} + 0.788) - q \cdot \sin(\theta_{dstb})(2.01\theta_{dstb} - 0.861) \quad (15)$$

Assuming the disturbance is instantaneous, ω_{dstb} can be related to ω, the static spin rate before the disturbance predicted by Eq. 14, according to the conservation of angular momentum: $\omega \cdot I_{spin}(\theta) = \omega_{dstb} \cdot I_{spin}(\theta_{dstb})$, where I_{spin} is a function of θ and can be determined based on the simplified geometrical model while ignoring the angular inertia of payload (considering the relatively low radius of the payload

vessel).

Then the recovering effect at a disturbed condition can be characterised by the angular acceleration of the shell's deploying motion: $\ddot{\theta} = M/I_{deploy}$, where I_{deploy} is evaluated according to the simplified geometrical model. Thus static stability requires $\ddot{\theta}/(\theta_{dstb} - \theta) < 0$, and a $\ddot{\theta}$ with higher absolute value means more rapid recovery. The dependences of $\ddot{\theta}$ on a and L are shown in Fig. 7, where the horizontal axis is the instantaneous deployment angle after the disturbance. Generally, the design shows that deployment is statically stable, though this does not guarantee dynamic stability (as discussed later in §4.2 and §4.3). It also worth noticing that the analysis only considers the rolling motion and deploying-folding motion, while pitch and yaw instabilities are not considered here.

The recovering effect of heat shields with different sizes and with two different initial equilibrium deployment angles are shown in Fig. 7a and 7b. It can be seen that $\ddot{\theta}$ reduces with increasing heat shield size as a result of increasing shell inertia. Analysis that is not presented here has also shown that the shell surface density has a similar impact. Meanwhile, a higher initial deployment angle before the disturbance leads to a higher recovering effect due to the higher loads. As shown by Fig. 7c, the size of the first stage has a non-monotonic impact on $\ddot{\theta}$. An a value of 0.577, which is chosen for the baseline design, gives a near optimum overall recovering effect, while instability could occur when the shell is pushed to a fully folded state of $\theta = 0°$ if a was zero.

4.2. Trajectory Simulation

The equations describing the axisymmetrical deploying-folding motion of the heat shield's flexible second stage are derived in §4.1. In this section, those equations are used to simulate the dynamic structural response during a 3 DoF trajectory

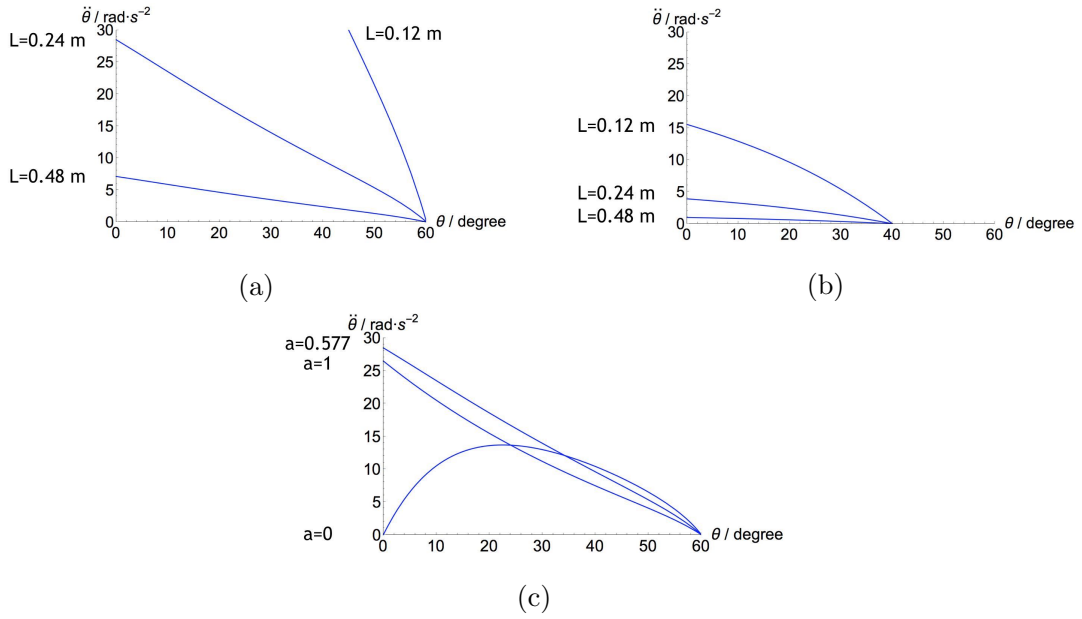

Figure 7: The effects of design parameters on the shell's ability to recover from instantaneous disturbance of deployment angle under a unit dynamic pressure, where a high (absolute value) deploying angular acceleration means rapid recovery, (a) the effect of size under a **60°** initial deployment angle before the disturbance, (b) the effect of size under an initial deployment angle of **40°**, (c) the effect of first stage size with a constant overall size.

simulation.

The previous equations can be used to determine the deployment angle according to spin rate and other internal and external conditions, while how the deployment influences the spiral shape and thus the spin rate is still needed to simulate the closed loop of the heat shield. Therefore, the axial aerodynamic torque τ is derived as a function of θ, ω, v and q using the simplified geometrical model and Newtonian aerodynamics and assuming a zero angle of attack. The result generally shows that the heat shield is similar to an unloaded wind turbine: spin rate under a condition of $\tau = 0$ is proportional to axial velocity. Meanwhile, the spin rate at $\tau = 0$ drops

linearly to zero as the deployment angle increases to a fully deployed condition. Such a relation can support a passive proportional control as described in §3.

The deployment angle can be calculated by integrating the instantaneous acceleration of deploying motion with respect to time, as shown below. The first integral (deploying angular velocity) is set to zero every time when the maximum deployment angle is reached to represent the mechanical constraint on deployment.

$$\theta = \iint \frac{M}{I_{deploy}} \cdot dt\, dt \tag{16}$$

Similarly, the spin rate of autorotation can be determined:

$$\omega = \frac{\int \tau \cdot dt}{I_{spin}} \tag{17}$$

The structural model is then incorporated into a 3 DoF trajectory simulator based on Simulink. The simulator is developed using Newton's second law and describes the point mass dynamics of the vehicle in various reference systems. It assumes zero angle of attack and ignores the gyroscopic effects from spinning. Such simplification is made as the presented study is focused on the heat shield's deployment rather than the full flight dynamics of the vehicle.

The re-entry of a CubeSat sized vehicle with the baseline design from a 145 km orbit at zero flight path angle is simulated, and the results are shown in Fig. 8. It can be seen that the deployment angle is above 50° through most of the descent until the heat shield reaches an altitude below 25 km. This can be explained by Eq. 13, since the low atmospheric density at high altitude leads to easy deployment, while at low altitude the shell starts to fold as the spiral shape is unable to provide sufficient spin rate (insufficient value of k). The reason for the deployment angle to drop at higher altitude especially during the simulation time from 300 s to 900 s is that the

aerodynamic torque at such high altitude is too low to accelerate autorotation. This phenomenon can be prevented by adding an initial spin before the re-entry.

Meanwhile, structural oscillation that causes rapid fluctuations in deployment angle can be seen in the figure. The oscillation's frequency varies within 0.1 Hz - 10 Hz simultaneously with dynamic pressure, and is discussed in §4.3. According to the simulation, the peak amplitude of the oscillation gradually changes during the descent and is always below 6°, and the oscillation leads to fluctuations of axial deceleration with a peak amplitude of below 0.05 g at high altitude and 0.3 g at the peak dynamic pressure. Figure 8 has also shown the fluctuations of spin rate, which is a result of the conservation of angular momentum when the heat shield flutters. The oscillation is a result of the system's coupled dynamic behaviours, and is not the focus of the presented study. Nevertheless, it worth noticing that no structural damping is modelled in the simulator, thus there is likely to be less oscillation in reality where damping exist.

As shown by Eq. 14, the equilibrium spin rate is proportional to the dynamic pressure at a certain deployment angle. In Fig. 8 it can be seen that the spin rate increases and then drops during the first 1800 s of flight, which is a result of changing dynamic pressure. From 1800 s, the change of spin rate is insignificant due to the generally constant dynamic pressure.

It should be noted that the simulated vehicle enters subsonic flight at ∼1720 s, which is when the spin rate is dropped to ∼2 rps, and deployment angle starts to decrease from 60° (Fig. 8). Since the simulator is developed using Newtonian aerodynamics, which is not suitable for subsonic speed, the simulator only provides a rough estimation of the flight after 1720 s.

It also worth noticing that the simulation model does not account for the deploying/anti-deploying effect from the heat shield material's elasticity, which is expected to be

minor as the objective of this design is to eliminate the reliance on elasticity and take advantage of centrifugal deployment. The most eminent effect may occur when the heat shield is near fully deployed (at higher altitude): since flattening a pre-folded shield made of thick fabric may require a relatively high fabric tension, the shield will tend to have a lower deployment angle. However, a less-deployed shape leads to an increased spin rate due to the aerodynamic roll-torque, which will eventually deploy the shield to a higher extent.

4.3. Structural Oscillation

To avoid resonance, the structural natural frequency of the flexible second stage must not overlap with the spin rate and the aerodynamic pitching frequency. In this section, those three frequencies are analytically assessed, and the former two are also analysed by FE simulations.

The structural natural frequency associated with the shell's deploying-folding motion can be calculated using Eq. 18 below, where κ, the torsional stiffness of the shell associated with the oscillation, can be evaluated by differentiating the total deploying moment M with respect to deployment angle θ: $\kappa = \partial M/\partial\theta$. This equation has close agreement with the oscillation frequency observed in the trajectory simulation. The full equation is not shown here due to its complexity.

$$f_{struc.} = \frac{1}{2\pi}\sqrt{\frac{\kappa}{I_{deploy}}} = F(\theta, q, \omega, \rho_S, L, m, a) \tag{18}$$

To validate Eq. 18, the calculations are compared to the oscillating frequencies observed in the FE transient structural analyses under various conditions as predicted by the trajectory simulator, as shown in Table 3. The conditions are: high altitude at 1350 s (No. 1); peak heating at 1580 s (No. 2); peak dynamic pressure at 1620 s (No. 3); near fully deployed at low altitude at 1800 s (No. 4); partially deployed at sea level

(No. 5). The shell is assumed to be made of a flexible material with a thickness of 1 mm, a modulus of 5 MPa, and a density of 1.1g/cm^3 according to the baseline design. The nonlinear FE transient structural analyses are carried out in ANSYS with the inertia force (centrifugal and deceleration) and aerodynamic force included, and the shell is divided into >10,000 shell element. The simulation provides a stabilised oscillation of ∼3 s, and a variable time-step solver is used with the maximum time-step set to 1/150 s. Running cases with varied shell material modulus also show that the effect of elasticity is neglectable, proving that the oscillation frequency is determined by dynamics.

Although the FE simulation uses a flexible model with a much higher degrees of freedom, the oscillations are always based on the deformation associated with deploying-folding motion. Therefore, as shown by Table 3, Eq. 18 has satisfactory agreement with the FE simulations except for conditions No. 1 and No. 5. The reason for these under-predictions is that the analytical model ignores the effect of elasticity, while as No. 1 and No. 5 are lightly loaded conditions (indicated by the low spin rates and deployment angles), the structural behaviours are dominated by the elasticity rather than the external/centrifugal load.

Equation 18 can be simplified to a function of q and L, by assuming $a = 0.577$, a fully deployed condition with $\theta = 60°$ (which is close to the shell's condition throughout high-speed regime), the mass scaling law based on the baseline design $m = 94L^3$, and the shell thickness (thus, surface density) proportional to vehicle size $\rho_S = 4.58L$. The result is below:

$$f_{struc.} = 0.160\sqrt{\frac{q}{L^2}} \qquad \text{(Hz)} \tag{19}$$

Similarly, the spin rate can be simplified to:

Table 3: Structural natural frequency from analytical analyses and FE simulations.

No.	Dynamic Pressure	Spin rate	Decele-ration	Deploy. angle	Eq. 18	FE sim-ulation	Differ.
1	1.5 Pa	0.43 rps	0.0 g	57°	0.77 Hz	1.6 Hz	-52%
2	100 Pa	3.6 rps	4.1 g	58°	6.4 Hz	5.7 Hz	12%
3	180 Pa	5.2 rps	8.0 g	60°	9.0 Hz	9.5 Hz	5%
4	26 Pa	1.8 rps	1.0 g	56°	3.2 Hz	3.2 Hz	0%
5	60 Pa	1.2 rps	1.0 g	35°	3.2 Hz	4.2 Hz	-24%

$$f_\omega = 0.0928\sqrt{\frac{q}{L^2}} \qquad \text{(Hz)} \tag{20}$$

The aerodynamic pitching frequency can be solved using Newtonian Aerodynamics according to literature [33]. Consider a fully deployed heat shield, which is the case during most of the descent, and ignore the angular inertia of payload, which is minor in comparison with the deployed heat shield, the pitching frequency can be expressed as below with minor approximations:

$$f_{pitch} = 0.574\sqrt{\frac{q}{L^2}} \qquad \text{(Hz)} \tag{21}$$

Combining Eqs. 19, 20 and 21, the ratios between the three frequencies for a vehicle with $a = 0.577$ at a fully deployed equilibrium condition:

$$f_\omega : f_{struc.} : f_{pitch} = 0.58 : 1 : 3.6 \tag{22}$$

It worth noticing that Eq. 22 is valid regardless of vehicle size and dynamic pressure. Meanwhile, the frequency ratios can be tuned by adjusting the value of

a. Therefore, the preliminary analyses presented here shows that the vehicle has designable and scalable dynamic behaviour.

5. Thermal Analysis

To provide a reference for the vehicle's thermal condition, the stagnation point heat flux is evaluated using the Sutton and Graves Equation shown below that accounts for convective heat transfer in non-reacting laminar flow [33, 34]. The radiative heating is neglected due to the low entry velocity from LEO as well as the small vehicle size [32].

$$Q_S = 1.83 \times 10^{-4}\, v^3 \sqrt{\frac{\rho}{R}} \qquad (\mathrm{W/m^2}) \tag{23}$$

Where atmospheric density ρ has unit $\mathrm{kg/m^3}$, stagnation point radius of curvature R is in m, velocity v is in m/s, and the constant 1.83×10^{-4} has dimension of $\mathrm{kg^{0.5}m^{-1}}$. Equation 23 is incorporated into the trajectory simulator, which predicts that, as shown in Fig. 8b, at the simulation time of 1540 s and an altitude of 87.5 km, the heat shield experiences a peak heat flux of 27 $\mathrm{W/cm^2}$, which is similar to the peak heat flux on NASA's High-Energy Atmospheric Reentry Test (HEART) vehicle, which utilises an IAD [35]. Since the pressure chamber material of IAD requires a maximum operating temperature of 250 °C to maintain air tightness [36], the FTPS in the HEART vehicle design contains insulating layers and hot gas barriers with a total surface density of 3-4 $\mathrm{kg/m^2}$, while the surface density of the temperature resisting front layers is approximately 1 $\mathrm{kg/m^2}$ (estimated based on the properties of 3M$^{\mathrm{TM}}$Nextel$^{\mathrm{TM}}$440 BF20 fabric) [35]. This is close to 1.1 $\mathrm{kg/m^2}$, the heat shield surface density of the presented CubeSat sized baseline design.

In comparison with IAD or conventional rigid heat shields, the centrifugally de-

ployed heat shield has advantage in terms of thermal control. First of all, the requirement on thermal and hot gas insulation can be eliminated since the heat shield is a single wall structure with no payload or temperature-sensitive structures attached onto the aft surface, which leads to a lightweight and compact system. Meanwhile, the aft surface may effectively participate in the radiative cooling due to its high temperature, which helps reduce the overall temperature. A simple analysis is conducted to assess this effect.

Consider a high temperature non-ablating wall under thermal equilibrium, the front surface aerodynamic heating Q_S, the front surface radiative cooling $Q_{R_{front}}$ and the heat conducting through the heat shield thickness Q_C should satisfy the relation: $Q_S = Q_{R_{front}} + Q_C$, while the backside radiative cooling $Q_{R_{back}}$ is in equilibrium with Q_C, thus $Q_C = Q_{R_{back}}$. Therefore, from the thermal transmission equations, we have:

$$Q_S = \sigma \, e_{front} \, {T_{front}}^4 + \frac{\lambda \, (T_{front} - T_{back})}{d} \tag{24}$$

$$\frac{\lambda \, (T_{front} - T_{back})}{d} = \sigma \, e_{back} \, {T_{back}}^4 \tag{25}$$

Note that λ and d have similar effect on the equations, and can be substituted by a normalised conductivity: $NC = \lambda/d$. Then the front surface temperature T_{front} can be resolved, which is a complicated function of Q_S, e_{front}, e_{back}, and NC. Assume $Q_S = 27\,\mathrm{W/cm^2}$ according to the trajectory simulation, $e_{front} = 1$ as the worst case scenario for backside radiative cooling, then T_{front} can be plotted against e_{back} and NC, as shown in Fig. 9.

Figure 9 shows that considerable reductions of front surface temperature can be achieved if the heat could be effectively conducted through the shell and radiated from the aft surface. For instance, the front surface temperature of an adiabatic wall

with only front surface radiative cooling is 1506 K, which can be reduced to 1397 K when $e_{back} = 0.5$, $NC = 500\,\mathrm{W/K \cdot m^2}$ (equivalent to $d = 1\,\mathrm{mm}$, $\lambda = 0.5\,\mathrm{W/m \cdot K}$), while the aft surface temperature is 1256 K.

6. Conclusions

An innovative deployable heat shield design concept is proposed, which utilises centrifugal force generated by autorotation to deploy the structure under aerodynamic load. As demonstrated by simulations, the autorotation and deployment angle regulates each other and achieves a passive control that lets the heat shield reach an equilibrium deployment state.

Furthermore, a baseline vehicle is designed. This vehicle has a conventional deployable first stage that is used to induce initial deployment and improve the performance of the second stage. The flexible second stage is centrifugally deployed and has a shape based on an origami pattern to initiate autorotation while achieving compact packaging and shape morphing.

Analytical equations are derived to characterise the structural dynamic behaviours of the second stage, which have satisfactory agreement with numerical FE and trajectory simulations. It is shown that at higher altitudes ($> 30\,km$), the heat shield always reaches near-fully deployed conditions, allowing it to effectively generate aerodynamic drag and survive the aerothermodynamic heating. Meanwhile, oscillations associated with deploying-folding motion exists throughout the descent. However, the oscillation amplitude is generally insignificant ($< \pm 10^{\circ}$), and the frequency (0.1 Hz - 10 Hz) can be designed to be away from spin rate or aerodynamic pitching frequency to prevent coupling.

In addition, the heat shield can be lightweight and compact as no thermal insulation is needed on the flexible components. This also means the flexible heat shield's

temperature can be reduced as a result of aft surface radiative cooling. For instance, on the baseline vehicle a reduction of 100 K is feasible under the heat flux of 27 W/cm^2.

The presented research is a preliminary study where simplified models are used to to reveal the basic performance of the heat shield, especially the baseline behaviour associated with deployment. The limitations of the models include: the structural model assumes axisymmetrical deployment and no structural damping; the three degree-of-freedom trajectory simulation assumes zero angle of attack and ignores gyroscopic effect.

References

[1] J. Cruz, J. Lingard, Aerodynamic decelerators for planetary exploration: past, present, and future, in: AIAA Guidance, Navigation, and Control Conference and Exhibit, AIAA paper 2006-6792, 2006.

[2] B. P. Smith, C. L. Tanner, M. Mahzari, I. G. Clark, R. D. Braun, F. M. Cheatwood, A historical review of inflatable aerodynamic decelerator technology development, in: Aerospace Conference, 2010 IEEE, IEEE, 2010, pp. 1–18.

[3] R. D. Braun, R. M. Manning, Mars exploration entry, descent, and landing challenges, Journal of Spacecraft and Rockets 44 (2) (2007) 310–323.

[4] B. Steinfeldt, J. Theisinger, A. Korzun, I. Clark, M. Grant, R. Braun, High mass mars entry, descent, and landing architecture assessment, in: AIAA SPACE 2009 Conference & Exposition, AIAA paper 2009-6684, 2009.

[5] B. G. Drake, S. J. Hoffman, D. W. Beaty, Human exploration of mars, design

reference architecture 5.0, in: Aerospace Conference, 2010 IEEE, IEEE, 2010, pp. 1–24.

[6] V. Carandente, R. Savino, New concepts of deployable de-orbit and re-entry systems for cubesat miniaturized satellites, Recent Patents on Engineering 8 (1) (2014) 2–12.

[7] B. Chan, N. Bauer, J. R. Juneau, S. Stout, K. Masuyama, D. Spencer, Recovery of in-space cubesat experiments (RICE) project, in: Seventh International Planetary Probe Workshop, Barcelona, Spain, 2010.

[8] G. Zuppardi, R. Savino, G. Mongelluzzo, Aero-thermo-dynamic analysis of a low ballistic coefficient deployable capsule in earth re-entry, Acta Astronautica 127 (2016) 593–602.

[9] I. G. Clark, A. L. Hutchings, C. L. Tanner, R. D. Braun, Supersonic inflatable aerodynamic decelerators for use on future robotic missions to mars, in: Aerospace Conference, 2008 IEEE, IEEE, 2008, pp. 1–17.

[10] H. Bohon, M. Mikulas, M, Development status of attached inflatable decelerators., Journal of Spacecraft and Rockets 6 (6) (1969) 654–660.

[11] C. Tanner, J. Cruz, R. Braun, Structural verification and modeling of a tension cone inflatable aerodynamic decelerator, in: 51st AIAA/ASME/ASCE/AHS/ASC Structures, Structural Dynamics, and Materials Conference 18th AIAA/ASME/AHS Adaptive Structures Conference 12th, AIAA paper 2010-2830, 2010.

[12] A. Mastropietro, J. Kempenaar, M. Redmond, M. Pauken, W. Ancarrow, First test flight thermal performance of the low density supersonic decelerator (LDSD)

supersonic flight dynamics test (SFDT) vehicle, in: 45th International Conference on Environmental Systems, 2015.

[13] D. Litton, D. Bose, F. Cheatwood, S. Hughes, H. Wright, M. Lindell, S. Derry, A. Olds, Inflatable re-entry vehicle experiment IRVE-4 overview, in: 21st AIAA Aerodynamic Decelerator Systems Technology Conference and Seminar, AIAA paper 2011-2580, 2011.

[14] D. Wilde, S. Walther, K. Pitchadze, S. Alexsaschkin, D. Vennemann, L. Marraffa, Flight test and ISS application of the inflatable reentry and descent technology (IRDT), Acta Astronautica 51 (1-9) (2002) 83–88.

[15] M. Wiegand, H. Konigsmann, A small re-entry capsule-BREM-SAT 2, in: 10th AIAA/USU Small Satellite Conference, Logan., Volume 1, 1996.

[16] D. L. Akin, The parashield entry vehicle concept-basic theory and flight test development, in: 4th AIAA/USU Small Satellite Conference, Logan, UT, Aug. 27-30, 1990, Proceedings. (A91-27376 10-18). Logan, Vol. 1, 1990.

[17] E. Stern, M. Barnhardt, E. Venkatapathy, G. Candler, D. Prabhu, Investigation of transonic wake dynamics for mechanically deployable entry systems, in: Aerospace Conference, 2012 IEEE, IEEE, 2012, pp. 1–10.

[18] E. Venkatapathy, K. Hamm, I. Fernandez, J. Arnold, D. Kinney, B. Laub, A. Makino, M. McGuire, K. Peterson, D. Prabhu, et al., Adaptive deployable entry and placement technology (ADEPT): a feasibility study for human missions to mars, in: 21st AIAA Aerodynamic Decelerator Systems Technology Conference and Seminar, AIAA paper 2011-2608, 2011.

[19] R. Detra, A. Kantrowitz, F. Riddell, P. Rose, The drag brake manned satellite system, in: Xth International Astronautical Congress London 1959/X. Internationaler Astronautischer Kongress/Xe Congrès International dAstronautique, Springer, 1960, pp. 728–747.

[20] M. Berzeri, A. A. Shabana, Study of the centrifugal stiffening effect using the finite element absolute nodal coordinate formulation, Multibody System Dynamics 7 (4) (2002) 357–387.

[21] V. Koshelev, V. Melnikov, Large space structures formed by centrifugal forces, CRC Press, 1998.

[22] J. M. Hedgepeth, Dynamics of a large spin-stiffened deployable paraboloidal antenna, Journal of Spacecraft and Rockets 7 (9) (1970) 1043–1048.

[23] S. Nakasuka, T. Funane, Y. Nakamura, Y. Nojiri, H. Sahara, F. Sasaki, N. Kaya, Sounding rocket flight experiment for demonstrating furoshiki satellite for large phased array antenna, Acta Astronautica 59 (1) (2006) 200–205.

[24] M. Gärdsback, G. Tibert, Deployment control of spinning space webs, Journal of guidance, control, and dynamics 32 (1) (2009) 40–50.

[25] G. Kiper, E. Soylemez, Deployable space structures, in: Recent Advances in Space Technologies, 2009. RAST'09. 4th International Conference on, IEEE, 2009, pp. 131–138.

[26] C. H. Wolowicz, J. Brown Jr, W. P. Gilbert, Similitude requirements and scaling relationships as applied to model testing, Technical Report TP-1435, NASA.

[27] J. M. Gere, Mechanics of materials, sixth ed., Thomson Learning, Belmont, 2004.

[28] W. Wade, A. Sinha, R. Singh, Study of wrap-rib antenna design, Technical Report CR-162929, NASA.

[29] S. Hughes, J. Ware, J. Del Corso, R. Lugo, Deployable aeroshell flexible thermal protection system testing, in: 20th AIAA Aerodynamic Decelerator Systems Technology Conference and Seminar, AIAA paper 2009-2926, 2009.

[30] D. Coatta, D. Jurewicz, B. Tutt, T. Rivellini, I. Clark, Development and testing of an 8 meter isotensoid supersonic inflatable aerodynamic decelerator, in: 22nd AIAA Aerodynamic Decelerator Systems Conference, AIAA paper 2013-1328, 2013.

[31] P. Wercinski, Adaptable deployable entry and placement technology (ADEPT), Oral/Visual Presentation ARC-E-DAA-TN31961, NASA.

[32] P. Gallais, Atmospheric re-entry vehicle mechanics, Springer Science & Business Media, 2007.

[33] A. Viviani, G. Pezzella, Aerodynamic and aerothermodynamic analysis of space mission vehicles, Springer, 2015.

[34] E. H. Hirschel, et al., Basics of aerothermodynamics, Springer, 2005.

[35] H. Wright, A. Cutright, J. Corliss, W. Bruce, D. Trombetta, A. Mazaheri, M. Coleman, A. Olds, S. Hancock, Heart flight test overview, in: 9th International Planetary Probe Workshop, 2012, pp. 16–22.

[36] D. Jurewicz, L. Lichodziejewski, B. Tutt, B. Gilles, G. Brown, Application of inflatable aeroshell structures for entry descent and landing, in: Aerospace Conference, 2013 IEEE, IEEE, 2013, pp. 1–10.

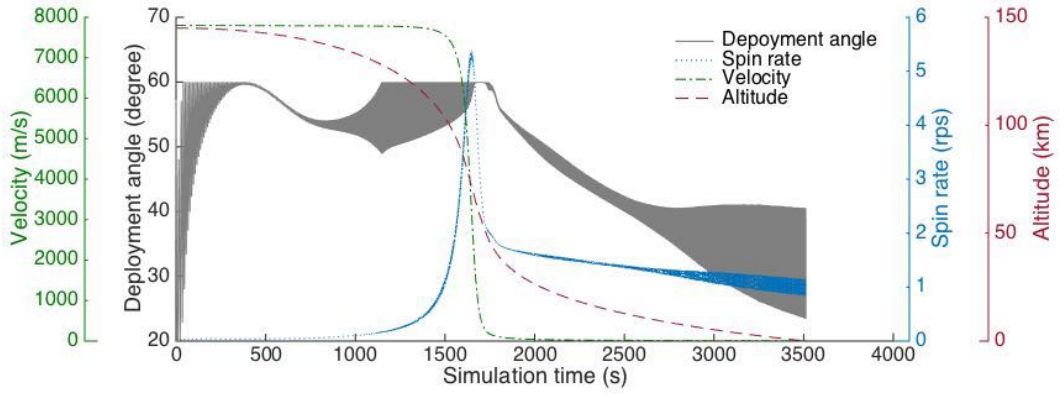

(a)

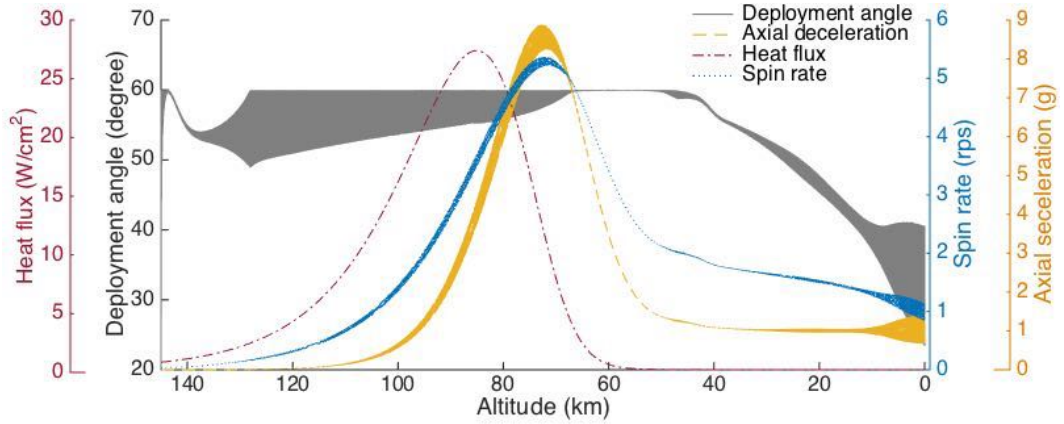

(b)

Figure 8: Trajectory simulation results on a CubeSat sized vehicle with baseline design plotted against (a) simulation time, (b) altitude, showing $> \mathbf{50°}$ deployment angle before reaching 25 km altitude accompanied by structural oscillation.

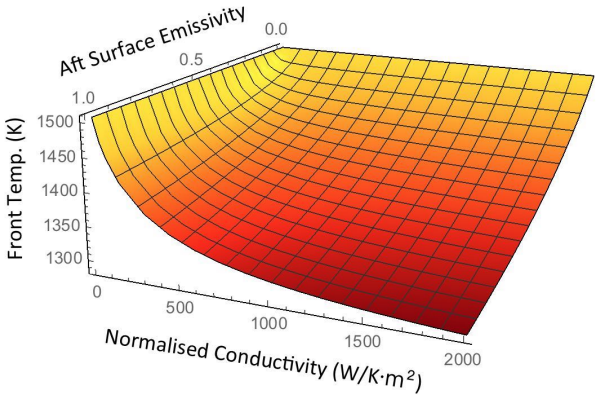

Figure 9: Prediction of the front surface temperature of an equilibrium non-ablating wall under 27 $\mathbf{W/cm^2}$ heating against aft surface emissivity and the wall's normalised conductivity, showing that temperature reduction can be achieved by aft surface radiative cooling.

2.2 Design of the heat shield geometry

Paper I has proposed the baseline design concept of the flexible heat shield. However, the exact spiral geometry, or in other words, the determination of the origami crease pattern is not covered by the paper, and is described here.

2.2.1 Design objectives

The design requires the origami to:

1. Form a conical shape when fully deployed and flattened;
2. Form a cylinder when folded up for storage;
3. Form a spiral shape when partially deployed, in order to generate aerodynamic roll-torque.

Although it is actually possible to only satisfy the requirements 1 and 2, and create a spiral shape that is independent of the origami pattern, the requirement 3 is set here for two reasons:

- When the heat shield is folded along the spiral shape, the creeping of material (during the time when the heat shield is packed) will not vary the spiral characteristics, which allows longer mission duration and earlier packaging prior to the spacecraft assembly;
- This allows local reinforcements (spars) with a higher flexural rigidity to be embedded along the spiral shape to improve the shell's mechanical behaviour and help maintain the spiral shape without affecting the packaging process, the utilisation of such reinforcement is described in Paper III.

2.2.2 The origami crease pattern

The baseline design used in Paper I is illustrated in Figure 2.1, which is a flasher-type origami crease pattern. The pattern fits on a conical surface, and allows packaging in a "wrap-rib" manner. The creases represented by thick lines form the spiral shape, and the thinner folds enable rib-wrapping. However, a shell in reality may not contain the thin lines since smooth curves rather than creases are formed during wrapping due to the compliance of material. The thin lines are plotted here only to illustrate the full pattern.

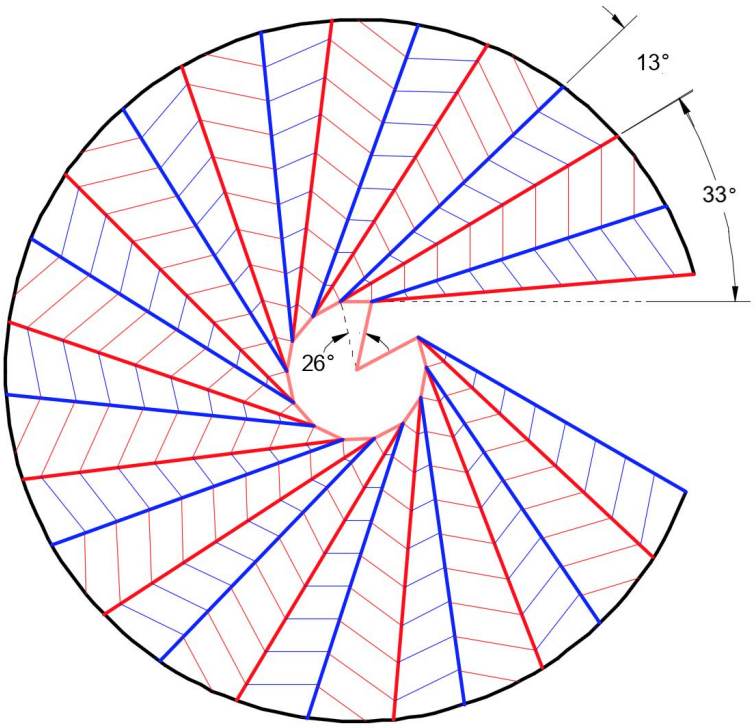

Figure 2.1: Baseline origami crease pattern (flattened) used in paper I, where mountain and valley folds are represented by red and blue lines respectively

Multiple paper prototypes are fabricated to explore the origami design, as shown in Figure 2.2. It can be seen that the compactness of the cylindrical package depends on two factors: the diameter of the cylinder is determined by the size of

the unfolded nose cone near the vertex; the length of the cylinder is defined by the wrapping angle illustrated in Figure 2.3.

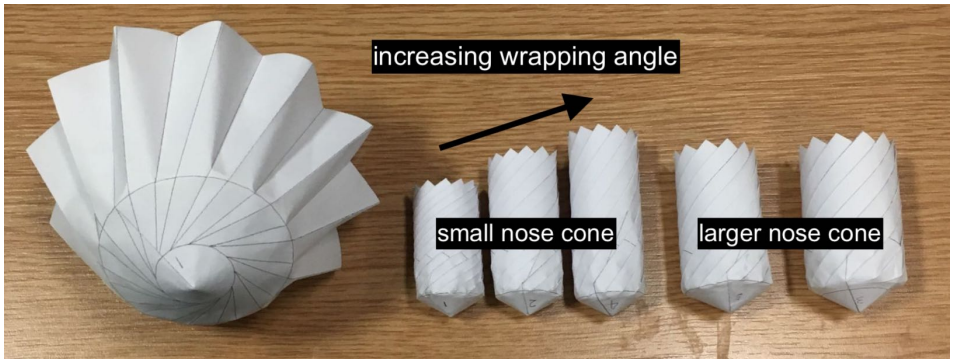

Figure 2.2: Paper prototypes of different origami patterns, left: partially deployed configuration that forms a spiral shape, right: folded configuration that forms a cylinder

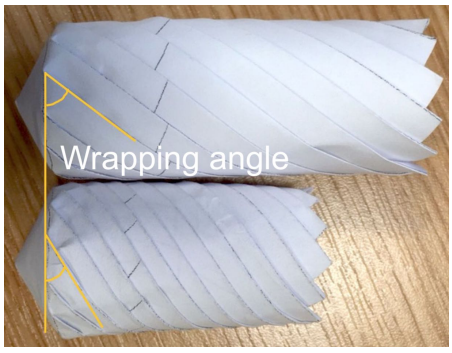

Figure 2.3: Wrapping angle of the origami pattern shown on fully-folded paper prototypes, which is a design-able parameter that influences the length of the package

Two typical origami patterns are shown in Figure 2.4. It contains 12 wrapping elements circumferentially aligned around the rigid nose cone. The number of 12 is chosen here since a larger number leads to excessive folding lines that affects packaging, and a lower number gives a rough shape that offsets from the circular nose cone. Each element consists of two panels with the same panel vertex angle in order to give a cylindrical shape when fully folded. The element separation angle

is set to 26° in order to provide a fully-deployed cone with 120° vertex angle, since $26° \times 12 = 312°$, which is the central angle of the whole pattern.

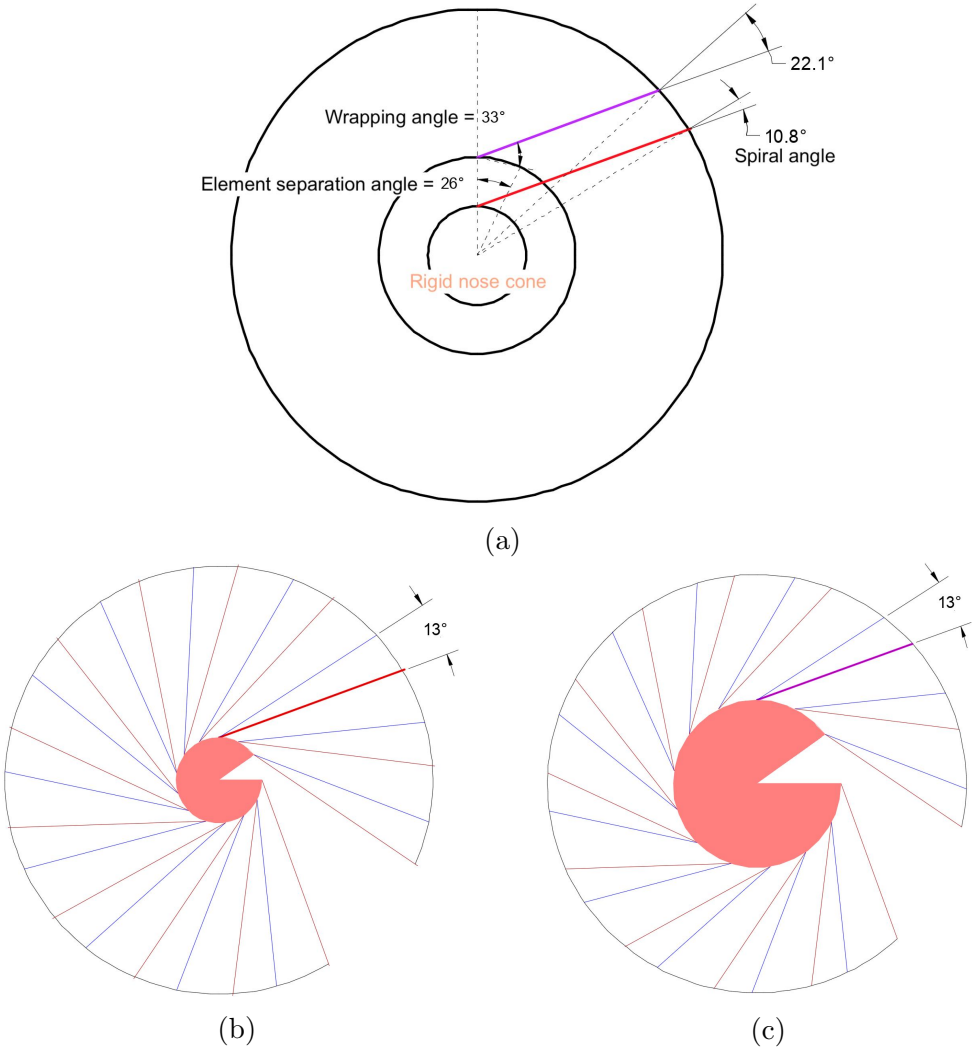

Figure 2.4: Design of the origami crease pattern, (a) critical design parameters, where wrapping angle is set to the lowest practical value to maximise packing ratio and spiral angle, while the size of the rigid nose cone is a trade-off between compactness and spiral characteristics, (b)(c) flattened origami patterns that form a 120° cone with different nose cone diameters, mountain and valley folds are illustrated by red and blue lines respectively

According to Figure 2.4a, there are four important parameters associated with the origami pattern: the element separation angle, the wrapping angle, the size of the

rigid nose cone, and the spiral angle which defines the spiral characteristic of the shape.

Ideally, the wrapping angle should be as low as possible to enable a compact packaging. However, a low wrapping angle leads to a packed configuration with a large amount of overlapping heat shield material. This significantly reduces the tolerance to material thickness, increases the resistance to initial deployment/unpacking due to surface friction, and leads to tight folding that could damage materials such as ceramic fabric. After multiple trails, the wrapping angle is set to 33°. It is the highest wrapping angle to provide a maximum number of overlapping materials of below 8 (Figure 2.4b design). Detailed analyses on the package configuration can be found in Appendix A.1.

Meanwhile, a high spiral angle is preferred since it enhances the spiral characteristic of the shell, which assists the autorotation and thereby the centrifugal deployment. As illustrated in Figure 2.4a, a high spiral angle requires a large rigid nose cone, as well as a low wrapping angle that is already achieved in the last design step. However, enlarging the nose cone leads to lower packing ratio, thus creating a trade-off between compactness and spiral characteristic. Figure 2.5 shows the trade in more detail, where spiral angle is near linearly related to nose cone diameter.

Paper I has proposed a deployable first stage that can increase the initial diameter of the shell to assist deployment. Figure 7 (c) in paper I has demonstrated that a first stage diameter ratio (first stage diameter/shell maximum diameter) of approximately 0.4 (which gives $\sim$ 0.577 in the paper) provides the optimum static stability of deployment. Therefore, the nose cone diameter ratio should be in the range of $0 \sim 0.4$ considering the trade-off between deployment stability and compactness. The Figure 2.4b design has the ratio set to 0.2 and is used as the baseline design in paper I. This allows the shell to be packed into a cylinder with a

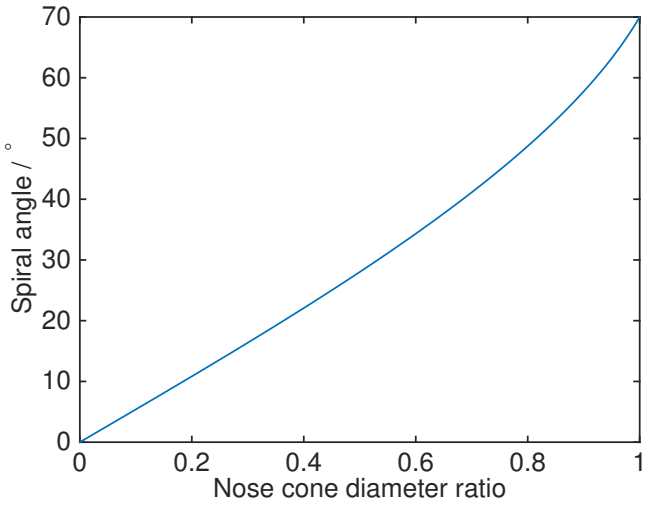

Figure 2.5: Trade-off between nose cone diameter ratio (nose cone diameter/shell maximum diameter) and spiral angle, with wrapping angle set to 33°

14 *cm* diameter and a 25 *cm* length, which fits outside a 3U CubeSat. The Figure 2.4c design has replaced the first stage with a large rigid nose cone, which is the simplified design used in Paper III.

Chapter 3

Downrange manoeuvre and oscillation suppression

This chapter is based on another submitted paper that demonstrates the active deployment control of the heat shield. Utilising an off-the-shelf reaction wheel controlled by an algorithm developed in the present study, an active control loop is added into the self-regulating system. It modulates the vehicle spin rate, thus the deployment angle and drag coefficient, and therefore achieves considerable downrange manoeuvrability. The limit-cycle oscillation of the heat shield, which persists throughout the entry, is also investigated. The proposed active control system is proven useful to suppress the simulated oscillation.

3.1 Paper II: Active deployment control and drag manoeuvre

Downrange Manoeuvre and Oscillation Suppression of a Self-Moderating Centrifugally Deployed Flexible Heat Shield Using Controlled Reaction Wheel

Authors: Rui Wu, Peter Roberts, Constantinos Soutis, Carl Diver

Journal: Acta Astronautica, (**Impact factor:** 1.536)

Submission date: July 2018

Statement of own contributions in joint authorship:

Main research idea and technological development;

Preparation of tables, figures, and the manuscript;

Interpretation of the heat shield system and its oscillatory behaviour;

Design of the control algorithm, and the baseline controlled vehicle;

MATLAB/SIMULINK simulator construction and result interpretation.

Note: Supplementary material is available in Appendix A.2.

Downrange manoeuvre and oscillation suppression of a self-regulating centrifugally deployed flexible heat shield using a controlled reaction wheel

Rui Wu[a,*], Peter C.E. Roberts[a], Constantinos Soutis[b], Carl Diver[a]

[a] *School of Mechanical, Aerospace and Civil Engineering, The University of Manchester, UK*
[b] *The University of Manchester Aerospace Research Institute, UK*

Abstract

A recent study has introduced a flexible deployable heat shield that passively deploys and stiffens due to centrifugal forces generated from a self-regulated autorotation. This paper demonstrates that the heat shield is similar to a PI controlled second order nonlinear system, which explains why the deployment is accompanied by a limit cycle structural oscillation that persists throughout a simulated re-entry. The heat shield design offers an unique capability to actively adjust the deployment using conventional attitude control devices. This operation is explored by simulating the re-entry of a CubeSat-sized vehicle equipped with an off-the-shelf reaction wheel controlled by a switching phase shift controller and gain-scheduled controllers. The effects of the control parameters are investigated, and successful oscillation suppression as well as an open-loop downrange manoeuvre of over 300 km is predicted for re-entry from low earth orbit.

Keywords:

entry vehicle, deployable aerodynamic decelerator, targeted re-entry, centrifugal

*Corresponding author
Email address: rui.wu@manchester.ac.uk (Rui Wu)

deployment, limit cycle oscillation

Nomenclatures

a, b: downrange control parameters

a_{dec}: deceleration of vehicle

C_D: drag coefficient

f: natural frequency of the oscillatory motion

F: ratio of reaction wheel angular velocity and wheel maximum (saturated) speed

g: gravitational acceleration

i: control signal

I: angular inertia

l: base diameter of the fully deployed heat shield

m: total mass of vehicle

M: total deploying moment

M_a: anti-deploying moment from aerodynamic force

M_E: anti-deploying moment from elastic force

M_{F_C}: deploying moment from centrifugal force

M_g: deploying moment from axial deceleration

$N_{torque\ factor}$: Torque factor

q: dynamic pressure

S: reference surface area of the vehicle

St: Strouhal Number

t: time

T_0: period of natural oscillation

v: descending velocity

θ: deployment angle

ω: spin rate of autorotation

ρ_S: shell surface density

τ: Aerodynamic roll-torque

CG: Centre of Gravity

$IRVE$: Inflatable Re-entry Vehicle Experiment

1. Introduction

Deployable aerodynamic decelerators for atmospheric entry have been attracting increasing attention due to the demand for a next generation Mars entry system for heavy payloads, as well as a small recoverable orbital scientific platform, such as a CubeSat that can de-orbit and recover the payload using a re-entry vehicle [1, 2, 3, 4, 5, 6, 7, 8, 9]. The advantages of deployable heat shields over conventional rigid ones mainly come from two aspects [4, 10]:

1. Low ballistic ratio (defined as m/SC_D) under the deployed condition leads to a higher deceleration in the upper atmosphere and thus reduced thermal load, as well as providing sufficient deceleration through planetary atmospheres that are less-dense than the Earth's (e.g. Mars), or even soft landing without a parachute system;
2. When stowed, the heat shield can be fitted into a limited space determined by the launch vehicle fairing or the acceptable payload volume.

Current developments mostly focus on two types of structures: the inflatable and the mechanically deployable structures. The inflatable structures are based on flexible thermal protection materials supported by air-tight chambers that deploy and stiffen when inflated by an on-board gas source or ram air [11, 12, 13, 14, 15, 16]. The

mechanically deployable structures are usually umbrella-like mechanisms consisted of rigid components as the skeleton and flexible thermal protection materials as the skirt [4, 17, 18, 19].

Meanwhile, a new type of centrifugally deployed heat shield has been proposed in a previous study by the authors [20]. The core of the concept is a flexible conical shell made of ceramic fabric. Since local reinforcements are applied along an origami pattern, the shell naturally buckles along the pattern and forms a spiral shape when folded, as shown in Figure 1. The spiral shape generates a roll-torque when descending through an atmosphere and leads to autorotation. In turn, the spin progressively flattens the shell, reducing the induced roll-torque. The rate of autorotation is thereby determined by the shell's deployment condition, and converges to a value where the centrifugal force on the flexible shell is in equilibrium with the aerodynamic load, thus enables a self-regulated spin and deployment. In this way, the structure is deployed and stiffened by inertia force generated from motion (i.e. centrifugal force from autorotation) rather than elastic forces from solid or gaseous materials, and as shown by the previous study, it could realise a CubeSat-sized reentry vehicle that is lightweight, concise and high packing density [20].

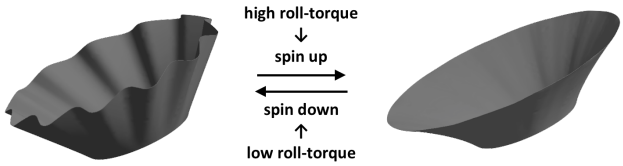

Figure 1: Shape of the centrifugally deployed flexible heat shield generated from FE simulation, showing that equilibrium can be achieved between the partially folded condition (left) and the fully deployed condition (right) when the centrifugal force (due to autorotation) on the shield balances the aerodynamic force [20].

Besides decelerating the payload while surviving aeorthermodynamic heating, advanced missions also require the entry vehicle to be manoeuvrable in order to

actively adjust the trajectory and enable a precise landing [21]. For a ballistic vehicle, this is usually achieved using a small lifting force generated by shifting the vehicle Centre of Gravity (CG) or changing the aerodynamic shape. The Inflatable Re-entry Vehicle Experiment (IRVE)-4 of NASA has proposed active CG shift to control the angle of attack of a 3-meter diameter inflatable aeroshell [13]. Meanwhile, a number of studies on inflatable aeroshells with the stacked tori configuration similar to the IRVE have demonstrated different ways to either permanently or actively vary the shape of the aeroshell. Some studies have proposed to deform the whole aeroshell by canting the tori [21], sliding the tori perpendicular to the initial axis of symmetry [22, 23], or morphing the tori using actuators [24]. Other concepts includes adding actuated flaps/trim tabs or compressible outer torus to change the aeroshell's centre of pressure [21, 23]. On the other hand, mechanically deployable heat shields can also generate lift by having a permanent unsymmetrical shape when deployed [25]. Alternatively, an umbrella-like structure can realise variable frontal area (thus ballistic ratio) by actively controlling the extent of deployment, thus enabling downrange control [17].

In comparison with inflatable and mechanically deployable heat shields, the centrifugally deployed heat shield offers an unique drag modulation capability by actively controlling the extent of deployment using conventional attitude control devices. This is because the centrifugal force, which deploys and stabilises the structure, depends on the vehicle's autorotating (rolling) motion. Therefore, when centrifugal force is altered by actively adjusting the roll rate using an actuator, the heat shield will deploy to a varied extent where it re-balances with the aerodynamic load, and effectively changes deployed drag area and therefore the trajectory.

Nevertheless, the reliance on centrifugal force and the structural flexibility also leads to problems. Lifting manoeuvres are not feasible since a non-zero angle of attack

can not be maintained without conning motion as a result of gyroscopic effects on the rotating vehicle. A previous numerical study has also revealed an oscillatory deploying-folding motion of the undamped heat shield throughout the descent [20].

The present work is a proof-of-concept study that focuses on utilising a reaction wheel to actively manipulate the extent of deployment and therefore, provides a way to suppress the oscillation. The feasibility to adjust the downrange trajectory using such a system is also discussed.

2. Analyses on the heat shield system

The proposed control method uses a single reaction wheel to adjust the rate of autorotation and thereby influence the deployment angle. Therefore, the analyses focus on the deploying-folding motion of the flexible heat shield as well as the autorotation of the vehicle, and all the analyses reported here are based on an aeroshell pointing stably into the flow with zero angle of attack, while the pitching and yawing motions as well as the gyroscopic effects from the autorotation are not considered. For a preliminary study, this is a reasonable simplification since the objective is to reveal the baseline effect of the proposed control, whilst the six Degree-of-Freedom (DoF) flight dynamics requires significantly more computational resource and is not analysed here.

During entry, the deployment of the heat shield is determined by three moments of forces (Figure 2): the deploying moment due to centrifugal force M_{F_C}, the deploying moment due to axial deceleration M_g, and the anti-deploying moment from aerodynamic load M_a. The total deploying moment M is:

$$M = M_{F_C} + M_g - M_a \tag{1}$$

Then the shell deployment angle θ can be expressed as below, where I_{deploy} is

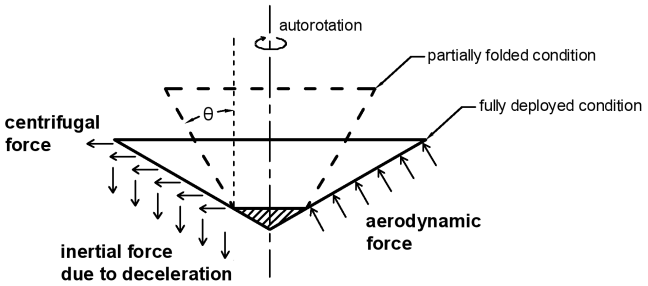

Figure 2: Schematic view of the centrifugally deployed heat shield, showing the three types of forces that contribute to the shield's deployment.

shell's inertia associated with the deploying/folding motion. The shell is therefore a second order dynamic system.

$$\theta = \iint \frac{M}{I_{deploy}} \cdot dt \cdot dt \tag{2}$$

Based on the understanding of the heat shield's structural dynamics [20], a block diagram of the heat shield is constructed, as shown in Figure 3. Ignoring the active control from the reaction wheel controller, the heat shield can be treated as a second order system regulated by feedback from the three deploying/anti-deploying moments M_{F_C}, M_g, and M_a [20]:

$$M_{F_C} \propto \omega^2(\theta + 1.38)cos\theta \tag{3}$$

$$M_g \propto a_{dec}sin\theta \tag{4}$$

$$M_a \propto \rho v^2 sin^3\theta \tag{5}$$

Where ω is the rate of autorotation, a_{dec} is vehicle axial deceleration, ρ is atmospheric density, and v is vehicle axial velocity. According to previous work [20], a_{dec}

can be derived using Newton's law of motion, thus M_g becomes:

$$M_g \propto \rho v^2(\theta - 0.347)sin\theta \tag{6}$$

Since the variation of v is usually minor except in the less-important low-speed regime, and is significantly slower than the structural oscillation, the phase lag due to the integration between a_{dec} and v (Figure 3) is negligible, and v can be regarded as constant. Meanwhile, since θ usually has values between $\pi/6$ and $\pi/3$ ($30° \sim 60°$), the θ-M_g and θ-M_a relationships are near linear, thus M_g and M_a can be treated as Proportional (P) control. M_{F_C} contains an Integral (I) control component since ω is a result of integrated aerodynamic torque, where τ is the roll-torque, and I_{spin} is the vehicle axial angular inertia:

$$\omega = \frac{\int \tau(\theta)dt}{I_{spin}(\theta)} \tag{7}$$

Therefore, the whole system is similar to a second order system regulated by a PI controller, while analytical analysis is difficult due to the complexity and non-linearity. According to Figure 3, the behaviour of the system can be influenced by three parameters: the vehicle mass, the origami pattern, and the atmospheric density.

To enable oscillation suppression, spin rate and axial deceleration are measured and fed into the reaction wheel controller, which controls a reaction wheel that exerts an axial torque to stabilise the oscillation of spin rate and thus stabilise the deployment angle. Spin rate measurement is used to indicate the deployment angle, since the latter is difficult to measure, and the oscillation of the two are strongly coupled (due to the dependence of spin angular inertia on deployment angle, Equation 7) with nearly no phase difference. The axial deceleration is used to compute a control

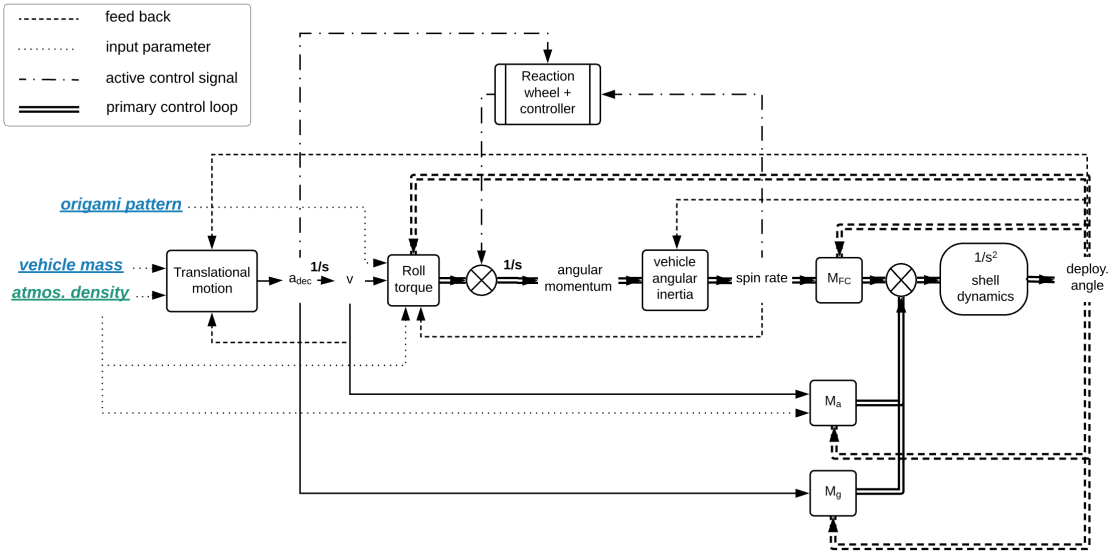

Figure 3: Block diagram of the heat shield assuming zero angle of attack, with the primary feedback loops emphasised by double lines.

parameter as discussed later.

Similarly, the reaction wheel is also used to adjust the overall deployment angle and enable open-loop downrange manoeuvre through drag modulation. This is achieved by varying the overall angular momentum of the system to increase/decrease M_{F_C}, which leads to a biased deployment condition. Aerodynamic drag is thereby manipulated as it depends on the deployment angle. To be noted, the present work only demonstrates the feasibility to achieve extended/shortened downrange trajectory, while the control method to carry out a guided re-entry is not discussed.

The detailed control strategy is shown in Figure 4. Phase shift control is an existing method that has been used to suppress the thermal-acoustic oscillation of gas turbines. Its popularity comes from its simplicity, and thus the ability to survive in harsh environment, as well as the low requirement for knowledge of the the complicated and highly non-linear system [26, 27]. For the same reason it is proposed

for oscillation suppression of the present heat shield, as it is a non-linear system that requires the control power and complexity to be minimised. The phase shift controller simply applies a time delay $K_T \cdot T_0$ to the input spin rate signal, and then outputs the difference between the original and the delayed signal (Figure 4). The measurement of axial deceleration is used to determine the control parameter T_0 for the phase shift controller, which is explained in details in section 4. Trails have shown that $K_T = 0.25$ provides satisfactory performance. Such a controller mimics a proportional-differential controller when the input is sinusoidal (note that the oscillating spin rate is near sinusoidal), but is less sensitive to noise. As an example, assume the input signal is $i_0 = \sin(2\pi t/T_0)$, with $K_T = 0.25$ the output will be:

$$i_1 = \sin(\frac{2\pi(t - 0.25T_0)}{T_0}) - \sin(\frac{2\pi t}{T_0}) = -\cos(\frac{2\pi t}{T_0}) - \sin(\frac{2\pi t}{T_0}) = -\frac{T_0}{2\pi} \cdot i_0' - i_0 \quad (8)$$

A major drawback of phase shift controllers is that they may induce the so called secondary peak, or in other words, the instability induced by the controller in frequencies away from the operation frequency [28, 29]. In the present research, such instability is observed, but is a non-essential problem considering its low amplitude, as further discussed in section 4.

The switching scheduled gain controllers then works out the gains to apply to the throttle. As can be seen in Figure 4, the function of the de-saturation gain scheduling is to reduce the motor throttle as the wheel is approaching its maximum speed (when $i_1 F > 0$):

$$i_2 = i_1(1 - |F|) \qquad \text{if} \quad i_1 F > 0 \quad (9)$$

$$i_2 = i_1 \qquad \text{if} \quad i_1 F \leq 0 \quad (10)$$

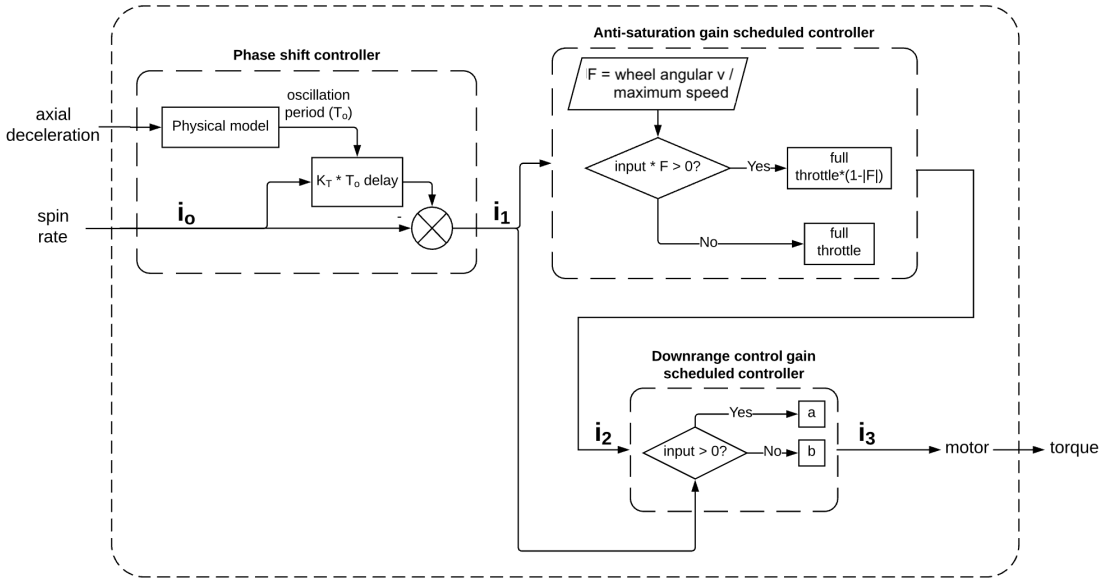

Figure 4: Control algorithm of the reaction wheel controller.

Where i_1 is the output from the phase shift controller, and F is the ratio of the wheel angular velocity and wheel maximum (saturated) speed, as shown in Figure 4. In this way, the controller tends to bring the wheel speed to zero and thereby prevents momentum saturation.

The gain scheduling for downrange control alters the deployment angle and drag coefficient by reducing the throttle value toward a certain direction and thus favour the increment/reduction in spin rate:

$$i_3 = a\, i_2 \qquad \text{if} \quad i_2 > 0 \tag{11}$$

$$i_3 = b\, i_2 \qquad \text{if} \quad i_2 \leq 0 \tag{12}$$

Downrange is shortened when $a > b$, which favours the increment of spin rate and thereby facilitates deployment and leads to a higher aerodynamic drag. The

simulated effects of the controller are discussed with more details in section 4 and 5.

3. Parameter study on the oscillatory behaviour

The results discussed in the present research are generated from a numerical simulator developed in Simulink. The simulator is based on Newtonian aerodynamic equations while assuming zero angle of attack, and Newton's second law is used to describe the point mass dynamics of the vehicle. The previous structural dynamic model is also incorporated to include the deploying/folding behaviours of the flexible shield [20]. It should be noted that the Newtonian method only provides a rough estimation of the base line behaviour for subsonic flight conditions. All the results are generated with a maximum time step of 0.5 ms using a variable-step continuous explicit solver (ode45).

It also worth noticing that the simulator has not included structural damping since damping depends on various unknown factors such as specific material selection and layup. This could lead to an overestimation of oscillation amplitude. However, the structural damping in the design is expected to be weak considering the low heat shield thickness ($\sim$1 mm).

Simulations have shown that a limit cycle oscillation of the flexible heat shield exists within nearly the whole flight regime, which leads to variations in C_D and thus fluctuates the deceleration. This phenomenon can be seen in Figure 10, where rapid fluctuations in deployment angle (for the uncontrolled scenarios with $a = b = 0$) are accompanied by fluctuations in deceleration. The vibration may cause damage to a payload especially when it has low natural frequencies (that is close to the oscillation frequency, which is usually 0.1 Hz $\sim$ 10 Hz depending on the flight regime). Thus efforts are made to understand this oscillation.

A typical limit cycle oscillation observed in the simulations is shown in Figure

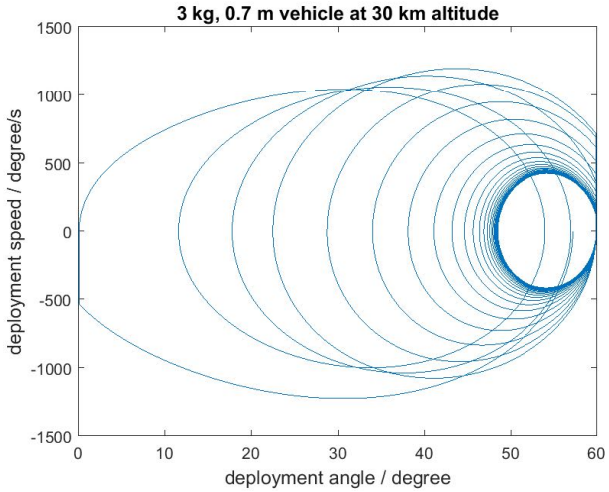

Figure 5: A typical limit cycle oscillation from the simulations, where the deployment speed is the derivative of the deployment angle.

5, which is the result on a CubeSat-sized vehicle with the baseline design [20], 3 kg entry mass, and under a flight condition at 30 km altitude during re-entry from LEO. Referring to Figure 3, running cases which neglect M_g and the coupling between deployment angle and spin angular inertia (by setting I_{spin} to constant, according to Equation 7) shows that the oscillation is unrelated to these factors. In fact, the oscillatory behaviour is due to the integration component that determines M_{F_C} (Equation 7). The aerodynamic roll torque is evaluated as shown in Figure 6. The calculation is based on Newtonian aerodynamics, while the torque depends on deployment angle and the slope of flow velocity vector with reference to the rim of the heat shield. It worth noticing that this slope is proportional to the dimensionless Strouhal Number:

$$St = \frac{\omega \cdot l}{v} \tag{13}$$

It can be seen from Figure 6 that the aerodynamic roll-torque is generally inversely-related to deployment angle. Therefore, when deployment angle is instantaneously

increased from an equilibrium condition (where $\tau = 0$ thus $\dot{\omega} = 0$ under static condition) due to oscillation, the roll-torque τ becomes negative. This negative torque then integrates over half oscillation period to reduce spin rate (Equation 7) and thus deployment angle with a phase lag, which assists the oscillation. Meanwhile, the variation of velocity vector slope is minor during the oscillation and thus has minor effect. Therefore, the primary feedback loop in Figure 3 that contains M_{F_C}, or in other words, the integral component is the cause of the oscillation.

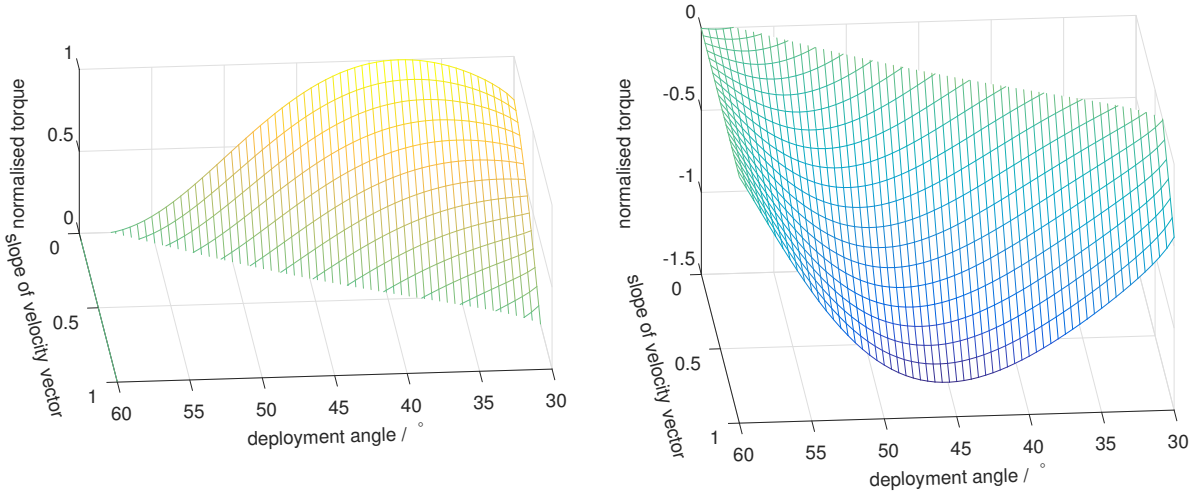

Figure 6: Evaluation of the axial aerodynamic roll torque (with normalised magnitude) using deployment angle and the slope of velocity vector (i.e. the Strouhal number).

The three factors that determine the actual behaviour of the heat shield, as illustrated in Figure 3, are listed below. Their effects on the oscillation are studied using simulations.

(1) Atmospheric density; simulation assumes Earth atmosphere with density values ranging from 150 km altitude to sea level;

(2) Characteristics of the origami pattern; in the simulation, the magnitude of aerodynamic roll torque varies from 0.25 to 2 times of the baseline design;

(3) Total mass of the vehicle; varies from 0.75 kg to 3 kg.

At each data point, the simulation assumes constant atmospheric density and runs until the magnitude and amplitude of deployment angle are stabilised. The simulator also assumes the vehicle axis to be along gravity unlike the real trajectory conditions which have shallow flight path angles at high altitudes. This simplification is made since the objective of this study is to reveal the basic dynamic behaviour of the heat shield, rather than the exact behaviour at various trajectory conditions.

The effect of factors (1), (2) and (3) are shown in Figure 7, where torque factor is a value that is multiplied to the baseline aerodynamic roll torque to manipulate its magnitude: $\tau_{simulated} = N_{torque\ factor} \cdot \tau$. It can be seen that the limit cycle oscillation exists throughout the flight regime, while the amplitude usually increases during descent. Generally, increasing torque factor leads to higher oscillation amplitude. This is because a higher torque factor is equivalent to a higher gain in the integral component that causes the oscillation (Equation 7).

The figure also show that the oscillation amplitude is usually higher in denser atmosphere. This is simply due to the fact that the simulator assumes the speed of the deploying motion becomes zero every time it reaches maximum/minimum deployment angle (60°/30°), thus the oscillation amplitude is mechanically constrained. Therefore, the amplitude can be higher when the equilibrium deployment angle is further away from 30° and 60°, which is the case in dense atmosphere. Similarly, in dense atmosphere there is a trend of increasing oscillation amplitude with decreasing vehicle mass, which is particularly notable in Figure 7b. This is because a lower mass leads to a higher equilibrium deployment angle that is further away from 30°

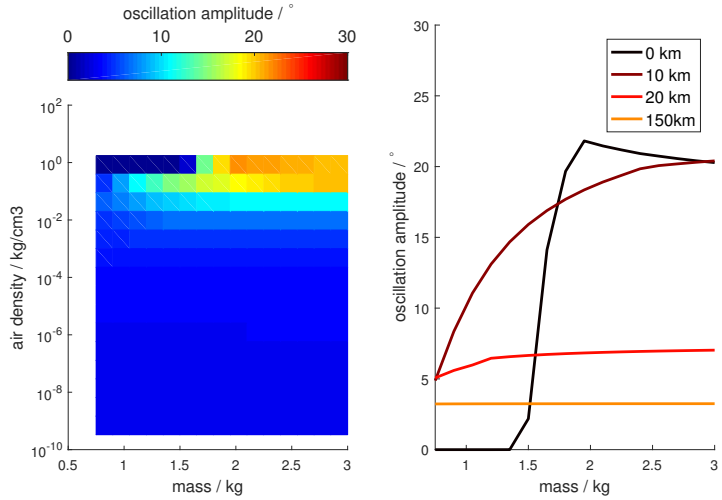

(a) Torque factor = 0.5

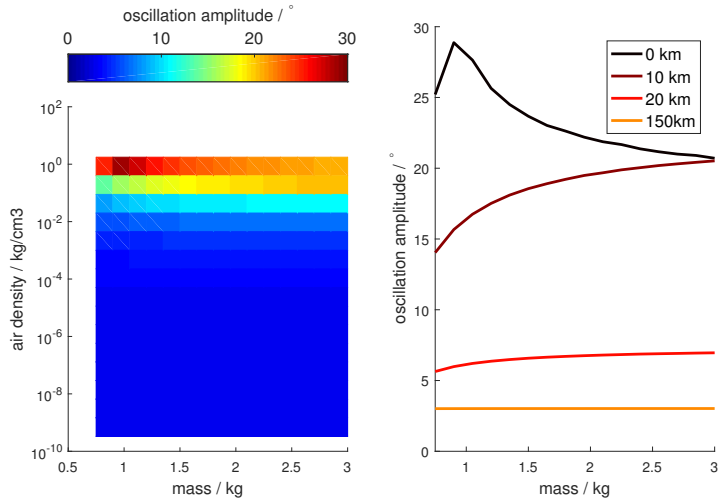

(b) Torque factor = 2

Figure 7: Effect of vehicle mass, atmospheric density (or equivalent altitude on Earth) and magnitude of aerodynamic torque on the oscillation amplitude of deployment angle; it can be seen that the oscillation is common throughout different flight conditions, while the effects that reduces aerodynamic roll-torque always lead to a lower oscillation except at very low altitude (<10 km).

and thus leads to higher oscillation amplitude.

Figure 7 has also shown another trend of reducing oscillation amplitude due to

decreasing vehicle mass, which exists at all the altitudes. This is because a lower mass leads to lower dynamic pressure, which, similar to a reducing torque factor, is equivalent to reducing the integration gain that causes the oscillation.

4. Oscillation suppression

The basic mechanism of the reaction wheel controller is already discussed in section 2: the controller feeds back and regulates the spin rate to alter the deployment angle. The control parameter T_0 in the phase shift controller is the period of the heat shield's natural oscillation, which can be approximated by Equation [20]:

$$f = \frac{1}{2\pi}\sqrt{\frac{\frac{\partial M}{\partial \theta}}{I_{deploy}}} \tag{14}$$

Where f is the natural frequency, M is the total deploying moment on the flexible shell evaluated according to Equation 1, θ is deployment angle, and I_{deploy} is the deploying angular inertia of the shell. After simplification and assuming a deployment angle close to 60°, Equation 14 becomes [20]:

$$f \approx 0.49\sqrt{\frac{a_{dec}\,(1.53\,m - 1.21\,l^2\rho_S)}{l^3\rho_S}} \qquad \text{(Hz)} \tag{15}$$

Where a_{dec} is deceleration (including the component of gravity along the vehicle's axis, in $\mathrm{m/s^2}$), l is the heat shield base diameter when deployed, m is the vehicle's mass (kg), and ρ_S is the surface density of the shell ($\mathrm{kg/m^2}$). The vehicle analysed in this section has a total mass of 3 kg, a surface density of 1.1 $\mathrm{kg/m^2}$ and a base diameter of 0.7 m. Thus, Equation 14 becomes:

$$f \approx 1.60\sqrt{a_{dec}} \qquad \text{(Hz)} \tag{16}$$

Equation 16 provides simple predictions with the error $< 25\%$ in comparison with simulation, and is incorporated into the reaction wheel controller.

Meanwhile, it should be noted that Equation 1 ignores the elasticity and damping of the flexible shell, which is difficult to predict as it depends on the actual material and structural properties, whilst the elastic forces also depend on the initial deployment angle at the unloaded condition. However, the effect of elastic and damping force is expected to be weak as the aim of this heat shield design is to eliminate the dependence on elasticity while taking advantage of the structure supported by inertia force. Nevertheless, the anti-deployment moment of elastic force, M_E, is included in the numerical simulators since it has notable effect on the heat shield's deployment angle at high altitude where the aerodynamic effect is weak. Thus Equation 1 becomes:

$$M = M_{F_C} + M_g - M_a - M_E \tag{17}$$

Where M_E is evaluated based on the bending rigidity of the shield's root using linear beam theory by assuming a shell thickness of 1 mm, a Young's modulus of 5 MPa, and assumes bending occurs in a region within 10 mm from the shell's root. This provides a reasonable example to show the effect of elasticity, but is not based on any real designs. The deployment angle of the heat shield at unloaded condition is set to the minimum deployment angle ($30\,^\circ$), thus the elasticity provides an anti-deployment effect. The effect of M_E is illustrated by the trajectory simulation in Figure 10, where the result on an uncontrolled vehicle without accounting for M_E is set in comparison with the same vehicle with M_E. It can be seen that the elastic force has notably reduced the deployment angle at high altitude and therefore increased the downrange, while its effect on the oscillatory behaviour is insignificant. Meanwhile,

the spin rate at high altitude is increased by adding M_E since the heat shield requires higher centrifugal force to maintain its equilibrium deployment angle.

The sensors in the reaction wheel controller are set to have a sample rate of 1000 Hz, which provides a near ideal scenario. The controller output at 1000 Hz is then transferred to 50 Hz by averaging in every 20 ms, thus the motor is controlled at a rate of 50 Hz, and with its torque response assumed to be instantaneous for simplicity. As spin rate varies due to oscillation, the evaluated parameter T_0 is smoothed by a simple moving average filter with the length of 1000 to prevent the interference caused by this oscillation. This filter has shown no adverse effect since T_0 changes slowly through descent and is not sensitive to phase lag. With this filter, the noise in deceleration is generally irrelevant to the controller's performance and is not considered as an issue. However, the spin rate measurement could have an excessive noise spectral density in the magnitude of $0.01°/\mathrm{s}/\sqrt{\mathrm{Hz}}$ (according to the gyro of a commercial IMU). This could be resolved using redundant sensors and signal processing techniques, but is not considered as the subject of this paper. Therefore, no noise is included in the simulations.

Since the simulation uses a baseline CubeSat-sized vehicle design, a reaction wheel is chosen accordingly to fit within such a system: the Sinclair Interplanetary RW3-0.060, which outputs torque of approx. $\pm 20\,\mathrm{mNm}$ with the wheel momentum within $\pm\,0.18\,\mathrm{Nms}$. Peak performance is achieved at roughly 25 W and 28 V. The reaction wheel assembly has a total mass of 226 g and a size of $77\,\mathrm{mm} \times 65\,\mathrm{mm} \times 38\,\mathrm{mm}$ [30].

To investigate the basic behaviours of the controlled vehicle, the simulator used to construct Figure 7 is revised to include M_E, the reaction wheel controller, and the flight path angles that are determined using full trajectory simulation (Figure 10). In order to eliminate the effect of initial conditions, the reaction wheel controller is

turned on from the simulation time of 150 s when the spin rate is generally stabilised. The results at different altitudes are shown in Figure 8. It can be seen that at lower altitude the oscillations are rapidly suppressed after the controller is enabled, whereas at higher altitudes where the oscillation suppression is slower since the phase shift controller becomes ineffective due to the large error in control parameter T_0. This is because Equation 16 no longer holds when the dynamic pressure is low and elasticity has considerable effect on the shell's natural frequency.

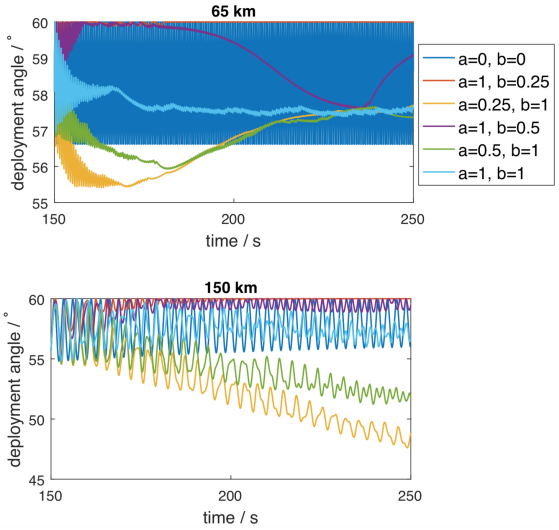

Figure 8: Effect of the reaction wheel controller with various downrange control gains (a and b) at different altitudes, the controller is enabled at the simulation time of 150 s when equilibrium is reached, it can be seen that oscillation suppression is effective at lower altitude (in comparison with the dark blue line, which is the uncontrolled scenario with $a = 0$, $b = 0$ according to Equation 11-12), while downrange control (with $a \neq b$) has effectively varied the average deployment angle before momentum saturation.

Meanwhile, a small residual oscillation always emerge after the suppression of the original oscillation, which is caused by the coupling between the phase shift controller and the heat shield system, and has a frequency higher than the structural natural oscillation. The details of a typical residual oscillation is shown in Figure 9. This

phenomena is reminiscent of the so called secondary peaks caused by phase shift controllers used to suppress thermal acoustic oscillations of gas turbines [28]. However, this is not a critical issue considering the low oscillation amplitude, especially during the flight regime with higher dynamic pressure.

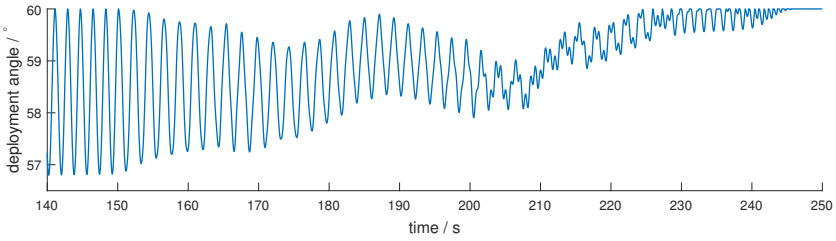

Figure 9: Details of a typical residual oscillation, showing secondary peaks at a frequency higher than the natural oscillation.

Then, the effect of oscillation suppression on the re-entry trajectory is assessed using the trajectory simulator, which assumes a re-entry starting from 150 km altitude at a velocity of 7800 m/s, with zero flight path angle, zero spin rate, and an initial deployment angle of 30°. Simulations are terminated when the vehicle reaches 30 km altitude since the vehicle has already entered the uncritical low speed regime at this altitude.

According to the results shown in Figure 10, the controller leads to effective oscillation reduction in both deployment angle and deceleration throughout descent. From the history of reaction wheel momentum it can be seen that the reaction wheel not only counteracts the oscillations that has relatively high frequency (0.1 Hz $\sim$ 10 Hz), but also undesirably counteracts the overall variation of spin rate during the descent. As a result, momentum saturation is inevitable regardless of downrange control gains. Therefore, the de-saturation gain scheduling (Equation 9-10) is always beneficial to the performance as it conserves some momentum that is useful for oscillation suppression when the reaction wheel approaches maximum speed, rather

than inducing a hard-stop when the reaction wheel is saturated. With this control strategy, a near saturated wheel could "harvest" momentum (from aerodynamic roll-torque) during oscillation and tend to bring the wheel speed back to zero. This is proven effective by the simulation as oscillation is suppressed even under the near-saturated condition before the peak dynamic pressure. Meanwhile, this de-saturation control also helps reducing reaction wheel power consumption as it reduces the motor speed.

5. Downrange control

As described in section 2, downrange manoeuvre can be achieved by manipulating the control gains a and b (Equation 11-12), which leads to an overall spin-up or spin-down of the vehicle, thus influences the deployment angle, thereby determines the drag coefficient of the heat shield. According to Figure 4, downrange can be shortened by letting $a > b$ as it tends to spin-up the vehicle, and vise versa. The effect of control parameters a and b is already validated by Figure 8, which shows that a higher a/b ratio leads to a lower deployment angle until the reaction wheel is near-saturated. Meanwhile, due to the limited torque and momentum that the reaction wheel can output, the effect of downrange control is only eminent when the axial aerodynamic torque is low (at high altitude). Therefore, as supported by Figure 8, the controller has a greater influence on the deployment angle at 150 km than at 65 km.

The effect of downrange control on re-entry trajectory is shown in Figure 11 and summarised in Table 1. The setup is similar to the simulations reported in Figure 10, with the elasticity factor M_E included. It has shown a total downrange variation of 322 km. According to the deceleration history, oscillation suppression is also achieved, while the peak deceleration ($\sim 8\,g$) is independent of the trajectory.

It should be noted that the downrange increment (202 km, with respect to the unbiased condition of $a = b = 1$) is higher than the decrement (120 km). The reason is discussed below.

Table 1: Summary of the results from trajectory simulations of re-entry from 145 km altitude.

Control parameter	Downrange shift
a=0.25, b=1	202 km
a=0.5, b=1	147 km
a=1, b=1	0 km
a=1, b=0.5	-89 km
a=1, b=0.25	-120 km

It worth noticing that, according to the reaction wheel momentum history from Figure 11, the controller counteracts the increasing spin rate at the start of re-entry for >200 s regardless of the downrange control gains (due to the phase shift controller). This affects the capability to reduce downrange, which requires high spin rate. It can also be seen from the figure that during the downrange-reducing manoeuvres (with $a = 1, b = 0.5$ and 0.25), the reaction wheel momentum is far from saturation throughout the high altitude flight regime. Therefore, the reaction wheel's capability is currently not fully utilised, and more effective manoeuvre can potentially be achieved by more sophisticated control algorithms.

6. Conclusions

In the previous study, a flexible heat shield that deploys and stiffens by a self-sustaining autorotation was designed. According to the present study, the passive self-regulated centrifugal deployment leads to a limit cycle structural oscillation, which persists throughout the simulated re-entry when assuming zero structural damping. This could be a problem for sensitive payloads. The present study also

showed that the heat shield is similar to a second order nonlinear system controlled by a PI controller, where the integral component is causing the oscillation.

Meanwhile, since centrifugal force is determined by the vehicle's roll rate, the heat shield shape can be easily regulated using conventional attitude control devices. Therefore, an off-the-shelf reaction wheel with a maximum power of 25 W and a mass of 226 g is proposed to regulate the autorotation (roll rate) of a CubeSat-sized vehicle and thereby achieve actively controlled deployment. The reaction wheel is controlled using a switching phase shift controller combined with gain scheduled controllers.

Specifically, the phase shift control realises oscillation suppression. The overall downrange manoeuvrability of over 300 km is achieved using a gain scheduled controller. Another gain scheduled controller keeps de-saturating the reaction wheel throughout the simulated re-entry. All the controls are successfully demonstrated by the numerical simulations based on Newtonian aerodynamics.

References

[1] M. Braun, P. Bruce, E. Levis, Strategies to utilize advanced heat shield technology for high-payload mars atmospheric entry missions, Acta Astronautica 136 (2017) 22–33.

[2] J. Cruz, J. Lingard, Aerodynamic decelerators for planetary exploration: past, present, and future, in: AIAA Guidance, Navigation, and Control Conference and Exhibit, AIAA paper 2006-6792, 2006.

[3] R. D. Braun, R. M. Manning, Mars exploration entry, descent, and landing challenges, Journal of Spacecraft and Rockets 44 (2) (2007) 310–323.

[4] G. Zuppardi, R. Savino, G. Mongelluzzo, Aero-thermo-dynamic analysis of a

low ballistic coefficient deployable capsule in earth re-entry, Acta Astronautica 127 (2016) 593–602.

[5] J. Andrews, K. Watry, K. Brown, Nanosat deorbit and recovery system to enable new missions, SSC11-X-3, presented at the 25th AIAA/USU Conference on Small Satellites, Logan, Utah, USA, 8-12 August, 2011.

[6] D. M. Bose, J. Shidner, R. Winski, C. Zumwalt, F. Cheatwood, S. J. Hughes, The hypersonic inflatable aerodynamic decelerator (HIAD) mission applications study, in: AIAA Aerodynamic Decelerator Systems (ADS) Conference, AIAA paper 2013-1389, 2013.

[7] J. Virgili, P. C. Roberts, N. C. Hara, Atmospheric interface reentry point targeting using aerodynamic drag control, Journal of Guidance, Control, and Dynamics 38 (3) (2015) 403–413.

[8] K. Yamada, Y. Nagata, T. Abe, K. Suzuki, O. Imamura, D. Akita, Suborbital reentry demonstration of inflatable flare-type thin-membrane aeroshell using a sounding rocket, Journal of Spacecraft and Rockets 52 (1) (2014) 275–284.

[9] E. Fantino, M. Grassi, P. Pasolini, F. Causa, C. Molfese, R. Aurigemma, N. Cimminiello, D. de la Torre, P. Dell'Aversana, F. Esposito, et al., The small mars system, Acta Astronautica 137 (2017) 168–181.

[10] I. G. Clark, A. L. Hutchings, C. L. Tanner, R. D. Braun, Supersonic inflatable aerodynamic decelerators for use on future robotic missions to mars, in: Aerospace Conference, 2008 IEEE, IEEE, 2008, pp. 1–17.

[11] B. P. Smith, C. L. Tanner, M. Mahzari, I. G. Clark, R. D. Braun, F. M. Cheat-

wood, A historical review of inflatable aerodynamic decelerator technology development, in: Aerospace Conference, 2010 IEEE, IEEE, 2010, pp. 1–18.

[12] H. Bohon, M. Mikulas, M, Development status of attached inflatable decelerators., Journal of Spacecraft and Rockets 6 (6) (1969) 654–660.

[13] D. Litton, D. Bose, F. Cheatwood, S. Hughes, H. Wright, M. Lindell, S. Derry, A. Olds, Inflatable re-entry vehicle experiment IRVE-4 overview, in: 21st AIAA Aerodynamic Decelerator Systems Technology Conference and Seminar, AIAA paper 2011-2580, 2011.

[14] A. Mastropietro, J. Kempenaar, M. Redmond, M. Pauken, W. Ancarrow, First test flight thermal performance of the low density supersonic decelerator (LDSD) supersonic flight dynamics test (SFDT) vehicle, in: 45th International Conference on Environmental Systems, 2015.

[15] C. Tanner, J. Cruz, R. Braun, Structural verification and modeling of a tension cone inflatable aerodynamic decelerator, in: 51st AIAA/ASME/ASCE/AHS/ASC Structures, Structural Dynamics, and Materials Conference 18th AIAA/ASME/AHS Adaptive Structures Conference 12th, AIAA paper 2010-2830, 2010.

[16] D. Wilde, S. Walther, K. Pitchadze, S. Alexsaschkin, D. Vennemann, L. Marraffa, Flight test and ISS application of the inflatable reentry and descent technology (IRDT), Acta Astronautica 51 (1-9) (2002) 83–88.

[17] V. Carandente, R. Savino, New concepts of deployable de-orbit and re-entry systems for cubesat miniaturized satellites, Recent Patents on Engineering 8 (1) (2014) 2–12.

[18] D. L. Akin, The parashield entry vehicle concept-basic theory and flight test development, in: 4th AIAA/USU Small Satellite Conference, Logan, UT, Aug. 27-30, 1990, Proceedings. (A91-27376 10-18). Logan, Vol. 1, 1990.

[19] E. Venkatapathy, K. Hamm, I. Fernandez, J. Arnold, D. Kinney, B. Laub, A. Makino, M. McGuire, K. Peterson, D. Prabhu, et al., Adaptive deployable entry and placement technology (ADEPT): a feasibility study for human missions to mars, in: 21st AIAA Aerodynamic Decelerator Systems Technology Conference and Seminar, AIAA paper 2011-2608, 2011.

[20] R. Wu, P. C. Roberts, C. Soutis, C. Diver, Flexible heat shields deployed by centrifugal force, Acta Astronautica (2018) https://doi.org/10.1016/j.actaastro.2018.06.021.

[21] R. K. Johnson, F. M. Cheatwood, A. M. Calomino, S. J. Hughes, A. M. Korzun, J. M. DiNonno, M. C. Lindell, G. T. Swanson, HIAD advancements and extension of mission applications, in: International Planetary Probe Workshop; 13th; 13-17 Jun. 2016; Laurel, MD; United States, 2016.

[22] B. Harper, R. D. Braun, Asymmetrically stacked tori hypersonic inflatable aerodynamic decelerator design study for mars entry, in: AIAA Atmospheric Flight Mechanics Conference, AIAA paper 2014-1095, 2014.

[23] N. Skolnik, H. Kamezawa, L. Li, G. A. Rossman, B. Sforzo, R. D. Braun, Design of a novel hypersonic inflatable aerodynamic decelerator for mars entry, descent, and landing, in: AIAA Atmospheric Flight Mechanics Conference, AIAA paper 2017-0469, 2017.

[24] J. S. Green, B. Dunn, R. Lindberg, Morphing hypersonic inflatable aerodynamic

decelerator, in: AIAA Aerodynamic Decelerator Systems (ADS) Conference, AIAA paper 2013-1256, 2013.

[25] P. Wercinski, Adaptable deployable entry and placement technology (ADEPT), Oral/Visual Presentation ARC-E-DAA-TN31961, NASA.

[26] K. McManus, T. Poinsot, S. Candel, A review of active control of combustion instabilities, Progress in Energy and Combustion science 19 (1) (1993) 1–29.

[27] M. L. Webber, Phase shift control: Application and performance limitations with respect to thermoacoustic instabilities, Ph.D. thesis, Virginia Tech (2003).

[28] J. Hathout, M. Fleifil, A. Annaswamy, A. Ghoniem, J. Hathout, M. Fleifil, A. Annaswamy, A. Ghoniem, Why do secondary peaks occur in experimental active controllers of thermoacoustic instability?, in: 33rd Joint Propulsion Conference and Exhibit, 1997, p. 2834.

[29] W. Saunders, M. Vaudrey, B. Eisenhower, U. Vandsburger, C. Fannin, Perspectives on linear compensator designs for active combustion control, in: 37th Aerospace Sciences Meeting and Exhibit, 1999, p. 717.

[30] Microsatellite reaction wheels (rw3-0.060), `http://www.sinclairinterplanetary.com/reactionwheels`, accessed: 2018-05-02.

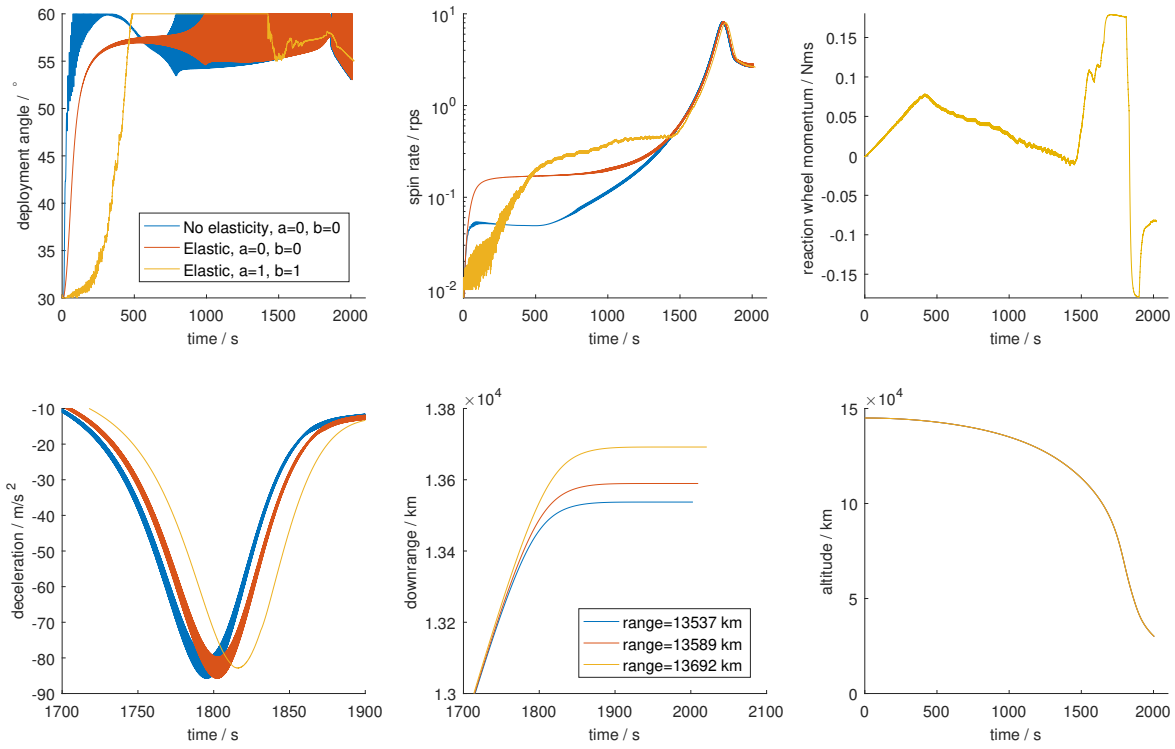

Figure 10: Trajectory simulation results without accounting for the shell's elasticity (blue), with elasticity (red), and with the controlled reaction wheel as well as elasticity (yellow), on a CubeSat-sized vehicle re-entering from 145 km LEO to 30 km altitude; it can be seen that for the uncontrolled scenarios ($a = b = 0$ according to Equation 11-12) oscillation persists throughout the descent, which leads to fluctuation in deceleration.

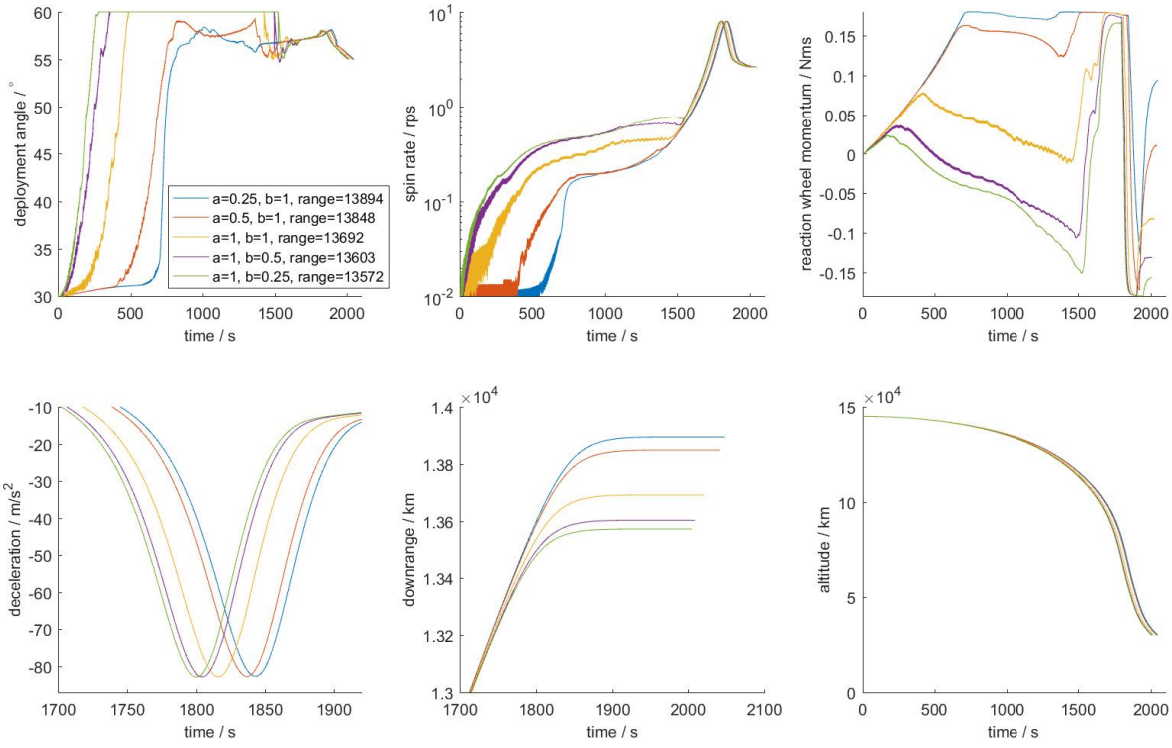

Figure 11: Trajectory simulation results on the vehicle with different downrange control gains, downrange are reported in km, showing a downrange shift of >300 km and oscillation suppressed.

Chapter 4

Design scalability and experimental validation

This chapter contains another paper, which demonstrates the scaling rules of the baseline vehicle design proposed in Chapter 2 as well as the controller designed in Chapter 3. It shows that the concept has the potential to be lightweight in comparison with IAD when scaled up to 5 ton, and can also be scaled down to a miniature size of $30g$ to enable small planetary probes. Furthermore, the trajectory simulator is verified/calibrated using data from ground experiments, and showed satisfactory agreement with low altitude drop test. The drop test model is also a prototype that demonstrates the stitched fabric architecture that could be used in future test vehicles.

4.1 Paper III: Scaling law and drop test

Flexible Heat Shield with Self-Moderating Centrifugal Deployment: Design Scalability and Low Altitude Drop Test

Authors: Rui Wu, Peter Roberts, Lulu Xu, Constantinos Soutis, Carl Diver

Journal: Acta Astronautica, (**Impact factor:** 1.536)

Article ready for submission.

Statement of own contributions in joint authorship:

Main research idea and technological development;

Preparation of tables, figures, and the manuscript;

Analytical scaling analyses;

Design and fabrication of the paper and latex rubber prototype;

Design and fabrication of the fabric prototype/drop test model with assistance from Lulu Xu;

Design of the test setup, construction of test equipment, and conduction of experiment, including the drop test and the wind tunnel test;

MATLAB program for test data analyses and interpretation;

Construction of the 3D models for concept illustration.

Note: Supplementary material is available in Appendix A.3.

Flexible Heat Shield with Self-Moderating Centrifugal Deployment: Design Scalability and Low Altitude Drop Test

Rui Wu[a,*], Peter C.E. Roberts[a], Lulu Xu[b], Constantinos Soutis[c], Carl Diver[a]

[a] *School of Mechanical, Aerospace and Civil Engineering, the University of Manchester, UK*
[b] *School of Materials, the University of Manchester, UK*
[c] *The University of Manchester Aerospace Research Institute, UK*

Abstract

Previous study has proposed a foldable heat shield with self-regulated centrifugal deployment. The design benefits from being lightweight and simple, having low requirement on thermal protection, and allowing downrange manoeuvre based on conventional attitude control devices. In the present study, the heat shield design is further explored to enable a variety of missions. Scaling rules are developed to allow a vehicle to achieve acceptable trajectory behaviours with a wide range of entry mass (from 30 g to 30 tonne). The scaled design also shows a mass-reduction of $> 25\%$ in comparison with a 8.3 m inflatable heat shield, as well as the potential to realise a swarm of low-cost small probes owing to its robustness. Meanwhile, a test model with a stitched fabric aeroshell and on-board sensors is drop-tested using a helium balloon at low altitude. The tests have shown satisfactory agreement with simulation, and no sign of instabilities. This result thereby verifies the key aspects of the simulator and paves the way for future higher fidelity tests. The similarity between the low speed drop-test result and hypersonic simulation suggests that the critical behaviours of the heat shield is dominated by geometrical rather than aerodynamic principles.

*Corresponding author
Email address: rui.wu@manchester.ac.uk (Rui Wu)

Nomenclatures

E: Young's modulus

f: focal length

F: thrust force

g: Earth gravity

I_{SP}: specific impulse

l: vehicle characteristic length

m: mass

M_E: deploying moment due to shell's elasticity

q: dynamic pressure

R: distance from a spot on image to the image centre

S: frontal area

St: Strouhal Number

t: heat shield thickness

v: velocity

β: ballistic ratio

θ: deployment angle

Θ: angle between the incident light and the optical axis

ρ: volumetric density

τ: roll torque

ω: vehicle spin rate (rps)

CFRP: Carbon Fibre Reinforced Plastic

CGT: Cold Gas Thruster

HEART: High-Energy Atmospheric Re-entry Test

IMU: Inertial Measurement Unit

LEO: Low Earth Orbit

MEMS: Micro-Electro-Mechanical Systems

TPS: Thermal Protection System

1. Introduction

Deployable atmospheric entry decelerators and heat shields have attracted increasing interest from space industry during the last decade. Unlike conventional rigid aerodynamic decelerators, deployable heat shields can be stowed compactly during launch, then deploy and achieve low ballistic ratio during entry. The reduced ballistic ratio leads to early deceleration, reduced terminal velocity, and lower aerothermodynamic heating, therefore enables soft-landing of heavy payloads through thin Martian atmosphere [1, 2, 3], as well as flights with extensive heating such as missions to Venus [4, 5]. Meanwhile, a low stowage profile is not only crucial for large entry vehicles to fit inside launcher fairings, but also realises entry systems as small as CubeSats [6, 7, 8, 9].

Current deployable entry systems are mostly based on inflatable structures or foldable mechanisms. Inflatable heat shields use flexible air-tight chambers that are folded before inflation, then deploy and rigidise under internal gas pressure. Flexible thermal protection layers based on commercial materials are wrapped onto the chambers to maintain an acceptable structural temperature [10, 11, 12, 13, 14, 15, 16, 17]. The foldable mechanisms utilise umbrella-like designs where a skirt made of flexible thermal protection materials is bounded onto rigid deployable ribs. Revolute or translational joints allow the ribs to fold and unfold, thereby deploy the skirt and potentially perform flight manoeuvres by manipulating the skirt's shape

[18, 19, 20, 21, 22].

Previous study has proposed a new type of deployable heat shield [23]. Unlike the current solutions that rely on elastic stabilising forces from either solid or gaseous (inflation gas) materials, this design concept utilises centrifugal force, which is an inertial force, to deploy and stiffen the heat shield structure. The design potentially benefits from the low structural mass enabled by centrifugal deployment, and realises a less-demanding thermal control scenario. Meanwhile, the deployment is achieved using a self-moderating autorotation during descent. This leads to a fully passive system that is closed-loop controlled. Study also suggested that the extend of deployment can be actively adjusted using conventional torque-generating attitude control devices, which moderates the rate of autorotation and thereby enables downrange manoeuvre [24].

In the present study, the design, especially the scalability of this heat shield is discussed in more details based on simulation results. The simulator, which is developed in the previous study, is constructed by coupling a trajectory simulator with analytical aerodynamic and structural dynamic models. However, as the design uses a very flexible structure, it is difficult for the simulator to fully capture the high-fidelity aeroelastic behaviour of the heat shield as well as its effect on the whole vehicle's flight dynamics. Therefore, a scaled-down test vehicle is fabricated and drop tested from $\sim$ 100 m altitude to reveal its behaviour at low speed and to verify the critical aspects of the simulator.

2. Design scalability of the centrifugally deployed heat shield

The proposed heat shield is a uniform flexible shell which buckles into a spiral shape when folded under aerodynamic load. The buckled shape generates aerodynamic roll-torque during descent in atmosphere, thus propels autorotation. Mean-

while, the centrifugal force caused by the autorotation deploys and flattens the flexible shell. The spin rate then reaches a point that the effect of inertial (centrifugal and axial deceleration) forces on the shell balances the aerodynamic force, while the shell is flattened to an extent that the roll-torque becomes zero. The shell's shape and the spin rate thereby reaches equilibrium.

Two conceptual designs are illustrated in Figure 1 and 2. Design 1 uses a deployable first stage to minimise the stowed diameter when folded (Figure 1c). When deploying, the first stage initiates the unfolding of the shell and facilitates the centrifugal deployment of the flexible second stage [23]. This first stage can be inflatable (for large vehicles) or mechanically deployable structures (for small vehicles), but is not the scope of the present study. The conventional rigid nose cone is installed to protect the payload vessel (an example is given in Figure 1b, note that the height of the columnar vessel can be increased to allow larger payload volume). The flexible shell can be made from woven ceramic fabrics such as the test-proven 3M^{TM}Nextel^{TM}based on alumina-boria-silica fibres [25, 26], and a stitched fabric architecture is illustrated by the test model discussed in section 3.2. Packing is demonstrated by a prototype made of latex rubber (Figure 1c), where the shell folds through an origami pattern with crease lines aligned along the spiral shape.

Design 2 (Figure 2a) has removed the first stage for simplicity, and replaced it with a larger nose cone. For a miniaturised vehicle, a symmetrical payload vessel can be used to realise a robust design that guarantees thermal protection even if the vehicle tumbled and flipped over before entry: an example is given in Figure 2b, where two identical nose cones are oppositely closed to provide a payload space in between. When flipped, the payload is still protected by the nose cone that was on the aft side before flipping, while the flexible shell snaps through into a reversed cone (the designed shape) under aerodynamic load. Such a design concept can be

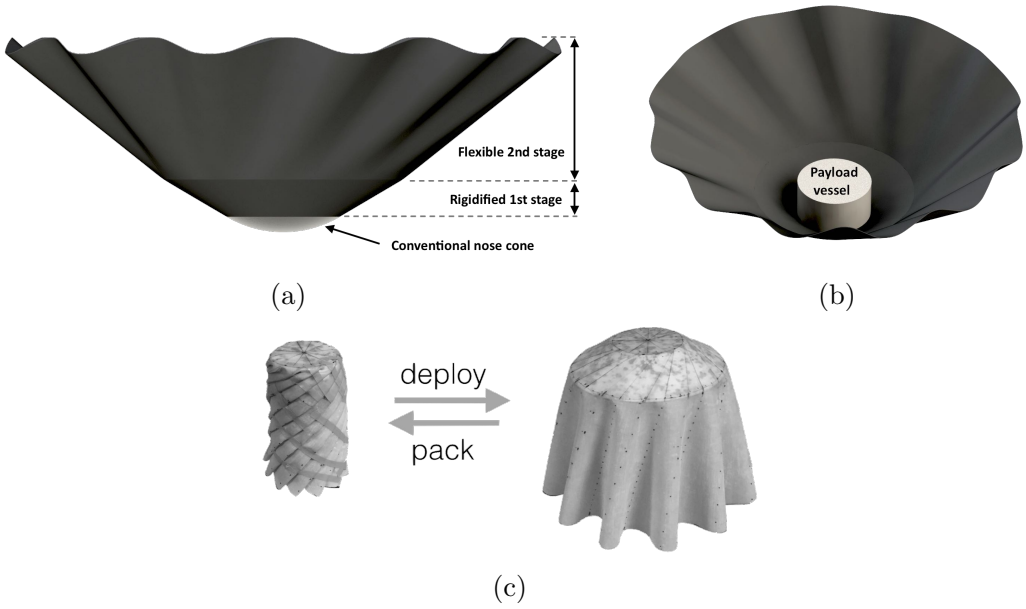

Figure 1: Design 1 vehicle with centrifugally deployed heat shield, (a) side view showing the basic components of a vehicle with two-stages deployment, (b) tilted view showing the payload vessel behind the rigid nose cone, (c) packing of the heat shield demonstrated by a latex rubber prototype, which folds along an origami crease pattern.

useful to enable a swarm of low-cost miniaturised probes without pre-spin or active attitude control. Alternatively, a payload vessel similar to Design 1 can be used to enable a larger payload volume.

Previous works have already demonstrated that a CubeSat sized vehicle can reach near full deployment (forming a blunt cone) throughout the hypersonic and supersonic flight regimes during a re-entry from Low Earth Orbit (LEO) [23], and a downrange manoeuvrability of 10^2 km is achievable using a commercial reaction wheel [24]. In this section, it is shown that the design can be scaled-up using simple scaling rules to achieve similar performance.

The vehicle entry mass is set according to volumetric scaling, where l is the vehicle's characteristic dimension:

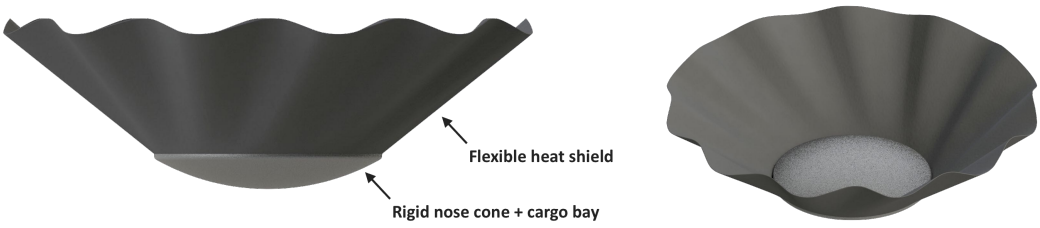

(a) (b)

Figure 2: Design 2 vehicle with a simplified centrifugally deployed heat shield, (a) side view of a vehicle with single-stage deployment and a enlarged nose cone, (b) tilted view of a miniaturised vehicle with a symmetrical cargo bay that allows reversed flight to relieve the requirement for attitude control or pre-spin.

$$m_{vehicle} \propto l^3 \tag{1}$$

All dimensions of the heat shield linearly scales with l except its thickness:

$$t \propto l^{0.7} \tag{2}$$

Assuming constant material density $\rho_{decelerator}$, then the heat shield mass satisfies: $m_{decelerator} \propto l^{2.7}$. The scaling exponent 0.7 in Eq. 2 is chosen since it provides reasonable heat shield thickness across a wide diameter range (0.15 m $\sim$ 15 m) as shown in Table 1, and allows a low heat shield mass ratio ($m_{decelerator}/m_{vehicle} \propto l^{-0.3}$) for large vehicles while maintaining acceptable deploy-ability. The deploy-ability slightly decreases with increasing vehicle size, which can be derived using Eq. 14 in [23], where ω is the rate of autorotation, q is dynamic pressure, and θ is deployment angle (instantaneous semi-vertex angle of the shell, with full deployment set to 60°):

$$\omega \propto \sqrt{\frac{q \cdot \tan(\theta)}{l \cdot \rho_{decelerator} \cdot t}} \tag{3}$$

Simplify using Strouhal Number, which stays constant during scaling due to the

similarity of shell geometry, where v is the flight velocity:

$$St = \frac{\omega \cdot l}{v} \tag{4}$$

Then we have Eq. 5, which suggests that the deployment angle under a certain altitude (or air density, ρ_{air}) tends to be slightly lower when the vehicle is scaled up (with larger l):

$$\tan(\theta) \propto \frac{\rho_{decelerator}}{\rho_{air} \cdot l^{0.3}} \tag{5}$$

The discussion above agrees with simulation results shown in Figure 3. The simulation includes seven design examples covering vehicle masses ranging across six orders of magnitude, and assumes Earth re-entry from 145 km altitude at 7.8 km/s and zero flight path angle. Miniaturised vehicles (with total mass of 30 g and 300 g) are included as they may allow new types of exploration missions with a swarm of low-cost small probes. It can be seen that the deployment angle decreases with increasing vehicle size as predicted by Eq. 5. For the same reason, a larger heat shield can reach a lower instantaneous deployment angle, leading to a higher aeroelastic oscillation (i.e. oscillation in deployment angle, which is investigated in the previous study [24]), which in turn increases the fluctuation in deceleration. However, it should be noted that the simulator has not included structural damping (since the baseline structural dynamic behaviours are of interest), which in reality will help reduce the oscillation during the low dynamic pressure flight regimes. Meanwhile, scaling the vehicle barely influences the peak deceleration and stagnation point heating (Table 1). Therefore, the basic structural layout and material selection can be passed between a wide range of vehicle sizes.

In addition, since ballistic ratio increases with vehicle size: $\beta \propto l$ (derived from

Eq. 1), the peak dynamic pressure also increases, which follows an empirical relation determined from the simulation: $q \propto l$. Then the scaling of spin rate (Eq. 3) becomes $\omega \propto l^{-0.35}$ if ignoring the insignificant variation in θ, which agrees with the simulation. The fact that a larger heat shield tends to have a lower spin rate is beneficial since it limits the tensile stress in the flexible structure. However, the exact stress can not be evaluated without a detailed heat shield design, thus is not further discussed.

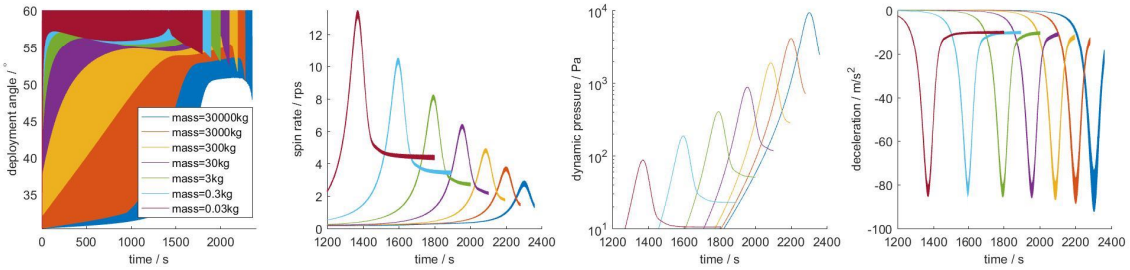

Figure 3: Scaling of a vehicle with total mass ranging from 30 g to 30 tonne, simulated for re-entry from 145 km LEO with zero flight path angle, descending to 30 km altitude, showing that scaling up leads to slight reduction of deployment angle and spin rate, increment in dynamic pressure, and nearly unchanged peak deceleration.

Table 1: Vehicle setup and simulation results corresponding to the scalability study in Figure 3.

Vehicle mass	Max. diameter	H.S. thickness	H.S. surface density	H.S. mass ratio	Peak spin rate	Peak P	Peak deceleration	Peak heating[b]
30 g	0.15 m	0.34 mm	0.37 kg/m^2	25%	13 rps	0.087kPa	8.4 ± 0.3 g	25.4W/cm^2
300 g	0.32 m	0.6 mm	0.66 kg/m^2	20%	10 rps	0.19 kPa	8.4 ± 0.3 g	25.3W/cm^2
3 kg	0.7 m	1.0 mm	1.1 kg/m^2	16%	8.1 rps	0.40 kPa	8.4 ± 0.3 g	25.4W/cm^2
30 kg	1.5 m	1.7 mm	1.9 kg/m^2	13%	6.3 rps	0.87 kPa	8.4 ± 0.4 g	25.6W/cm^2
300 kg	3.2 m	2.9 mm	3.2 kg/m^2	9.9%	4.8 rps	1.9 kPa	8.4 ± 0.5 g	25.5W/cm^2
3 $tonne$	7 m	5.0 mm	5.5 kg/m^2	7.9%	3.7 rps	4.2 kPa	8.4 ± 0.6 g	25.8W/cm^2
30$tonne$	15 m	8.6 mm	9.5 kg/m^2	6.3%	2.8 rps	9.3 kPa	8.5 ± 0.9 g	26.2W/cm^2

[a] H.S.: Heat Shield
[b] Stagnation point convective heating

Besides the basic behaviours discussed above, the downrange manoeuvrability can also be scaled up. In the previous study, an off-the-shelf reaction wheel is used to actively adjust the spin rate of a CubeSat-sized vehicle, and thereby influence the

deployment angle and drag coefficient, which has achieved an open-loop downrange manoeuvre of over 300 km during a simulated re-entry. The same system has also simultaneously suppressed the aeroelastic oscillation of the shell [24]. Here a scalable system is designed with actively controlled Cold Gas Thrusters (CGTs), which is more straightforward to scale up than reaction wheels used in the previous study. The CGTs are tangentially installed at the edge of the design 1 payload vessel to generate a roll-torque, τ_{CGT}. On the other hand, the aerodynamic roll-torque generated from the spiral shell geometry satisfies (note that $q \propto l$ as discussed earlier):

$$\tau_{aero.} \propto q \cdot S \cdot l \propto l^4 \tag{6}$$

The total roll-torque $\tau_{aero.} + \tau_{CGT}$ then determines the spin rate and thereby the deployment. The similitude of control therefore requires $\tau_{CGT} \propto \tau_{aero.}$, which means the control similitude factor can be defined as:

$$\frac{\tau_{CGT}}{l^4} \tag{7}$$

Since $\tau_{CGT} \propto F_{CGT} \cdot l$, we have $F_{CGT} \propto l^3$. Assuming Nitrogen-propellant CGTs with a specific impulse of 70 s, the propellant consumption rate can be evaluated using the equation below [27]:

$$F_{CGT} = g \cdot I_{SP} \cdot \dot{m} \tag{8}$$

Where g is Earth's gravity, I_{SP} is specific impulse, and $\dot{m}$ is fuel mass flow rate. The controller developed in the previous study is then scaled and simulated with two vehicle sizes. The results are shown in Figure 4 and Table 2. Note that the control similitude factor of 0.04 is chosen here as it provides satisfactory control

authority with acceptable propellant consumption rate. For simplicity, the vehicle mass variation due to propellant consumption is not considered in the simulations.

According to Figure 4, the oscillation in deployment angle is suppressed, removing the fluctuation in deceleration (comparing with Figure 3). Meanwhile, downrange shifts of $\sim$ 540 km are achieved for both vehicle sizes with propellant consumption below 7% of vehicle mass.

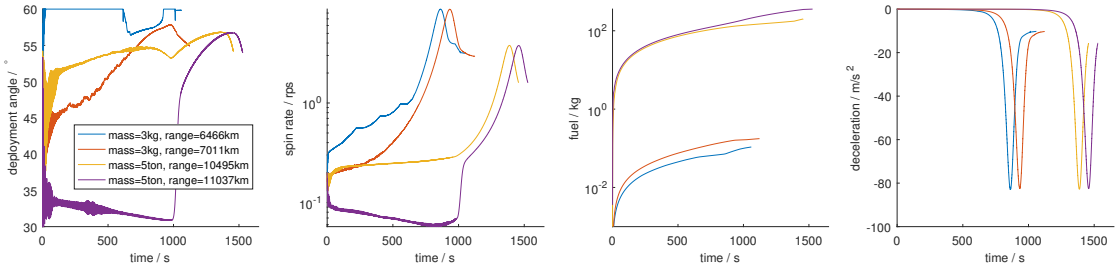

Figure 4: Scaling of a vehicle with total mass of 3 kg and 5 tonne, and actively controlled CGTs with similitude factor $\tau_{CGT}/l^4 = 0.04$ to adjust downrange, simulated for re-entry from 125 km LEO with zero flight path angle, descending to 30 km altitude, showing that a $\sim$ 540 km downrange manoeuvrability can be achieved while suppressing aeroelastic oscillation.

Table 2: Vehicle setup and simulation results corresponding to the scalability study in Figure 4, with control similitude factor $\tau_{CGT}/l^4 = 0.04$.

Vehicle mass	τ_{CGT}	Total downrange shift	Propell. consumption	Propell./Vehicle mass	Downrange goal
3 kg	0.0094 $N \cdot m$	545 km	0.11 kg 0.18 kg	4% 6%	Reduce Increase
5 tonne	186 $N \cdot m$	542 km	200 kg 357 kg	4% 7%	Reduce Increase

The 5 tonne vehicle scaled in this study has a maximum diameter of 8.3 m. This is similar to NASA's High-Energy Atmospheric Re-entry Test (HEART) vehicle, which is a ballistic entry vehicle concept with an inflatable blunt-cone heat shield designed for space station cargo exchange as well as other planetary entry missions [26]. The key design parameters and entry environments are compared in Table 3.

The heat shield mass ratio of HEART is approximated by summarising the mass of the inflatable structure made of silicone-coated Kevlar toris, the Thermal Protection System (TPS) made of layers of fabrics and blankets, and the inflation subsystem consisted of pressure vessel, valves, etc. (while excluding rigid structures and nose cone) [26]. Mass ratio of the present design is evaluated using the flexible shell's mass (note that design 1 has higher shell mass since it contains a first stage), which makes a reasonable comparison in this preliminary study since the shell is designed to serve as the deployable structure and the TPS at the same time. Meanwhile, the stowed diameters reported in the table are based on the size of rigid nose cones (for present designs) as well as literature (for HEART) [26].

It is worth noticing that the TPS on HEART has two 3M$^{\text{TM}}$Nextel$^{\text{TM}}$440 BF-20 alumina-boria-silica fabrics as the outer layer, which is proven to withstand the flight temperature and provides structural integrity during folding, handling and flight. Five layers of insulating blankets and a gas barrier are stitched onto the outer layer's aft side to protect the silicone-coated inflatable toris [26]. However, the present design is deployed and stiffened by inertial (centrifugal) force and thus mostly relies on the mass rather than the elastic response from heat shield materials. Therefore, it tolerates high material temperature, thus no insulation blankets or gas barriers are needed, and the heat shield can potentially be made solely from high temperature fabrics. The required heat shield surface density, according to the scaling rule (Eq. 2), is 6.2 kg/m^2, which can be achieved with 12 layers of Nextel$^{\text{TM}}$440 BF-20 fabric. This provides sufficient thermal protection with high safety factor since the entry environment of the proposed vehicle is similar to HEART (Table 3).

According to Table 3, the centrifugally deployed heat shields have lower mass than HEART. While the mismatch in peak dynamic pressure and deceleration of the two designs is related to shape difference, as the HEART vehicle has a conical shape

Table 3: Comparison between the centrifugally deployed heat shield and NASA's HEART inflatable system.

Vehicle	Entry mass	Max. dia.	Stowed dia.	H.S. mass ratio	Peak P	Peak decel.	Peak heating[a]
Present study	5 tonne	8.3 m	1.5 m (design 1) 3.3 m (design 2)	7.5% (design 1) 6.5% (design 2)	5.8 kPa	8 g	28 W/cm^2
HEART	5 tonne	8.3 m	$\sim$ 2.3 m	10%	5.5 kPa	7 g	27 W/cm^2

[a] Stagnation point convective heating

with 55° constant semi-vertex angle, and the present design has a varying semi-vertex angle and a diameter below 8.3 m during flight (below full-deployment).

Therefore, a conclusion can be drawn here that the proposed design has the potential to be applied to entry systems with a wide range of sizes, and mass-reduction in comparison with existing inflatable systems is potentially achievable. This also means the behaviour of a scaled-down vehicle is representative for a larger system, thus test results on a scaled-down vehicle can be valuable and instructive.

3. Low-speed low-altitude drop test

Experimenting in higher atmosphere under a hypersonic speed is ideal but costly, thus the present work focuses on experimenting under a low-speed low-altitude condition. Such a test certainly can not capture all the interested aspects especially the full vehicle dynamics under hypersonic condition and aerothermodynamic heating, but will still provide useful insights and increase the confidence of successfully conducting a higher fidelity test (i.e. orbital/suborbital launch).

In this section, a scaled-down test vehicle is constructed and used to demonstrate the flight dynamics during a free-fall drop test from $\sim$ 100 m height as well as to verify key aspects of the simulator.

3.1. Basic information about the simulator

Trajectory prediction is a major component of the simulator, which utilises Newton's laws of motion and Newtonian hypersonic aerodynamics to numerically simulate the 3D trajectory of a point-mass ballistic entry vehicle. On the other hand,

the structural dynamic as well as the hypersonic autorotation behaviours are predicted using analytical equations derived from a simplified geometrical model. For simplicity, the model assumes the heat shield to have an axisymmetric origami shape and a zero angle of attack [23]. The simulator is then constructed by coupling the analytical equations with the point-mass trajectory solution.

The difference between the low-speed and hypersonic aerodynamic behaviours associated with autorotation is an important concern which may reduce the significance of the low-speed drop test results. Nevertheless, a series of wind tunnel tests have shown that the difference is not eminent. As sown in Figure 5, a scaled-down paper origami model is attached to a jig which allows free rolling of the model through an axle supported by bearings, and a tachometer with a code disk is used to measure the roll rate. The folding of the paper origami can be constrained from the axle and thereby set the deployment angle for testing. For each deployment angle (35°,40°,45°,50°, and 57°), the test is carried out at freestream velocities of: 14 m/s, 16 m/s and 18 m/s, and Strouhal Number (Eq. 4) is evaluated.

The difference between results at the three speeds is not eminent, thus the average of the three is reported. Ideally, as the tests are done by free spinning, the measured spin rates should be the equilibrium spin rate, or in other words, the spin rate at which zero aerodynamic roll-torque is generated. In Figure 6a, the analytical aerodynamic roll-torque with only positive value is plotted (coloured mesh), thus the edge of the plotted area corresponds to the equilibrium Strouhal Number. It can be seen that the test results (red dots) roughly resembles the analytical prediction except at high deployment angles. This is because the test condition is not ideal and the frictional torque resists the spinning of the model, thus the test points are actually conditions with a small rather than zero aerodynamic roll-torque. Therefore, better agreement is achieved in Figure 6b, which plots the analytical roll-torque higher than

a small value (10% of the maximum torque) in comparison with test.

Figure 5: The wind tunnel setup, with a paper origami model mounted on a free-spinning axle that spins with a code disk used for spin rate measurement.

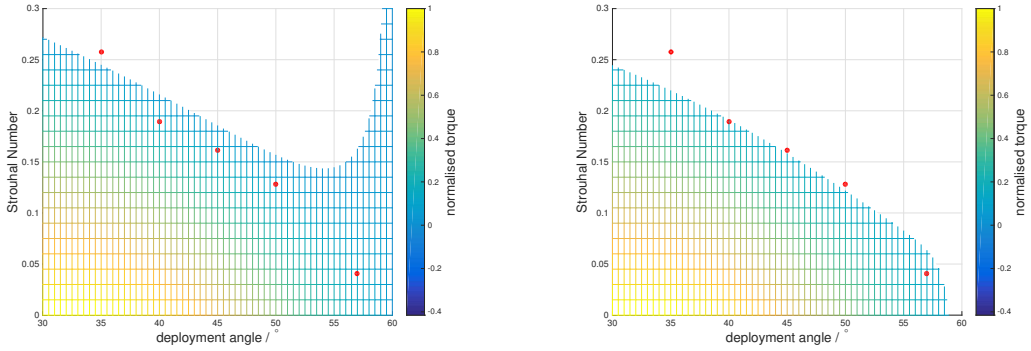

(a) (b)

Figure 6: Aerodynamic roll-torque, where low-speed wind tunnel results are plotted as red dots, together with the analytical results based on Newtonian hypersonic aerodynamics, (a) analytical torque with positive value is plotted, showing disparity at high deployment angles, (b) to compensate the friction in the tests, the analytical torque with normalised value of > 0.1 is plotted, showing better agreement with tests.

Such an agreement between low speed and hypersonic results is somehow unusual, which suggests that the autorotation of the origami model is dominated by geometric rather than aerodynamic principles. It also suggests that a low-speed low-altitude drop test could generate meaningful results since the important spinning motion can be captured with precision.

Meanwhile, aerodynamic damping on the deployment of the flexible heat shield

is added into the simulator since it has notable effect at low speed. This is done by revising the dynamic pressure term used to predict deployment behaviours to account for the local velocity variation caused by the shell's deploying motion:

$$v_{local} = v_{freestream} + 0.5\, l_{shell} \cdot \dot{\theta} \tag{9}$$

Where $\dot{\theta}$ is the angular velocity of the shell's deploying motion, L_{shell} is the generatrix length of the flexible shell. The effect of the shell's elasticity is also considered to improve the fidelity of the model. The elastic effect tends to let the shell recover to a neutral deployment angle, which is assumed to be 50°. It is not set to the full deployment angle of 60° since the neutral shape of the fabric shell (section 3.2) is not flat considering the effect of repeated folding and stitching. According to the fact that under a $-1\,g$ environment (unsupported shell under a bottom-up static condition similar to Figure 8b) the deployment angle is 28.5° rather than zero due to the effect of elasticity, the elastic deploying moment at 28.5° can be evaluated. Then the elastic deploying moment at any deployment angle can be predicted by assuming a linear relation to deployment angle, where M_E is the deploying moment caused by the shell's elasticity:

$$M_E(\theta) = \frac{50 - \theta}{50 - 28.5} \cdot M_E(28.5^\circ) \tag{10}$$

3.2. Test model construction

The drop test model shown in Figure 8 is based on design 2 (Figure 2) and is consisted of two parts: a flexible shell with the max. diameter of 0.7 m, and a cargo bay. The shell is fabricated using a heavy duty fabric with sufficient resistance to in-plane shear. The origami pattern has twelve repeating elements around the perimeter as shown in Figure 7, thus the fabric is tailored into the element's shape

and stitched together along the edges by creating double lap seams with top-stitch. Such a seam structure has high strength and creates a pocket that can be used to hold structural members for local reinforcement [28]. The local reinforcements made of Carbon Fibre Reinforced Plastic (CFRP) strips are added to induce structural anisotropy and therefore, inducing a predictable spiral shape when the shell folds by buckling (Figure 8b). The CFRP strips are lightweight (approx. 3 g each) thus has ignorable effects on the deployment behaviour. The rim of the shell also has a lap seam that forms a pocket (Figure 8c), which not only secures the edge yarns, but also creates a rounded shoulder that prevents excessive local aerothermodynamic heating. This stitched fabric architecture is similar to NASA's ADEPT concept [29]. Hanger rings made of Kevlar ropes are installed onto the rim of the shell, which is used to connect the vehicle to a helium balloon through a hanger equipped with releasing mechanism.

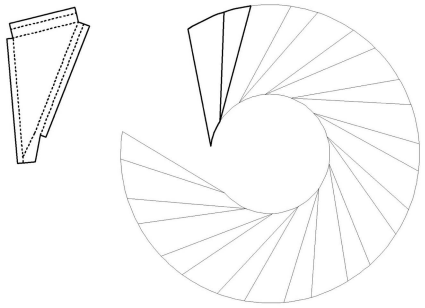

Figure 7: The origami pattern (right) upon which the shell is designed, and the fabric element for the test vehicle (left) where dashed lines are folding line.

The cargo bay is consisted of a carrier board and a lower piece. The carrier board is used to install the attitude sensor (Pixhawk), camera and power system (Figure 8c). The lower piece is made of expanded polypropylene with a near spherical shape that can deform under the landing impact (the white part in Figure 8). It is bonded

onto the flexible shell using sealant, and then bolted onto the carrier board.

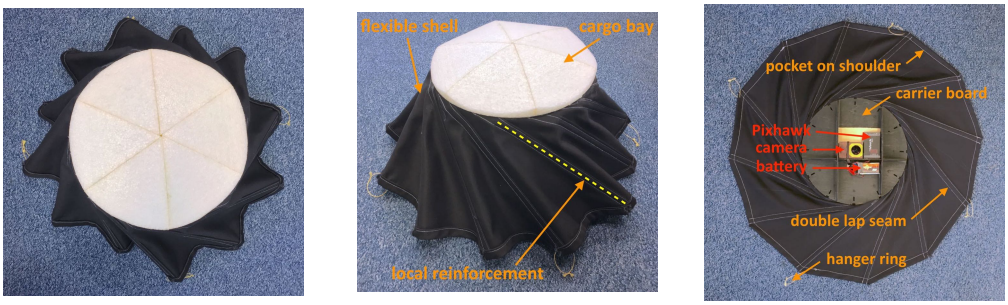

(a) (b) (c)

Figure 8: The test vehicle, (a) bottom view and (b) side view, showing the spiral shape that simultaneously forms when the shell folds by buckling, (c) top view showing the carrier board on the cargo bay.

The whole system used for drop test is shown in Figure 9. The test vehicle hangs below the hanger through releasing mechanisms that are manually controlled using a remote controller. Floating of the balloon is also manually controlled from ground using a continuous cable that passes through the hanger via two pulleys.

3.3. On-board sensors & data processing

All measurements are made on board the test vehicle using a video camera with fisheye lens, as well as a commercial UAV flight controller (Pixhawk) which has a MEMS (Micro-Electro-Mechanical Systems) IMU (Inertial Measurement Unit), a MEMS barometer, and a micro-SD card for data-logging. The function of these sensors are listed in Table 4.

Velocity, which is mainly vertical, is evaluated from the altitude information acquired using the barometer. The spin rate is measured using solely the gyroscope. The vehicle's attitude is recorded by the IMU, which fuses the measurement from various sensors using an extended Kalman filter and outputs the three Euler angles

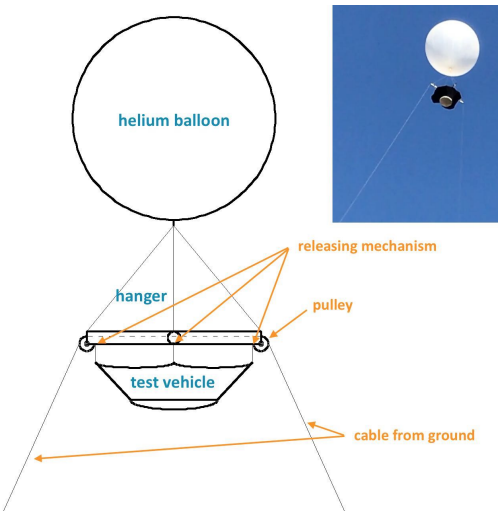

Figure 9: The drop test system consisted of a lifting helium balloon, a hanger controlled from ground, and test vehicle hanging under the hanger through remote-controlled releasing mechanisms.

Table 4: Measurements from the sensors on board the test vehicle.

Measurement	Sensor	Specification
Velocity (altitude)	Barometer	MS5611 IMU
Spin rate	Gyroscope in IMU	MS5611, allowing up to $2000°/s$
Attitude	IMU	MS5611, with Kalman filter
Deployment angle	Upward facing camera	Fisheye lens with equidistant projection, 1280×960 pixels

(roll, pitch and yaw). All the measurements made by the Pixhawk have a sample rate of 10 Hz.

The measurement of deployment angle is made by processing the image captured by the upward facing camera. The images are converted from a video shot at 60 frames per second and the resolution is 1280×960 pixels. The lens has a 220° view angle and equidistant projection, or in other words, the mapping function is:

$$R = f \cdot \Theta \tag{11}$$

Which means the distance between a spot on the image and the image centre (i.e. the height of the image) is proportional to the view angle. However, the real projection is slightly off-equidistant due to distortion. In Figure 10, the real mapping function provided by the lens supplier is plotted in comparison with the theoretical mapping function of an equidistant lens. During the evaluation of deployment angle, the distortion is calibrated using this data.

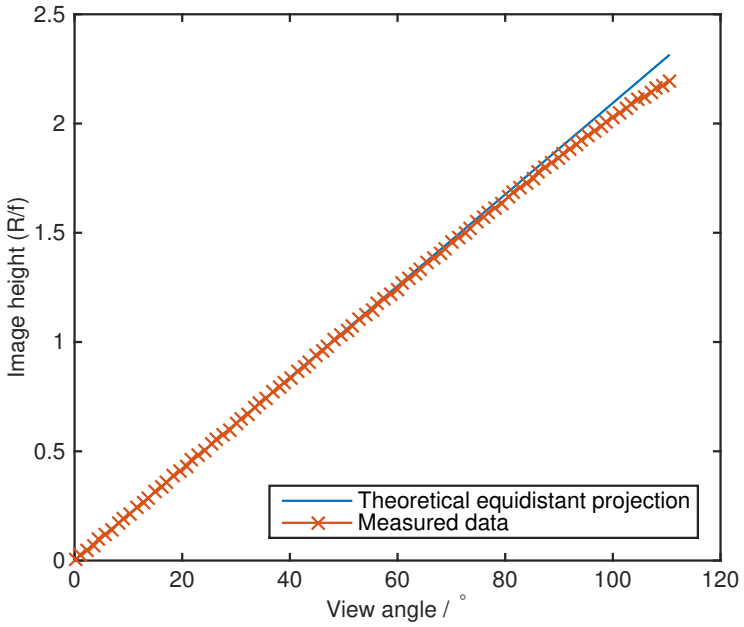

Figure 10: Mapping function of the fisheye lens set in comparison with an ideal equidistant lens, showing distortions to be calibrated during image processing.

The objective of the image processing is to separate the flexible shell from the background, and therefore distinguish the edges of the shell, which can then be used to evaluate deployment angle. Figure 11 shows three typical images taken during the drop test. It can be seen that only the centre of the image is within the projection area of the lens and the corners are dark. The vehicle and the flexible

shell are also dark except the white yarns used to stitch the shell together. The rest of the image is mostly blue sky that is relatively bright especially in the blue colour channel. Therefore, a threshold is applied to binarise the image by setting all the pixels with brightness in the blue channel lower than a certain value (the threshold value is studied later, here it is set to 62.5%) to black and the rest to white. Ideally, the resulted image should have a single white cluster that overlaps with the sky background thus the edge of the white cluster marks the shell's edge. However, as shown by Figure 11, the resulted image contains defects including lens flares caused by direct sunlight, strong reflection from the vehicle, and the bright white yarn stitched on the shell. The rest of the processing focuses on removing those defects.

It can be seen in Figure 11 that an erosion process, which offsets the black clusters by 3 pixels, is used to remove the white yarn. Then an extensive dilation of 15 pixels is used to remove the dark spots in the background caused by less bright part of the sky as well as the hanger at the beginning of the test. Finally, the small white and black clusters with the size lower than 50k pixels are removed, and the image is eroded by 12 pixels to compensate the previous dilation. The process reported here is developed by trails with the aim to minimise artifacts in the final result.

At this stage, the edge of the white cluster can be used to evaluate deployment angle using the following method. Every pixel on the edge is treated as an equal section of the edge, and the deployment angle of such a section can be solved from the view angle (which is converted from image height using Figure 10) using simple geometry. Figure 12 shows the distribution of deployment angles corresponding to all the edge pixels on 40 processed frames taken during 8 s $\sim$ 12 s of the descent. As the flexible shell in real world is not axisymmetric and always contains wrinkles and defects, the edge pixels have a range of deployment angles rather than a single

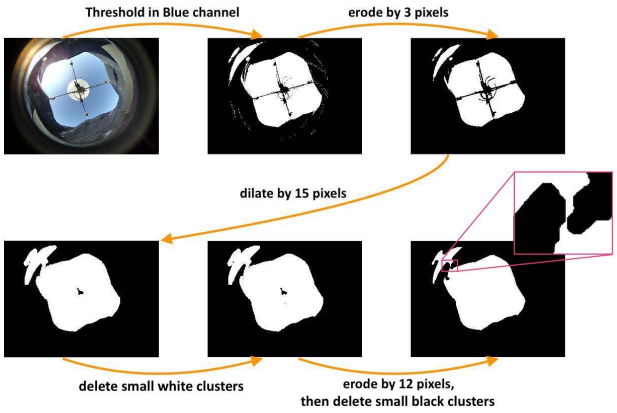

(a)

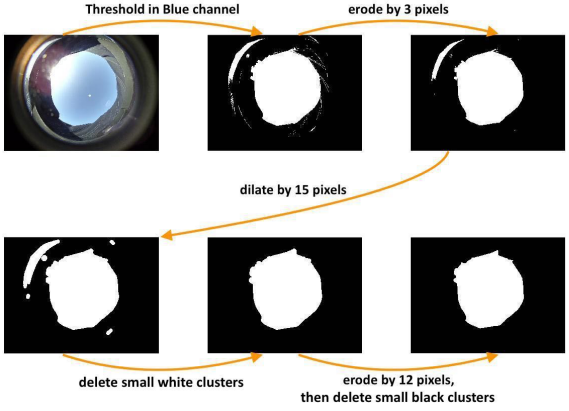

(b)

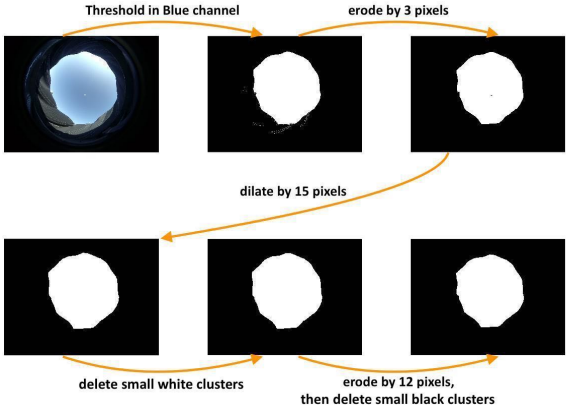

(c)

Figure 11: Image processing method used to pick up the shell's edge from shots taken by on-board camera, (a) a typical scene at the beginning of test, note that the lens flare and strong reflection from the vehicle caused by direct sunlight is causing defect, this rarely persists to the final processed image (b) another typical scene with lens flare, which is removed from the final image by the processing method, (c) a typical clean image.

value as assumed by the simulator. However, a distinct peak at approx. $50° \sim 53°$ exists in the data from all the three test runs, which means most part of the edge has similar deployment angle, thus the shape of the shell is regular and predictable.

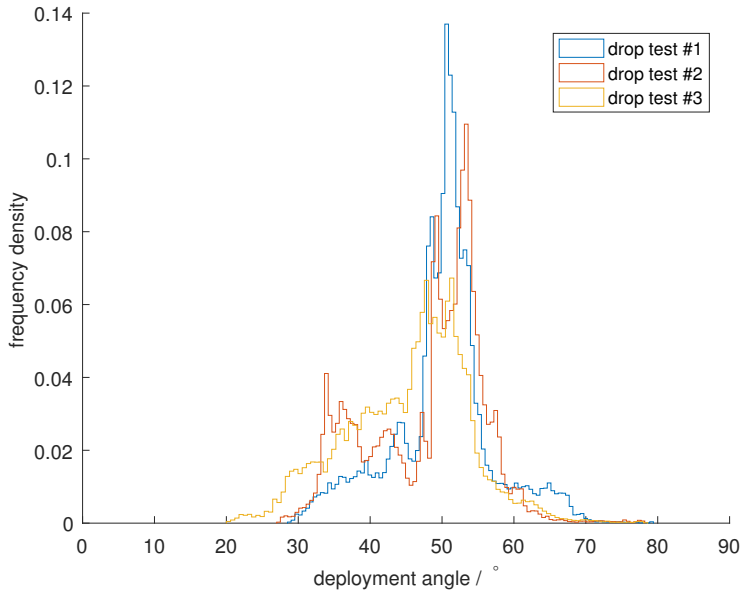

Figure 12: Distribution of deployment angles corresponding to all the edge pixels on 40 processed frames taken during $8 \sim 12$ s of descent, note that most part of the shell has deployment angle of $50° \sim 53°$, suggesting a shell geometry that is regular and predictable.

At each frame, the average of the deployment angles corresponding to all edge pixels is defined as the overall deployment angle. In Figure 13, the overall deployment angle is plotted against time. It can be seen that the difference in threshold value has notable but insignificant effect on the final result.

3.4. Results & Discussion

In Figure 14, the drop test results are plotted in comparison with simulation results. Note that the difference in test duration is caused by the different releasing altitude, which is determined visually from ground. According to Figure 14a, where

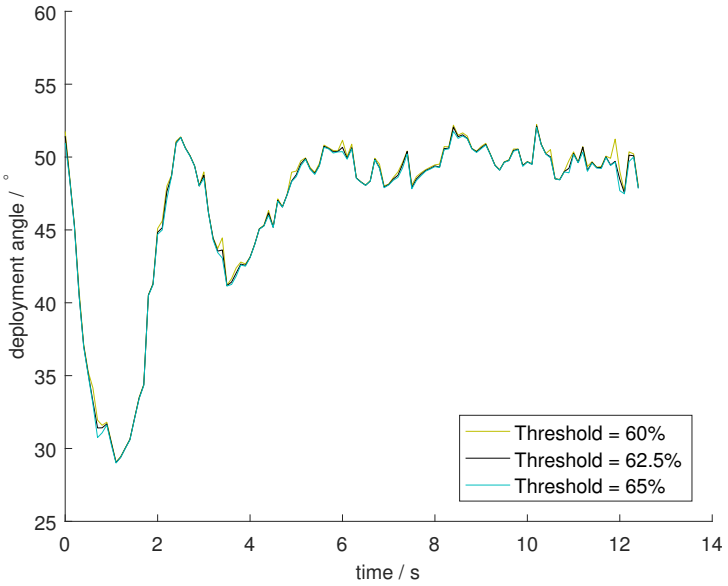

Figure 13: Overall deployment angle of the shell during the first test run plotted against time, where three threshold values are used to process the image, showing that the result is robust in terms of threshold.

the zero altitude is set as the releasing altitude, the descending predicted by simulation has shown satisfactory agreement with the tests. Meanwhile, the spin rate and deployment angle shown in Figure 14b and Figure 14c have shown close agreement with simulation except at the beginning of descent, where the spin-up of the vehicle and the initial deployment of the aeroshell is not as rapid as predicted by the simulator. However, as shown by Figure 15, the agreement between simulation and tests can be improved after the aerodynamic roll-torque in the simulation is reduced to 50% of the original magnitude.

According to this result, the simulation is making reasonable prediction of the equilibrium spin rate, as well as the deployment of the aeroshell under inertial and aerodynamic load, though the magnitude of the aerodynamic roll-torque is over-

predicted.

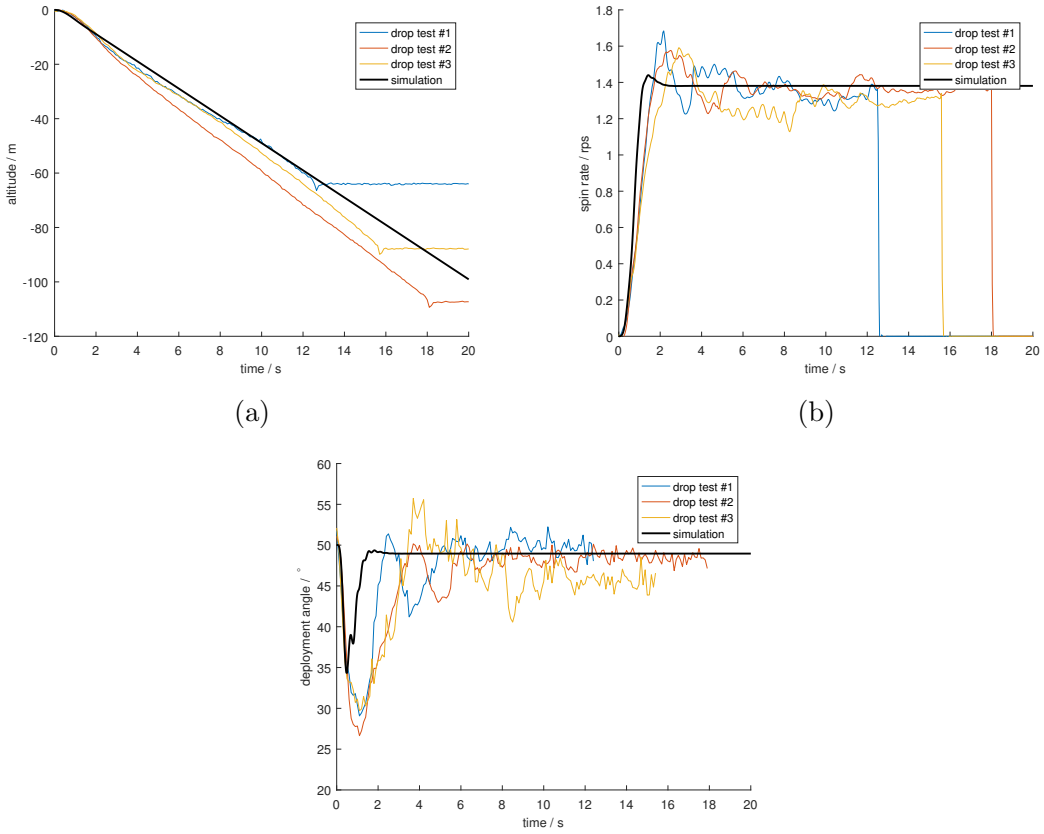

(a) (b) (c)

Figure 14: Drop test results plotted in comparison with simulation, (a) altitude, with zero point set as the releasing altitude of the test vehicle, showing satisfactory agreement, (b)(c) spin rate and deployment angle, showing close agreement except at the beginning of the drop, suggesting that the simulator has reasonable prediction of equilibrium condition, though it reaches equilibrium more rapidly.

Besides validating the key simulation parameters (i.e. spin rate and deployment angle), the flight dynamics of the vehicle is also of interest. It worth noticing that the peak of the deployment angle distribution as shown in Figure 12, is between 50° and 53°, which is different from the equilibrium overall deployment angle of approx. 49°

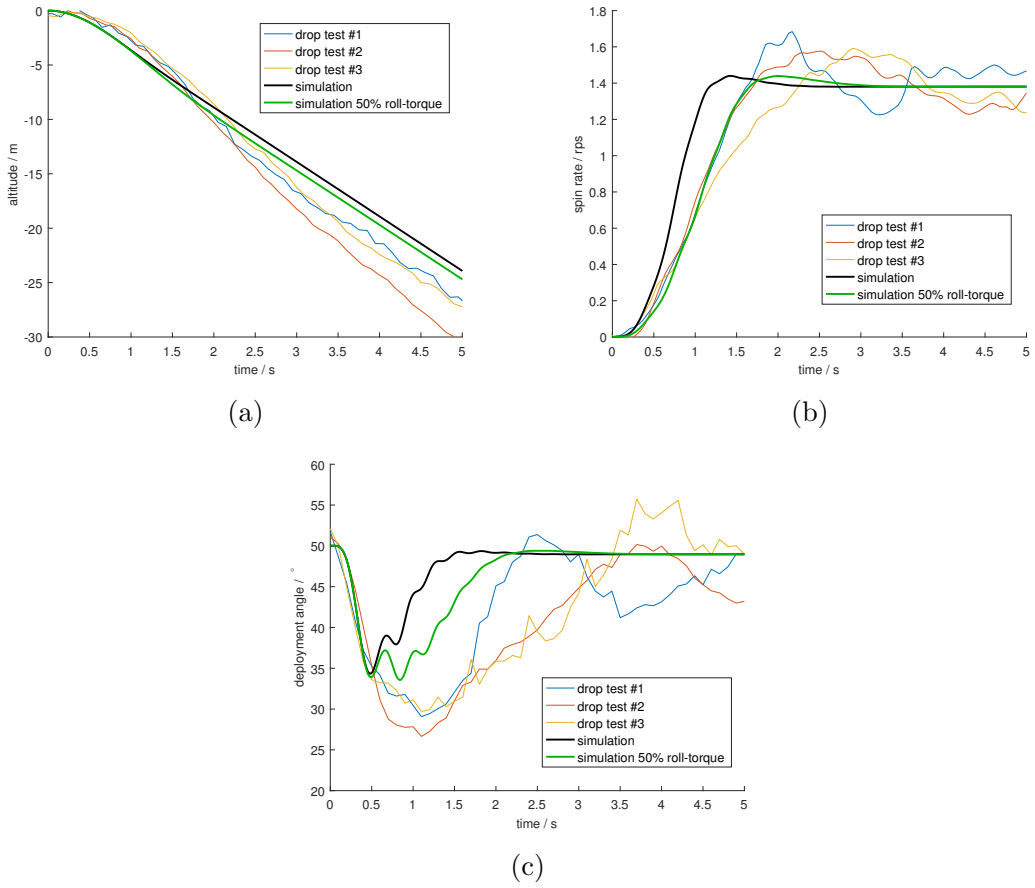

Figure 15: Drop test results compared to simulation with augmented aerodynamic roll-torque, showing improved agreements, (a) altitude, (b) spin rate, (c) deployment angle, which suggests that the simulator over-predicts the aerodynamic roll-torque.

as shown in Figure 14c. This is due to the fact that at such a low overall deployment angle, the shell buckles into an unsymmetrical mode as it folds. It can be seen from Figure 16 that from before 3 s into the descent, this mode starts to cause the fabric elements on the lower left side of the shell in the image to fold up extensively, leaving the rest elements relatively flat. The relatively flat elements thereby have deployment angles of between 50° and 53°, and the extensively folded elements have

a lower deployment angle, while the overall (i.e., the average) deployment angle generally satisfies the simulation prediction based on the axisymmetric geometrical model.

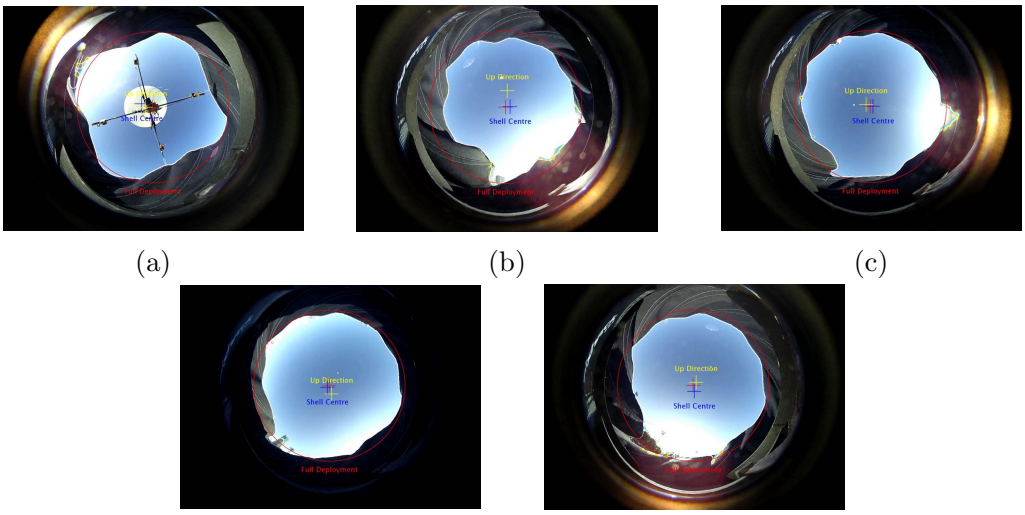

Figure 16: Images from the upward facing camera taken at (a) 0 s, (b) 3 s, note that an unsymmetrical shape is formed due to the low deployment angle, which causes the fabric elements on the lower left to fold extensively, such buckling mode persists to the end of the descent, (c) 6 s, (d) 9 s, (e) 12 s.

The unsymmetrical shape of the aeroshell discussed above also leads to a non-zero angle of attack of the vehicle. Figure 17 shows the vehicle attitude dynamics history, where the angle between the gravity vector and the downward facing vector bonded to the vehicle is plotted. According to the figure, the vehicle always has a non-zero angle of attack, which decays during the descent, and the motion contains autorotation and nutation (conning motion).

The nutation motion is illustrated with better clearance by setting the vehicle's yaw angle to zero and plotting the pitch angle in the vehicle frame (Figure 18). It can be seen from Figure 18a-18c that the nutation angle is reducing during the descent.

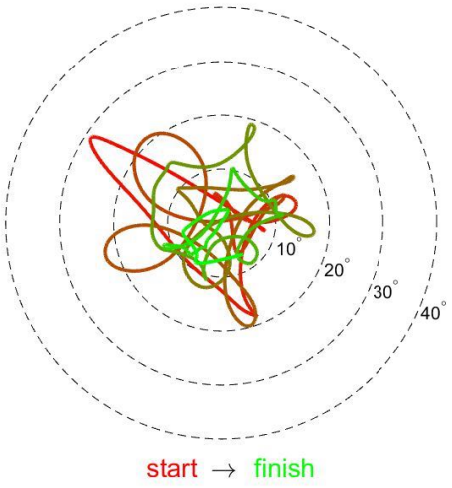

Figure 17: Vehicle attitude dynamics history during the first test run, plotted using the pitch angle and pitch direction in the inertial frame, with colour representing descending time, the motion caused by autorotation and nutation can be seen from this plot.

The frequency of the nutation motion evaluated from Figure 18d is approx. 1.9 Hz, which is different from the rate of autorotation (1.4 Hz).

4. Conclusions

The present study has demonstrated the scalability of the flexible heat shield design with self-regulated centrifugal deployment. Following a simple scaling rule, vehicles with entry mass ranging across six orders of magnitude (from 30 g to 30 tonne) have achieved acceptable trajectory behaviours during simulated re-entries from Low Earth Orbit (LEO). The design also shows a lower heat shield mass when scaled to compare with NASA's HEART inflatable entry vehicle. Meanwhile, downrange manoeuvre enabled by a roll-attitude controller proposed in the previous study is also scalable. Vehicles with 3 kg and 5 tonne entry mass have achieved similar downrange shift ($\sim$ 540 km) and propellant consumption ($<$ 7% of vehicle mass) in

simulated LEO re-entries.

On the other hand, according to low speed wind tunnel tests, the simulator, although developed using hypersonic aerodynamics, can reliably predict equilibrium autorotation at low speed. Therefore, the critical aspects of the simulator can be verified by comparing to the low-speed ($\sim$ 5 m/s) low-altitude ($\sim$ 100 m) drop tests conducted in the present research. The simulator shows close agreement to the tests in equilibrium spin rate and deployment angle, though the aerodynamic roll-torque is over-predicted. The reason for such a similarity between hypersonic and low speed results is that the critical behaviours of the aeroshell, including autorotation and deployment, is dominated by geometrical rather than aerodynamic principles.

Meanwhile, the drop tests have also shown that the aeroshell forms unsymmetrical shape when folded to a relatively low deployment angle by unsymmetrical buckling. However, the shell's shape and the vehicle's attitude are stable. A nutation motion with the amplitude decaying during descent has been observed.

Furthermore, two design variations of the deployable entry vehicle are proposed. In order to address different mission requirements, the designs feature low stowage volume and structural simplicity respectively. Particularly, the design 2 allows a miniaturised vehicle to survive entry even when flipped over, thus relieving the requirement for attitude control or pre-spin. This potentially provides an entry vehicle solution for low-cost probe swarms. The stitched fabric heat shield construction based on such a design is demonstrated by the drop-test vehicle.

Reference

[1] R. D. Braun, R. M. Manning, Mars exploration entry, descent, and landing challenges, Journal of spacecraft and rockets 44 (2) (2007) 310–323.

[2] B. Steinfeldt, J. Theisinger, A. Korzun, I. Clark, M. Grant, R. Braun, High mass

mars entry, descent, and landing architecture assessment, in: AIAA SPACE 2009 Conference & Exposition, 2009, p. 6684.

[3] B. G. Drake, S. J. Hoffman, D. W. Beaty, Human exploration of mars, design reference architecture 5.0, in: Aerospace Conference, 2010 IEEE, IEEE, 2010, pp. 1–24.

[4] J. Cruz, J. Lingard, Aerodynamic decelerators for planetary exploration: past, present, and future, in: AIAA Guidance, Navigation, and Control Conference and Exhibit, 2006, p. 6792.

[5] S. Dutta, B. Smith, D. Prabhu, E. Venkatapathy, Mission sizing and trade studies for low ballistic coefficient entry systems to venus, in: Aerospace Conference, 2012 IEEE, IEEE, 2012, pp. 1–14.

[6] V. Carandente, R. Savino, New concepts of deployable de-orbit and re-entry systems for cubesat miniaturized satellites, Recent Patents on Engineering 8 (1) (2014) 2–12.

[7] J. Andrews, K. Watry, K. Brown, Nanosat deorbit and recovery system to enable new missions, paper no, SSC11-X-3, presented at the 25th AIAA/USU Conference on Small Satellites, Logan, Utah, USA, 8-12 August, 2011.

[8] B. Smith, A. Cassell, C. Kruger, E. Venkatapathy, C. Kazemba, K. Simonis, Nano-adept: An entry system for secondary payloads, in: Aerospace Conference, 2015 IEEE, IEEE, 2015, pp. 1–11.

[9] M. Wiegand, H. Konigsmann, A small re-entry capsule-BREM-SAT 2, in: 10th AIAA/USU Small Satellite Conference, Logan., Volume 1, 1996.

[10] B. P. Smith, C. L. Tanner, M. Mahzari, I. G. Clark, R. D. Braun, F. M. Cheatwood, A historical review of inflatable aerodynamic decelerator technology development, in: Aerospace Conference, 2010 IEEE, IEEE, 2010, pp. 1–18.

[11] I. G. Clark, A. L. Hutchings, C. L. Tanner, R. D. Braun, Supersonic inflatable aerodynamic decelerators for use on future robotic missions to mars, in: Aerospace Conference, 2008 IEEE, IEEE, 2008, pp. 1–17.

[12] H. Bohon, M. MIKULAS, M, Development status of attached inflatable decelerators., Journal of Spacecraft and Rockets 6 (6) (1969) 654–660.

[13] C. Tanner, J. Cruz, R. Braun, Structural verification and modeling of a tension cone inflatable aerodynamic decelerator, in: 51st AIAA/ASME/ASCE/AHS/ASC Structures, Structural Dynamics, and Materials Conference 18th AIAA/ASME/AHS Adaptive Structures Conference 12th, 2010, p. 2830.

[14] A. Mastropietro, J. Kempenaar, M. Redmond, M. Pauken, W. Ancarrow, First test flight thermal performance of the low density supersonic decelerator (LDSD) supersonic flight dynamics test (SFDT) vehicle, in: 45th International Conference on Environmental Systems, 2015.

[15] D. Litton, D. Bose, F. Cheatwood, S. Hughes, H. Wright, M. Lindell, S. Derry, A. Olds, Inflatable re-entry vehicle experiment IRVE-4 overview, in: 21st AIAA Aerodynamic Decelerator Systems Technology Conference and Seminar, 2011, p. 2580.

[16] D. Wilde, S. Walther, K. Pitchadze, S. Alexsaschkin, D. Vennemann, L. Mar-

raffa, Flight test and ISS application of the inflatable reentry and descent technology (IRDT), Acta Astronautica 51 (1-9) (2002) 83–88.

[17] Y. Takahashi, D. Ha, N. Oshima, K. Yamada, T. Abe, K. Suzuki, Aerodecelerator performance of flare-type membrane inflatable vehicle in suborbital reentry, Journal of Spacecraft and Rockets 54 (5) (2017) 993–1004.

[18] D. L. Akin, The parashield entry vehicle concept-basic theory and flight test development, in: 4th AIAA/USU Small Satellite Conference, Logan, UT, Aug. 27-30, 1990, Proceedings. (A91-27376 10-18). Logan, Vol. 1, 1990.

[19] E. Venkatapathy, K. Hamm, I. Fernandez, J. Arnold, D. Kinney, B. Laub, A. Makino, M. McGuire, K. Peterson, D. Prabhu, et al., Adaptive deployable entry and placement technology (ADEPT): a feasibility study for human missions to mars, in: 21st AIAA Aerodynamic Decelerator Systems Technology Conference and Seminar, 2011, p. 2608.

[20] E. Fantino, M. Grassi, P. Pasolini, F. Causa, C. Molfese, R. Aurigemma, N. Cimminiello, D. de la Torre, P. Dell'Aversana, F. Esposito, et al., The small mars system, Acta Astronautica 137 (2017) 168–181.

[21] G. Zuppardi, R. Savino, G. Mongelluzzo, Aero-thermo-dynamic analysis of a low ballistic coefficient deployable capsule in earth re-entry, Acta Astronautica 127 (2016) 593–602.

[22] V. Carandente, R. Savino, V. DOriano, R. Fortezza, A study on earth re-entry capsules with deployable aerobrakes for recoverable microgravity experiments, Microgravity Science and Technology 27 (3) (2015) 181–191.

[23] R. Wu, P. C. Roberts, C. Soutis, C. Diver, Flexible heat shields deployed by centrifugal force, Acta Astronautica.

[24] R. Wu, P. C. Roberts, C. Soutis, C. Diver, Downrange manoeuvre and oscillation suppression of a self-moderating centrifugally deployed flexible heat shield using controlled reaction wheel, submitted to Acta Astronautica.

[25] S. Hughes, J. Ware, J. Del Corso, R. Lugo, Deployable aeroshell flexible thermal protection system testing, in: 20th AIAA Aerodynamic Decelerator Systems Technology Conference and Seminar, 2009, p. 2926.

[26] H. Wright, A. Cutright, J. Corliss, W. Bruce, D. Trombetta, A. Mazaheri, M. Coleman, A. Olds, S. Hancock, Heart flight test overview, in: 9th International Planetary Probe Workshop, Toulouse, France, 2012.

[27] G. P. Sutton, O. Biblarz, Rocket propulsion elements, John Wiley & Sons, 2016.

[28] R. M. Crow, M. M. Dewar, Comparison of seam types, Tech. rep., DEFENCE RESEARCH ESTABLISHMENT OTTAWA (ONTARIO) (1983).

[29] P. Wercinski, Adaptable deployable entry & placement technology (ADEPT) for cubesat delivery to mars surface, Tech. rep., NASA ARC-E-DAA-TN19332 (2014).

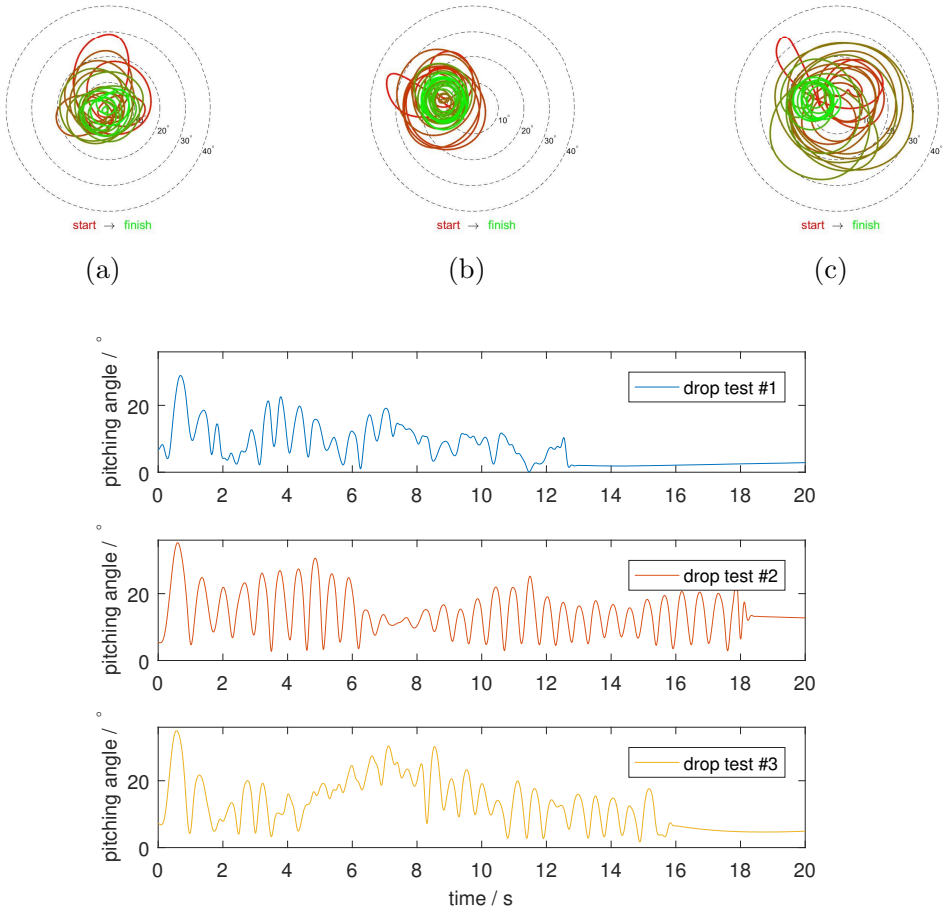

Figure 18: Vehicle attitude dynamics history of test runs 1∼3, (a) (b) (c) pitch angle and direction plotted in the vehicle frame with colour representing descending time, the decaying nutation motion is clearly shown by these plots, (d) pitch angle plotted against time, showing a nutation frequency (1.9 Hz) that is different from autorotation (1.4 Hz).

4.2 Comparison between experimental methods

Besides the low-speed drop test discussed in paper III, experimental methods including wind tunnel test and balloon drop test have also been considered to verify the trajectory simulation as well as the deployment and flight dynamic behaviours of the proposed vehicle. This section provides a comparison between these methods and points out that the low-peed drop test is the most practical and cost-effective experiment.

4.2.1 Wind tunnel test

Wind tunnel test of a flexible heat shield model is designed to reveal its dynamic deployment behaviours during the flight regime with peak dynamic pressure, which is the most critical stage of re-entry. The flight condition during this regime is predicted using the trajectory simulator and reported in Table 4.1. The simulation assumes a CubeSat-sized vehicle with the baseline design re-entering from 145 km LEO at 7800 m/s and zero flight path angle.

Table 4.1: Critical flight conditions of a CubeSat-sized vehicle under peak dynamic pressure during a simulated re-entry from LEO

Parameter	Simulation prediction
Shell base diameter	0.7 m
Freestream temperature	$\sim$ 230 K
Static pressure	$<$ 10 Pa
Dynamic pressure	$\sim$ 200 Pa
Spin rate	$<$ 10 rps

Since the structural dynamic behaviour is of interest, the test setup and model design requires dynamic aeroelastic scaling. The similitude factors are shown in Table 4.2, where v is freestream velocity, T is fluid temperature, ρ is fluid density,

ρ_S is the shell's areal density, E is the shell material's Young's modulus, t is shell thickness, l is shell base diameter, and P is dynamic pressure. Note that the similitude factors reported here are the reduced expressions, and the derivation is documented in Appendix A.4.

Table 4.2: Wind tunnel scaling factors for the heat shield model

Scaling factor	Reduced expression	Test Requirement
Mach number	$v/T^{0.5}$	Hypersonic regime ($M > 5$)
Reynolds number	$\rho v l$	Less critical
Relative density Mass moment of inertia "Deploy-ability"	$\rho_S/\rho l$	Keep generally constant
Aeroelastic bending	Et^3/Pl^3	Keep generally constant
Spin rate	$\sqrt{P/\rho_S l}$	Keep sufficiently low

The major obstacle is that existing wind tunnel facilities usually provide static and dynamic pressures that are over one order of magnitude higher than the flight condition shown in Table 4.1, while the model size has to be scaled down at the same time. Therefore, a sufficiently low spin rate ($\propto \sqrt{\frac{P}{\rho_S l}}$ according to Table 4.2), which is necessary to prevent excessive vibration, requires a high model areal density ρ_S. Similitude of relative density scaling factor ($\propto \frac{\rho_S}{\rho l}$) calls for a similar requirement. This high areal density ρ_S inevitably leads to a high shell thickness t. For simplicity, assume constant material volume density, then we have:

$$\rho_S \propto t$$

Then the relative density scaling factor becomes:

$$\frac{\rho_S}{\rho l} = \frac{t}{\rho l}$$

Thus, the aeroelastic scaling factor becomes (substituting $t = \rho l$):

$$\frac{Et^3}{Pl^3} = \frac{E\rho^3}{P} = \frac{E\rho^2}{v^2}$$

Since freestream velocity v in the wind tunnel is at the same order of magnitude as under the flight condition, and the wind tunnel fluid density ρ is significantly higher, the similitude of aeroelastic bending can only be satisfied together with relative density if the material modulus E was significantly lower than the baseline design. This is not feasible considering that the baseline design uses a flexible fabric shell with a flexural modulus that is already very low. Therefore, a high fidelity wind tunnel test is not viable.

In addition, flow direction in a wind tunnel is usually horizontal, which causes another issue that during spinning, gravity may have complex oscillatory effect on a horizontally-mounted flexible model. This creates another drawback of wind tunnel experiments.

Nevertheless, a wind tunnel test on a flexible model could still help understanding the dynamic behaviours of the heat shield even if some of the similitude factors were not matched. However, acceptable test conditions are still not achievable, as illustrated by Table 4.3, which reports the prediction from the trajectory simulator that is revised to simulate the dynamics behaviour in a wind tunnel. According to the table, near fully-deployed condition can be obtained despite of the reduced relative density factor, but a low static pressure is still required to prevent over-spin. Although this can be achieved using facilities such as the SCIROCCO plasma wind tunnel in CIRA, it is not further considered since a more cost-effective experimental method exists.

Meanwhile, efforts have also been made to design a rigid/semi-rigid model test in the High-SuperSonic-Tunnel (HSST) in the University of Manchester. However, the required model construction is impractical and the design is discarded, as documented in Appendix A.5.

Table 4.3: Simulated hypersonic wind tunnel test at Mach 6 and $\sim 300\,K$ on a flexible test model with 0.35 m base diameter

Static pressure	Surface density	Deployment angle	Spin rate
50 Pa	$2\,kg/m^2$	$59° \sim 60°$	16 rps
50 Pa	$1\,kg/m^2$	$59° \sim 60°$	23 rps
100 Pa	$2\,kg/m^2$	$59° \sim 60°$	23 rps
100 Pa	$1\,kg/m^2$	$58° \sim 60°$	32 rps
1000 Pa	$2\,kg/m^2$	$56° \sim 60°$	70 rps

4.2.2 Drop test from high altitude balloon

Although a hypersonic wind tunnel test is impractical, it is feasible to use a weather balloon to perform a high altitude low speed drop test at a much lower cost, which could simulate the dynamic pressure of interest while having no limitation on model size. This section demonstrates that a drop test from weather balloon can practically provide information on the deployment as well as flight dynamic behaviours at subsonic speeds and under a varying atmospheric conditions, although the speed regime is not matched.

The maximum accessible altitude is set to 35 km according to an online weather balloon performance calculator developed by High Altitude Science [151]. The calculator shows that a 3 kg class balloon could reach above 35 km before burst and within a reasonable time ($< 3\,h$), while higher altitude ($> 40\,km$) is difficult to access due to insufficient buoyancy. The trajectory simulator is used to analyse the condition of a test vehicle during the drop test. Results are shown in Table 4.5. It can be seen that the peak velocity is always low, which can be increased by using a 2-stage test vehicle that deploys from a stowed condition (with high ballistic ratio) at a certain time during descent. However, simulations have shown that although this allows the peak velocity to be doubled, supersonic velocities are still difficult to achieve due to the insufficient ballistic ratio as well as the

resulted high dynamic pressure and excessive spin rate ($> 10\,rps$, which increase the requirements on the onboard sensors). Therefore, a single stage test vehicle should be used.

Table 4.4: Simulation predictions of 35 km free fall tests

Base dia.	Total mass	Payload mass	Surface density	Spin rate	Deploy. angle at 35 km	Deploy. angle at 0 km	Peak velocity	Terminal velocity
0.35 m	600 g	475 g	$1\,kg/m^2$	$\sim 3.5\,rps$	$55 \sim 60°$	$37 \sim 60°$	100 m/s	$< 15\,m/s$
0.7 m	1.3 kg	800 g	$1\,kg/m^2$	$\sim 1.7\,rps$	$55 \sim 60°$	$30 \sim 57°$	75 m/s	$< 10\,m/s$
0.7 m	1.3 kg	300 g	$2\,kg/m^2$	$\sim 1\,rps$	$56 \sim 59°$	$43 \sim 55°$	75 m/s	$< 10\,m/s$
0.7 m	3 kg	2 kg	$2\,kg/m^2$	$\sim 2\,rps$	$55 \sim 60°$	$35 \sim 60°$	110 m/s	$< 15\,m/s$

Simulation has also suggested that dropping from $25\,km$ altitude provides a peak deployment angle of $> 50°$ while the other parameters are similar to the 35 km test. Thus a 25 km drop test can provide similar information while loosening requirements on sensors (barometers on commercial flight controller units usually supports static pressure up to 30 km altitude) and allowing shorter mission duration (< 1 hour for ascent). For such a test, the vehicle should operate at $55\,mbar$ to $25\,mbar$ and $-56°C$ to $-50°C$, equipped with sensors, power supplies and location devices for recovery after landing, a weather balloon system, as well as a releasing system either on the vehicle or on the balloon that could release the vehicle at the prescribed altitude.

4.2.3 Comparison

The experimental methods discussed above are summarised in Table 4.5. It can be seen that the drop tests are more cost effective and practical than wind tunnel tests. Therefore, a low altitude drop test was carried out in the present study to provide a quick verification of the simulation. It also sets a foundation for the future high altitude drop test as well as other high fidelity experiments such as suborbital launch.

Table 4.5: Comparison between experimental methods

Method	Advantages	Drawbacks
Low density hypersonic/plasma wind tunnel test	Matches the flight condition of interest	Limited availability of suitable test facilities; Lateral gravity complicates the behaviour; Limited freedom of motion
Drop test from 25 km altitude	Captures full vehicle flight dynamic behaviour; Allows full-scale CubeSat-sized test vehicle; Provides varying atmospheric condition	Not matching the speed regime and atmospheric density of interest; Operation not covered by UK regulations
Drop test from low altitude	Simplicity; Lowest cost and requirement on test facility; Allows rapid equipment design iterations	Provides only one test condition at low speed regime

Part II

Application to Solar Sails

Chapter 5

Passive centrifugal deployment of an origami heliogyro

This chapter includes a submitted paper on a heliogyro concept with self-regulated passive centrifugal deployment. The operation is enabled by an origami-inspired meta-structure reflector that generates an in-plane SRP thrust to propel the rotation of the solar sail. The SRP vector is stress-dependent thus responds to the centrifugal force. Combined with a passive blade releasing mechanism, closed-loop passive control over spin rate and sail deployment can be achieved. In the mean time, the sail remains flat and thereby has simplified dynamic behaviour. The paper discusses the design of the origami pattern, as well as the mechanical and optical characteristics of the reflector. Then a baseline vehicle design is simulated to demonstrate its ability to follow a pre-defined spin rate history during deployment, while preventing over-spin after fully deployed.

5.1 Paper IV: Design concept and preliminary analyses

Heliogyro Solar Sail with Self-Regulated Centrifugal Deployment Enabled by an Origami-Inspired Morphing Reflector

Authors: Rui Wu, Peter Roberts, Constantinos Soutis, Carl Diver

Journal: Acta Astronautica, (**Impact factor:** 1.536)

Publication date: August 2018

Statement of own contributions in joint authorship:

Main research idea and technological development;

Preparation of tables, figures, and the manuscript;

Design and prototyping of the origami reflector;

MATLAB program for photonic propulsion simulation and mechanical analyses;

SIMULINK deployment dynamic simulator construction and MATLAB result interpretation.

Heliogyro Solar Sail with Self-Regulated Centrifugal Deployment Enabled by an Origami-Inspired Morphing Reflector

Rui Wu[a,*], Peter C.E. Roberts[a], Constantinos Soutis[b], Carl Diver[a]

[a] *School of Mechanical, Aerospace and Civil Engineering, the University of Manchester, UK*
[b] *The University of Manchester Aerospace Research Institute, UK*

Abstract

Solar sails utilise solar radiation pressure to propel spacecraft without the need for propellant. Existing solar sail concepts also achieve propellantless flight control by actively twisting the sail or altering the sail surface reflectivity. However, this usually consumes energy and leads to structural dynamic issues. In the present study, we propose an innovative method, which uses origami to convert the 2D sail into a 3D optical meta-structure with design-able and manoeuvrable optical properties. Such a device could adjust both the magnitude and the direction of solar radiation pressure without inducing overall distortion in the sail and therefore achieve flight control through a quasi-static process. As an example, a centrifugally deployed heliogyro solar sail with meta-structure morphing reflectors is designed. The reflectors generate stress-dependent solar radiation pressure vector, which propels the spinning of the sail and, according to structural dynamic simulation, achieves a closed-loop controlled centrifugal deployment that is fully passive.

Keywords:

*Corresponding author
Email address: rui.wu@manchester.ac.uk (Rui Wu)

photonic propulsion, self-moderating, passive control, gossamer structure, meta material

---

Nomenclatures

a, b, c: dimensions of Miura crease pattern

d: length of hinge

E: energy of solar radiation

f: surface reflectivity

F: Force

l: length of folded Miura element

I: angular inertia

L: extension of meta-structure reflector

m: mass

M: moment of force

n: number of reflections

p: momentum of a ray of photon

P_{SRP}: solar radiation pressure

R: span of conventional blade

T: tensile load

U: elastic potential energy

v_c: speed of light

W: solar radiation energy density

α: surface absorptivity

θ: dihedral angle (hinge angle) of origami

θ_0: neutral hinge angle

ϵ: surface emissivity

η: edge angle of origami

ϕ: Miura angle

σ: Stefan-Boltzmann constant $= 5.67 \times 10^{-8}\, W \cdot m^{-2} \cdot K^{-4}$

κ: torsional modulus of $1\, m$ hinge $(N \cdot m/rad)$

τ: torque from hinge

ω: angular velocity

AoA: Angle of Attack

LEO: Low Earth Orbit

RCD: Reflection Control Device

SRP: Solar Radiation Pressure

1. Introduction

Solar sail provides a practical way to achieve propellantless propulsion for a spacecraft using Solar Radiation Pressure (SRP). Efforts towards its technical realisation have started in the 1960s [1, 2, 3], and various design concepts have been proposed since then. The existing designs can be classified into two categories: rigid sails that achieve structural rigidity from elastic force, and spinning sails rigidised by inertial (centrifugal) force.

Rigid solar sails are formed by attaching reflective membranes onto bracing structures such as deployable booms or spars, which not only constrains the deflection of the membrane when fully deployed, but also initiates and controls the deployment process. Since a large surface area to mass ratio, or low sail loading, is required to maximise the acceleration gained from SRP, it is crucial to minimise structural mass [1]. However, rigid solar sails rely on the elastic bending rigidity of the bracing structures, which makes it disadvantageous and unpractical for large sails due to the

high structural mass as well as the buckling limit [4].

Spinning solar sail utilise centrifugal force that is generated from the spinning motion to deploy and stiffen a membrane reflector. Such a design can realise a compression-free structure, eliminating the risk of buckling, and thereby allowing the structure to be thin and flexible. This not only leads to a lower structural mass than the rigid solar sails especially when the sail is large, but also a smaller storage volume when packed, and a lower deployment power consumption [5]. Centrifugal deployment in orbit was first successfully demonstrated in 1993 [6], and the world's first interplanetary solar sail IKAROS launched by JAXA in 2010 was a centrifugally deployed spinning disk sail, which has a square reflector of $14\,m \times 14\,m$ that is folded and wrapped onto the central spacecraft using a wrap-rib method [7, 8, 9]. Besides spinning disk sails, the concept of heliogyro was first introduced in the 1960s [10], and uses multiple centrifugally deployed and stiffened reflective membrane strips to form a helicopter-rotor-like sail. The strips, due to the simple geometry and high slenderness, could be stowed by simply winding around a reel rather than folding along complicated patterns like a disk sail. This allows a higher packing ratio as well as more straightforward packing/deploying process, which make it suitable for solar sails that require large sail area or small storage volume: such as NASA's ambitious Halley Rendezvous sailer designed in the late 1970s with twelve $8m \times 7.5km$ rectangular blades [11]; or smaller designs such as NASA's HELIOS concept built upon a CubeSat architecture with six $0.75\ m \times 220\ m$ blades [12]. However, the extreme slenderness ($\sim 1:1000$) of a heliogyro blade leads to high tensile stress at the blade root, difficulty in attitude control due to the high blade inertia, as well as risk associated with coupled structural dynamic behaviours [4, 10, 13, 14].

Meanwhile, propellantless flight control of a solar sail propelled spacecraft can be realised by controlling the SRP generated by the sail. In the existing solar sail

concepts, this is usually achieved by twisting the reflector, which simultaneously changes the magnitude and direction of the SRP vector. For example, the pitch of different blades of a heliogyro can be controlled in a collective or cyclic manner during each revolution of the spinning motion to achieve spin/thrust control or attitude control like a helicopter [10]. Similarly, the IKAROS disk sail can be divided into multiple panels that are independently pitched to realise spin control [15]. The methods to tilt a sail include directly twisting the sail [10], or generating a pitching moment from SRP by shifting the sail's centre of mass relative to its centre of SRP using moving ballast mass or hinged flaps [16, 17, 18]. Besides those methods that regard the sail as a simple reflector with fixed optical properties, the IKAROS mission has also demonstrated SRP control using Reflection Control Devices (RCD) based on liquid crystal [7, 8]. The RCDs alter the reflectivity, and thus the magnitude of SRP at certain regions on the sail surface, therefore steer the spacecraft [9]. Similar concepts have also been proposed to control the pitch of heliogyro blades by tip RCDs [12, 19]. However, RCD manipulates only the magnitude of SRP rather than the direction of it, thus it is still not possible to generate an in-plane thrust component unless the RCD is used to induce overall distortion or displacement in the sail (e.g., when the RCD is used to control the pitch of a Heliogyro blade). On the other hand, the possibility of controlling both the magnitude and direction of the SRP vector, and therefore achieving complex flight control without distorting the whole sail remains to be discovered.

In fact, a better control over SRP vector is viable using origami-based meta-structure with design-able optical properties. Origami provides a method to convert a 2D sheet such as a solar sail into a 3D device with programmable properties and even built-in functionalities, thus is widely regarded as a building block for meta-materials [20, 21, 22, 23, 24]. In the present study, a morphing reflector that forms an origami-

inspired meta-structure is proposed for spinning sails, which manipulates the SRP vector and thereby can be used to enable a self-regulated centrifugal deployment. The meta-structure is based on a 4-vertex origami [25, 26], which achieves self-regidisation as well as the desired optical properties when folded.

In addition, de-orbiting drag sails, which deploy from a satellite and generate aerodynamic drag in Low Earth Orbit (LEO) to reduce the satellite's orbital altitude and ultimately remove it from the orbit or bring it down for a targeted re-entry, has also attracted interests from the industry [27]. Drag sails have similar design strategies to solar sails since both utilise lightly loaded deployable structures that are large and lightweight [28, 29]. Therefore, the visions and development on solar sails could also benefit drag sail technologies.

2. Geometrical properties of the origami-inspired morphing reflector

The geometry of the proposed meta-structure reflector is based on a 4-vertex (degree-4 vertex) origami pattern that contains two types of elements as shown in Figure 1a: Miura element and right-angled zigzag element. The parameters used to describe the folded configuration, including dihedral angles θ_A, θ_Z, edge angles η_A, η_Z, and the length of the Miura element l are shown in Figure 1b and 1c. The subscript A and Z denotes the auxiliary line (along x-direction) and zigzag line (along y-direction) respectively.

During folding, this origami design has one degree-of-freedom, thus all the dihedral and edge angles are related and depend on each other. The relationships are captured by Eq. 1-3 according to literature [30].

$$2\,sin^2\eta_Z\,(1-cos\,\eta_A) = 4\,cos^2\phi \tag{1}$$

$$cos\,\eta_A = sin^2\phi\,cos\,\theta_Z - cos^2\phi \tag{2}$$

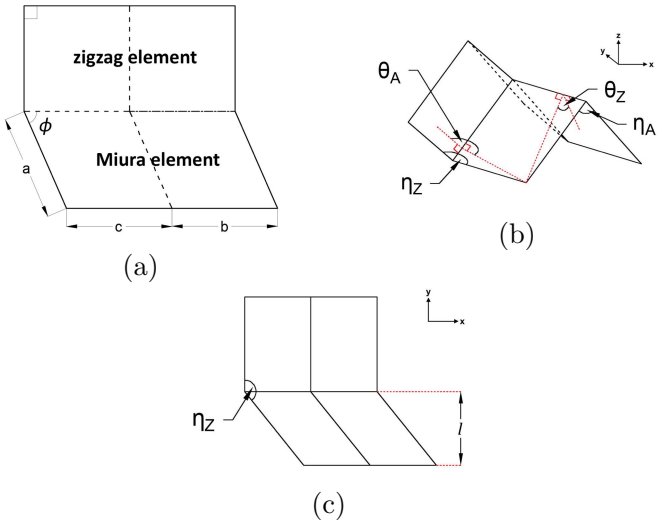

Figure 1: Parameters of the 4-vertex origami pattern that defines the geometry of the proposed morphing reflector, (a) crease pattern on the flat sail surface containing two types of construction elements, (b)(c) parameters describing a folded configuration

$$(2\,sin^2\eta_Z - 1) = sin^2\phi\,(2\,sin^2\theta_A - 1) + cos^2\phi \tag{3}$$

Where ϕ is a constant for a certain origami design, and once one of the four angles θ_A, θ_Z, η_A and η_Z is determined, the rest can be evaluated using Eq. 1-3. Therefore, the origami can morph with one degree-of-freedom. The linear dimensions a, b and c are independent to each other, and can be determined freely.

The overall size of the origami also changes during folding. Particularly, the Miura element's length along y direction can be expressed as below [30]:

$$l = -a\,cos(\eta_Z) \tag{4}$$

In this origami design, the purpose of the zigzag type element is to generate SRP, while the Miura element controls the folding (η_A) of the zigzag element and therefore controls the SRP. The angle between the zigzag elements, which is equal to the edge angle of the Miura elements η_A, is referred to as zigzag angle in the following text.

As discussed later in section 3, when $b \neq c$, an non-zero in-plane (the x-y plane shown in Figure 1) SRP component can be generated under a direct sunlight along z-direction.

The usefulness of origami structures partly comes from its design-ability. In other words, the properties of an origami structure can be adjusted by tailoring the crease pattern or how different elements are assembled. The detailed discussions on the design of optical and mechanical properties can be found in Sections 3-4.

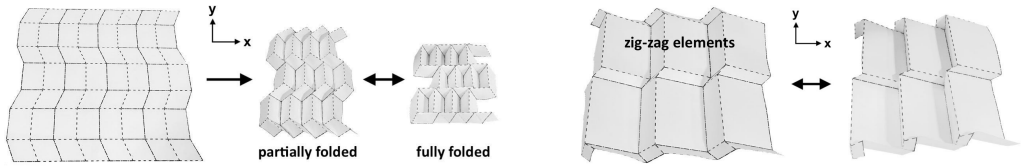

(a) (b)

Figure 2: Paper prototypes of the assembled 4-vertex origami with different design parameters, showing that the origami can morph between the partially and fully folded configurations and the amount of shrinkage can be designed, (a) folding process of a design with $a = b = c$, the overall dimension of which significantly shrinks during folding, (b) a design with $a = b/2 = c/4$ and extended zigzag elements, which has identical folding angles to (a) but shows much lower shrinkage

Figure 2 shows two examples of assembled origami. It can be seen that the zigzag angle η_A decreases during folding until the Miura elements are fully folded with $l = 0$, $\theta_Z = 0°$ and $\theta_A = \eta_Z = 90°$. Meanwhile, as shown in Figure 2a, the overall area as well as the in-plane linear dimensions (x and y) of the origami shrinks during folding. However, as suggested by Figure 2b, this shrinkage can be reduced without influencing the zigzag angle η_A: by reducing the design parameter a in comparison with b and c, by reducing the b/c ratio, or by increasing the relative size of the zigzag elements. A low-shrinkage design allows the optical properties, which depend on the zigzag angle, to vary during folding without inducing significant change in the sail's dimensions and thus avoids structural dynamic problems. The same results can be derived from Eq. 1-4: the angles in the origami θ_A, θ_Z, η_A, and η_Z are not

determined by the length parameters a, b and c. Therefore, the shrinkage along y direction, which depends on the dimension of the Miura elements l, can be designed independently to the angles and thus the optical properties.

3. Propulsive properties of the origami-inspired morphing reflector

According to the discussions above, the optical and geometrical functionalities of the meta-structure can be separated into the two types of elements: when the size of Miura element (a) is minor in comparison with zigzag elements, optical properties will almost solely depend on the zigzag elements, while the Miura elements controls folding.

In order to analyse the SRP generated by the zigzag element made from a reflective membrane, a numerical simulator is constructed. It simulates the parallel incident light using 1000 rays equally spaced along the auxiliary line (x-axis), and allows multiple reflections. The evaluation of SRP is based on the momentum transfer between the incident ray and the reflector, as well as between the reflector and the reflected ray. Let the momentum of a ray of photon be p, then the force induced on the reflector by the momentum transfer from a incident ray can be calculated by differentiating the momentum by time [1]:

$$F = \frac{dp}{dt} \tag{5}$$

According to relativity, we have:

$$F = \frac{dE}{v_c \cdot dt} \tag{6}$$

Therefore,

$$P_{SRP} = \frac{W}{v_c} \tag{7}$$

Similarly, the SRP induced by a reflecting ray is below, note that the direction of P_{SRP} is along the speed of the ray:

$$P_{SRP} = -\frac{W}{v_c} \tag{8}$$

The analyses are carried out on the 2D cross section of a zigzag element along the auxiliary line. As shown by Figure 3a, the simulation inputs include surface reflectivity, the dimensionless ratio b/c, the zigzag angle η_A, and Angle of Attack (AoA), which is the angle between the incident light and the meta-structure's normal direction. It should be noted that the incident light is always in the x-z plane since the simulation is 2D. The AoA in the y-z plane is not considered since it has the same effect on the zigzag element as on a flat sail. The zigzag angle η_A changes continuously during folding. For convenience of the simulations, it is varied from the unfolded configuration of $\eta_A = 180°$ to the configuration where the right hand side panel with length b shown in Figure 3 is perpendicular to the sail's central plane. Meanwhile, the AoA is also varied between $\pm 45°$.

At the beginning of the simulation, the angle and incident point of each ray is geometrically evaluated using η_A and AoA. After each reflection, the new incident angle is evaluated using the previous incident angle, and the power density of the ray can be expressed as:

$$W_n = W \times f^n \tag{9}$$

Where W_n is the power density of the ray after n times of reflection, and f is the surface reflectivity. The thrust caused by this reflection, dF_x and dF_z are

evaluated using Eqs. 7-8, and then the moment of the thrust, dM_y is calculated with respect to the cross-section's centroid. The steps above are repeated until this ray no longer intersects with the origami. During the simulations reported in this paper, the maximum number of reflections encountered by a ray is 3.

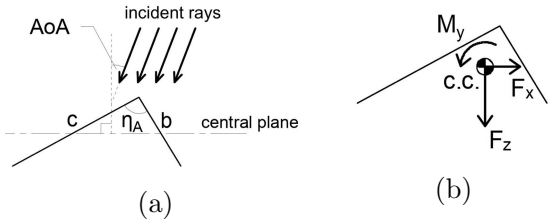

Figure 3: 2D cross-section of a zigzag element that is simulated with the input parameters shown in (a), and results are shown in (b), where AoA stands for Angle of Attack, and c.c. stands for Cross-section's Centroid

The simulations assume a specular surface reflectivity of 95%, a surface absorptivity of 5%, a solar radiation power density of $1360\,W/m^2$ (at $1.0\,AU$), a sail surface area of $1\,m^2$ when unfolded, and $b + c = 1\,m$. Two meta-structure designs listed in Table 1 are simulated to demonstrate the effect of design parameter b/c. The results, as shown in Figure 3b, include the x and z components of the force generated from SRP (F_x and F_z), as well as the moment about the cross-section's centroid (M_y). Note that the centroid coincides with centre of mass when assuming uniform sail surface density. M_y is of interest since it induces twist of the heliogyro blade: due to the blades low torsional stiffness, a small magnitude of M_y is required. According to Figure 4 and Table 1, the design objective is achieved: both designs generate a significant in-plane thrust F_x without twisting/pitching the sail; and the force can be tuned by simply adjusting the folding angle η_Z and without inducing significant change of the sail's overall shape or dimensions. This allows the direction of SRP to be adjusted without causing structural dynamic issues. As an example, in section 5

this in-plane thrust is utilised to propel the spinning of a heliogyro.

From Table 1 it can be seen that the two designs yield similar out-of-plane force F_z, which is the major propulsion that accelerates the spacecraft, while F_x and M_y can be designed by adjusting b/c. It should be noted that the non-zero moment M_y about the cross-section's centroid is high enough to induce sail distortion and thus structural dynamic problems. However, since M_y is proportional to the chord length of the zigzag element (or in other words, $b + c$) multiplies the sail area, it can be reduced without influencing F_x and F_z by reducing $b + c$ while keeping b/c and the total sail area unchanged (i.e. increasing the number of elements per unit sail area).

Table 1: Simulation results on the SRP-induced forces/moment generated from the zigzag origami element, according to Figure 4

Origami design	Peaks of F_x	Peaks of F_z	Peaks of M_y
$b/c = 0.5$	$2.95\ \mu N$	$8.83\ \mu N$	$0.92\ \mu N \cdot m$
	$-5.00\ \mu N$	$3.62\ \mu N$	$-1.22\ \mu N \cdot m$
$b/c = 0.25$	$1.78\ \mu N$	$8.83\ \mu N$	$0.40\ \mu N \cdot m$
	$-2.65\ \mu N$	$3.96\ \mu N$	$-1.03\ \mu N \cdot m$

Besides the results discussed above, according to Figure 5, a lower b/c leads to a lower dependence of F_x on AoA. This could have importance since a lower dependence of F_x on AoA leads to lower fluctuation of the in-plane load on the sail during spinning or structural oscillation, and thus a lower tendency of structural dynamic couplings or fatigue. In other words, the determination of b/c leads to a trade-off between the magnitude and the robustness of F_x.

Furthermore, besides the instantaneous in-plane thrust discussed above, the effective in-plane thrust generated under oscillating AoA is approximated by averaging F_x over a period of a harmonic oscillation by time. This represents the AoA fluctuation due to the inclination of the sails spinning axis to the sun or due to harmonic oscillation in the sail structure. 3D analyses are also conducted to account for the

effect of AoA in the y-z plane, while the results are very similar and are not reported here. In each subfigure of Figure 6, the five sets of data represented by the five curves assumes different average AoAs, and the amplitude of the AoA oscillation is set to $\pm 20°$. As an example, a $\pm 20°$ oscillation with $10°$ neutral AoA represents the condition of blades with $10°$ constant pitching angle (which can be a result of other types of manoeuvres) and a rotating axis with a $20°$ inclination to the sun. By comparing the results to Figure 5, it can be seen that the oscillation has no significant influence on the effective in-plane thrust.

Therefore, it can be concluded that the origami-inspired meta-structure can effectively generate a tuneable in-plane thrust. Such thrust can be robust as the time-average thrust generated by the meta-structure is not significantly influenced by oscillations in AoA (Figure 6), and the effect of a constant AoA can also be limited by adjusting the design parameter b/c (Figure 5c).

4. Mechanical properties of the origami-inspired morphing reflector

In this section, the morphing reflector's elastic behaviour under a stretching force along y-direction, or in other words, the elastic resistance to shape morphing, is analysed. In the analyses, the reflector is treated as a perfect origami formed by hinged rigid panels, and one basic module as shown in Figure 1 is considered. The hinges are linearly elastic, with the hinges' neutral angle assumed to be θ_0:

$$\tau = \kappa \cdot (\theta - \theta_0) \cdot d \tag{10}$$

Therefore, the elastic potential energy of a hinge can be expressed as:

$$U = \frac{1}{2} (\theta - \theta_0)^2 \kappa \, d \tag{11}$$

Solving Eq. 1-4, the hinge folding angles in the Miura element, θ_A and θ_Z, as well as in the zigzag element, η_A, can be expressed in terms of the origami's length along y-direction l. Thus, the elastic potential energy of the whole origami module, $U_{origami}$ can be expressed in terms of l. Then the force reaction along y-direction can be solved by differentiating $U_{origami}$ with l (the exact expression is not shown here due to its complexity):

$$F(l, a, b, c, d_{zigzag}, \phi, \kappa, \theta_0) = \frac{d\, U_{origami}}{d\, l} \tag{12}$$

Evaluating F requires the determination of a, b, c, d_{zigzag}, ϕ, κ and θ_0. To decide those parameters, a morphing reflector is designed based on NASA's HELIOS concept (Table 2). The design has $b = 2.5\,cm$ and $c = 10\,cm$ to provide an acceptable b/c ratio according to previous discussions. θ_0 depends on the initial folding angle of the membrane material, which can be designed to have any value within $0° \sim 180°$. Here it is set to 90° to give an example. Based on Figure 5, in order to achieve a monotonous variation of F_x during folding/unfolding and maximise its peak value, ϕ is set to 45° so that $\eta_A = 90°$ when the reflector is fully folded. κ is approximated to $2.2 \times 10^{-5}\, N \cdot m/rad$ by assuming that the reflector is made of kapton ($2.5\, GPa$ young's modulus) with $7\mu m$ thickness and the bending of the hinges occurs within a width of $3\, mm$. Then the elastic force F is evaluated with $a = 1\, cm$, $2\, cm$ and $4\, cm$ respectively, the results are shown in figure 7. $d_{zigzag} = 100\, cm$ is chosen here to let the zigzag elements dominate the reflector's propulsive properties.

It can be seen that the elastic property of the reflector is dominated by the zigzag element (in Figure 7, F_{zigzag} is one order of magnitude greater than F_{θ_A}), since it colonises the most sail area. Meanwhile, the total force generated by the stretched origami F_{total}, or in other words, the overall resistance to shape morphing,

is shown in Figure 8. It can be seen that the elastic resistance to shape morphing can be increased by decreasing a or increasing d_{zigzag}. According to Eq. 12, this tailoring is a trade-off between the reflector's resistance to morphing and its overall shrinkage/expansion during morphing.

In addition, the resistance to morphing also depends on the way that the origami modules are assembled: setting n modules in parallel (along x-direction) results in a n times of a single module's resistance, while setting modules in series (along y-direction) does not change the resistance.

Meanwhile, as a by-product of turning the 2D membrane into a 3D meta-structure, the flexural rigidity also increases significantly. This is illustrated in Figure 9, where a $6\,cm \times 25\,cm$ strip of print paper cantilevered in $1g$ is set in comparison with a partially folded origami with 195 modules made from a similar strip of paper. Therefore, the shape stability of the meta-structure reflector is expected to be significantly better than a simple film, which could potentially improve the structural dynamic behaviour of a heliogyro. However, the exact effect depends on the detailed hinge design, etc. and is not the scope of the present research.

5. Heliogyro concept based on the origami-inspired morphing reflector

As mentioned in introduction, conventional heliogyros utilise helicopter-blade-like flat sails deployed from mandrels to generate SRP. The blade can be pitched by twisting the blade root, shifting the blade centre of mass, or locally adjusting the sail's reflectivity using RCDs. A pitched blade generates an in-plane SRP, thereby achieves attitude manoeuvre and spin control. However, instead of pitching the blade, a in-plane SRP can also be generated using the present meta-structure morphing reflector. This not only allows the blade to remain in the plane of rotation during manoeuvre and thereby significantly simplifies the blade's structural dynamic behaviour, but

also, as demonstrated in this section, realises self-regulating deployment.

In this section, we propose a novel heliogyro blade concept as shown in Figure 10. The blade is consisted of four sections (from left to right): conventional flat heliogyro blade equipped with RCD, meta-structure spin-up reflector, meta-structure braking reflector, and tip mass. The four sections are joined together by transition structures, which allow the morphing of the meta-structure reflectors while transmitting tensile load.

The meta-structure reflectors can be realised using pre-folded polyimide film, which automatically returns to the origami shape when unconstrained. Alternatively, self-folding smart materials could be used to transform a flat reflective membrane into origami when unrolled from the mandrel. However, the material aspect is not within the scope of this article, and remains for future study.

The function of the meta-structure reflectors are focused on realising self-regulated spin and deployment. Under a static condition as shown in Figure 10, the spin-up reflector generates positive (spin-up) in-plane thrust, which is partially cancelled by the negative in-plane thrust generated by the braking reflector, thus the vehicle will spin-up. At a certain spin rate, centrifugal force stretches the meta-structure reflectors and thereby reduces the in-plane thrusts. However, the tensile strain of the two meta-structure reflectors are different due to the different tensile modulus as well as tensile load. The spin-up reflector, which is designed to have a lower modulus and is under higher tensile load, then generates a much lower spin-up torque that is now fully cancelled out by the negative torque from the braking reflector. Therefore, the spin rate reaches equilibrium under this condition, and a self-regulating spin is achieved. This spin rate will be the final spin rate after the blade is fully deployed.

Meanwhile, as the blade deploys by rolling-off from the mandrel under centrifugal load, the deployment can be passively controlled by the rotational resistance of the

mandrel. When the centrifugal force exceeds a threshold, the mandrel will rotate and a small portion of the blade will be released. Release of the blade increases the angular inertia of the whole vehicle, thereby reduces spin rate and centrifugal force. Therefore, the deployment is self-regulated, and the centrifugal force always equals the rotational resistance of the mandrel under an static condition. This offers a way to design a deployment path, or in other words, a spin rate history throughout deployment, by programming the resistance of the mandrel.

Furthermore, the conventional blade is equipped with a RCD in order to realise attitude control. Such RCD is located on the blade centre chord and only effects the magnitude of SRP without inducing pitching or twisting of the blade. Since the aims of the present study is to demonstrate the self-regulated spin and centrifugal deployment enabled by the meta-structure reflectors, the operation of this RCD is not further discussed.

In order to demonstrate the behaviour of this heliogyro with meta-structure reflectors, a sample design based on NASA's HELIOS vehicle is made and the self-regulated deployment is simulated. The parameters of the proposed design, listed in Table 2, are mostly identical or similar to HELIOS. According to the table, both designs have an initial blade length of $20\,m$ before the main deployment step begins. This initial deployment is carried out while spinning the vehicle up using thrusters, etc. on the vehicle. In the proposed design, all of this pre-deployed $20\,m$ blade is consisted of the meta-structure reflectors.

The simulations are performed using a Newtonian structural dynamic simulator. It captures the in-plane span-wise motion of the four sections of blade during deployment, as well as the vehicle's spin rate. The simplified model used in the simulation is illustrated by Figure 11. In the model, the blade unrolls from the mandrel, which elastically resists the deployment by the force T_{root}. The meta-structure spin-up

Table 2: Design parameters of HELIOS and the proposed heliogyro [11, 14]

Property	HELIOS design parameters	Proposed design parameters
Vehicle mass except blade assembly	$13.3\,kg$	
Vehicle angular inertia except blade assembly	-	$6\,kg \cdot m^2$
No. of blades	6	
Blade chord length	$0.75\,m$	
Full blade length	$220\,m$	
Initial blade length before deployment	$20\,m$	
Length of meta-structure spin-up reflector	-	$18\,m$
Length of meta-structure braking reflector	-	$2\,m$
Initial spin rate before deployment	$1\,RPM$[14] $\sim 5\,RPM$[11]	$1\,RPM$
Final equilibrium spin rate	$1\,RPM$	$1.1\,RPM$
Average sail material density	$1.5\,g/cm^3$	
Sail material	$2.54\,\mu m$ Mylar + $2 \times 0.1\mu m$ Al coatings	
Spin-up reflector substrate material	-	$7\,\mu m$ Kapton + $2 \times 0.1\mu m$ Al coatings
Braking reflector substrate material	-	$25\,\mu m$ Kapton + $2 \times 0.1\mu m$ Al coatings
Blade tip mass	$7\,g$	
Blade batten mass	$3 \times 3\,g = 9\,g$	
Blade assembly mass	$693\,g$	$835\,g$
Blade root tensile load when fully deployed	$1\,N$	$1.4\,N$

reflector is modelled as an homogeneous elastic element, which uniformly elongates under the span-wise tensile load due to the stretch of the origami elements along y-direction. It is worth noticing that in order to achieve a near homogeneous response to the centrifugal-stretch, the span-wise distribution of the origami elements needs to be designed based on the non-uniform tensile stress along the span. This is possible considering the meta-structure's design-able mechanical behaviours. However, the actual design is beyond the scope of the present study. Meanwhile, the meta-structure braking reflector is treated as a rigid panel with constant dimensions and SRP. This is a realistic assumption since the braking reflector is designed to be made of thicker Kapton films in order to prevent elongation and maintain the desired braking SRP force during rotation.

The response of the vehicle's spin rate ω to the total SRP torque M_{SRP} generated by the blades is evaluated as below, where I is the angular inertia of the vehicle including the deployed blades, which changes due to blade deployment and stretch:

$$\dot{\omega} = \frac{M_{SRP}}{I} \tag{13}$$

F_1, F_2, F_3 and F_4 are inertial forces from the four sections including the tip mass (F_4). The forces are evaluated using centrifugal acceleration and translational acceleration associated with span-wise motions, and always satisfies:

$$T_{root} = F_1 + F_2 + F_3 + F_4 \tag{14}$$

Then the mechanical response of the meta-structure spin-up section under a span-wise stretch can be predicted according to Eq. 12:

$$d\,U_{origami} = (F_3 + F_4) \cdot d\,l + F_2 \cdot 0.5 \cdot d\,l \tag{15}$$

From this equation, it can be seen that an effective tensile force, which characterises the tension in the spin-up reflector, can be defined as:

$$T_{effective} = \frac{d\,U_{origami}}{d\,l} = 0.5 \cdot F_2 + F_3 + F_4 \tag{16}$$

According to the results in Figure 7, the mechanical properties of the meta-structure reflector is dominated by the zigzag hinges. For simplicity, elastic force from only the zigzag elements is considered in the simulation. The zigzag elements have parameters of $b = 2.5\,cm$ and $c = 10\,cm$ (based on the design in section 4), thus a $0.75\,m$ blade chord accommodates 6 zigzag elements, which has 11 zigzag hinges. Since the zigzag hinges are aligned along span, which is $18\,m$ according to Table 2, the total hinge length is then $11 \times 18\,m = 198\,m$. Then the elastic energy stored in the origami can be evaluated using Eq. 11, and the mechanical response of the spin-up reflector under span-wise tension can be resolved. Combining with SRP analysis results from section 3, Figure 12 is plotted. It can be seen that a zero

total SRP spin-up torque is generate when $T_{effective} = 0.39\,N$, which is the effective tension at the final target spin rate of $1.1\,RPM$ under a fully deployed condition ($R = 200m$). Therefore, the spin rate will be stabilised at $1.1RPM$ after deployment. This result requires the sum of the origami parameter a of a series of Miura elements along the spin-up reflector's span to be $12.9\,cm$. It should be noted that the final equilibrium spin rate $1.1\,RPM$ is an asymptote that will never be reached under an ideal condition. It is therefore set to be slightly higher than he final target spin rate of HELIOS ($1\,RPM$) to guarantee that $1\,RPM$ can be achieved in a reasonable time.

As discussed above, the deployment process is controlled by T_{root}, since it determines the centrifugal force threshold beyond which the mandrel starts to rotate and release the blade. Here we assume that T_{root} comes from a torque-regulating device which connects the mandrel to the spacecraft. The torque from such device can be "programmed" corresponding to the mandrel's angular displacement, thus corresponding to the length of the deployed blade. Two examples are given in Figure 13. The target spin rate history during deployment is designed by "programmming" the centrifugal force threshold, and the simulation results perfectly agree with the design. However, as shown by Figure 14 and Table 3, the two sets of thresholds yield significantly different time to achieve full deployment. In fact, as the vehicle's angular momentum increases during deployment, the rate of deployment is determined by the spin-up SRP torque generated by the meta-structure reflectors. Therefore, a rapid deployment such as simulation #2 needs a high positive in-plane SRP, which, according to Figure 12, requires a low centrifugal force threshold. Meanwhile, Figure 13b and 14b also shows that the spin rate grows towards the final (equilibrium) spin rate of $1.1\,RPM$ after full deployment is reached.

Therefore, as demonstrated by the simulation, by implementing the proposed meta-structure reflectors on the tips of a heliogyro's blades, a vehicle similar to

Table 3: Summary of simulation results

Case	Spin rate during deployment	Time to full deployment	Condition at day 120
#1	$1\,rpm$	$> 120\,days$	$186\,m$ (partially deployed), $1\,rpm$
#2	$0.5\,rpm - 1\,rpm$	$\sim 24\,days$	$220\,m$ (fully deployed), $1.07\,rpm$

NASA's HELIOS concept can achieve self-regulated spin and passively controlled blade deployment.

6. Challenges and future work

Construction of the meta-structure reflector is a critical challenge to the implementation of the proposed design, and opens up opportunities for future innovations. Either as a pre-folded membrane material that automatically returns to the origami shape when unconstrained, or a smart self-folding material that transforms from a flat sheet into a folded origami, the material system has to resist creeping and fatigue and maintain its elastic properties in the harsh space environment.

Another potential challenge is to minimise the shape error in the origami meta-structures and transition structures (see Figure 10), in order to prevent the built-in twist in the reflector. Although the present study has already pointed out that the SRP thrust is generally robust against a varied AoA, the effect of such a twist on the whole sail blade is still unknown. The design of the material system should also consider this effect.

Last but not least, the analyses in this research is based on a simplified mathematical model without considering the deformation of material due to SRP force, or in other words, the solar-elastic effect. Although such effect is weak considering the rigidity of the origami reflector, its influence on the overall shape and the dynamic behaviours of the sail blades remains to be explored.

7. Conclusions

A meta-structure solar sail reflector, which has tailor-able geometrical, mechanical and optical properties, is designed based on degree-4-vertex origami. Unlike conventional reflectors that are usually treated as simple reflecting devices, the meta-structure reflector can manipulate the direction and the magnitude of Solar Radiation Pressure (SRP) without changing its orientation to the sun. This could prevent structural dynamic issues of large space membrane reflectors such as heliogyro blades, as it enables flight control without inducing overall distortion (twisting) or out-of-plane motion (pitching) of the sail. Furthermore, the origami folding angles varies under in-plane stretching force in a design-able way, thereby realises a stress-dependent SRP, which can be used to enable a more intelligent system.

As an example, a heliogyro concept with passive self-regulated centrifugal deployment is made, which utilises the stress-dependent in-plane SRP thrust from the meta-structure reflector to propel the spinning motion. During deployment, blades are released from a mandrel, and the behaviour of the vehicle is designed by adjusting the rotational resistance of the mandrel as well as the specific design of the reflector. According to structural dynamic simulations, the spin rate of the vehicle automatically follows the pre-designed deployment path defined by the rotational resistance of the mandrel, and after deployment, the spin rate is regulated by the reflector to prevent over-spin. Using tip-mounted reflectors with $20\,m$ span on a vehicle similar to NASA's HELIOS design, the full deployment can be achieved within 24 days at $1\,AU$.

Therefore, a fully passive heliogyro system with self-regulated centrifugal deployment can be realised using the proposed meta-structure reflector.

Reference

[1] B. Fu, E. Sperber, F. Eke, Solar sail technologya state of the art review, Progress in Aerospace Sciences 86 (2016) 1–19.

[2] F. Tsander, The use of light pressure for flight in interplanetary space, problems of flight by jet propulsion, Israel Program for Scientific Translations, Jerusalem, Israel (1964) 303–321.

[3] M. Urbanczyk, Solar sails-a realistic propulsion for spacecraft, Tech. Rep. 67N40314, NASA (1967).

[4] H. Price, J. Ayon, C. Garner, G. Klose, E. Mettler, G. Sprague, Design for a solar sail demonstration mission, in: Space Technology and Applications International Forum, Albuquerque, NM, 2001.

[5] M. Gardsback, G. Tibert, Deployment control of spinning space webs, Journal of guidance, control, and dynamics 32 (1) (2009) 40.

[6] V. Koshelev, V. Melnikov, Large space structures formed by centrifugal forces, CRC Press, 1998.

[7] H. Sawada, O. Mori, N. Okuizumi, Y. Shirasawa, Y. Miyazaki, M. Natori, S. Matunaga, H. Furuya, H. Sakamoto, Mission report on the solar power sail deployment demonstration of ikaros, in: Proceedings of 52nd AIAA/ASME/ASCE/AHS/ASC Structures, Structural Dynamics, and Materials Conference, 2011, pp. 1–11.

[8] Y. Tsuda, O. Mori, R. Funase, H. Sawada, T. Yamamoto, T. Saiki, T. Endo, K. Yonekura, H. Hoshino, J. Kawaguchi, Achievement of ikarosjapanese deep space solar sail demonstration mission, Acta Astronautica 82 (2) (2013) 183–188.

[9] Y. Tsuda, O. Mori, R. Funase, H. Sawada, T. Yamamoto, T. Saiki, T. Endo, J. Kawaguchi, Flight status of ikaros deep space solar sail demonstrator, Acta Astronautica 69 (9) (2011) 833–840.

[10] R. H. MacNeal, The heliogyro-an interplanetary flying machine, Tech. Rep. 67N27627, NASA (1967).

[11] W. K. Wilkie, J. E. Warren, L. G. Horta, K. H. Lyle, J.-N. Juang, J. D. Littell, R. G. Bryant, M. W. Thomson, P. E. Walkemeyer, D. V. Guerrant, et al., Heliogyro solar sail research at nasa, in: Advances in Solar Sailing, Springer, 2014, pp. 631–650.

[12] W. K. Wilkie, J. E. Warren, M. Thompson, P. Lisman, P. Walkemeyer, D. Guerrant, D. Lawrence, The heliogyro reloaded, in: JANNAF Interagency Propulsion Committee Meeting, Huntsville, AL, 2011.

[13] R. S. Blomquist, Heliogyro control, Ph.D. thesis, Carnegie Mellon University (2009).

[14] W. K. Wilkie, J. E. Warren, L. G. Horta, J.-N. Juang, S. C. Gibbs, E. Dowell, D. Guerrant, L. Dale, Recent progress in heliogyro solar sail structural dynamics.

[15] F. J. Kikuchi, S. T. Chujo, T. Y. Shirasawa, F. O. Mori, Windmill torque estimation of spin-type solar power sail with shape control, in: 3rd AIAA Spacecraft Structures Conference, 2016, p. 1218.

[16] P. Wiwattananon, R. G. Bryant, Steering concept of a 2-blade heliogyro solar sail spacecraft, Tech. Rep. NF1676L-24944, NASA (2017).

[17] P. Janhunen, Photonic spin control for solar wind electric sail, Acta Astronautica 83 (2013) 85–90.

[18] P. Janhunen, Electric sail, photonic sail and deorbiting applications of the freely guided photonic blade, Acta Astronautica 93 (2014) 410–417.

[19] D. Guerrant, W. K. Wilkie, D. Lawrence, Heliogyro blade twist control via reflectivity modulation, in: 13th AIAA Gossamer Systems Forum, 2012, pp. 23–26.

[20] Z. You, Folding structures out of flat materials, Science 345 (6197) (2014) 623–624.

[21] C. Lv, D. Krishnaraju, G. Konjevod, H. Yu, H. Jiang, Origami based mechanical metamaterials, Scientific reports 4.

[22] L. H. Dudte, E. Vouga, T. Tachi, L. Mahadevan, Programming curvature using origami tessellations, Nature materials 15 (5) (2016) 583–588.

[23] M. Eidini, G. H. Paulino, Unraveling metamaterial properties in zigzag-base folded sheets, Science advances 1 (8) (2015) e1500224.

[24] E. T. Filipov, T. Tachi, G. H. Paulino, Origami tubes assembled into stiff, yet reconfigurable structures and metamaterials, Proceedings of the National Academy of Sciences 112 (40) (2015) 12321–12326.

[25] H. Fang, S. Li, K. Wang, Self-locking degree-4 vertex origami structures, in: Proc. R. Soc. A, Vol. 472, The Royal Society, 2016, p. 20160682.

[26] H. Fang, S. Li, J. Xu, K. Wang, Locking mechanisms in degree-4 vertex origami structures, in: Proc. SPIE, Vol. 9799, 2016, p. 979910.

[27] P. C. Roberts, P. G. Harkness, Drag sail for end-of-life disposal from low earth orbit, Journal of Spacecraft and Rockets 44 (6) (2007) 1195–1203.

[28] J. Kingston, S. Hobbs, P. Roberts, C. Juanes-Vallejo, F. Robinson, R. Sewell, B. Snapir, J. V. Llop, M. Patel, Use of cypres cutters with a kevlar clamp band for hold-down and release of the icarus de-orbit sail payload on techdemosat-1, Acta Astronautica 100 (2014) 82–93.

[29] V. Melnikova, A. Borovikov, M. Koretskii, Y. Smirnova, E. Timakova, Z. Yu, A. Kuznetsov, K. Frolov, S. Tenenbaum, D. Rachkin, et al., Nanosatellite aerobrake maneuvering device, arXiv preprint arXiv:1708.07417.

[30] J. M. Gattas, W. Wu, Z. You, Miura-base rigid origami: parameterizations of first-level derivative and piecewise geometries, Journal of mechanical design 135 (11) (2013) 111011.

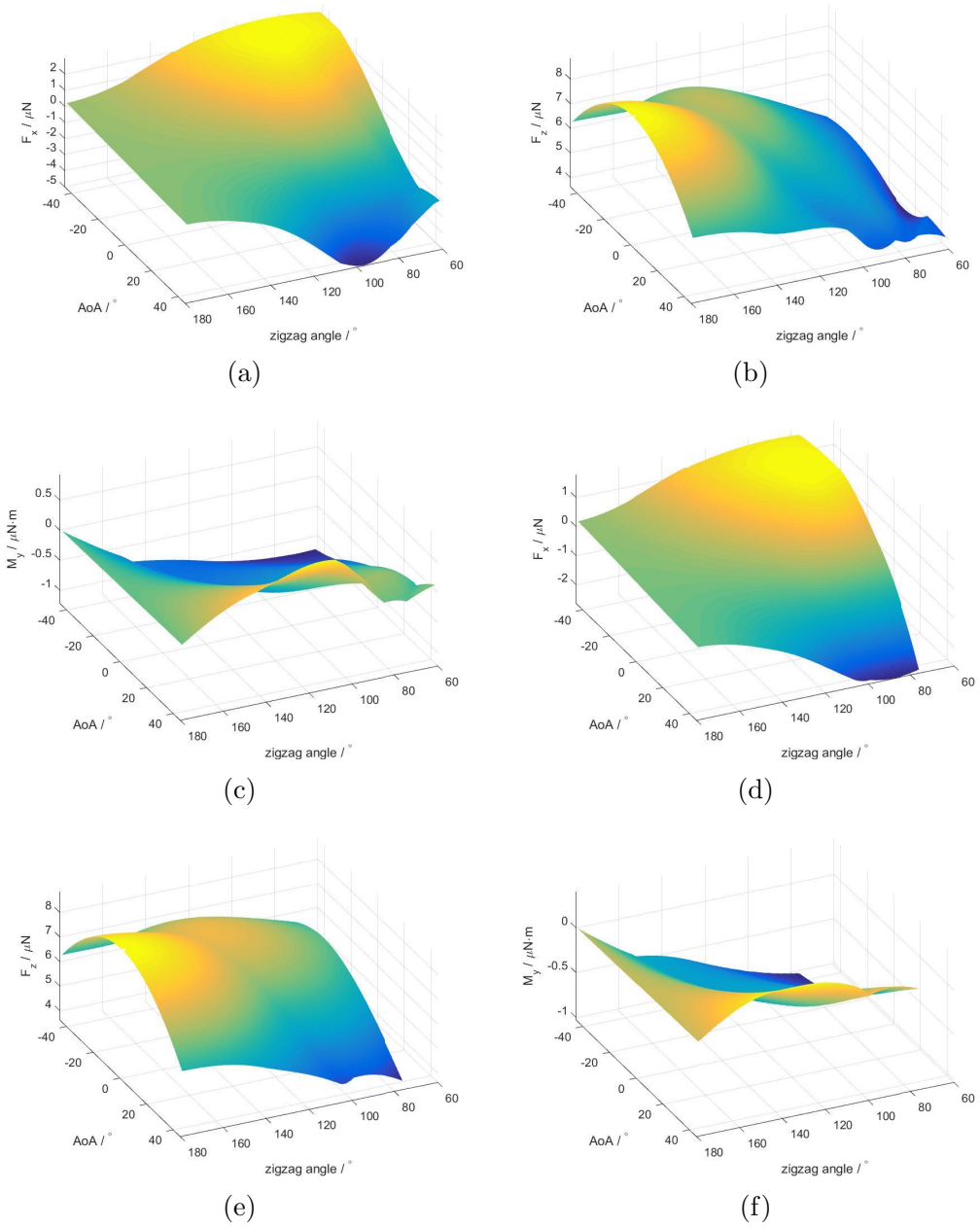

Figure 4: Simulation results on the SRP-induced forces/moment generated from the zigzag origami element with (a)-(c) $b/c = 0.5$, and (d)-(f) $b/c = 0.25$, where the torque M_y is evaluated by assuming $b + c = 1\ m$, note that the small fluctuations/discontinuities in the curve are associated with multiple reflections between the origami panels

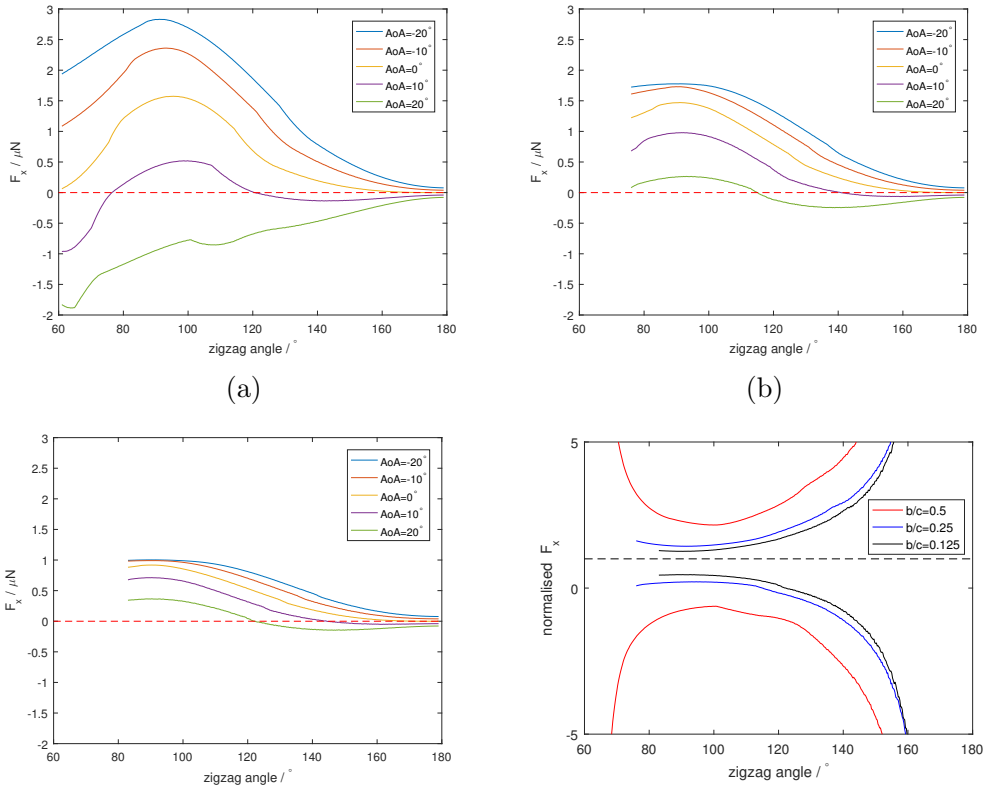

Figure 5: In-plane thrust F_x generated from the zigzag origami element at five different AoAs with (a) $b/c = 0.5$, (b) $b/c = 0.25$, and (c) $b/c = 0.125$, showing that a low b/c ratio gives robust instantaneous in-plane thrusting against AoA oscillation, this is also illustrated in (d), which shows the F_x generated at $\pm 20°$ AoA normalised by the value at $0°$, note that the small fluctuations/discontinuities in the curve are associated with multiple reflections between the origami panels

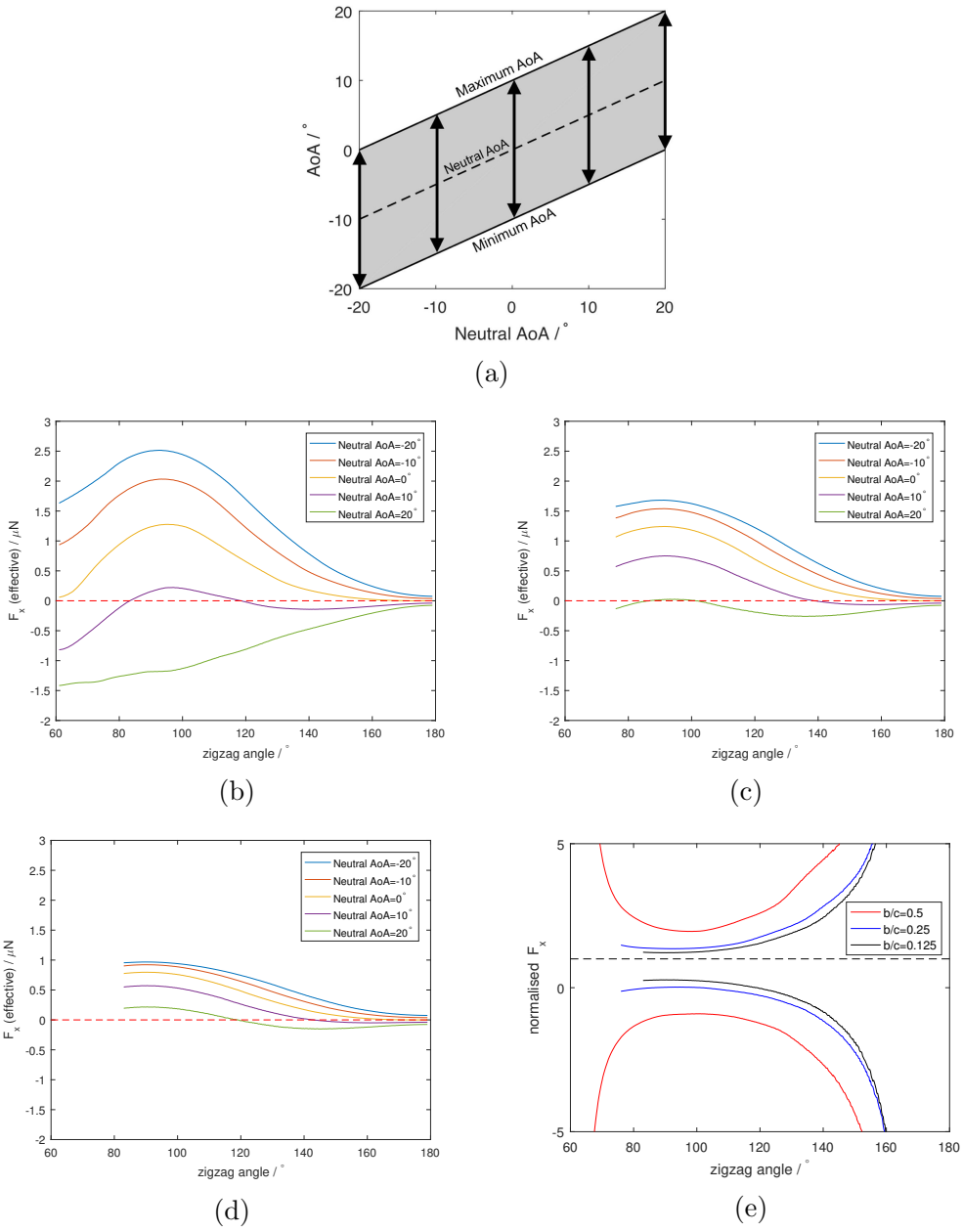

Figure 6: Time-average of the in-plane thrust generated under oscillating AoAs with five different neutral values and an amplitude of $\pm 20°$ as illustrated by (a), with (b) $b/c = 0.5$, (c) $b/c = 0.25$, (d) $b/c = 0.125$; and (e) plots the F_x generated at $\pm 20°$ AoA normalised by the value at $0°$; showing similar results to Figure 5, thus the effective in-plane thrust is robust against AoA oscillation

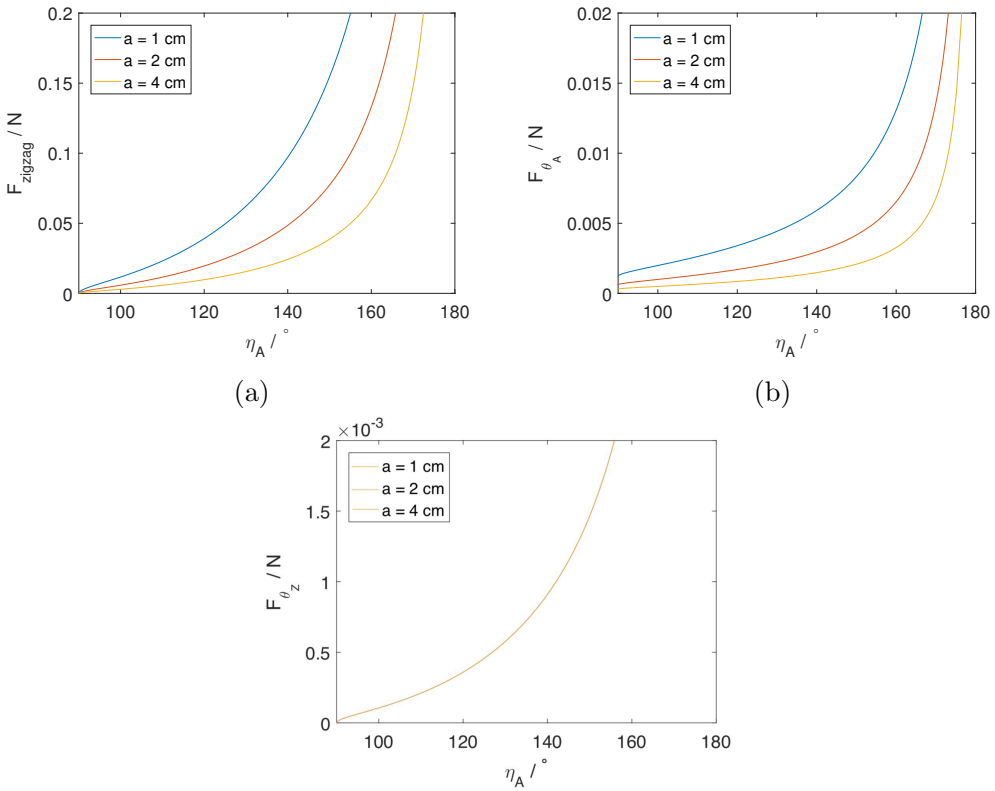

Figure 7: Elastic recovering force F from an origami module stretched along y-direction, evaluated with three different values of a, showing that the elastic property is dominated by the zigzag element (note the difference in axis scaling), (a) force generated from the zigzag element, (b) force generated from the hinges associated with θ_A, which is one order of magnitude lower than F_{zigzag}, (c) force generated from the hinges associated with θ_Z, which is two orders of magnitude lower than F_{zigzag}, note that the three curves overlaps in (c)

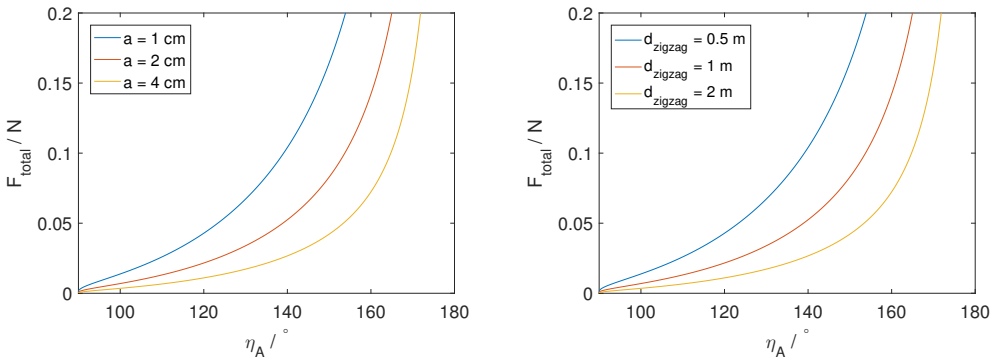

(a) (b)

Figure 8: Total elastic recovering force F from an origami module stretched along y-direction, showing that the elastic property can be tailored, (a) with $d_{zigzag} = 1\,m$ and a varied, (b) with $a = 2\,cm$ and d_{zigzag} varied

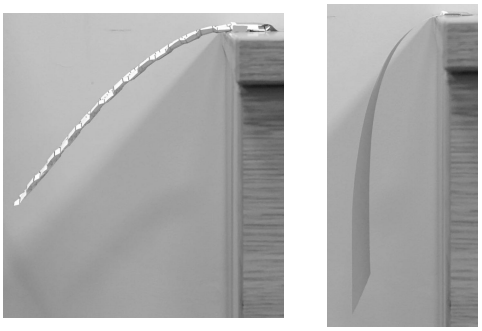

(a) (b)

Figure 9: Besides achieving desired optical and morphing properties, the origami also have higher out-of-plane rigidity after folding, as illustrated by paper prototypes cantilevered in $1g$: (a) partially folded origami, (b) flat paper

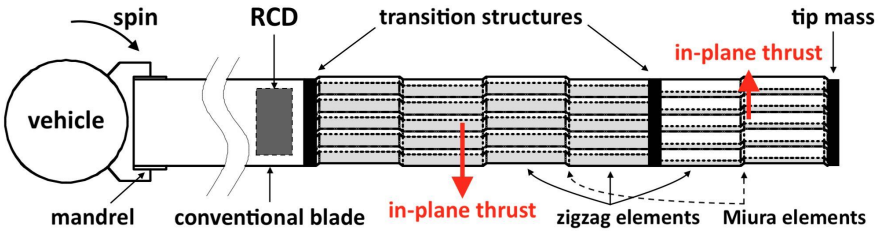

Figure 10: The proposed heliogyro blade concept which achieves passive closed-loop control of centrifugal deployment; the blades is consisted of a conventional flat blade equipped with RCDs, two sections of meta-structure reflectors with different in-plane thrusts and tensile modulus, and a tip mass, joined together by transition structures; note that the vehicle is axisymmetric, though only one blade is shown in this draft

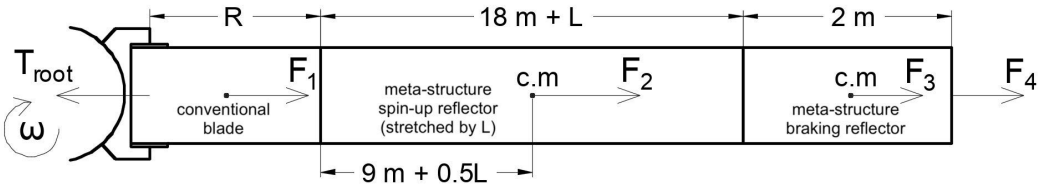

Figure 11: Simplified model for the structural dynamic simulations, where the meta-material spin-up reflector is treated as a homogeneous elastic element that elongates by L under load to simulate the stretch-induced unfolding of the origami, and the meta-material braking reflector is treated as rigid since it is designed to be made of stiffer materials, the inertial forces F_1, F_2, F_3 and F_4 as well as the force from the mandrel T_{root} are shown in this figure (c.m. stands for centre of mass)

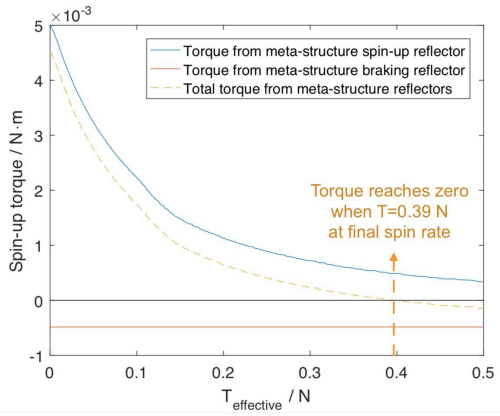

Figure 12: Tension-dependent Spin-up torque generated by the two meta-structure reflectors, which enables the torques to cancel out when reaching the final target spin rate of 1.1 RPM and therefore achieve self-regulated spin

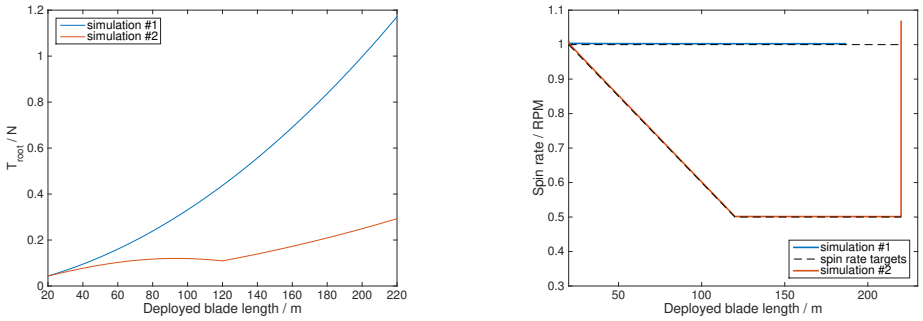

(a) (b)

Figure 13: The simulations use two sets of centrifugal force thresholds, which are "programed" in order to give a certain spin rate history during deployment, where # 1 gives a constant spin rate during deployment, and # 2 allows a more rapid deployment, (a) the two sets of centrifugal force thresholds, (b) the simulated spin rate histories, which match the design targets, note that the full deployment of $220\,m$ is not achieved at the end of simulation #1 (at day 120), while full deployment is achieved in simulation #2, after which the spin rate increases toward the final target of $1.1\,RPM$

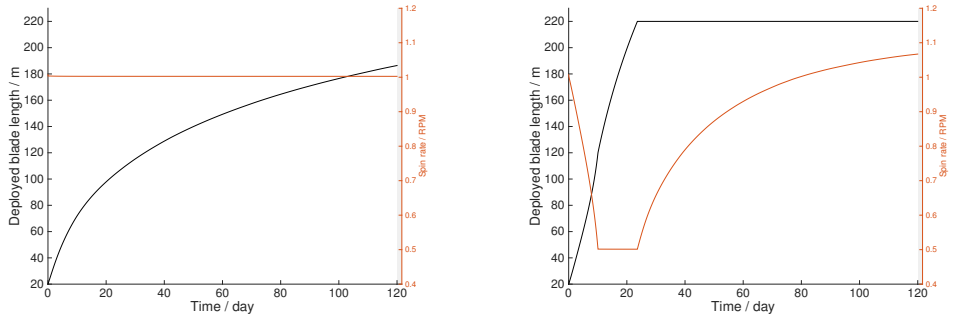

(a) (b)

Figure 14: The simulation results showing the deployed blade length and spin rate histories plotted against time, (a) simulation #1, in which $186\,m$ of blade is deployed after 120 days, (b) simulation #2, in which full deployment is achieved within 24 days

Chapter 6

Self-formation of origami meta-structure reflector

Fully passive operation of the heliogyro discussed in Chapter 5 requires a method to automatically transform a 2D reflective sail membrane into the 3D meta-structure reflector. This chapter is based on a submitted paper, which proposed a self-folding membrane that is based on space-qualified materials and is potentially mass-producible. It utilises an innovative "kirigami hinge" design to overcome the issues faced by other self-folding materials, while realising a lightweight design. Meanwhile, the heat activated folding of an origami sheet is successfully demonstrated in lab. According to analytical thermal radiation analysis, automatic folding upon exposure to sunlight is feasible, and only requires conventional spacecraft thermal control coatings.

6.1 Paper V: Sunlight-activated self-folding material

Rigidisation of Deployable Space Polymer Membranes by Heat-Activated Self-Folding

Authors: Rui Wu, Peter Roberts, Shida Lyu, Constantinos Soutis, Fei Zheng, Carl Diver, Matthieu Gresil, Jonny J Blaker

Journal: Smart Materials and Structures, (**Impact factor: 2.909**)

Publication date: September 2018

Statement of own contributions in joint authorship:

Main research idea and technological development;

Preparation of tables, figures, and the manuscript;

Design of the "kirigami" hinge structure and the semi-automatic processing technique;

Prototyping and testing of the self-folding hinge, origami sheet and the deployable boom;

Analytical thermal radiation and mechanical analyses.

Rigidisation of Deployable Space Polymer Membranes by Heat-Activated Self-Folding

Rui Wu[1], Peter C.E. Roberts[1], Shida Lyu[2], Constantinos Soutis[2], Fei Zheng[3], Carl Diver[1], Matthieu Gresil[2,4] and Jonny J Blaker[3]

[1] School of Mechanical, Aerospace and Civil Engineering, the University of Manchester, UK

[2] The University of Manchester Aerospace Research Institute, UK

[3] School of Materials, the University of Manchester, UK

[4] i-Composites Lab, School of Materials, The University of Manchester

E-mail: rui.wu@manchester.ac.uk

Abstract. Current gossamer space structures such as solar sails usually rely on bracing structures, inflation gas, or centrifugal force to deploy and maintain a structural shape, which leads to a system that is sometimes complicated, while a concise system can be achieved if the gossamer structure could self-rigidise and support load. The present study proposes a self-folding polymer membrane based on space-qualified materials and is potentially mass-producible by industrial roll-to-roll processes. It can permanently transform a flat gossamer membrane into a load-bearing 3D configuration when heated by sunlight in space, while the folding-induced shape bifurcation and buckling are prevented using a kirigami hinge design. The shape transformation is demonstrated in lab by a tubular and an origami structure that are formed from a flat membrane when heated to $82\,^{\circ}C$ in oven. Thermal

radiation analyses have also verified the feasibility of sunlight-activated folding in space when vapour-deposited metallic coatings are applied onto the hinges. The proposed material offers a new generation of gossamer space membrane that can automatically morph from a stowed configuration to a load-bearing structure, and potentially provide built-in functionalities.

Keywords: active material, smart material, morphing, bi-stable, meta-structure, kirigami

Nomenclatures

D: flexural rigidity

E: Young's modulus

I: second moment of area

Q: heat transfer

q_s: solar constant = $1.36\,kW/m^2$

T: temperature

α: surface absorptivity

ϵ: surface emissivity

σ: Stefan-Boltzmann constant = $5.67 \times 10^{-8}\,W \cdot m^{-2} \cdot K^{-4}$

1. Introduction

Various space missions require the deployment of gossamer structures, or in other words, large structures with high flexibility and ultra-low-mass [1, 2], such as the reflective membrane of solar sails [3, 4], drag sails [5], and reflectors for communication antennae or space telescopes [6, 7]. Due to the very limited flexural rigidity of thin membrane materials, their in-space deployment is usually achieved using rigidisable deployable booms that drive the unfolding and constrain the out-of-plane deflection during deployment, whilst achieving load-carrying capability when fully deployed [8]. Efforts have also been made to let the membrane deploy and support itself without bracing structures: the fibrous material called microtruss fabric can elastically return to a flat shape when unrolled from a mandrel, while having low surface density owing to its porosity [9]; inflatable structures utilise an inflation gas to carry compressive structural load and a bladder made of membrane material to carry tensile load [10, 11]. Alternatively, centrifugal force has been proposed to deploy and stiffen gossamer structures, including antennae and solar sails [12, 13, 14]. Such a centrifugal deployment removes the bracing structures and therefore significantly reduces the structural mass and improves packing ratio, though the structural dynamic behaviours can be complicated and problematic [15, 16]. Furthermore, it has also been reported that a self-rigidisable membrane material could assist the structural performance of those deployable structures: inflatables could benefit from self-rigidising composite bladders that allows the structure to stay rigid after inflation without maintaining the gas pressure [17, 18, 19]; heliogyro, a helicopter-rotor-like centrifugally deployed solar sail could use reinforcing battens

to improve dynamic behaviours [20], and a self-assembling batten structure, which utilises a sheet material that automatically rolls up into a slender tube due to residual stress, has been proposed [21].

On the other hand, self-folding sheets based on smart materials which fold up along pre-defined hinges under external stimulus have attracted great interests from researchers during the last decade, as it provides a method to convert a 2D sheet into a 3D device. Such a device not only achieves load-carrying capacity, but also could provide highly design-able behaviours and serve as a building block of future meta-structures [22, 23, 24, 25, 26]. If mass-produced using space-grade materials, it could lead to a new generation of deployable gossamer structures with self-rigidising features and potentially more built-in functionalities. As an example, previous study has proposed an origami-inspired meta-structure reflector for heliogyro solar sail, which can be formed by folding a 2D film. Utilising its tuneable optical properties and enhanced structural rigidity, a concise and robust heliogyro system with passive self-regulation can be realised [27].

Self-folding is usually activated using active materials that expand/shrink when stimulated by heat, light, moisture, etc., while the folding (i.e. bending) deformation is achieved by differential expansion/shrinkage through the sheet's thickness. Such a differential activation can be realised by either an unsymmetrical stimulus [28] or a double-layer material layup [22, 29, 30, 31]. Meanwhile, the folding induced by an isotropic expansion/shrinkage with a through-the-thickness gradient that is homogeneous across the sheet leads to bifurcation of the final shape (Figure 1), or in other words, the folding can be along any direction [32, 33]. Therefore, a

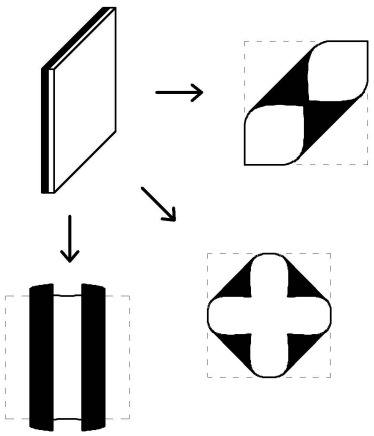

Figure 1: Activation of an isotropic bilayer sheet leads to bifurcation, creating different folded shapes; the white layer is isotropically shrinking.

precisely controlled crease pattern requires either an anisotropic active material that expands/shrinks perpendicularly to the hinge line, or an anisotropic flexural rigidity with softened crease lines.

Homogeneous sheet materials with residual tensile stress, which soften and shrink when heated up, can be used to construct self-folding devices (Figure 2a). The temperature gradient leads to different levels of relaxation (thus shrinkage) through the thickness and therefore, activates the folding. Meanwhile, the bifurcation shown in Figure 1 is prevented by localised heating (thus softening) using a laser or light-absorbing ink [34, 35, 36]. In this case, bifurcation is prevented by anisotropic flexural rigidity. Alternatively, illuminating the sheet material by an ultraviolet light while applying a temporary in-plane unidirectional stretch, then the illuminated side will relax, and a unidirectional compressive stress will build up when the stretching force is removed. When a photo mask is used to constrain the light on certain crease

lines, the sheet can be "programmed" to fold into a certain shape [37]. In this case, bifurcation is prevented by anisotropic stress.

Furthermore, various concepts have been proposed utilising a multi-layer architecture. Thin metallic (chromium, copper and nickel) layers bonded onto each other using vapour deposition, lithography and electrodeposition could realise a thin sheet that precisely folds along an origami pattern. The chromium layer with residual stress left by the deposition process actuates the folding of a copper layer, and an anisotropic flexural rigidity is built into the sheet using the reinforcing nickel layer [38, 39, 40]. However, the products are usually at submillimeter size and can not be easily scaled up. Na, Evans et al. [41] have provided an attractive solution (Figure 2b), where a heat shrinking polymer membrane is sandwiched and bonded between two thermally stable polymer membranes, making a trilayer structure. Hinges can be made by cutting off a strip from one of the outer membranes, leaving a bilayer structure at the hinge. The bilayer parts bend when heated up, while the trilayer sections are constrained by the thermally stable membranes thus remains flat. Meanwhile, the removed strip also leads to a region with low flexural rigidity and prevents bifurcation.

The present study focuses on developing a self-folding thin membrane that can be rolled-up into a cylinder to minimise storage volume, then activated by heat radiation from the sun when unrolled in space. Due to the low sheet thickness and varying lighting conditions, folding by a differential stimulus through its thickness (Figure 2a) is not practical, thus a multi-layered architecture is chosen. The trilayer sheet (Figure 2b) developed by Na, Evans et al. [41] offers a viable solution, but

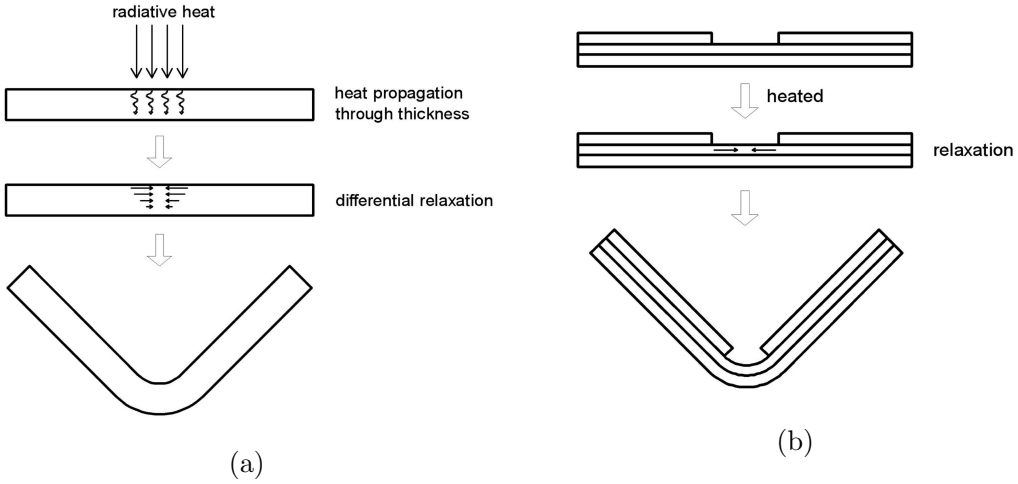

Figure 2: Two types of existing self-folding membranes, (a) folding induced by differential relaxation through the thickness, (b) folding enabled by multi-layered structure based on designs from [41].

a heavier structure compared to Figure 2a, which makes it unsuitable for certain applications such as solar sails [3].

In the present study, a self-folding Mylar/Kapton composite laminate with kirigami hinges is designed while keeping space application and industrial production in mind.

2. Design of the self-folding kirigami hinge

The proposed design uses a thermally stable DuPont™ Kapton® membrane as the substrate. An isotropic heat shrinking DuPont™ Mylar® HS film (supplied by UK Insulation Ltd) is the active layer, which is bonded onto the Kapton using 3M™ Adhesive Transfer Tape 966. The properties of the three materials are listed in Table

1 according to manufacturer datasheets. Kapton® is a polyimide, and DuPont™ Mylar® is made from stretched polyethylene terephthalate (PET), both have been used in space applications. Mylar® HS, where "HS" stands for Heat Shrink, is not heat stabilised and will shrink with considerable force when heated up. The 3M™ Adhesive Transfer Tape 966 is made from 3M™ High Temperature Acrylic Adhesive 100, which is a gel-like soft material with low "outgassing" properties.

Table 1: Materials associated with the presented self-folding membrane design.

Material	$T_g/^\circ C$	Thickness	Modulus/GPa	UT Strength/MPa	UT Elongation	Shrinkage/%	Operating temp.
Kapton® HN	360∼410	25 μm	5 (-196°C) 2.5 (23°C) 2 (200°C)	300 (-196°C) 230 (23°C) 140 (200°C)	19% (-196°C) 72% (23°C) 83% (200°C)	0.17 (150°C) 1.25 (400°C)	-269∼400°C
Mylar® HS	80	16 μm	3.1 (23°C)	210 (23°C)	115 (23°C)%	50 (100°C)	-
Mylar®	80	12-38μm	6.9 (-70°C) 3.4 (23°C) 0.14 (200°C)	200 (-70°C) 160 (23°C) 70 (200°C)	55% (-70°C) 104% (23°C) 135% (100°C)	1.8 (150°C)	-250∼200°C
966 acrylic	-	60 μm	gel-like	-	$\gg$100% (23°C)	-	-40∼232°C

In the present design, Mylar HS is only placed where it is needed: on the kirigami hinges, which guarantees the highly efficient use of the material. Bifurcation is prevented by kirigami structures in the Mylar and adhesive layers that allow the stress along the hinge line to relax, providing a near unidirectional shrinkage that drives the folding. As shown by Figure 3a, a strip of Mylar HS is bonded onto Kapton using the acrylic adhesive. The adhesive is in the form of a transfer tape and therefore has a consistent thickness. Then, through-thickness slits are cut into the Mylar and the adhesive layers using an automatic cutting machine (the detailed process is discussed later in section 3). For the convenience of manufacturing, the slits are not cut throughout the width of the hinge, so that the Mylar strip remains continuous. When heated up, Mylar shrinks and opens the slits (Figure 3b),

generating shear strain between Mylar and Kapton, which is accommodated by the flexible adhesive. The opened slits effectively relaxes the shrinkage along x-direction, while the relaxation along y-direction is minor since the Mylar strip's width is higher than (in this case, three times of) the separation between the slits. The membrane thereby folds along the hinge under the y-shrinkage without bifurcation.

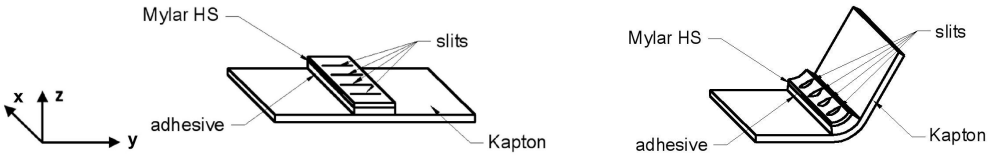

(a) (b)

Figure 3: Schematic draft of the proposed design, containing Kapton substrate and Mylar HS film bonded together through acrylic adhesive, and slits are cut into Mylar and adhesive; (a) a kirigami hinge before activation, (b) a kirigami hinge that after heating, the slits are opened by the shrinking force and the stress along x-direction is relaxed, creating an anisotropic shrinkage that folds the membrane along the hinge

However, a tape-spring-type buckling [42] has been observed in test samples (Figure 4a). This is the result of a reversed bending deformation perpendicular to the hinge line triggered by initial unflatness of the membrane, thus will not occur under an ideal condition. Figure 4a also suggests that the reversed bending is facilitated by the slits, which lead to local low bending rigidity and high surface curvature, both are adverse to the recovery from the buckled shape.

Therefore, the kirigami hinge is modified with staggered slits (design 2 in Figure 4d) to prevent a through-width reversed bending and thereby reduce its tendency

to buckle. However, fully preventing buckling still requires the membrane to be generally flat when folding is activated, which is discussed in section 5.

The hinge design shown in Figure 4 provides a hinge folding angle close to 180°, which is the maximum folding angle that an origami may require. The folding angle can be seen from Figure 7b.

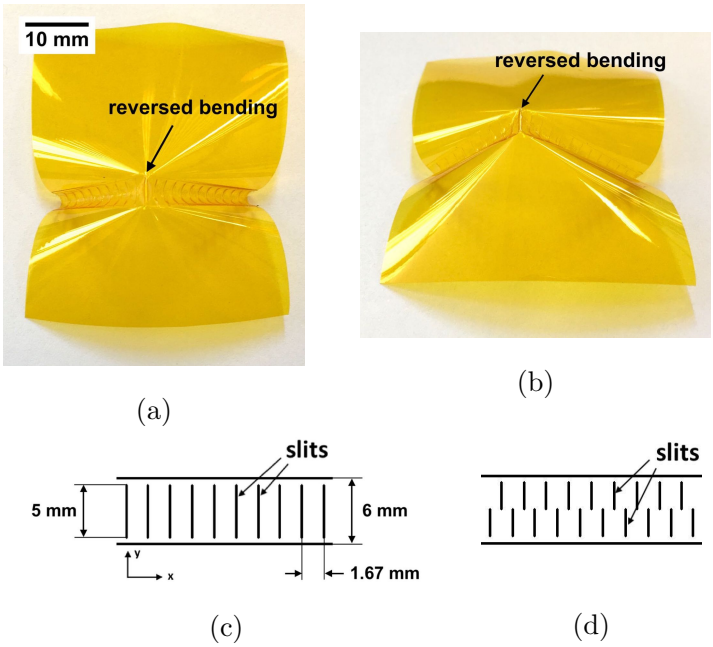

Figure 4: Design iteration of the kirigami hinge, (a)(b) tape-spring-type buckling of a design 1 kirigami hinge triggered by a reversed bending deformation along a slit, viewed from different angles, (c) design 1 that leads to high tendency of buckling due to the low bending rigidity along a slit, (d) design 2 with staggered slits that offers enhanced flexural rigidity and reduces the tendency of buckling.

3. Production of the self-folding membrane

Test samples are fabricated using a partially automatic method. As illustrated by Figure 5b, the production starts with a Mylar HS film bonded to an adhesive transfer tape 966 with a liner adhered to the other side (step 1). Then the layup is loaded onto a CNC (Computer Numerical Control) cutting machine (Figure 5a), which uses a blade to cut the input pattern (hinges profiles and slits) into the Mylar-adhesive layers while leaving the liner mostly intact (step 2). After cutting, the unwanted parts (scrap materials outside the hinge regions, Figure 6b) of the Mylar-adhesive layers are manually removed, leaving only the hinges (step 3). Then the remaining Mylar-adhesive layers are transported from the liner onto Kapton using a vinyl transfer tape with low adhesion (step 4-6). Then the above steps are repeated on the other side of the Kapton (step 7).

This semi-automatic method can be converted to a fully automatic roll-to-roll process. Such a process could enable a cost-effective rapid production of the self-folding membrane and make its large-scale applications feasible. As shown by Figure 6, the process is based on the same steps as in the semi-automatic method (Figure 5). In order to allow the scrap to be easily lifted off from the liner in step 3, the pattern cut into the Mylar and adhesive layer in step 2 can be designed to form one continuous piece of scrap as shown by Figure 6b.

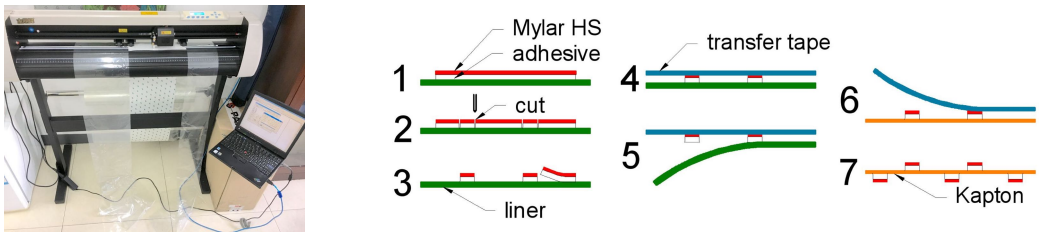

(a) (b)

Figure 5: The semi-automatic method used to fabricate test samples, (a) the CNC pattern cutting machine, (b) the detailed process steps: 1-Mylar+adhesive layer prepared on a liner, 2-pattern cut by the CNC machine, 3-unwanted part removed, leaving only the hinges, 4-transfer tape applied to the top of the Mylar layer, 5-liner removed from the adhesive layer, 6-Mylar-adhesive layer transferred to Kapton, and transfer tape is removed, 7-repeating process 1-6 on the other side of Kapton.

4. Folding behaviour of the kirigami hinge

Folding is activated using an oven where heat is transmitted to the sample by forced air convection at $85°C$, which is slightly higher than the glass transition temperature of Mylar HS ($T_g = 82°C$). It was observed that the hinges without slits failed to fold along the hinge line due to bifurcation (Figure 1), while the kirigami hinges folded successfully after $\sim 0.5\,min$ of heating (Figure 7).

The effect of heating duration is studied by measuring the average shrinkage of the Mylar HS layer at different heating times (Figure 8 and Table 2). Results in Table 2 suggest that the folding is completed after $0.5\,min$, with no significant shrinkage observed when heating is extended to $6.5\,min$. The hinge remains in a stable folded configuration after repeated heating and cooling, which is crucial for

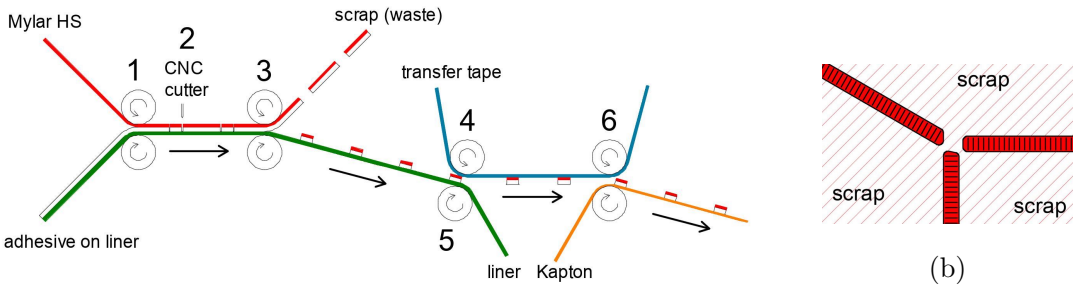

(a) (b)

Figure 6: The fully automatic roll-to-roll production method converted from the semi-automatic method, (a) the basic process: 1-Mylar rolled onto adhesive on liner, 2-pattern cut by the CNC machine, 3-scrap part removed, leaving only the hinges, 4-transfer tape rolled onto the top of the Mylar layer, 5-liner removed from the adhesive layer, 6-Mylar-adhesive layer transferred to Kapton, and transfer tape is removed, then the process 1∼6 can be repeated on the other side of the Kapton, (b) a typical pattern (thick black lines) cut by the CNC machine, which leaves the scrap in one piece to assist waste removal.

its space application.

Furthermore, it appears that the shrinkage of Mylar HS has become anisotropic due to relaxation at the densely distributed slits, with more distortion along the x-direction. The y-shrinkage is lower since it is resisted by the Kapton film, and thus induces a higher residual stress after shrinkage. This residual stress enforces a primary folding direction along the hinge line which prevents bifurcation.

It worth noticing that the results reported in Table 2 are measured while the hinge is held flat. Such constraint will slightly reduce the y-shrinkage, but this does

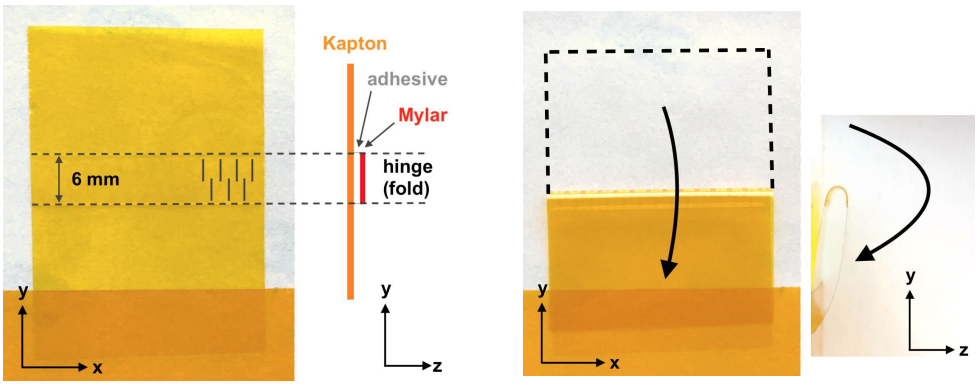

(a) (b)

Figure 7: Test sample with kirigami hinge with hinge design illustrated, (a) before heating, (b) after heating at $85°C$ for $0.5\,min$, the kirigami hinge successfully folds along the hinge line.

Table 2: Anisotropic shrinkage of the Mylar HS layer evaluated from Figure 8.

Heating time	Shrinkage along y	Shrinkage along x
$30\,s$	22%	35%
$1.5\,min$	27%	39%
$6.5\,min$	30%	40%

not affect the discussion above considering the large differences between the x and y-shrinkage.

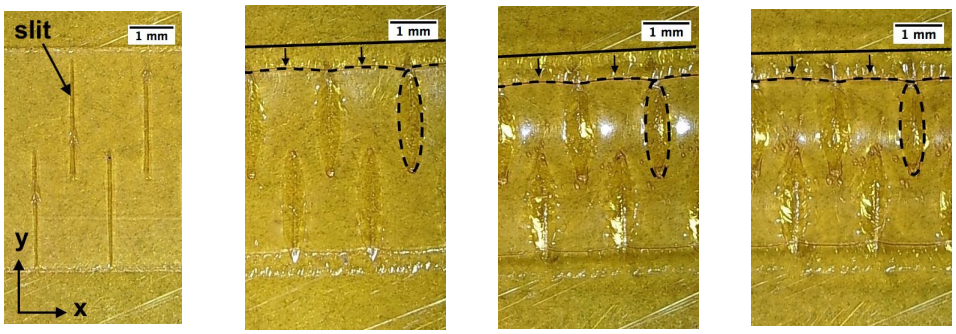

(a) (b) (c) (d)

Figure 8: Optical microscopic images of the kirigami hinge (hinge lies along x-direction): (a) before heating, (b) after $t = 0.5\,min$ of convective heating at $85°C$, (c) $t = 1.5\,min$ at $85°C$, (d) $t = 6.5\,min$ at $85°C$ (the dotted lines illustrate the expansion of the slits due to the Mylar shrinkage), note that the hinge is held flat while the images are taken.

5. Experiment on a self-folding origami sheet

This section demonstrates that the heat-activated kirigami hinge can be used to realise a new type of gossamer structure based on self-folding origami. Current gossamer structures are usually packed and stored as a folded origami, and then deploy and achieve the target shape under external supporting forces. However, the folded origami offers limited packing ratio especially for very large membranes, while keeping the membrane flat and rolling it onto a mandrel could realise the optimum packing. Therefore, we propose a gossamer structure that is stored as flat by winding into a cylinder and automatically fold along an origami crease pattern when unrolled and heated. This is illustrated by Figure 9 (not to scale), where the 2D film is stored

on a mandrel, unrolled, and then folded. As mentioned in the introduction, this folded 3D configuration not only self-rigidises, but also has the potential to provide design-able properties and built-in functionalities of origami meta-structures. The origami reported in Figure 10 and 11 is based on an optical meta-structure solar sail reflector reported in a previous study [27]. It is designed to induce tuneable optical properties while achieving self-rigidisation. This origami uses a rigid-foldable non-flat degree-four vertex pattern with self-locking behaviour [43, 44, 45], which can be regarded as a variation of Miura-origami pattern [46, 47]. The detailed design is available from the previous paper [27].

Folding of an origami is naturally more predictable than a stand-alone hinge, since origami has limited degrees of freedom (the folding of origami creases are coupled). However, as shown by Figure 10, the methods preventing bifurcation are still necessary. The No. 1 membrane in the figure has hinges without slits, and the origami is barely folded due to the stress concentration in the Kapton regions where multiple hinges intersect. The No. 2 membrane is similar to No. 1, but holes are cut into the Kapton layer at the intersections of hinges to prevent stress concentration. It shows better folding behaviour, but bifurcation occurs in most of the hinges, leading to shape errors. The No. 3 and the No. 4 (a scaled-up version of No. 3) membranes use the design 2 kirigami hinges, and both fold as designed.

To prevent the tape-spring buckling as mentioned in section 2, all the samples shown in Figure 10 are heated while being constrained on a flat plate in order to guarantee the initial flatness of the membrane. The detailed activation process is described according to Figure 11. At the beginning (Figure 11a), the membrane is

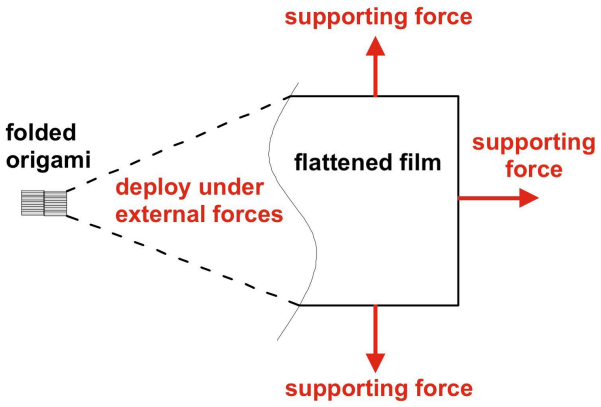

(a)

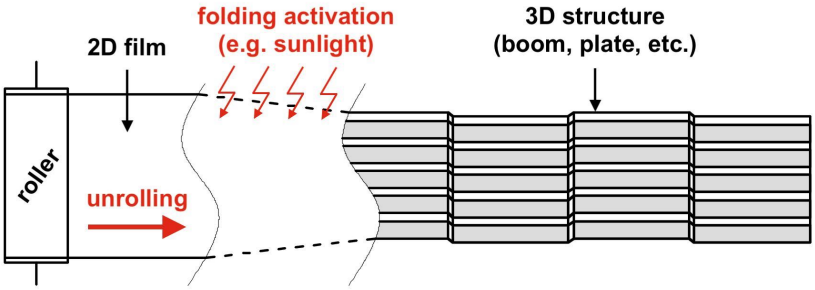

(b)

Figure 9: Unlike the conventional gossamer structures that are packed as folded origami and deploy by flattening under supporting forces (as illustrated in (a)), we propose a new solution (illustrated in (b)), where the gossamer structure is stored as flat by winding onto a roller, which maximises the volumetric packing ratio; then released by unrolling, and transformed into a 3D configuration by self-folding; the 3D structure can be designed to support load, and also provide built-in functionalities of origami meta-structures (sketches not to scale).

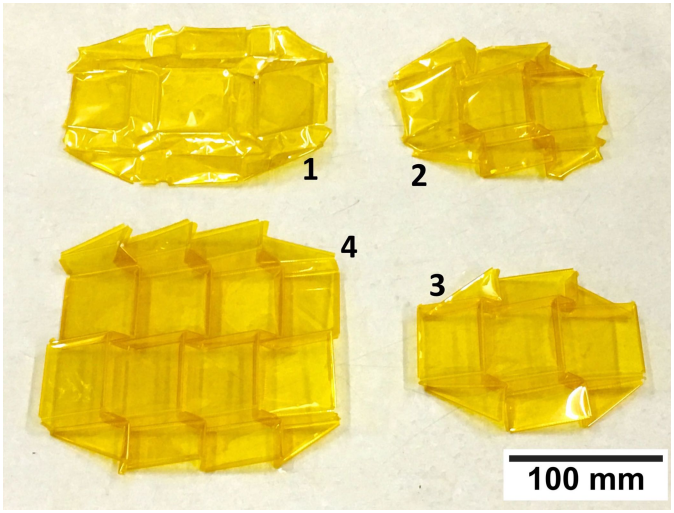

Figure 10: The self-folding membrane with a 4-vertex origami pattern, where 1: with no slits in the hinge, which barely folds along the origami pattern, 2: similar to 1 but with holes at the intersections of hinges to prevent stress concentration, which folds with significant shape error due to bifurcation at hinges, 3: similar to 2 but with kirigami hinges, which folds as designed, 4: a larger version of 3, which is also properly folded.

loosely bonded onto the flat plate at edges while leaving space for shrinkage. Then the first activation step is carried out by heating the membrane, together with the plate, in the oven at $85°C$ for $5\,min$. The membrane is then removed from the oven (Figure 11b). It can be seen that all the hinges are curved, while no bifurcation or buckling are observed. Owing to the rigidising effect of the curved hinges, the membrane can be set free from the flat plate with no risk of further bifurcation or buckling. As shown by Figure 11c, the origami is cut off from the plate, and then reheated for another $5\,min$. The final result (Figure 11d) shows that the origami is

fully folded.

The reason why such out-of-plane constraint (from the flat plate) is necessary is discussed here. Since an ideal origami has only one degree of freedom, while a flexible membrane has infinite degrees of freedom due to its flexibility, a film with initial defect is likely to enter a state with a "wrong shape" if no external out-of-plane guiding force was applied [26, 48]. Automatic recovery to the target shape is hindered by a strain energy barrier between the "wrong shape" and the target shape [49, 50]. Although the hinge design with staggered slits (Figure 4d) has significantly improved the resistance to local buckling, it has limited contribution to the overall behaviour of a complex origami. However, by constraining the out-of-plane deformation (or in other words, the folding angle), the strain energy barrier between different shapes can be reduced [51], thus the target shape, which has the lowest strain energy, will finally emerge. The speculative discussion above only describes the behaviour superficially, and more rigorous study is still required to understand such problem.

To summarise, by utilising the kirigami hinge design and keeping the membrane generally flat during the initial activation, bifurcation and buckling can be prevented. In real applications, parallel constraining plates, centrifugal force or mechanical tensioners can also be used to guarantee the flatness of membrane during the early stage of deployment and realise a flawless folding.

6. Experiment on a self-forming tube

Deployable tubular structures (booms) that can be rolled-up when flattened and then deploy to achieve high specific structural stiffness can be used as a universal

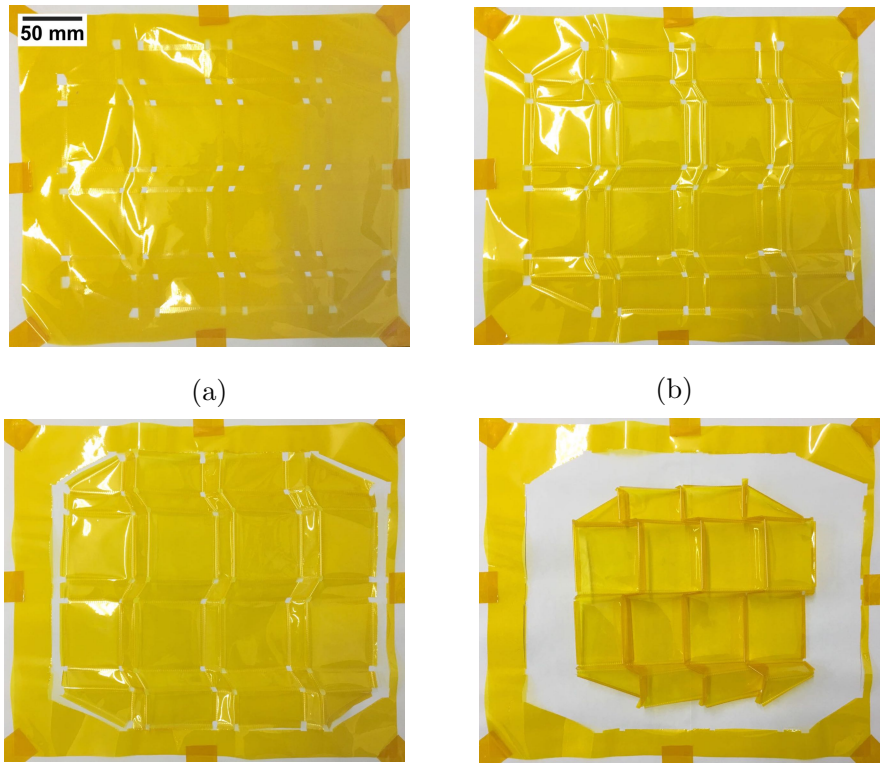

Figure 11: Process to activate the self-folding origami sheet: (a) the membrane is loosely bonded onto a flat plate to maintain flatness while leaving space for shrinkage during the initial activation step, (b) after the first hot-air heating of 5 min at 85°C, the sheet shows no bifurcations, and the hinges are slightly curved, preventing them from tape-spring buckling, (c) the origami sheet is cut off from the plate before reheated, (d) the fully folded origami sheet after reheated at 85°C for 5 min.

structural element for deployable space structures [4, 8]. In this section, the kirigami hinge is used to realise a membrane structure that automatically transforms from a

flat shape into a tube upon heating. This allows it to be embedded into a flexible membrane and then deploy to rigidise the gossamer structure. The design is shown in Figure 12, which consists of two kirigami hinges facing each other. When folded, each hinge will form one half of the tube that is bonded to the other half using the acrylic adhesive. In terms of thermal control, the feasibility of self-deployment upon exposure to sunlight is demonstrated in section 7.

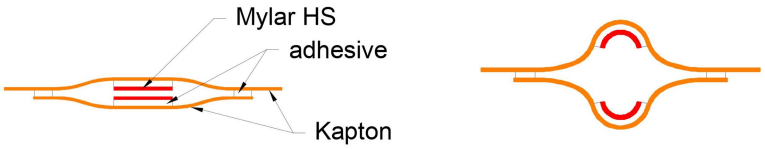

(a) (b)

Figure 12: Cross-section of the self-forming tubular structure, (a) before heating, (b) after heating, the tube is formed with the kirigami hinge folded.

As shown by Figure 13, the formation of the tube is completed in under 1.5 min of heating at 85°C, and the resulted structure shows a significantly higher stiffness in both bending and torsion. For instance, as shown in Figure 14, a cantilever tube made of 25 μm thick Kapton film and 16 μm Mylar that weighs 0.1 g and is 4 cm long can carry 4 g of load at its tip without any permanent deformation. As the load increases to 5 g, local buckling is observed at the support end.

7. Analysis of Sunlight-Activated Folding

In space applications, a protective/reflective metallic layer is needed on the polymer membrane to protect it from environmental attack, improve the tear resistance, and

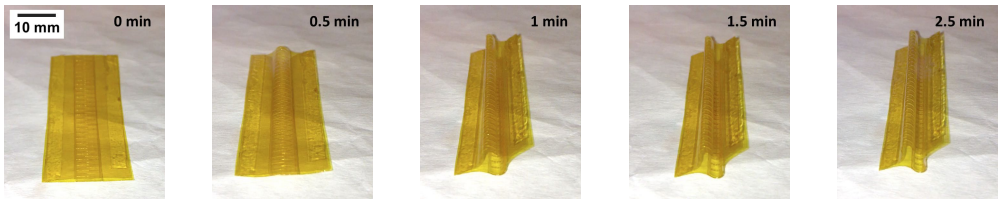

(a) (b) (c) (d) (e)

Figure 13: Formation of the tubular structure, (a) beginning of heating, (b) at $t = 0.5\,min$ at $85°C$, (c) $t = 1\,min$ at $85°C$, (d) $t = 1.5\,min$ at $85°C$ the formation is fully completed, (e) $t = 2.5\,min$ at $85°C$.

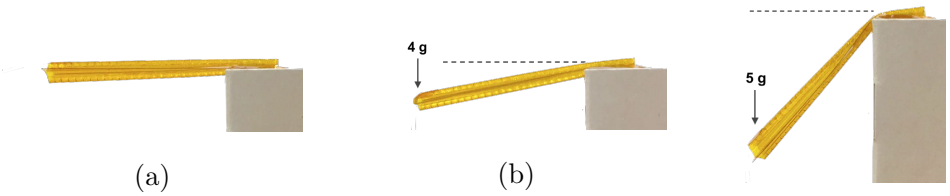

(a) (b) (c)

Figure 14: Bending of the cantilever self-forming tube of 4 cm length and 0.1 g structural mass, (a) initial shape without applied load, (b) the tube deflects under 4 g of load at its tip, (c) the tube buckles locally under a load of 5 g.

increase photonic-propulsion when used on solar sails [52]. This section provides a proof-of-concept thermal analysis, which demonstrates the concept of utilising such metallic coatings to activate folding in orbital environment by absorbing solar energy.

The orbital thermal condition with the absence of convection is determined by radiation and conduction only. For a thin membrane facing the sun, the through-thickness conduction is almost instant. Therefore, the temperature of a uniform film

can be treated as homogeneous and determined by radiative heat transmission.

Conventional vapour-deposited metallic coatings can achieve various thermal radiation properties. For instance, an aluminium coating has a reflectivity close to 90% throughout a wide spectrum including infrared, while a silver coating yields significantly above 90% [53]. In terms of an emissive coating that helps to radiate thermal energy away from a membrane for either cooling or heat transfer purposes, vapour-deposited chromium yields an emissivity of over 20%. While for picking up heat from the environment, nickel provides a near 40% absorptivity and low emissivity [54]. Typical coating materials that can be useful for the thermal control of the proposed membrane are listed in Table 3.

Table 3: Typical coatings useful for the thermal control of the proposed self-folding membrane [54].

Coating	Solar absorptivity	Emissivity	Typical usage
Vapour-deposited Ag	4%	2%	Reflection
Vapour-deposited Al	12%	3%	Reflection
Vapour-deposited Ni	38%	4%	Absorption
Vapour-deposited Cr	57%	24%	Emission & Heat dissipation
Carbon black paint	96%	88%	Absorption & Emission

According to the discussion above, the temperature of a single membrane can be resolved using the equation below [53], which assumes thermal equilibrium between radiation absorption and emission:

$$T = \sqrt[4]{\frac{\alpha \cdot q_s}{\sigma \cdot (\epsilon_1 + \epsilon_2)}} \tag{1}$$

Where ϵ_1 and ϵ_2 are the surface emissivities of the sun side and the rare side respectively. Consider a membrane directly facing the sun on a spacecraft in Low Earth Orbit (LEO), the solar radiation power density will be $q_s = 1.36\ kW/m^2$ [53]. Here we provide several examples under this typical thermal control scenario. Assuming both sides of the membrane are vapour-deposited Al shown in Table 3, and ignore the dependence of materials properties on temperature, the membrane will be at $195\,°C$. Changing the front coating to Ag will reduce the temperature to $99\,°C$. Such configurations can activate folding as the membrane temperature is well above the glass transition point of Mylar HS ($T_g = 82\,°C$) to initiate shrinkage. In case a lower operating temperature is required, a vapour-deposited Cr coating can be used on the rear surface, which could reduce the membrane temperature of an Al-coated membrane to $48\,°C$. Under such condition, the kirigami hinges need to be covered by light-absorbing materials on the sun side to activate folding. This can be achieved using the carbon black paint on top of the hinges, which leads to a hinge temperature of $106\,°C$.

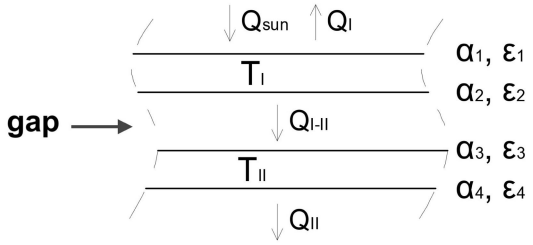

Figure 15: Thermal condition of two overlapped membranes with a gap in between.

Certain designs such as the self-forming tube discussed in section 6 (Figure 12) may use overlapped membranes with a gap (which is vacuum) in between, as

shown schematically in Figure 15. Considering the thermal equilibrium of the whole structure, the absorbed solar energy equals the total radiative cooling, i.e.,

$$Q_{sun} = Q_I + Q_{II} \tag{2}$$

Thus we have,

$$\alpha \cdot W = \sigma\epsilon_1 {T_I}^4 + \sigma\epsilon_4 {T_{II}}^4 \tag{3}$$

The thermal equilibrium of the rear membrane alone, is given by:

$$Q_{I-II} = Q_{II} \tag{4}$$

According to literature [55], Q_{I-II} represents the radiative thermal transmission between two infinite planes and has the expression:

$$Q_{I-II} = \frac{\sigma\epsilon_2 {T_I}^4 \cdot \alpha_3 - \sigma\epsilon_3 {T_{II}}^4 \cdot \alpha_2}{\alpha_2 + \alpha_3 - \alpha_2 \times \alpha_3} \tag{5}$$

It should be noted that the radiation spectrum between the two membranes is very different to solar spectrum, and the absorptivities from Table 3 do not hold. For simplicity, assume the coatings on both sides of the gap in Figure 15 are identical, while the emissivity and absorptivity are the same for the surfaces with the same coating at similar temperatures: $\alpha_2 = \alpha_3 = \epsilon_2 = \epsilon_3 = \alpha = \epsilon$, an Ag front coating and an Al back coating are used. Then the membranes temperature T_I and T_{II} can be evaluated using Eq. 2-5. The result (Figure 16) suggests that self-folding upon exposure to sunlight, which requires $T_I > 82\,^{\circ}C$ and $T_{II} > 82\,^{\circ}C$, can be achieved with a wide range of absorptivity and emissivity (α, $\epsilon > 0.1$).

Furthermore, the vapour-deposited metallic coating changes the flexural rigidity of the polymer membranes and thus the resistance to folding. Consider a Kapton

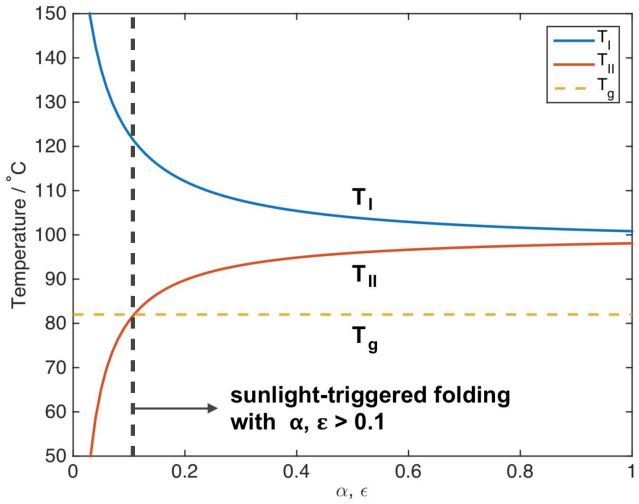

Figure 16: Temperature of two overlapped membranes, T_I and T_{II} plotted against the absorptivity α and emissivity ϵ of the coatings on both sides of the gap between the membranes, showing that the glass transition point of Mylar HS, $T_g = 82\,°C$ can be reached with α and $\epsilon > 0.1$.

film with 100 nm Al coating on both sides, then assuming 70 GPa and 2.5 GPa Young's modulus for Al and Kapton, respectively, the flexural rigidity, D of the coated and uncoated film can be evaluated according to Euler-Bernoulli linear beam theory, where I is the second moment of area (geometric parameter) [56]:

$$D_{coated} = E_{Al} I_{Al_1} + E_{kapton} I_{kapton} + E_{Al} I_{Al_2} \tag{6}$$

$$D_{uncoated} = E_{kapton} I_{kapton} \tag{7}$$

The ratio between the flexural rigidity, $D_{coated}/D_{uncoated}$, is then plotted in Figure 17. It can be seen that the effect of coating on the membrane's bending rigidity increases with decreasing Kapton thickness. The rigidity ratio is 1.47 for the 25 μm

Kapton used in the present study, and such coating will have no significant effect on the self-folding behaviour of the proposed polymer membrane.

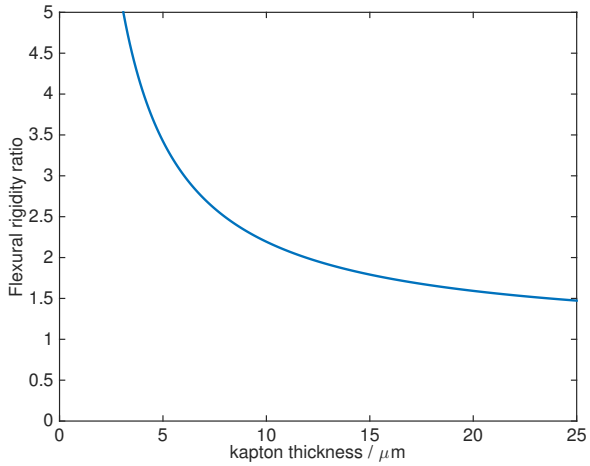

Figure 17: Ratio between the flexural rigidity of coated and uncoated membranes, $D_{coated}/D_{uncoated}$, plotted against Kapton thickness, assuming aluminium coatings with 100 nm thickness on both sides of the Kapton film.

8. Summary

Self-folding membrane that can permanently fold along complex crease patterns when heated up to a certain temperature is designed and fabricated. It is based on a thermally stable Kapton substrate, and folding is activated by an isotropic heat shrinking film, Mylar HS, which is bonded along the hinges using a flexible acrylic adhesive. The specially designed kirigami hinges have slits cut into the Mylar and the adhesive layers to relax the stress caused by shrinkage and convert the isotropic

shrinkage to unidirectional (i.e., anisotropic), thereby realise a predictable folding without bifurcation. In comparison with the existing self-folding membranes, the proposed innovative design is based on space-qualified materials, and is potentially mass-producible. It also features weight saving since most part of the membrane is single layered Kapton and only the hinge region is multi-layered, which is important for certain space missions such as solar sails.

Test samples of a self-folding origami structure and a self-forming tubular structure are fabricated using a semi-automated production method that can potentially be converted to an industrial roll-to-roll process. Tests carried out in an oven suggest that the kirigami hinge design, as well as the actuation process that keeps the membrane generally flat during the deployment has successfully prevented bifurcation. The 2D membranes were successfully transformed into 3D structures.

Furthermore, thermal radiation analysis has demonstrated that the folding can be activated using sunlight in a space environment by applying conventional spacecraft thermal control coatings onto the membranes. This creates a different type of deployable gossamer structures: when stored, the flexible membrane can be winded up into a cylinder instead of packed as a pre-folded origami, which potentially saves stowage volume and allows simpler packaging process; for deployment, the membrane is released from the package and heated by sunlight, which activates the folding along a pre-defined crease pattern. The folded membrane not only achieves self-rigidisation, but could also serve as a building block of future origami meta-structures with various design-able behaviours and built-in functionalities.

Reference

[1] Jenkins CH. Progress in Astronautics and Aeronautics: Gossamer Spacecraft: Membrane and Inflatable Structures Technology for Space Applications. vol. 191. Aiaa; 2001.

[2] Ruggiero EJ, Inman DJ. Gossamer spacecraft: recent trends in design, analysis, experimentation, and control. Journal of Spacecraft and Rockets. 2006;43(1):10–24.

[3] Fu B, Sperber E, Eke F. Solar sail technologyA state of the art review. Progress in Aerospace Sciences. 2016;86:1–19.

[4] Block J, Straubel M, Wiedemann M. Ultralight deployable booms for solar sails and other large gossamer structures in space. Acta Astronautica. 2011;68(7):984–992.

[5] Roberts PC, Harkness PG. Drag sail for end-of-life disposal from low earth orbit. Journal of Spacecraft and Rockets. 2007;44(6):1195–1203.

[6] Santiago-Prowald J, Baier H. Advances in deployable structures and surfaces for large apertures in space. CEAS Space Journal. 2013;5(3-4):89–115.

[7] Chu Z, Deng Z, Qi X, Li B. Modeling and analysis of a large deployable antenna structure. Acta Astronautica. 2014;95:51–60.

[8] Puig L, Barton A, Rando N. A review on large deployable structures for astrophysics missions. Acta Astronautica. 2010;67(1):12–26.

[9] Garner C, Diedrich B, Leipold M. A Summary of Solar Sail Technology Developments and Proposed Demonstration Missions. In: AIAA-99-2697, presented at 35th AIAA Joint Propulsion Conference. Citeseer; 1999. .

[10] Häuplik-Meusburger S, Sommer B, Aguzzi M. Inflatable technologies: adaptability from dream to reality. Acta Astronautica. 2009;65(5):841–852.

[11] Babuscia A, Corbin B, Knapp M, Jensen-Clem R, Van de Loo M, Seager S. Inflatable antenna for cubesats: Motivation for development and antenna design. Acta Astronautica. 2013;91:322–332.

[12] Hedgepeth JM. Dynamics of a large spin-stiffened deployable paraboloidal antenna. Journal of Spacecraft and Rockets. 1970;7(9):1043–1048.

[13] MacNeal RH. The heliogyro - an interplanetary flying machine. NASA Contractors Report

CR 84460, 1967;.

[14] Janhunen P. Photonic spin control for solar wind electric sail. Acta Astronautica. 2013;83:85–90.

[15] Mao H, Sinn T, Vasile M, Tibert G. Post-launch analysis of the deployment dynamics of a space web sounding rocket experiment. Acta Astronautica. 2016;127:345–358.

[16] Gardsback M, Tibert G. Deployment control of spinning space webs. Journal of guidance, control, and dynamics. 2009;32(1):40.

[17] Vinogradov AM, Jenkins CH, Su J, Bar-Cohen Y, Pollard EL. Functional Materials for Smart Gossamer Spacecraft. Progress in Astronautics and Aeronautics. 2006;212:165.

[18] Salama M, Jenkins C. Intelligent gossamer structures-A review of recent developments and future trends. In: 19th AIAA Applied Aerodynamics Conference; 2013. p. 1196.

[19] Cadogan DP, Scarborough SE. Rigidizable materials for use in gossamer space inflatable structures. AIAA paper. 2001;1417:2001.

[20] Bryant RG, Seaman ST, Wilkie WK, Miyauchi M, Working DC. Selection and manufacturing of membrane materials for solar sails. In: Advances in Solar Sailing. Springer; 2014. p. 525–540.

[21] Blomquist RS. Heliogyro control. Ph.D. Thesis, Carnegie Mellon University, Pittsburg, Pennsylvania; 2009.

[22] Liu Y, Genzer J, Dickey MD. "2D or not 2D": Shape-programming polymer sheets. Progress in Polymer Science. 2016;52:79–106.

[23] Dudte LH, Vouga E, Tachi T, Mahadevan L. Programming curvature using origami tessellations. Nature materials. 2016;15(5):583–588.

[24] Lv C, Krishnaraju D, Konjevod G, Yu H, Jiang H. Origami based mechanical metamaterials. Scientific reports. 2014;4:5979–5981.

[25] Filipov ET, Tachi T, Paulino GH. Origami tubes assembled into stiff, yet reconfigurable structures and metamaterials. Proceedings of the National Academy of Sciences. 2015;112(40):12321–12326.

[26] Liu X, Gattas JM, Chen Y. One-DOF Superimposed Rigid Origami with Multiple States.

Scientific reports. 2016;6:36883.

[27] Wu R, Roberts PC, Soutis C, Diver C. Heliogyro Solar Sail with Self-Regulated Centrifugal Deployment Enabled by an Origami-Inspired Morphing Reflector. Acta Astronautica. 2018;Accepted manuscript.

[28] Deng D, Yang Y, Chen Y, Lan X, Tice J. Accurately controlled sequential self-folding structures by polystyrene film. Smart Materials and Structures. 2017;26(8):085040.

[29] Tolley MT, Felton SM, Miyashita S, Aukes D, Rus D, Wood RJ. Self-folding origami: shape memory composites activated by uniform heating. Smart Materials and Structures. 2014;23(9):094006.

[30] Miyashita S, Meeker L, Tolley MT, Wood RJ, Rus D. Self-folding miniature elastic electric devices. Smart Materials and Structures. 2014;23(9):094005.

[31] Cui J, Adams J, Zhu Y. Pop-up assembly of 3D structures actuated by heat shrinkable polymers. Smart Materials and Structures. 2017;26(12):125011.

[32] Abdullah AM, Braun PV, Hsia KJ. Bifurcation of self-folded polygonal bilayers. Applied Physics Letters. 2017;111(10):104101.

[33] Caruso N, Cvetkovi A, Lucantonio A, Noselli G, Desimone A. Spontaneous morphing of equibiaxially pre-stretched elastic bilayers: the role of sample geometry. International Journal of Mechanical Sciences, 2017;.

[34] Liu Y, Miskiewicz M, Escuti MJ, Genzer J, Dickey MD. Three-dimensional folding of pre-strained polymer sheets via absorption of laser light. Journal of Applied Physics. 2014;115(20):043505–12445.

[35] Lee Y, Lee H, Hwang T, Lee JG, Cho M. Sequential Folding using Light-activated Polystyrene Sheet. Scientific Reports. 2015;5:16544.

[36] Davis D, Mailen R, Genzer J, Dickey MD. Self-folding of polymer sheets using microwaves and graphene ink. Rsc Advances. 2015;5(108):89254–89261.

[37] Ryu J, DAmato M, Cui X, Long KN, Qi HJ, Dunn ML. Photo-origamiBending and folding polymers with light. Applied Physics Letters. 2012;100(16):82–87.

[38] Leong TG, Benson BR, Call EK, Gracias DH. Thin Film Stress Driven Self-Folding of

Microstructured Containers. Small. 2008;4(10):16051609.

[39] Bassik N, Stern GM, Gracias DH. Microassembly based on hands free origami with bidirectional curvature. Applied Physics Letters. 2009;95(9):91901.

[40] Leong TG, Randall CL, Benson BR, Bassik N, Stern GM, Gracias DH. Tetherless thermobiochemically actuated microgrippers. Proceedings of the National Academy of Sciences of the United States of America. 2009;106(3):703.

[41] Na JH, Evans AA, Bae J, Chiappelli MC, Santangelo CD, Lang RJ, et al. Programming reversibly self-folding origami with micropatterned photo-crosslinkable polymer trilayers. Advanced Materials. 2015;27(1):79–85.

[42] Seffen K, Pellegrino S. Deployment dynamics of tape springs. In: Proceedings of the Royal Society of London A: Mathematical, Physical and Engineering Sciences. vol. 455. The Royal Society; 1999. p. 1003–1048.

[43] Fang H, Li S, Wang K. Self-locking degree-4 vertex origami structures. Proc R Soc A. 2016;472(2195):20160682.

[44] Fang H, Li S, Xu J, Wang K. Locking mechanisms in degree-4 vertex origami structures. In: Active and Passive Smart Structures and Integrated Systems 2016. vol. 9799. International Society for Optics and Photonics; 2016. p. 979910.

[45] Gattas JM, Wu W, You Z. Miura-base rigid origami: parameterizations of first-level derivative and piecewise geometries. Journal of Mechanical Design. 2013;135(11):111011.

[46] Sareh P, Guest SD. A Framework for the Symmetric Generalisation of the Miura-ori. International Journal of Space Structures. 2015;30(2):141–152.

[47] Sareh P, Guest SD. Design of non-isomorphic symmetric descendants of the Miura-ori. Smart Materials and Structures. 2015;24(8):085002.

[48] Santangelo CD. Extreme Mechanics: Self-Folding Origami. Annual Review of Condensed Matter Physics. 2017;8:165–183.

[49] Silverberg JL, Evans AA, McLeod L, Hayward RC, Hull T, Santangelo CD, et al. Using origami design principles to fold reprogrammable mechanical metamaterials. Science. 2014;345(6197):647–650.

[50] Silverberg JL, Na JH, Evans AA, Liu B, Hull TC, Santangelo CD, et al. Origami structures with a critical transition to bistability arising from hidden degrees of freedom. Nature materials. 2015;14(4):389.

[51] Liu B, Silverberg JL, Evans AA, Santangelo CD, Lang RJ, Hull TC, et al. Topological kinematics of origami metamaterials. Nature Physics. 2018;p. 1.

[52] Macdonald M. Advances in solar sailing. Springer Praxis, Chichester, UK; 2014.

[53] Wright JL. Space sailing. Gordon and Breach Science Publications, Amsterdam; 1992.

[54] Kauder L. Spacecraft thermal control coatings references. NASA/TP-2005-212792, 2005;.

[55] Spakovszky Z. 16. Unified: Thermodynamics and Propulsion;. Unified Engineering, 2009. http://web.mit.edu/16.unified/www/SPRING/propulsion/notes/notes.html, (accessed 1 Dec 2017).

[56] Gere JM, Goodno BJ. Mechanics of materials, 8th. Stamford, Connecticut: Cengage Learning; 2012.

Chapter 7

Conclusions and future work

7.1 Summary of research findings

The present research originated from the idea that when a deployable structure spins up utilising the energy from an external power source, while the driving-torque has a magnitude depending on the deployment condition, a passive self-regulating centrifugal deployment can be established. The study has demonstrated its possible applications to deployable space systems including atmospheric entry heat shields and gossamer solar sails, as well as its potential benefits to realise more concise, lightweight and compact systems than existing solutions.

Centrifugally deployed flexible aerodynamic decelerator. Utilising a flexible aeroshell with a spiral shape, which generates an aerodynamic roll-torque that is coupled to deployment condition, a self-regulated centrifugal deployment can be achieved. The system is passive since the autorotation is driven by the descending kinetic energy. This allows a concise and robust system that also achieves compact packaging and low structural mass. Furthermore, an active control loop can

be added into the passive system using conventional attitude control devices to actively adjust the deployment shape and thereby realise downrange manoeuvre.

In comparison with existing solutions, it contains less critical components such as the inflation devices in an inflatable aeroshell, or hinged/sliding mechanisms and actuators in a mechanically deployed decelerator. The dependence on inertial forces rather than material stiffness also improves its temperature tolerance that, especially when compared to an inflatable structure with air-tight bladders, allows a lightweight thermal protection system. The design also benefits from its scalability, which enables a scaled up version to decelerate an entry mass of 5 ton or beyond while being lighter than NASA's HEART inflatable heat shield, or scaling down to 30 g entry mass to realise miniaturised systems.

When used on a CubeSat-sized entry system, it could enable a low-cost sample return from LEO while being advantageous due to its simplicity and robustness. The downrange manoeuvrability can be particularly useful for such a system that initiates re-entry through orbital decay. Similar or even smaller entry systems could potentially be used in a low-cost probe swarm that may realise new types of planetary explorations. On the other hand, scaled-up decelerators could realise soft-landing of heavy payload on Mars or landing on Martian mountains, which benefits from its compactness and low structural mass that are crucial for deep space missions.

Passive centrifugal deployment of heliogyro. Enabled by a meta-structure reflector that generates a centrifugal-stress-dependent in-plane solar radiation propulsion, a self-regulated spin and deployment of a heliogyro solar sail can be achieved. The tip-mounted meta-structure reflectors are formed from flat reflective membranes in space utilising origami that automatically folds when exposed to sunlight. This enables a fully passive operation and prevents over-spin when fully deployed.

Combined with a torque-regulating blade releasing device, a passive servo system with "programmable" spin rate throughout blade deployment can be realised.

The proposed concept not only benefits from its conciseness. Unlike the existing designs that use simple reflective membranes and achieve flight manoeuvres by inducing overall sail distortion, which leads to structural dynamic issues, the proposed design keeps the reflector flat and free from overall deformations and thus realises a quasi-static operation. Meanwhile, the in-plane photonic propulsion is proven to be robust against structural oscillation, and the reflector self-rigidises through folding to further facilitate the dynamic behaviour.

Besides the application as a solar sail, the proposed design could also be used as a solar-radiation-deployed drag sail. Meanwhile, the design of the origami metastructure reflector, combined with the self-folding material developed in this study, has provided a methodology to realise a broad range of self-rigidising passive gossamer space structures with built-in functionalities.

7.2 Closing remark and future implication

The present research provides proof-of-concept studies of two designs, where the critical functions are demonstrated by analyses and low-fidelity numerical simulations, then partially verified by experiments in laboratory environment. The future work should focus on further concept validation in a more relevant environment.

For the deployable heat shield which has achieved a Technology Readiness Level (TRL) of 4, the future work may include:

- High fidelity aerodynamic simulations to replace the analytical model for roll-torque and deployment moment prediction, thus providing a higher fidelity

simulator;

- Low-speed high-altitude ($25 \sim 35\,km$) drop test from a balloon, which could further verify the simulation and validate the design at varying atmospheric conditions and high velocity;
- Plasma wind tunnel tests to validate the thermal resistance of the stitched fabric heat shield architecture, and potentially partially verify the heat shield's dynamic behaviour in a relevant hypersonic flow (TRL 5);
- Suborbital test to further validate the concept from the aspects of structural dynamics, flight dynamics and aerothermodynamics (TRL 6).

In terms of the heliogyro, which has a TRL of 3, the future work may include:

- High fidelity FE simulations to reveal the solar-elastic behaviours of the heliogyro throughout deployment;
- Lab demonstration of solar radiation activated self-folding of membranes with metallic thermal control coatings, as well as the effect of long-duration heating, with the aim to bring the self-folding membrane to a TRL of 5;
- Exploring other applications of the origami gossamer structures, including self-deploying/rigidising passive devices and different types of photonic propulsion manipulators.

Bibliography

[1] M. Berzeri, A. A. Shabana, Study of the centrifugal stiffening effect using the finite element absolute nodal coordinate formulation, Multibody System Dynamics 7 (4) (2002) 357–387.

[2] R. H. MacNeal, The heliogyro-an interplanetary flying machine, Tech. Rep. 67N27627, NASA (1967).

[3] W. K. Wilkie, J. E. Warren, L. G. Horta, K. H. Lyle, J.-N. Juang, J. D. Littell, R. G. Bryant, M. W. Thomson, P. E. Walkemeyer, D. V. Guerrant, et al., Heliogyro solar sail research at nasa, in: Advances in Solar Sailing, Springer, 2014, pp. 631–650.

[4] Y. Tsuda, O. Mori, R. Funase, H. Sawada, T. Yamamoto, T. Saiki, T. Endo, K. Yonekura, H. Hoshino, J. Kawaguchi, Achievement of ikarosjapanese deep space solar sail demonstration mission, Acta Astronautica 82 (2) (2013) 183–188.

[5] J. M. HEDGEPETH, Dynamics of a large spin-stiffened deployable paraboloidal antenna, Journal of Spacecraft and Rockets 7 (9) (1970) 1043–1048.

[6] V. Koshelev, V. Melnikov, Large space structures formed by centrifugal forces, CRC Press, 1998.

[7] S. Nakasuka, T. Funane, Y. Nakamura, Y. Nojiri, H. Sahara, F. Sasaki, N. Kaya, Sounding rocket flight experiment for demonstrating furoshiki satellite for large phased array antenna, Acta Astronautica 59 (1-5) (2006) 200–205.

[8] H. Mao, T. Sinn, M. Vasile, G. Tibert, Post-launch analysis of the deployment dynamics of a space web sounding rocket experiment, Acta Astronautica 127 (2016) 345–358.

[9] M. Gärdsback, G. Tibert, Deployment control of spinning space webs, Journal of Guidance, Control, and Dynamics 32 (1) (2009) 40–50.

[10] G. Kiper, E. Soylemez, Deployable space structures, in: Recent Advances in Space Technologies, 2009. RAST'09. 4th International Conference on, IEEE, 2009, pp. 131–138.

[11] M. Gärdsback, G. Tibert, D. Izzo, Design considerations and deployment simulations of spinning space webs, in: 48th AIAA/ASME/ASCE/AHS/ASC Structures, Structural Dynamics, and Materials Conference, 2007, p. 1829.

[12] H. Sawada, O. Mori, N. Okuizumi, Y. Shirasawa, Y. Miyazaki, M. Natori, S. Matunaga, H. Furuya, H. Sakamoto, Mission report on the solar power sail deployment demonstration of ikaros, in: 52nd AIAA/ASME/ASCE/AHS/ASC Structures, Structural Dynamics and Materials Conference 19th AIAA/ASME/AHS Adaptive Structures Conference 13t, 2011, p. 1887.

[13] R. Routledge, J. H. Pepper, Discoveries and inventions of the nineteenth century, G. Routledge and sons, 1876.

[14] Z.-M. Ge, H.-S. Yang, H.-H. Chen, H.-K. Chen, Regular and chaotic dynamics of a rotational machine with a centrifugal governor, International journal of engineering science 37 (7) (1999) 921–943.

[15] A. Viviani, G. Pezzella, Aerodynamic and aerothermodynamic analysis of space mission vehicles, Springer, 2015.

[16] R. D. Braun, R. M. Manning, Mars exploration entry, descent, and landing challenges, Journal of Spacecraft and Rockets 44 (2) (2007) 310–323.

[17] J. Cruz, J. Lingard, Aerodynamic decelerators for planetary exploration: past, present, and future, in: AIAA Guidance, Navigation, and Control Conference and Exhibit, 2006, p. 6792.

[18] B. P. Smith, C. L. Tanner, M. Mahzari, I. G. Clark, R. D. Braun, F. M. Cheatwood, A historical review of inflatable aerodynamic decelerator technology development, in: Aerospace Conference, 2010 IEEE, IEEE, 2010, pp. 1–18.

[19] B. Steinfeldt, J. Theisinger, A. Korzun, I. Clark, M. Grant, R. Braun, High mass mars entry, descent, and landing architecture assessment, in: AIAA SPACE 2009 Conference & Exposition, 2009, p. 6684.

[20] B. G. Drake, S. J. Hoffman, D. W. Beaty, Human exploration of mars, design reference architecture 5.0, in: Aerospace Conference, 2010 IEEE, IEEE, 2010, pp. 1–24.

[21] I. G. Clark, R. D. Braun, Ballute entry systems for lunar return and low-earth-orbit return missions, Journal of Spacecraft and Rockets 45 (3) (2008) 619–630.

[22] V. Carandente, R. Savino, New concepts of deployable de-orbit and re-entry

systems for cubesat miniaturized satellites, Recent Patents on Engineering 8 (1) (2014) 2–12.

[23] B. Chan, N. Bauer, J. R. Juneau, S. Stout, K. Masuyama, D. Spencer, Recovery of in-space cubesat experiments (rice) project, in: Seventh International Planetary Probe Workshop, Barcelona, Spain, 2010.

[24] J. Andrews, K. Watry, K. Brown, Nanosat deorbit and recovery system to enable new missions, Paper no SSC11-X-3, presented at the 25th AIAA/USU Conference on Small Satellites, Logan, Utah, USA, 8-12 August, 2011.

[25] M. S. Murbach, K. M. Boronowsky, J. E. Benton, B. White, E. Fritzler, The spqr as an option for returning payloads from the iss after the termination of sts flights, AIAA-2010-6223, 40th International Conference on Environmental System, Barcelona, Spain, 2010.

[26] G. Herdrich, J.-P. Baumann, P. Geissler, R. Geshnizjani, M. Bartomeu, P. Ortwein, D. Winter, B. Wirth, A. Zach, A. Preci, et al., Mirka2: Small re-entry demonstrator for advanced miniaturized sensors, in: International Workshop on Instrumentation for Planetary Missions, Vol. 1683, 2012, p. 1083.

[27] D. M. Bose, J. Shidner, R. Winski, C. Zumwalt, F. Cheatwood, S. J. Hughes, The hypersonic inflatable aerodynamic decelerator (hiad) mission applications study, in: AIAA Aerodynamic Decelerator Systems (ADS) Conference, 2013, p. 1389.

[28] E. Fantino, M. Grassi, P. Pasolini, F. Causa, C. Molfese, R. Aurigemma, N. Cimminiello, D. de la Torre, P. Dell'Aversana, F. Esposito, et al., The small mars system, Acta Astronautica 137 (2017) 168–181.

[29] A. Wachi, R. Takahashi, R. Sakagami, Y. Koshiro, Y. Kasai, S. Nakasuka,

Mars entry, descent, and landing by small thz spacecraft via membrane aeroshell, in: AIAA SPACE and Astronautics Forum and Exposition, 2017, p. 5313.

[30] R. Sakagami, R. Takahashi, A. Wachi, Y. Koshiro, H. Maezawa, Y. Kasai, S. Nakasuka, Integral design method for simple and small mars lander system using membrane aeroshell, Acta Astronautica 144 (2018) 103–118.

[31] I. G. Clark, A. L. Hutchings, C. L. Tanner, R. D. Braun, Supersonic inflatable aerodynamic decelerators for use on future robotic missions to mars, Journal of Spacecraft and Rockets 46 (2) (2009) 340–352.

[32] R. W. Leonard, G. W. Brooks, H. G. McComb Jr, Structural considerations of inflatable reentry vehicles, Technical Report 72N71001, NASA.

[33] H. Bohon, M. Mikulas, M, Development status of attached inflatable decelerators., Journal of Spacecraft and Rockets 6 (6) (1969) 654–660.

[34] R. R. Rohrschneider, R. D. Braun, Static aeroelastic analysis of thin-film clamped ballute for titan aerocapture, Journal of Spacecraft and Rockets 45 (4) (2008) 785–801.

[35] J. Hall, A review of ballute technology for planetary aerocapture, International Conference on Low-Cost Planetary Missions, Laurel, MD, United States, 2000.

[36] C. Park, A survey of aerobraking orbital transfer vehicle design concepts, in: 25th AIAA Aerospace Sciences Meeting, 1987, p. 514.

[37] E. Axdahl, J. Cruz, M. Schoenenberger, A. Wilhite, Flight dynamics of an aeroshell using an attached inflatable aerodynamic decelerator, in: 20th

AIAA Aerodynamic Decelerator Systems Technology Conference and Seminar, 2009, p. 2963.

[38] D. Bose, M. Toniolo, S. O'Keefe, F. Cheatwood, S. Hughes, R. Dillman, Impact of vehicle flexibility on irve-ii flight dynamics, in: 21st AIAA Aerodynamic Decelerator Systems Technology Conference and Seminar, 2011, p. 2571.

[39] S. Hughes, R. Dillman, B. Starr, R. Stephan, M. Lindell, C. Player, F. Cheatwood, Inflatable re-entry vehicle experiment (irve) design overview, in: 18th AIAA Aerodynamic Decelerator Systems Technology Conference and Seminar, 2005, p. 1636.

[40] J. W. Sawyer, C. F. Whitcomb, Subsonic and transonic pressure distributions around a bluff afterbody in the wake of a 120 deg cone for various separation distances, Technical Note TN-D-6569, NASA.

[41] M. S. Anderson, H. L. Bohon, M. M. Mikulas Jr, A structural merit function for aerodynamic decelerators, Technical Note TN-D-5535, NASA.

[42] A. Mastropietro, J. Kempenaar, M. Redmond, M. Pauken, W. Ancarrow, First test flight thermal performance of the low density supersonic decelerator (ldsd) supersonic flight dynamics test (sfdt) vehicle, 45th International Conference on Environmental Systems, 2015.

[43] D. Coatta, D. A. Jurewicz, B. A. Tutt, I. G. Clark, T. Rivellini, Development and testing of an 8m isotensoid supersonic inflatable aerodynamic decelerator (siad), in: AIAA Aerodynamic Decelerator Systems (ADS) Conference, 2013, p. 1328.

[44] M. S. Anderson, J. C. Robinson, H. G. Bush, R. W. Fralich, Tension

shell structure for appliaction to entry vehicles, Technical Note TN-D-2675, NASA.

[45] T. R. Creel Jr, Longitudinal aerodynamic characteristics of a tension shell entry configuration at mach 20, Technical Report 66N33452, NASA.

[46] T. Abe, A self-consistent tension shell structure for application to aerobraking vehicle and its aerodynamic characteristics, in: 24th Joint Propulsion Conference, 1988, p. 3405.

[47] C. Tanner, J. Cruz, R. Braun, Structural verification and modeling of a tension cone inflatable aerodynamic decelerator, in: 51st AIAA/ASME/ASCE/AHS/ASC Structures, Structural Dynamics, and Materials Conference 18th AIAA/ASME/AHS Adaptive Structures Conference 12th, 2010, p. 2830.

[48] I. Clark, J. Cruz, M. Hughes, J. Ware, A. Madlangbayan, R. Braun, Aerodynamic and aeroelastic characteristics of a tension cone inflatable aerodynamic decelerator, in: 20th AIAA Aerodynamic Decelerator Systems Technology Conference and Seminar, 2009, p. 2967.

[49] W. C. Alexander, R. A. Lau, State-of-the-art study for high-speed deceleration and stabilization devices, Technical Report 66N36856, NASA.

[50] K. Yamada, Y. Nagata, T. Abe, K. Suzuki, O. Imamura, D. Akita, Reentry demonstration of flare-type membrane aeroshell for atmospheric entry vehicle using a sounding rocket, in: AIAA Aerodynamic Decelerator Systems (ADS) Conference, 2013, p. 1388.

[51] Y. Takahashi, D. Ha, N. Oshima, K. Yamada, T. Abe, K. Suzuki, Aerodecelerator performance of flare-type membrane inflatable vehicle in suborbital reentry, Journal of Spacecraft and Rockets 54 (5) (2017) 993–1004.

[52] Y. Nagata, K. Yamada, T. Abe, K. Suzuki, Attitude dynamics for flare-type membrane aeroshell capsule in reentry flight experiment, in: AIAA Aerodynamic Decelerator Systems (ADS) Conference, 2013, p. 1285.

[53] A. Ceruti, S. Pettenuzzo, M. Tuveri, Conceptual design and preliminarily structural analysis of inflatable basket for an asteroid capturing satellite, Strojniški vestnik-Journal of Mechanical Engineering 61 (5) (2015) 341–351.

[54] D. Litton, D. Bose, F. Cheatwood, S. Hughes, H. Wright, M. Lindell, S. Derry, A. Olds, Inflatable re-entry vehicle experiment (irve)-4 overview, in: 21st AIAA Aerodynamic Decelerator Systems Technology Conference and Seminar, 2011, p. 2580.

[55] A. Olds, R. Beck, D. M. Bose, J. White, K. T. Edquist, B. R. Hollis, M. Lindell, F. Cheatwood, V. Gsell, E. L. Bowden, Irve-3 post-flight reconstruction, in: AIAA Aerodynamic Decelerator Systems (ADS) Conference, 2013, p. 1390.

[56] R. K. Johnson, F. M. Cheatwood, A. M. Calomino, S. J. Hughes, A. M. Korzun, J. M. DiNonno, M. C. Lindell, G. T. Swanson, Hiad advancements and extension of mission applications, in: International Planetary Probe Workshop, Laurel, MD, United States, 2016.

[57] B. Harper, R. D. Braun, Asymmetrically stacked tori hypersonic inflatable aerodynamic decelerator design study for mars entry, in: AIAA Atmospheric Flight Mechanics Conference, 2014, p. 1095.

[58] D. Jurewicz, G. Brown, B. Gilles, A. Taylor, R. Sinclair, B. Tutt, D. Lichodziejewski, C. Kelley, S. Hughes, Design and development of inflatable aeroshell structure for irve-3, in: 21st AIAA Aerodynamic Decelerator Systems Technology Conference and Seminar, 2011, p. 2522.

[59] H. Wright, A. Cutright, J. Corliss, W. Bruce, D. Trombetta, A. Mazaheri, M. Coleman, A. Olds, S. Hancock, Heart flight test overview, in: 9th International Planetary Probe Workshop, Toulouse, France, 2012.

[60] L. Marraffa, D. Kassing, P. Baglioni, D. Wilde, S. Walther, K. Pitchkhadze, V. Finchenko, Inflatable re-entry technologies: flight demonstration and future prospects, ESA bulletin (2000) 78–85.

[61] M. Gräßlin, U. Schöttle, Flight performance evaluation of the re-entry mission irdt-1, in: IAF, International Astronautical Congress, 52 nd, Toulouse, France, 2001.

[62] D. Wilde, S. Walther, K. Pitchadze, S. Alexsaschkin, D. Vennemann, L. Marraffa, Flight test and iss application of the inflatable reentry and descent technology (irdt), Acta Astronautica 51 (1-9) (2002) 83–88.

[63] R. Wang, A. Hou, Y. Niu, The optimal design and analysis of the irdt system based on two-dimensional ballistic trajectory in atmosphere reentry, in: 20th AIAA International Space Planes and Hypersonic Systems and Technologies Conference, 2015, p. 3672.

[64] K. Pichkhadze, V. Finchenko, S. Aleksashkin, B. Ostreshko, Transformable descent vehicles, Solar System Research 50 (7) (2016) 489–497.

[65] N. Skolnik, H. Kamezawa, L. Li, G. A. Rossman, B. Sforzo, R. D. Braun, Design of a novel hypersonic inflatable aerodynamic decelerator for mars entry, descent, and landing, in: AIAA Atmospheric Flight Mechanics Conference, 2017, p. 0469.

[66] A. C. Young, Large payload hiad systems: Development of computationally efficient modeling strategies and structural investigations, Ph.D. thesis, The University of Maine, Orono (2017).

[67] J. S. Green, B. Dunn, R. Lindberg, Morphing hypersonic inflatable aerodynamic decelerator, in: AIAA Aerodynamic Decelerator Systems (ADS) Conference, 2013, p. 1256.

[68] Z. Bassett, J. Pei, A. Milne Slagle, B. N. Pamadi, Application of an optimal control allocation scheme with structural load and aero heating feedback for a morphing inflatable aerodynamic decelerator, in: 2018 AIAA Atmospheric Flight Mechanics Conference, 2018, p. 0014.

[69] M. Sparapany, Enabling mars exploration using inflatable purdue aerodynamic decelerator with deployable entry systems (ipaddles) technology, Ph.D. thesis, Purdue University, West Lafayette.

[70] D. Lichodziejewski, C. Kelley, B. Tutt, D. Jurewicz, G. Brown, B. Gilles, D. Barber, R. Dillman, C. Player, Design and testing of the inflatable aeroshell for the irve-3 flight experiment, in: 53rd AIAA/ASME/ASCE/AHS/ASC Structures, Structural Dynamics and Materials Conference 20th AIAA/ASME/AHS Adaptive Structures Conference 14th AIAA, 2012, p. 1515.

[71] J. A. DelCorso, W. E. Bruce III, S. J. Hughes, J. A. Dec, M. D. Rezin, M. A. B. Meador, H. Guo, D. G. Fletcher, A. M. Calomino, M. Cheatwood, Flexible thermal protection system development for hypersonic inflatable aerodynamic decelerators, in: 9th International Planetary Probe Workshop, Toulouse, France, 2012.

[72] W. E. Bruce III, N. J. Mesick, P. G. Ferlemann, P. M. Siemers III, J. A. DelCorso, S. J. Hughes, S. A. Tobin, M. P. Kardell, Aerothermal ground testing of flexible thermal protection systems for hypersonic inflatable aerodynamic decelerators, in: 9th International Planetary Probe Workshop, Toulouse,

France, 2012.

[73] J. Del Corso, F. Cheatwood, W. Bruce, S. Hughes, A. Calomino, Advanced high-temperature flexible tps for inflatable aerodynamic decelerators, in: 21st AIAA Aerodynamic Decelerator Systems Technology Conference and Seminar, 2011, p. 2510.

[74] S. Hughes, J. Ware, J. Del Corso, R. Lugo, Deployable aeroshell flexible thermal protection system testing, in: 20th AIAA Aerodynamic Decelerator Systems Technology Conference and Seminar, 2009, p. 2926.

[75] K. H. Peterson, B. Yount, N. R. Schneider, D. K. Prabhu, J. O. Arnold, T. H. Squire, P. F. Wercinski, J. F. Chavez-Garcia, E. Venkatapathy, Thermal and structural performance of woven carbon cloth for adaptive deployable entry and placement technology, in: AIAA Aerodynamic Decelerator Systems (ADS) Conference, 2013, p. 1370.

[76] R. Detra, A. Kantrowitz, F. Riddell, P. Rose, The drag brake manned satellite system, in: Xth International Astronautical Congress London 1959/X. Internationaler Astronautischer Kongress/Xe Congrès International dAstronautique, Springer, 1960, pp. 728–747.

[77] D. Akin, The parashield entry vehicle concept: Basic theory and flight test development, in: 4th AIAA/ USU Conference on Small Satellites, Logan, UT, 1990.

[78] M. Wiegand, H. Konigsmann, A small re-entry capsule-brem-sat 2, in: 10th AIAA/USU Small Satellite Conference, Logan, UT, 1996.

[79] P. Wercinski, Adaptable deployable entry & placement technology (adept) for cubesat delivery to mars surface, Mars CubeSat/NanoSat Workshop, Pasadena, CA, 2014.

[80] E. Venkatapathy, K. Hamm, I. Fernandez, J. Arnold, D. Kinney, B. Laub, A. Makino, M. McGuire, K. Peterson, D. Prabhu, et al., Adaptive deployable entry and placement technology (adept): a feasibility study for human missions to mars, in: 21st AIAA Aerodynamic Decelerator Systems Technology Conference and Seminar, 2011, p. 2608.

[81] E. Venkatapathy, P. Wercinski, D. Prabhu, Mechanically-deployed hypersonic decelerator and conformal ablator technologies for mars missions, in: Mars Exploration Workshop, Houston, TX, 2012.

[82] E. Venkatapathy, P. Wercinski, A. Cassell, B. Smith, B. Yount, Adept-a mechanically deployable entry system technology in development at nasa, ARC-E-DAA-TN31194, NASA.

[83] S. Dutta, B. Smith, D. Prabhu, E. Venkatapathy, Mission sizing and trade studies for low ballistic coefficient entry systems to venus, in: Aerospace Conference, 2012 IEEE, IEEE, 2012, pp. 1–14.

[84] B. Smith, A. Cassell, E. Venkatapathy, Adept for secondary payloads, in: 11th International Planetary Probe Workshop, Vol. 1795, 2014.

[85] E. Bassano, R. Savino, R. L. Forti, A. Ferrarotti, C. Richiello, G. Russo, R. Aurigemma, F. Punzo, P. DellAversana, Irene–italian re-entry nacelle for microgravity experiments, in: 62nd International Astronautical Congress, Cape Town (South Africa), 2011.

[86] R. Savino, R. Aurigemma, P. DellAversana, L. Gramiccia, L. Marraffa, J. Longo, F. Punzo, Irene preliminary study (italian re-entry nacelle preliminary study), in: 10th International Planetary Probe Workshop, 2013.

[87] S. Pagano, R. Savino, Adjustable aerobraking heat shield for satellites deployment and recovery, in: Proceedings of the World Congress on Engineering, Vol. 2, 2017.

[88] R. Wernicke, Preliminary tests of model spacecraft rotor landing system, Tech. rep., Technical report, Bell Helicopter Corporation (1959).

[89] C. R. Haig, The Use of Rotors for the Landing and Re-entry Braking of Manned Spacecraft, Institute of the Aeronautical Sciences, 1960.

[90] H. Glauert, A general theory of the autogyro, Vol. 1111, HM Stationery Office, 1926.

[91] J. Hagen, Rotor landing technology for crew exploration vehicle earth-to-orbit crew transport, in: 1st Space Exploration Conference: Continuing the Voyage of Discovery, 2005, p. 2508.

[92] R. A. Diaz-Silva, D. Arellano, M. Sarigulklijn, N. Sarigul-Klijn, Rotary decelerators for spacecraft: Historical review and simulation results, in: AIAA SPACE 2013 Conference and Exposition, 2013, p. 5361.

[93] A. Levin, R. Smith, Experimental aerodynamics of a rotor entry vehicle, in: 2nd Aerodynamic Deceleration Systems Conference, 1968, p. 950.

[94] R. G. Struth Jr, A theoretical examination of a re-entry capsule incorporating an autorotating rotor., Tech. rep., Naval Postgraduate School Monterey, CA (1986).

[95] A. Levin, R. Smith, Heat-transfer measurements on the rotor blade of a rotor entry vehicle model, Technical Report 67N30684, NASA.

[96] L. A. Young, G. Briggs, E. Aiken, G. Pisanich, Rotary-wing decelerators for

probe descent through the atmosphere of venus, Tech. rep., NASA Moffett Field CA Rotorcraft Division (2004).

[97] T. Lutz, U. Westerholt, P. Noeding, S. Ransom, J. Köhler, Application of auto-rotation for entry, descent and landing on mars, in: 7th International Planetary Probe Workshop, 2010.

[98] T. J. Steiner, L. A. Young, Rotary wing decelerator use on titan, in: Proceedings of the International Planetary Probe Workshop, Vol. 8, 2011.

[99] D. Robinson Jr, Summary of rotochute development, Tech. rep., Kaman Aircraft Corp. Bloomfield CT (1956).

[100] A. LEVIN, An analytical investigation of the aerodynamic and performance characteristics of an unpowered rotor entry vehicle, in: 6th Aerospace Sciences Meeting, 1968, p. 172.

[101] B. Fu, E. Sperber, F. Eke, Solar sail technologya state of the art review, Progress in Aerospace Sciences 86 (2016) 1–19.

[102] F. Tsander, The use of light pressure for flight in interplanetary space, problems of flight by jet propulsion, Israel Program for Scientific Translations, Jerusalem, Israel (1964) 303–321.

[103] M. Urbanczyk, Solar sails-a realistic propulsion for spacecraft, Tech. Rep. 67N40314, NASA (1967).

[104] P. Janhunen, Electric sail, photonic sail and deorbiting applications of the freely guided photonic blade, Acta Astronautica 93 (2014) 410–417.

[105] P. C. E Roberts, P. G. Harkness, Drag sail for end-of-life disposal from low earth orbit, Journal of Spacecraft and Rockets 44 (6) (2007) 1195–1203.

[106] J. Block, M. Straubel, M. Wiedemann, Ultralight deployable booms for solar

sails and other large gossamer structures in space, Acta Astronautica 68 (7-8) (2011) 984–992.

[107] J. M. Fernandez, G. Rose, O. R. Stohlman, C. J. Younger, G. D. Dean, J. E. Warren, J. H. Kang, R. G. Bryant, K. W. Wilkie, An advanced composites-based solar sail system for interplanetary small satellite missions, in: 2018 AIAA Spacecraft Structures Conference, 2018, p. 1437.

[108] T. Luo, M. Xu, Q. Qu, Design concept for a solar sail with individually controllable elements, Journal of Spacecraft and Rockets (2017) 1–9.

[109] L. Puig, A. Barton, N. Rando, A review on large deployable structures for astrophysics missions, Acta Astronautica 67 (1-2) (2010) 12–26.

[110] M. Leipold, M. Eiden, C. Garner, L. Herbeck, D. Kassing, T. Niederstadt, T. Krüger, G. Pagel, M. Rezazad, H. Rozemeijer, et al., Solar sail technology development and demonstration, Acta Astronautica 52 (2-6) (2003) 317–326.

[111] H. Price, J. Ayon, C. Garner, G. Klose, E. Mettler, G. Sprague, Design for a solar sail demonstration mission, in: Space Technology and Applications International Forum, Albuquerque, NM, 2001.

[112] L. Johnson, R. M. Young, E. E. Montgomery Iv, Recent advances in solar sail propulsion systems at nasa, Acta Astronautica 61 (1-6) (2007) 376–382.

[113] L. Johnson, M. Whorton, A. Heaton, R. Pinson, G. Laue, C. Adams, Nanosail-d: A solar sail demonstration mission, Acta Astronautica 68 (5-6) (2011) 571–575.

[114] O. Mori, H. Sawada, F. Hanaoka, J. Kawaguchi, Y. Shirasawa, M. Sugita, Y. Miyazaki, H. Sakamoto, R. Funase, Development of deployment system for small size solar sail mission, Transactions of the Japan Society for

Aeronautical and Space Sciences, Space Technology Japan 7 (ists26) (2009) Pd_87–Pd_94.

[115] N. Okuizumi, A. Muta, S. Matsunaga, H. Sakamoto, Y. Shirasawa, O. Mori, Small-scale experiments and simulations of centrifugal membrane deployment of solar sail craft'ikaros', in: 52nd AIAA/ASME/ASCE/AHS/ASC Structures, Structural Dynamics and Materials Conference 19th AIAA/ASME/AHS Adaptive Structures Conference 13t, 2011, p. 1888.

[116] Y. Tsuda, O. Mori, R. Funase, H. Sawada, T. Yamamoto, T. Saiki, T. Endo, J. Kawaguchi, Flight status of ikaros deep space solar sail demonstrator, Acta Astronautica 69 (9-10) (2011) 833–840.

[117] R. Funase, Y. Shirasawa, Y. Mimasu, O. Mori, Y. Tsuda, T. Saiki, J. Kawaguchi, Fuel-free and oscillation-free attitude control of ikaros solar sail spacecraft using reflectivity control device, in: 28th International Symposium on Space Technology and Science, 2011.

[118] D. Ma, J. Murray, J. N. Munday, Controllable propulsion by light: Steering a solar sail via tunable radiation pressure, Advanced Optical Materials 5 (4).

[119] S. Debnath, L. Fei, Origami theory and its applications: A literature review, World Academy of Science, Engineering and Technology (2013) 1131–1135.

[120] S. A. Zirbel, M. E. Wilson, S. P. Magleby, L. L. Howell, An origami-inspired self-deployable array, in: ASME 2013 Conference on Smart Materials, Adaptive Structures and Intelligent Systems, American Society of Mechanical Engineers, 2013, pp. V001T01A026–V001T01A026.

[121] W. K. Wilkie, J. E. Warren, M. Thompson, P. Lisman, P. Walkemeyer,

D. Guerrant, D. Lawrence, The heliogyro reloaded, in: JANNAF Interagency Propulsion Committee Meeting, Huntsville, AL, 2011.

[122] R. H. MacNeal, J. M. Hedgepeth, H. U. Schuerech, Heliogyro solar sailer: summary report, Vol. 1329, National Aeronautics and Space Administration, 1969.

[123] R. S. Blomquist, Heliogyro control, Carnegie Mellon University, 2009.

[124] E. H. Dowell, Can solar sails flutter?, AIAA journal 49 (6) (2011) 1305–1307.

[125] W. K. Wilkie, J. E. Warren, L. G. Horta, J.-N. Juang, S. C. Gibbs, E. Dowell, D. Guerrant, L. Dale, Recent progress in heliogyro solar sail structural dynamics, in: European Conference on Spacecraft Structures, Materials and Environmental Testing, Brunswick, Germany, 2014.

[126] W. K. Wilkie, J. Warren, L. G. Horta, K. H. Lyle, J.-N. Juang, S. C. Gibbs, E. Dowell, D. V. Guerrant, D. A. Lawrence, Recent advances in heliogyro solar sail structural dynamics, stability, and control research, in: 2nd AIAA Spacecraft Structures Conference, 2015, p. 0431.

[127] D. Guerrant, K. Wilkie, D. Lawrence, Heliogyro blade twist control via reflectivity modulation, in: 53rd AIAA/ASME/ASCE/AHS/ASC Structures, Structural Dynamics and Materials Conference 20th AIAA/ASME/AHS Adaptive Structures Conference 14th AIAA, 2012, p. 1746.

[128] D. Guerrant, D. Lawrence, Heliogyro solar sail blade twist stability analysis of root and reflectivity controllers, in: AIAA Guidance, Navigation, and Control Conference, 2012, p. 4842.

[129] D. V. Guerrant, D. A. Lawrence, Nonlinear torsional dynamics and control of

heliogyro solar sail blades, in: 2nd AIAA Spacecraft Structures Conference, 2015, p. 0435.

[130] P. Wiwattananon, R. G. Bryant, Steering concept of a 2-blade heliogyro solar sail spacecraft, in: International Symposium on Solar Sailing, Kyoto, 2017.

[131] C. A. Rogers, Intelligent material systemsthe dawn of a new materials age (1993).

[132] J. Tani, T. Takagi, J. Qiu, Intelligent material systems: application of functional materials, Applied Mechanics Reviews 51 (8) (1998) 505–521.

[133] R. C. Smith, Smart material systems: model development, Vol. 32, Siam, 2005.

[134] L. M. Schetky, Shape memory alloy applications in space systems, Materials & Design 12 (1) (1991) 29–32.

[135] H. Nagano, A. Ohnishi, Y. Nagasaka, Development of a lightweight deployable/stowable radiator for interplanetary exploration, Applied Thermal Engineering 31 (16) (2011) 3322–3331.

[136] C. Garner, B. Diedrich, M. Leipold, A summary fo solar sail technology developments and proposed demonstration missions, Technical Report JPC-99-2697, NASA.

[137] S. E. Scarborough, D. P. Cadogan, Applications of inflatable rigidizable structures, in: Proc. of Int. SAMPE Symposium and Exhibition, Vol. 51, 2006, pp. 1–15.

[138] R. S. Blomquist, Design study of a solid-state heliogyro solar sail, Ph.D. thesis, Massachusetts Institute of Technology (1990).

[139] A. M. Vinogradov, C. H. Jenkins, J. Su, Y. Bar-Cohen, E. L. Pollard, Functional materials for smart gossamer spacecraft, Progress in Astronautics and Aeronautics 212 (2006) 165.

[140] M. Salama, C. Jenkins, Intelligent gossamer structures-a review of recent developments and future trends, in: 19th AIAA Applied Aerodynamics Conference, 2013, p. 1196.

[141] Y. Liu, J. Genzer, M. D. Dickey, 2d or not 2d: Shape-programming polymer sheets, Progress in Polymer Science 52 (2016) 79–106.

[142] L. H. Dudte, E. Vouga, T. Tachi, L. Mahadevan, Programming curvature using origami tessellations, Nature materials 15 (5) (2016) 583.

[143] C. Lv, D. Krishnaraju, G. Konjevod, H. Yu, H. Jiang, Origami based mechanical metamaterials, Scientific reports 4 (2014) 5979.

[144] E. T. Filipov, T. Tachi, G. H. Paulino, Origami tubes assembled into stiff, yet reconfigurable structures and metamaterials, Proceedings of the National Academy of Sciences 112 (40) (2015) 12321–12326.

[145] X. Liu, J. M. Gattas, Y. Chen, One-dof superimposed rigid origami with multiple states, Scientific reports 6 (2016) 36883.

[146] Y. Liu, M. Miskiewicz, M. J. Escuti, J. Genzer, M. D. Dickey, Three-dimensional folding of pre-strained polymer sheets via absorption of laser light, Journal of Applied Physics 115 (20) (2014) 204911.

[147] Y. Lee, H. Lee, T. Hwang, J.-G. Lee, M. Cho, Sequential folding using light-activated polystyrene sheet, Scientific reports 5 (2015) 16544.

[148] D. Davis, R. Mailen, J. Genzer, M. D. Dickey, Self-folding of polymer sheets

using microwaves and graphene ink, RSC Advances 5 (108) (2015) 89254–89261.

[149] J. Ryu, M. DAmato, X. Cui, K. N. Long, H. Jerry Qi, M. L. Dunn, Photo-origamibending and folding polymers with light, Applied Physics Letters 100 (16) (2012) 161908.

[150] J.-H. Na, A. A. Evans, J. Bae, M. C. Chiappelli, C. D. Santangelo, R. J. Lang, T. C. Hull, R. C. Hayward, Programming reversibly self-folding origami with micropatterned photo-crosslinkable polymer trilayers, Advanced Materials 27 (1) (2015) 79–85.

[151] H. A. Science, Balloon performance calculator, https://www.highaltitudescience.com/pages/balloon-performance-calculator, [Online; accessed 8-June-2018].

Appendix A

Supplementary materials to papers I, II and III

A.1 Prediction of the package configuration

Packaging process is illustrated in Figure A.1. By folding along the thick lines, the blue panels are turned to the back side of the red panels. At the same time, the 12 elements will overlap as demonstrated in Figure A.1b, while the panel vertex angle of 13° guarantees that the red creases are parallel to each other. Since the lower edges of the elements are bounded to the nose cone perimeter, the overlapped elements will simultaneously form a cylinder. The wrapping angle, which is the angle between the red crease and the nose cone perimeter, is set to 33°. Under such condition, the maximum number of overlapping panels is 8, as illustrated in Figure A.1b. This number, as well as the length of the cylindrical package, can be evaluated by simple geometry. It should be noted that material thickness effect is not considered in the design and evaluation, as the number of overlapping layers

is not great, and a precise packaging is not required.

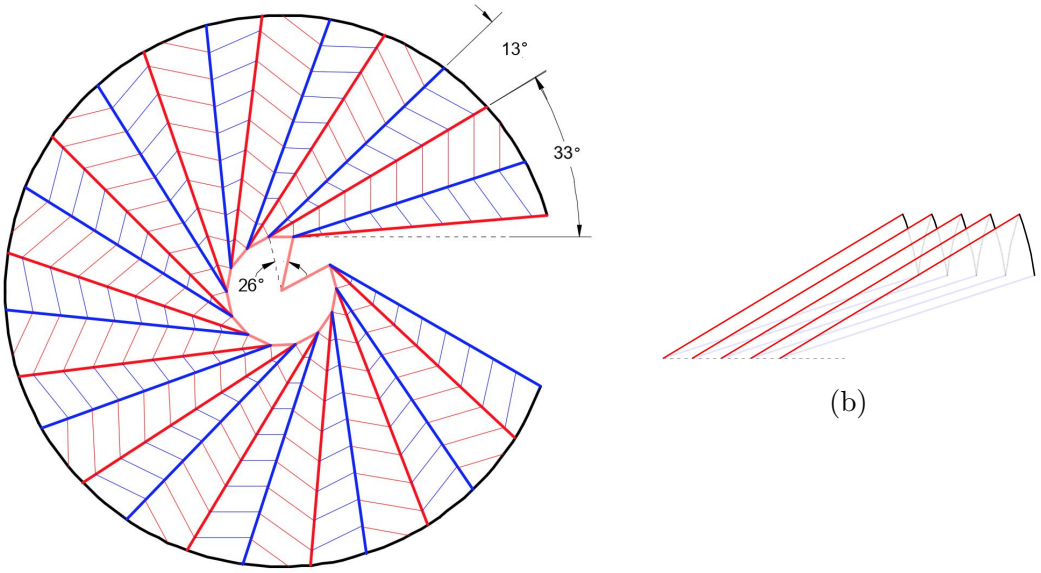

(a) (b)

Figure A.1: Packaging enabled by the origami crease pattern, (a) the baseline design identical to Figure 2.1, (b) example of the folded configuration, where the blue panels are folded to the back of the red panels, creating overlaps, and the panels are simultaneously wrapped around the nose cone

A.2 Simplified geometrical model and calculations

Utilisation of the origami crease pattern allows the shape of the heat shield to be described using a simplified geometrical model based on the origami. The model has been used in the analyses and trajectory simulations reported in paper I, II and III, and has shown acceptable agreement with the drop test and wind tunnel test results reported in paper III. Specifically, the model is used to evaluate: deploying/anti-deploying moments on the shell, oscillating frequencies, Newtonian

aerodynamic roll torque, and vehicle inertia. The detailed calculation are documented in this section.

As an example, the heat shield with Figure 2.4b design is modelled as multiple hinged panels as shown in Figure A.2. Figure A.2a shows two adjacent panels. Assuming zero angle of attack, the flow's horizontal component (due to autorotation) should always be parallel to the local heat shield perimeter. Therefore, transforming the panel geometries to align the horizontal flow directions along the x-axis will align the perimeter-wise edges along x-axis, as shown in Figure A.2b. After transformation, the panels become planar when the shell is fully deployed. When the shell folds, the upper edge will rotate while the lower edges cannot rotate as they are hinged to the rigidified first stage, thus the panel will be twisted, as shown in Figure A.2c. Thus, the calculation of the aerodynamic torque should include an integration of line elements with different twist angles along the generatrix.

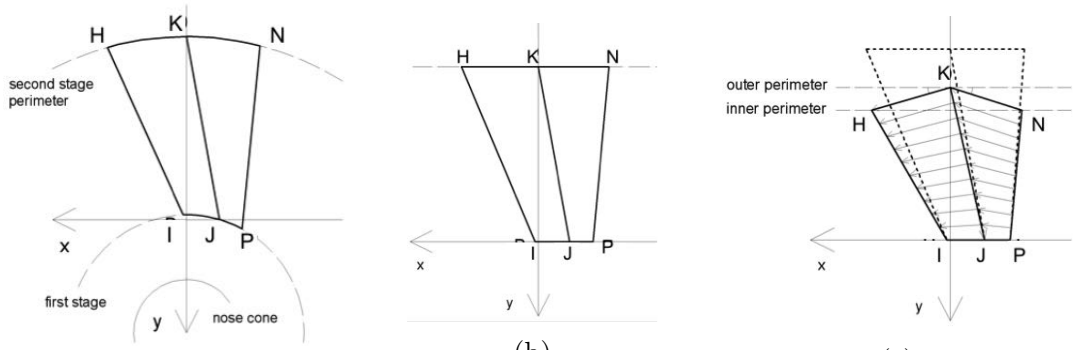

Figure A.2: Schematic draft of two adjacent panels, z-axis is pointing outward, (a) condition in a fully deployed vehicle, (b) after the transformation to align flow directions along x-axis, (c) partially folded condition

Newtonian theory is used to calculate the surface pressure at hypersonic speed, and can still be treated as an assumption at lower speed. It predicts zero pressure difference to ambient at the aft surface, and the front surface pressure is related

to the surface angle of attack:

$$\Delta p = \rho v^2 \cdot \sin^2(\alpha)$$

Surface angle of attack α equals θ when the "skirt" is near fully deployed at high altitude, but α will vary when the "skirt" folds and the spiral shape starts to emerge. In order to reduce the complexity of the calculation, the geometry is simplified to the one in Figure A.3a, where the "skirt" is treated as multiple panels with the local angle of attack denoted as α. The panels have rotated by the angle of ψ due to folding.

Now look at one panel, EF. It is a part of the perimeter when fully deployed, so the length of EF is proportional to $\sin(60°)L+aL$, where L is the generatrix length of the flexible "skirt". The new perimeter is formed by virtual lines such as EG, the length of which is therefore proportional to $\sin(\theta)L + aL$. Thus, in ΔEFG, we have:

$$\cos(\psi) = \frac{\sin(\theta)L + aL}{\sin(60°)L + aL}$$

Then, it is still necessary to relate the angle of attack α to ψ. It is easy to relate α to φ, which, as shown in Figure A.3b, is the angle between the tangent line and the edge BD on a horizontal section plane. In Figure A.3b, OC is the major axis of the vehicle, OB is the generatrix of the fully deployed "skirt", and OD is the generatrix of a partially deployed "skirt". From geometry we have:

$$BC = OB \cdot \sin(\theta)$$

$$DC = BC \cdot \cos(\varphi)$$

$$\sin(\alpha) = DC/OD$$

Assume OB=OD, we have:

$$\sin(\alpha) = \frac{OB \cdot \sin(\theta)\cos(\varphi)}{OD} = \sin(\theta)\cos(\varphi)$$

From geometry, we also have:

$$\varphi = \arctan(\frac{\tan(\psi)}{\cos(\theta)})$$

Thus,

$$\sin(\alpha) = \sin(\theta)\cos(\arctan(\frac{\tan(\arccos(\frac{\sin(\theta)L+aL}{\sin(60°)L+aL}))}{\cos(\theta)}))$$

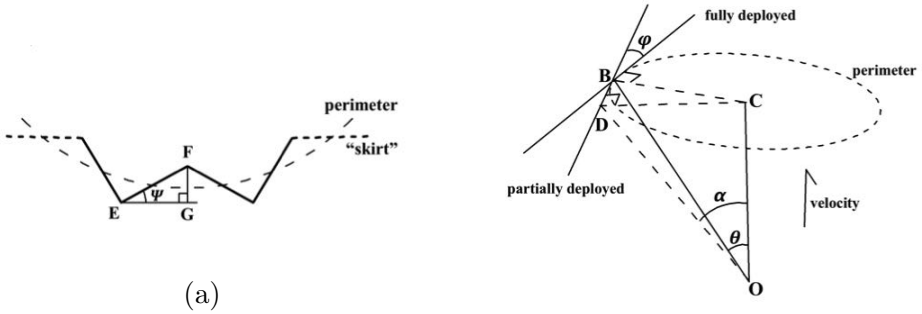

(a) (b)

Figure A.3: Mathematical interpretation of the "skirt"

On any panel on the skirt, the aerodynamic moment can be divided into two components: the folding moment (tangential) and the shear moment (radial), and here we are only interested in the folding moment. Therefore, the aerodynamic anti-deployment moment can be approximated as:

$$M_A = \int \rho v^2 \cdot \sin^2(\alpha) \cdot dS \cdot l$$

Where $dS = 2\pi(l\sin\theta + aL)dl$. It should be noted that a simplified expression with approximation where α is replaced by θ is used in paper I to keep the paper concise and smooth. Such simplification will not cause significant difference when θ is within $30° \sim 60°$.

For the baseline design, the equation above can be simplified to:

$$M_A = \pi\rho v^2 L^3 \sin(\theta)(\frac{2}{3}\sin^2\theta + a\sin\theta)\cos(\arctan(\frac{\tan(\arccos(\frac{\sin(\theta)L+aL}{\sin(60°)L+aL}))}{\cos(\theta)}))$$
$$\approx \pi\rho v^2 l^3 \sin(\theta)(0.0242\theta - 0.565)$$

Similarly, the deploying moment from centrifugal force is:

$$M_{F_C} = \int \omega^2 r l \cos(\theta) \cdot dm$$

Where $dm = 2\pi(l\sin 60° + aL)dl\rho_S$. For the baseline design, the equation above can be simplified to:

$$M_{F_C} = \pi\rho_S\omega^2 L^4 \cos(\theta)(\frac{1}{2}\sin\theta\sin 60° + \frac{2}{3}a\sin\theta + \frac{2}{3}a\sin 60° + a^2)$$
$$\approx \pi\rho_S\omega^2 L^4 \cos(\theta)(0.01\theta + 0.788)$$

The deploying moment from deceleration inertial force is:

$$M_g = \int a_{dec} l \sin(\theta) \cdot dm$$

For the baseline design, the equation above can be simplified to:

$$M_g = \pi\rho_S L^3 a_{dec}\sin(\theta)(\frac{2}{3}\sin 60° + a)$$
$$\approx 1.16\pi\rho_S L^3 a_{dec}\sin(\theta)$$

The equation above can be furture simplified by subsituting:

$$a_{dec} = \frac{qSC_D}{m} \approx \frac{q(0.0117\theta - 0.232)}{\rho_S}$$

Therefore the spin rate at a certain deployment angle θ and under the static equilibrium condition, $\omega_{equi.}$ can be evaluated by solving:

$$M = M_{F_C} + M_g - M_a = 0$$

Paper I has also shown that the shell's natural frequency has a similar expression to equilibrium spin rate and aerodynamic pitching frequency.

The natural frequency can be expressed as below:

$$f_{natural} = \frac{1}{2\pi}\sqrt{\frac{\frac{\partial M}{\partial \theta}}{I_{deploy}}}$$

Where the expression of M contains ω. For paper I, ω is substituted by $\omega_{equi.}$ in order to compare to the FE simulation which assumes constant angular velocity. For paper II it is substituted by $\omega = \omega_{equi.} I_{spin_{equi.}}/I_{spin}$ to account for the coupling between ω and θ due to the conservation of angular momentum. Where I_{spin} is the vehicle angular inertia associated with the autorotating motion that is discussed later in this section as a function of θ, and $I_{spin_{equi.}}$ is the inertia under the equilibrium deployment angle. The prediction using the two methods show acceptable difference. For instance, the paper II expression ($0.179\sqrt{q/l^2}$ Hz) is $\sim 10\%$ higher than the paper I result ($0.160\sqrt{q/l^2}$ Hz) for a baseline design.

The pitching frequency is derived from the expression shown below [1]:

$$f_{pitch} = \sqrt{\frac{C_{N_\alpha} \cdot l_{static.margin} \cdot q \cdot S}{I_{pitch}}} \approx \sqrt{\frac{C_{N_\alpha} \cdot x_{cp} \cdot q \cdot S}{I_{pitch}}}$$

From literature, the aerodynamic normal force coefficient and C.P. location of a circular cone can be derived using Newtonian Theory [2]:

$$C_N = \cos^2\theta \cdot \sin 2\alpha$$

$$x_{cp} = L_{height}(-\frac{2}{\cos^2\theta})$$

Thus,

$$C_{N_\alpha} = 2\cos^2\theta$$

[1] Platus, D. H. A Simple Analysis of Reentry Vehicle Roll Resonance. (1967).

[2] Viviani, A. & Pezzella, G. Aerodynamic and Aerothermodynamic Analysis of Space Mission Vehicles. (2015).

Given that the distance from vertex to C.P. is similar to the static margin since the vehicle c.m. is relatively close to the vertex, we have:

$$f_{pitch} \approx \sqrt{\frac{4L_{height}qS}{3I_{pitch}}}$$

The pitching moment of inertia of the fully deployed heat shield about the vertex is:

$$(\frac{\sin^2 60^\circ}{4} + \frac{\cos^2 60^\circ}{6})\pi\rho_S \cdot \sin 60^\circ \cdot L^4_{generatrix}$$

The inertia of the payload has been ignored in the calculations. This is not expected to induce significant error since the payload is located at centre and near the vertex.

Then consider the aerodynamic roll-torque. Assume the spin axis is aligned along z-axis, a horizontal upper edge of the "skirt" HK in Figure A.2 (the line element at $l = L$) is aligned along x-axis (1,0,0) when the "skirt" is fully deployed and rotates around z-axis by angle φ during folding. The twist angle of an element with a distance of l from the first stage is $\varphi \cdot l/L$. Meanwhile, the twist angle of the adjacent panel's upper edge is set to $-\arcsin(\sin\varphi/0.92)$ where 0.92 is the ratio KN/HK, so N falls onto the inner perimeter.

The normal vector of elements in the left and right panel can be expressed as below respectively in MATHEMATICA style, where $\overrightarrow{DC} = (-10, 60\sin(\theta), -60\cos(\theta))$ according to the baseline design, and $\overrightarrow{DA} = (1, 0, 0)$ when the shell is fully deployed:

$$\overrightarrow{P_{left}} = Normalise[Rotation\ matrix[\frac{\varphi \cdot l}{L}, \vec{z}] \cdot \overrightarrow{DA} \times \overrightarrow{DC}]$$

$$\overrightarrow{P_{right}} = Norm.[R.m.[-\arcsin(\frac{\sin(\frac{\varphi \cdot l}{L})}{0.92}), \vec{z}] \cdot \overrightarrow{DA} \times \overrightarrow{DC}]$$

The aerodynamic pressure has two components: the component parallel to the y-z plane that causes folding and the component along x-axis that causes autorotation.

The first is not of interest since the deploying-folding behaviour is already modelled with sufficient accuracy, while the second can be resolved by $\vec{P_x} = \vec{P} \cdot (-1, 0, 0)$, where (-1,0,0) is the direction of pressure that drives the desired autorotation.

Then, the direction of the flow needs to be resolved to determine the angle of attack, and therefore, the magnitude of Newtonian aerodynamic pressure. The flow direction referred to the perimeter of a fully deployed "skirt" is defined as (c,0,1), where the dimensionless value c is the ratio between the horizontal and the axial flow velocity at the rim of a fully deployed shell. Thus the direction of flow at a line element at a distance l from the first stage is:

$$\vec{v} = (\frac{(aL + l \cdot \sin(\theta)) \cdot c}{aL + L \cdot \sin(60°)}, 0, 1)$$

Therefore, the angle of attack can be resolved in MATHEMATICA:

$$\alpha_{left} = 90° - angle\, between[\vec{P}_{left}, \vec{v}]$$
$$\alpha_{right} = 90° - angle\, between[\vec{P}_{right}, \vec{v}]$$

Thus, the axial aerodynamic torque can be calculated by integrating the torque from the aerodynamic pressure along the x direction as below, where $aL + l \cdot \sin(\theta)$ is the arm of force.

$$\tau = \rho v^2 S \int_0^L \frac{\sin^2(\alpha_{left}) \cdot \vec{P}_{x_{left}} + \sin^2(\alpha_{right}) \cdot \vec{P}_{x_{right}}}{1.92} \cdot (aL + l \cdot \sin(\theta)) \cdot dl$$

The trajectory simulator also requires the input of vehicle angular inertia. This is assumed to be equal to the heat shield angular inertia, which changes with deploy angle, and is calculated by integrating the inertia of conical ring elements along the axis as below, where r and dm are the radius and mass of the ring element:

$$I_{spin} = \int r^2 dm = \int_0^L r^2 2\pi r \rho_S dl$$

Calculate separately for the rigid 1st stage and the flexible 2nd stage, we have:

$$I_{spin} = \int_0^{L_{total}-L} 2\pi\rho_S(\sin 60^\circ \cdot l)^3 dl + \int_0^{L} 2\pi r\rho_S(aL + \sin\theta \cdot l)^2(aL + \sin 60^\circ \cdot l)dl$$

Integrating, we have:

$$\begin{aligned} I_{spin} &= 0.5\pi r\rho_S \sin^3 60^\circ (L_{total} - L)^4 \\ &\quad + \frac{1}{6}\pi r\rho_S[4a(3 + 3\sin\theta + \sin^2\theta) + \sin 60^\circ(6 + 8\sin\theta + 3\sin^2\theta)]L^4 \\ &= 0.5\pi r\rho_S \sin^3 60^\circ (L_{total} - L)^4 + \pi r\rho_S L^4(0.679 + 1.34\sin\theta + 0.819\sin^2\theta) \end{aligned}$$

To save computational resource, note that mass is already calculated at the beginning of simulation:

$$m_1 = \pi \sin 60^\circ (L_{total} - L)^2 \rho_S$$

$$m_2 = 2.02\pi L^2 \rho_S$$

Thus,

$$\begin{aligned} I_{spin} &= 0.5m_1 \sin^2 60^\circ (L_{total} - L)^2 + 0.405m_2(0.828 + 1.63\sin\theta + \sin^2\theta)L^2 \\ &\approx 0.5m_1 \sin^2 60^\circ (L_{total} - L)^2 + m_2(0.0149\theta + 0.324)L^2 \end{aligned}$$

A.3 Prototype elasticity measurement by powered spin test

Before the drop test, another experiment has been carried out to partially verify the analytical model as well as the elastic effect of the flexible shell. The drop test has weaved the importance of this work. However, it is still documented here as it demonstrates the method used to correct the elastic effect in paper III.

First of all, a simple latex rubber prototype is fabricated using a single-sided mould. The mould is built upon a foam core, which is cut out from foam block using a customised jig, as shown in Figure A.4 (a). It utilises a straight hot wire to cut out a first-order curved surface that is generally the same as a 3D model produced by lofting. The mould shape is based on the shell geometry with 55° deployment angle. Then the mould is completed by covering the foam core with glass fibre reinforced epoxy and aluminium foil tape, which improves handling and assists the releasing of cured latex rubber. The completed mould is shown in Figure A.4 (b).

Figure A.4: The single-sided mould for latex rubber prototype fabrication, (a) cutting foam core using the customised jig, (b) the finished mould

Then the latex rubber is brush-coated onto the mould. Each coating has a thickness of approx. 0.04 mm, thus a 1 mm thickness can be formed by 25 layers of coatings. Result is shown in Figure A.5. It worth noticing that the folded (by gravity) shape closely matches the paper origami design.

Powered spin test jig that can hold and spin up the prototype is developed using off-the-shelf devices (Figure A.6). Geared motor is used to directly drive the spin, the speed of which can be adjusted within a certain range ($0 \sim 85\,rpm$ for the current motor and gearbox) by adjusting the input voltage. Single direction bearing is used to transmit torque from the motor only in the primary direction,

Figure A.5: The prototypes, (a) side view, (b) top view, (c) top view of the paper prototype

thus eliminating the shock on the prototype in case of abrupt stop. Hall effect sensor is used to measure the spin rate and display it on a LCD in real time. Spin rate is adjusted manually, which allows an accuracy of $\pm 0.5\, rpm$.

A series of deployment angles from 15°to 60° with 5° interval is set as deployment targets, and the spin rate required to achieve those targets are evaluated using the analytical model. The tests are then carried out by spinning up the prototype to the calculated spin rates and measure the deployment angles using the IMU in an iPhone. The measurement is done twice on both sides of the prototype and the average is reported. The accuracy is approximately ±1°.

The analytical equation used to evaluate spin rate is revised by eliminating the aerodynamic terms, thus the static deployment criterion becomes:

$$M_{F_C} + M_g = \pi \rho_S L^3 [\cos\theta \cdot \omega^2 L \cdot (\frac{1}{2}\sin\theta \sin 60° + \frac{2}{3}a \cdot \sin\theta + \frac{2}{3}a \cdot \sin 60° + a^2) + a_{dec} \sin\theta \cdot (\frac{2}{3}\sin 60° + a)] = 0$$

Where $a = 0.5$ is the ratio of the first stage. Thus we can solve for the required

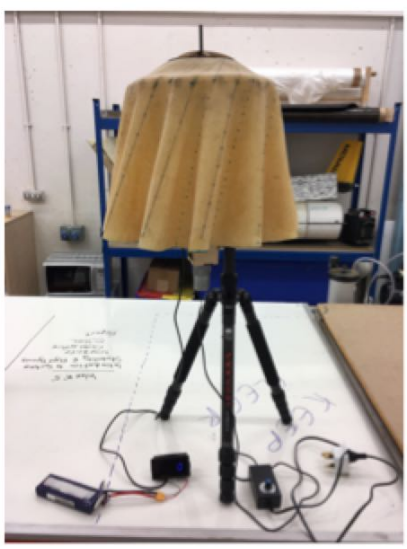


Figure A.6: The motor-sensor-prototype assembly is mounted onto a tripod for sturdiness; the prototype with deployable first stage is used

spin rate ω by substituting θ with the target deployment angle:

$$\omega = \sqrt{\frac{-a_{dec} \cdot \sin\theta \cdot (\frac{2}{3}\sin 60° + a)}{\cos\theta \cdot L \cdot (\frac{1}{2}\sin\theta \sin 60° + \frac{2}{3}a \cdot \sin\theta + \frac{2}{3}a \cdot \sin 60° + a^2)}}$$

The results are shown in Figure A.7. The red curve is from the tests with spin rates evaluated from the equation above. It can be seen that the resulted deployment angles differ from prediction. Those differences are acceptable as a preliminary study since within the critical flight regime predicted by the trajectory simulator the deployment angle is always above 45°, at which the difference is low.

The analytical model is then revised to account for the elastic effects and provide a better agreement with tests, thus the model can be validated better. In the tests, the input of spin rate yields a certain value of deployment angle. Therefore, the correction should be done to change the spin rate input in order to achieve a deployment angle closer to the target. To realise this, the elastic effect is assumed to be equivalent to the effect of a spin. E.g. at rest in the -1g environment, the

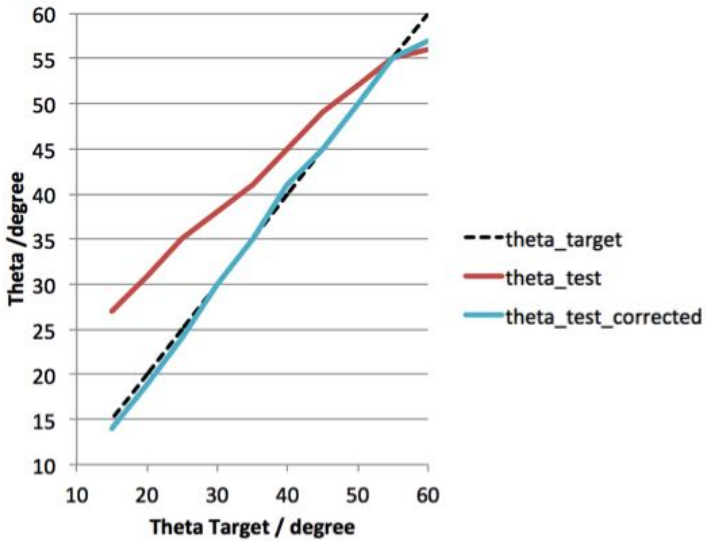

Figure A.7: Test results using the spin rates evaluated using the original analytical model (red) and the model corrected for elasticity (blue)

shell has a deployment angle of 14° rather than 0° due to the elasticity, which is equivalent to a spin rate of 36.17 rpm according to the previous equation. Set this value as $\omega_{14^\circ} = 36.17$. Now set the target deployment angle to $\theta = 14^\circ$, the deployment criterion becomes:

$$M_{F_C}+M_g = \pi\rho_S L^3[\cos\theta\cdot(\omega_{test}^2+\omega_{14^\circ}^2)L\cdot(\frac{1}{2}\sin\theta\sin 60^\circ+\frac{2}{3}a\cdot\sin\theta+\frac{2}{3}a\cdot\sin 60^\circ+a^2) + a_{dec}\sin\theta\cdot(\frac{2}{3}\sin 60^\circ + a)] = 0$$

Where M_E is the deploying moment caused by elasticity, and ω_{test} is the real spin rate of the prototype. Thus the effective spin rate consisted of the elasticity and the prototype's real spin rate becomes:

$$\omega_{effective} = \sqrt{\omega_{test}^2+\omega_{14^\circ}^2} = \sqrt{\frac{-a_{dec}\cdot\sin\theta\cdot(\frac{2}{3}\sin 60^\circ + a)}{\cos\theta\cdot L\cdot(\frac{1}{2}\sin\theta\sin 60^\circ + \frac{2}{3}a\cdot\sin\theta + \frac{2}{3}a\cdot\sin 60^\circ + a^2)}}$$

Solving under the condition of $\theta = 14^\circ$ and a=0.5 (according to the dimension of

the prototype), we have:

$$\omega_{effective} = \omega_{14^\circ}$$

$$\omega_{test} = 0$$

This means the prototype does not needs to spin to reach $\omega = 14^\circ$, which is true.

Then the correction can be generalised to work at more deployment targets. We know that the deployment angle of 55° there is no elastic effect since this is the shell's initial fabricated state, thus the equivalent spin rate at $\omega = 55^\circ$ is $\omega_{55^\circ} = 0$. Now assume the following relation between the equivalent spin rate and θ shown below, which gives a near linear elastic behaviour $M_E \propto \theta$.

$$\omega^2_{equivalent\,\theta} = \omega^2_{14^\circ} \cdot \frac{55^\circ - \theta}{55^\circ - 14^\circ}$$

Then we can evaluate the spin rate for reaching a certain θ target with the correction of elasticity ω_{test}. The result is satisfactory as plotted in blue in Figure A.7, which has very close agreement with prediction (difference $< 1^\circ$).

A.4 Wind tunnel scaling

The parameters for dynamic aeroelasticity similitude that should be kept constant during scaling-down are discussed below.

Mach number, which influences the flow condition at transonic speed or above, where a is sonic speed and T is freestream temperature:

$$M = \frac{v}{a} \propto \frac{v}{T^{0.5}}$$

Thus,

$$v \propto T^{0.5}$$

Reynolds number is related to the ratio between the inertia and viscous force of fluid in boundary layer, and influences the transition of laminar to turbulent flow, boundary layer thickness, flow separation, etc., where ρ is fluid density, μ is viscosity:

$$Re = \frac{\rho v l}{\mu} \propto \frac{Pl}{T^{0.5}}$$

Since

$$P \propto \rho \cdot T$$

Strouhal number is related to the flow induced by periodic perturbations of the vehicle, which takes into account the flow caused by spinning.

$$N_{Str} = \frac{\omega l}{v}$$

Ignoring the secondary effects such as Reynolds number, the scaling of Strouhal number is naturally satisfied ($N_{Str} = constant$) since the vehicle is in free-spinning.

Relative density related to the linear acceleration of structure under aerodynamic force, assuming constant v:

$$\mu_m = \frac{m}{\rho l^3} \propto \frac{m}{Pl^3}$$

For heat shield with similar shape and dynamic behaviour dominated by surface density ρ_S,

$$\mu_m \propto \frac{\rho_S}{Pl}$$

Relative mass moment of inertia related to angular acceleration of structure under aerodynamic torque:

$$\mu_{I_m} = \frac{I_m}{\rho l^5} \propto \frac{I_m}{Pl^5}$$

For heat shield with similar shape and dynamic behaviour dominated by surface density,

$$\mu_{I_m} \propto \frac{\rho_S}{Pl} \propto \mu_m$$

Which is satisfied simultaneously with relative density.

Aeroelastic bending parameter related to the bending of structure under aerodynamic load:

$$\epsilon = \frac{EI}{\rho v^2 l^4} \propto \frac{EI}{Pl^4}$$

Where E is Young's modulus, I is the area moment of inertia of cross section. For the fabric on heat shield, which is dominating,

$$\epsilon \propto \frac{Et^3}{Pl^3}$$

Where t is the shell's thickness.

"Deploy-ability", related to the stabilised deploy angle:

$$\tan\theta = \frac{lk^2\rho_S}{\rho} \propto \frac{\rho_S}{\rho l}$$

A.5 Rigid/semi-rigid model test in the HSST tunnel

The High SuperSonic Tunnel (HSST) in the University of Manchester could provide Mach 4 $\sim$ 6 flow that lasts for 8 s, which is longer than enough for the models to reach equilibrium state. Since the static pressure reduces with increasing Mach number, the highest possible Mach number, Mach 6, is chosen in order to obtain a better scaling. Available data shows two possible static temperatures: 300K and 700K. Both included in the scaling analysis in Table A.1, where the vehicle condition corresponds to peak dynamic pressure of 180 Pa at an altitude of 66.5 km (simulated with interpolation atmospheric model and starts from 145 km orbit with zero flight path angle).

Table A.1: HSST test scaling, with Mach 6 flow and two static temperatures

Title	Simulated condition	HSST 400kPa 300K	HSST 400kPa 700K
Base diameter / m	0.70	0.036	
Fluid density / kg/m^3	1.22×10^{-4}	0.0250	0.0108
Temperature / K	227	37	86
Static pressure / Pa	7.94	260	
Dynamic pressure / Pa	180	6600	
Scaling parameters	Reynolds number	4.18	2.74
	Relative density	$\rho_S/10.6$	$\rho_S/4.6$
	Aeroelastic bending	$225Et^3$	

It can be seen that for the rigid model to which only Mach number and Reynolds number are important, the test with 700 K static temperature could provide reasonable result, and the test with 300 K static temperature may also be acceptable. For the semi-rigid model test, it is necessary to scale the deploy-ability (equivalent to relative density), which, as shown in Table A.1, requires the shell thickness to be increased to 4.6 mm (so the surface density is increased without changing the shell material) for a test with 700 K static temperature, or 10.6 mm for a test with 300 K static temperature. It can also be seen that the aeroelastic bending is not likely to be scaled together with deploy-ability, etc. unless a very dense ($10 \sim 20\ g/cc$) and at the same time flexible shell material is available, or sophisticated structures are built into the model to induce anisotropic rigidity.

The rigid model test is to find out how the equilibrium spin rate (at a certain velocity, the spin rate at which the spiral shape generates zero axial aerodynamic torque) and the axial aerodynamic torque are influenced by the "skirt" shape when it deploys and folds. When a model is mounted on a jig that allows free spinning, the equilibrium spin rate of a certain shape can be measured using tachometer or high speed camera, and when the spinning is constrained, axial aerodynamic torque can be measured by a load balance.

The condition with maximum dynamic pressure has a velocity of 1815 m/s equivalent to Mach 6, an equilibrium spin rate of 5.6 rps, and the test will be done at 1115 m/s at the same Mach number. According to Strouhal number, the spin rate from the test is expected to be 67 rps. Test with a 300 K static temperature allows a lower spin rate of 44 rps due to the lower sonic speed. Despite of the high spin rate, which can lead to vibration, the model shape has surface fluctuations with amplitude lower than 100 μm after scaled down to the model size, which is not achievable by most 3D printers, and high resolution CNC machining is needed to capture the critical characteristics.

The semi-flexible model test is to demonstrate the deploy-ability under a condition close to the peak dynamic pressure. This can be done using a silicone model with 36 mm base diameter. The scaling of deploy-ability (i.e. density ratio) can be achieved by increasing the thickness to 4.6 mm. It is true that the thickness can be reduced at the cost of deploy-ability. However, reduced thickness leads to increased equilibrium spin rate, which could lead to various failures since a slight imbalance, which is inevitable for a flexible model, will cause excessive centrifugal force on the jig and completely change the response of the flexible model.

FE simulations are carried out to validate the model design, which has a neutral shape with 30° deployment angle, so that the model can be fabricated using a 3D-printed mould. Simulation showed that the shell cannot be effectively flattened (Figure A.8) even when the thickness is reduced to 1 mm and an excessive spin rate of 270 rps ($> 16,000\, rpm$) is used. Therefore, the semi-flexible model test using such simple silicone model is not viable. This is not surprising considering the unmatched aeroelastic bending factor. This means a more sophisticated model with hinged panels is needed for the semi-flexible model test, which is not practical considering the small model size ($\Phi 36\, mm$).

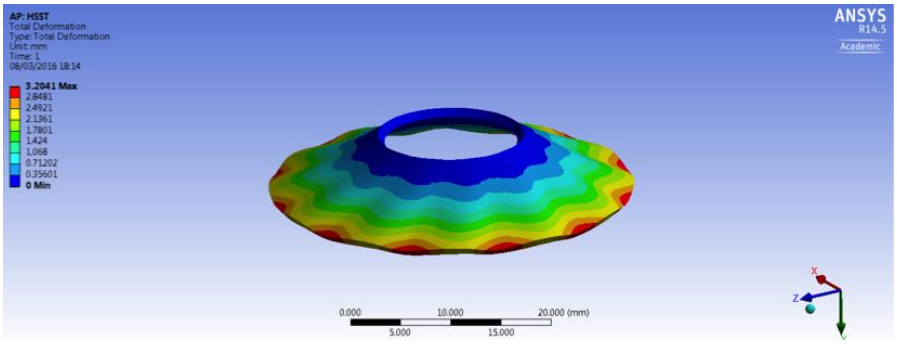

Figure A.8: The silicone model with 1 mm thickness under an excessive spin rate ($> 16,000\,rpm$) shows insufficient flattening

Nevertheless, a free-spinning jig that allow 1DoF free spin of the model was designed at the early stage of this work, and is documented here for future reference.

The jig should minimise the rotational resistance of the spinning part, operate under $\sim 1kg$ axial load and 37 K flow temperature, while minimise the frontal area to reduce blockage. Considering the low temperature, no liquid lubricant is allowed. Therefore, ceramic bearings are ideal for the design, and Zirconia ceramic is chosen for its relatively high thermal expansion coefficient ($\sim 10 \times 10^{-6}/K$). Most steels including mild steel, tool steel and most stainless steels has thermal expansion coefficient around $20 \times 10^{-6}/K$, which, if assembled with ceramic bearings, could lead to a notable relative change in dimension that causes gaps or excessive stress when temperature changes. Gaps should be eliminated since a waggling axle could absorb rotational energy and lead to resistance. Therefore, 410/416 stainless steel is selected for the parts that fit with ceramic bearings, due to their lower thermal expansion coefficient ($\sim 10 \times 10^{-6}/K$) and acceptable manufacturability.

The jig assembly is shown in Figure A.9. It has three components: the axle that rotates freely in the housing, the housing that supports the bearings and the axle, and the adaptor that can be screwed onto the housing after the axle and housing are assembled and then mounted onto the load balance on the right end. The thrust

bearing on the left side balances the axial aerodynamic load, and the double slim nuts on the right end of the axle provide another axial constrain while prevent loosening. Wave washer should be used between the left slim nut and the bearing inner ring to tighten the axle without inducing excessive stress. The tolerances in the drawing are chosen to allow manual installation of bearings while minimising the gaps. All standard components are available online.

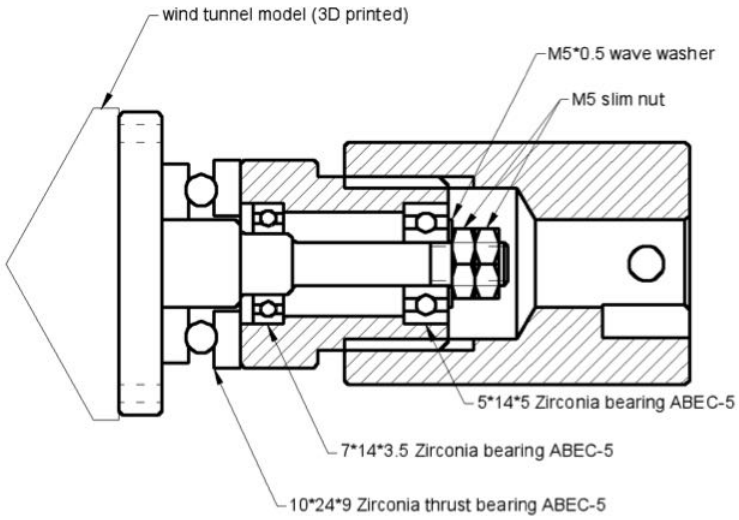

Figure A.9: Free-spinning jig designed for the HSST tunnel: assembly

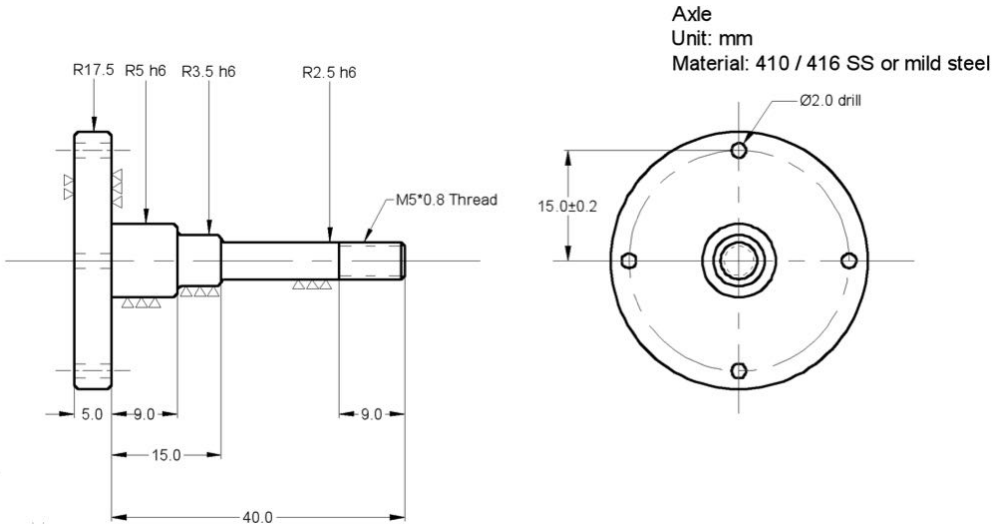

Figure A.10: Free-spinning jig designed for the HSST tunnel: axle

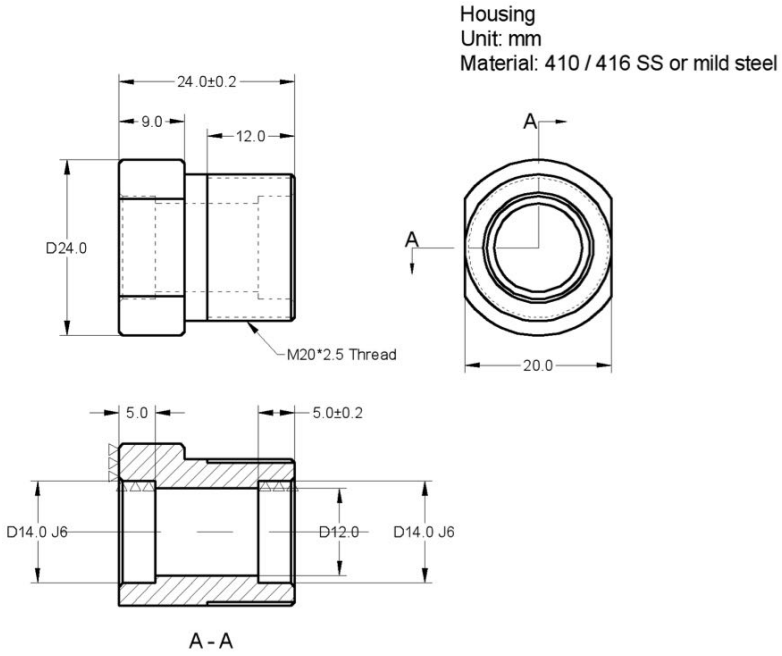

Figure A.11: Free-spinning jig designed for the HSST tunnel: housing

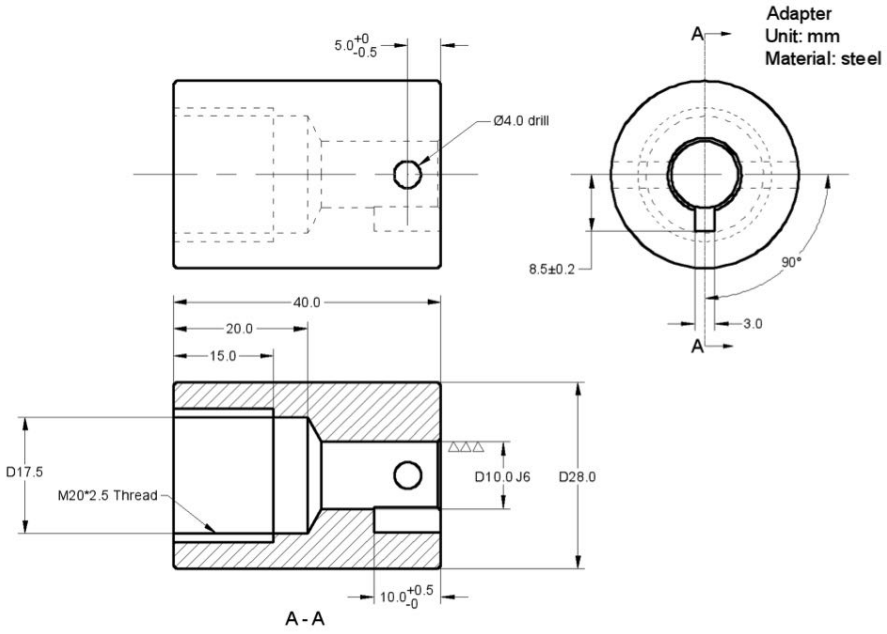

Figure A.12: Free-spinning jig designed for the HSST tunnel: adaptor